

Measurements Of Hard Cosmic X-rays  
With Special Reference To Burst Phenomena

by

John Stewart Mills

Thesis submitted for the degree of  
Doctor of Philosophy  
of the University of London

Blackett Laboratory  
Imperial College  
Prince Consort Road  
London S.W.7

June, 1978

## ABSTRACT

Burst phenomena can be separated into two distinct categories, gamma-bursts and X-ray bursts. The former were discovered more than four years ago by detectors on board the Vela satellites and about 50 such events have been observed to date. The bursts have a well established event average spectrum with an appreciable flux up to several MeV. Their sources follow a roughly isotropic distribution. X-ray bursts are a more recent phenomenon and were discovered in 1975. They display a variety of spectra but rarely have a measurable signal above 30 keV. Their sources are clustered along the galactic plane. The different spectra and source distributions together with other phenomenological differences strongly suggests that the two burst types are unrelated.

The bulk of this work is concerned with the development and subsequent flights of two balloon-borne gamma-burst detectors. The first was a 1 m<sup>2</sup> device which accumulated a total of 13½ hours flying time at a latitude of 40°. The second was a large 7 m<sup>2</sup> detector which was flown from Alice Springs, N. Australia. Both detectors were sensitive to 50 keV - 2 MeV X-rays. The results of these flights are discussed with particular reference to the origin of gamma-bursts.

The nature of X-ray bursts is also discussed, together with the results of observations by Experiment F on Ariel V, of the region of the sky centred on the rapid burster MXB1730-335.

The last chapter is concerned with the development of a large area hard X-ray detector. This device is designed to be built in modular form and have a total collecting area up to 1 m<sup>2</sup>. It is sensitive to X-rays in the range 20 - 200 keV and is collimated by a tantalum honeycomb which has a field of view of 2° FWHM. A small version of this detector was flown on the same platform as the large burst detector.

# C O N T E N T S

	<u>Page</u>
ABSTRACT	1
ACKNOWLEDGEMENTS	2
CHAPTER 1. SATELLITE OBSERVATIONS OF GAMMA-RAY BURSTS	3
1.1.    Introduction	3
1.2.    Vela Satellites	4
1.3.    Imp-6 and Imp-7	7
1.4.    OGO-5	9
1.5.    OSO-6	10
1.6.    Other Detectors	12
1.7.    Burst Structure	14
1.8.    Energy Spectrum	22
1.9.    Burst Size	29
1.10.   Source Directions	37
1.11.   Size Spectra	39
1.12.   Discussion of Source Latitudes	42
CHAPTER 2. THE ONE SQUARE METER BALLOON BORNE BURST DETECTOR	44
2.1.1.   Introduction	44
2.1.2.   Description of Apparatus	44
2.2.    The Detector	46
2.2.1.   Design Criteria	46
2.2.2.   Scintillator Elements	46

		<u>Page</u>
2.2.3.	Light Collection Efficiency	48
2.2.4.	Timing	51
2.2.5.	Lower Threshold	53
2.2.6.	Upper Threshold	57
2.2.7.	Efficiency of Detector	59
2.2.8.	Calibration	65
2.2.9.	Background Count Rate	68
2.2.10.	Mechanical Structure and Thermal Shielding	71
2.2.11.	Environmental Checks	71
2.2.12.	Data Encoding and Transmission	72
2.3.	Flight and Results	75
2.3.1.	Flight Details	75
2.3.2.	Results	75
2.3.3.	Analysis of Results	82
2.4.	The Modified Detector	89
2.4.1.	Configuration	89
2.4.2.	Angular Response	91
2.4.3.	Detector Orientation	95
2.4.4.	Data Encoding	97
2.5.	Flight and Results	98
2.5.1.	Flight Details	98
2.5.2.	Results	98
2.5.3.	Analysis of Results	100
2.5.4.	Conclusions	108

	<u>Page</u>
CHAPTER 3. THE LARGE AREA BURST DETECTOR	109
3.1. Experimental Aim	109
3.2. The Detector	110
3.2.1. General Description	110
3.2.2. Scintillator Elements	112
3.2.3. Slab Calibration	115
3.2.4. Angular Resolution	116
3.2.5. Housekeeping and Attitude Monitors	121
3.2.6. Commands	122
3.2.7. Data Encoding and Transmission	124
3.2.8. Thermal Insulation	128
3.2.9. Environmental Tests	135
3.3. Flight and Results	136
3.3.1. Flight Details	136
3.3.2. Results and Conclusions	138
3.4. Source Models	143
3.4.1. Introduction	143
3.4.2. Stellar Flare Model	144
3.4.3. Accreting Compact Objects	147
3.4.4. Thermonuclear Flash Model	156
CHAPTER 4. X-RAY BURSTS	160
4.1. Introduction	160
4.2. Detection Systems	161
4.3. Burst Source Locations	165
4.4. Burst Structure	169

	<u>Page</u>	
4.5.	Burst Sizes and Burst Separation	174
4.6.	Burst Spectra	179
4.7.	Source Activity Periods	183
4.8.	Long X-Ray Bursts (Flares)	184
4.9.	The Association of X-Ray Bursts with Gamma-bursts	189
4.10.	Hard X-Ray Bursts	193
4.10.1.	COSMOS-428 and OSO-6 Results	193
4.10.2.	Coincident Observations of Hard and Soft Bursts	196
4.11.	Burst Production Mechanisms	203
CHAPTER 5.	THE DESIGN OF A LARGE AREA HARD X-RAY DETECTOR	207
5.1.	Introduction	207
5.1.1.	Need for Correlated Hard and Soft X-Ray Measurements with High Time Resolution	207
5.1.2.	Description of the Detector	210
5.2.	Scintillator Elements and Light Collection	213
5.2.1.	Detectors used in X-Ray Astronomy	213
5.2.2.	Scintillator Element	218
5.2.3.	Energy Resolution and Light Collection	221
5.3.	The Collimator	236
5.3.1.	Collimator Requirements	236
5.3.2.	Collimation Techniques	236
5.3.3.	Design Criteria	237
5.3.4.	Gold Collimator	240

	<u>Page</u>	
5.3.5.	Lead Collimator	241
5.3.6.	Tantalum Collimator	247
5.3.7.	Computer Model	250
5.3.8.	Signal Detection	254
5.4.	Performance	259
5.4.1.	Detection Efficiency	259
5.4.2.	Energy Resolution	261
5.5.	Balloon Flight of Test Module	262
5.5.1.	Introduction	262
5.5.2.	Description of Detector	262
5.5.3.	Environmental Tests	264
5.5.4.	Performance During Flight	266
REFERENCES		270

## A C K N O W L E D G E M E N T S

I am indebted to several people who have helped me to obtain the results presented in this thesis. My supervisor, Dr. J.J. Quenby, has been an unfailing source of advice and encouragement which I greatly appreciate, and I have Professor H. Elliot to thank for giving me the opportunity to carry out research in a very stimulating field.

In connection with the gamma-burst detectors, I am very grateful to Mr. A. Bewick and Mr. K. Beurle with whom I have worked closely, and to Mr. T. Beek whose electronic circuitry made the whole experiment possible.

I wish to thank the Science Research Council for their financial support.

I am grateful to Dr. A.R. Engel with whom I have had many helpful discussions and who has always shown an interest in my work.

Finally, I would like to express my gratitude to my wife Sheenagh whose encouragement and understanding have proved immeasurable.



## CHAPTER 1

### 1.1. Introduction

The first description of the phenomenon now known as a cosmic gamma ray burst was published more than four years ago. Since then about fifty bursts have been detected by satellite borne instruments, usually designed for other purposes. Gamma-bursts are so intense that they temporarily dominate all other celestial sources of gamma rays by several orders of magnitude. If a comparable phenomenon happened to occur within the visible region of the spectrum, it would have been known to primitive man and described in the earliest astronomical writings. Despite this, there is still no generally accepted model which explains how the bursts are generated, and apart from eliminating the solar system, it is impossible to determine from the satellite data where in the universe they are produced.

This chapter describes the various satellite systems which have featured in the detection of gamma-bursts and discusses the general characteristics of the events.

## 1.2. Vela Satellites

The first Vela satellites were launched fourteen years ago for the purpose of monitoring the nuclear test-ban treaty of 1963, which forbids the signatories from exploding nuclear devices in the atmosphere or in outer-space. The Vela spacecraft are launched in pairs into a geocentric orbit of radius  $1.2 \times 10^5$  km with the individual vehicles diametrically opposed. Six such pairs have been launched to date. The satellites carry instrumentation designed by the Los Alamos Laboratory capable of detecting radiations of the type released by nuclear explosions, namely gamma-rays emitted at the moment of fission or fusion, thermal x-rays, and energetic neutrons. As far back as 1965, the launch date of Vela 3, the equipment used was capable of recording enhanced fluxes of photons with energies  $>300$  keV. A search for increased signal levels at the times of supernovae in data produced by the early Vela spacecraft failed to produce any results (Klebesadel et al. 1973).

Vela 4 data were the first to be processed in a form in which the times of recorded events are referred to a common standard, the timing accuracy being  $\pm 2$  secs. These data were searched for near coincident increases with the object of demonstrating that no natural backgrounds were capable of stimulating the various satellites in coincidence. Surprisingly three events were found representing simultaneous responses, one of which was large enough to produce distinctive time records from both spacecraft. These were found to be in excellent agreement.

The Vela 5 and 6 spacecraft were the next to be launched bearing similar but improved instrumentation to Velas 4A and 4B.

The basic detector consists of a 1.9 x 1.9 cm crystal of CsI coupled to a single photomultiplier. The crystal is shielded with 0.1 mms of lead foil, which prevents the direct penetration to the scintillator of electrons with energy below 0.75 MeV, and protons with energy below 20 MeV. Pulse discriminators define an energy window from 0.15 to 0.75 MeV for Vela 5 and 0.3 to 1.5 MeV for Vela 6. The average detection efficiency varies between 17 and 50%. (Klebesadel et al. 1976). Six such detectors are used on each satellite, arranged so as to provide a nearly uniform omnidirectional response. Discrete counts within the energy window are summed and inputted in parallel into a data accumulator and a trigger circuit. This senses rapid increases in the total count rate and initiates data storage in quasi-logarithmically increasing time intervals, starting at 16 ms and going up to 128 s. The time base employed can be related to universal time with an accuracy of  $\sim 20$  ms.

The generation of individual records on the Vela 5 spacecraft is relatively high. However, the increased detection threshold of the Vela 6 satellites has reduced this to an insignificant level. Data analysis only considers events which are observed at two or more spacecraft with a deviation from simultaneity of  $< 4$  s (c/f transit time of light = 0.8 s).

The four satellites operated with virtually continuous coverage from July 1969 to December 1973. During that time twenty-eight events occurred which satisfy the timing criterion and can be proved not to be initiated by solar activity. The events all have detection times which differ by amounts smaller than the light transit time between satellites. Furthermore, the detailed time structure of each increase is reproduced at each of the spacecraft recording the event, even though the radiation

must have traversed an appreciable portion of the geomagnetic field. Simple calculations show, that electron energies of many GeV and proton energies of many MeV are required to satisfy the high value of magnetic rigidity implied by the lack of deflection in the field. Such particles would have created observable effects in other Vela detectors, very sensitive to such phenomena. As no such increases were observed it was concluded that the satellites were indeed responding to bursts of gamma rays (Klebesadel et al. 1973).

Nine other events during this period, which were observed by only one Vela detector, were also seen by other spacecraft and confirmed to be bursts.

The Vela system was operated with a much reduced duty cycle until 1976. Data analysis for that year has so far revealed six bursts during the period January to August, all of which were observed by other spacecraft in addition to the Vela detectors.

### 1.3. Imp-6 and Imp-7

The Imp-6 satellite was launched on 14 March 1971 into an ecliptic orbit with an apogee of  $\sim 2 \times 10^5$  km. The detector was virtually in continuous operation from launch until September 1972, and consisted of a 2.25 inch diameter x 1.5 inch thick CsI crystal viewed by a single photomultiplier. Charged particle rejection was provided by a thin plastic scintillator which entirely surrounded the crystal. The detector operated as a scanning device and was mounted perpendicular to the satellite's spin axis. In addition to full time monitoring of the rates of particle intensity and gamma ray intensity, the energies of incident photons were measured by a fourteen channel analyser. Spectra were accumulated during alternate 2.5 s intervals and read out once every 5.1 s. The energy window employed was either 53-880 keV or 69-1190 keV. The spin period of the satellite was  $\sim 10.5$  s which meant that individual spectra were obtained during different satellite aspects.

During its period of operation the instrument observed six gamma bursts in coincidence with the Vela satellites. All the events were found to have a common spectrum, apart from discrepancies which can be ascribed to differences in the source aspect with respect to the satellite. (Cline et al. 1973.)

The Imp-7 satellite was launched in October 1972 and placed into an approximately circular earth orbit of radius  $2 \times 10^5$  km. The detector on board has been in almost continuous operation since launch and is still functioning correctly. The instrument is identical to the one carried on Imp-6, but different spin rates, data collection modes and duty cycles are used. Data is accumulated in one of two modes.

(1) A continuous mode of operation in which counts are accumulated for 40.9 s in the fourteen channel analyser and then read out. During this time there are about thirty satellite rotations of 1.3 s each which ensures that the detector is more effectively omnidirectional than Imp-6.

(2) Alternatively, data is only stored throughout the 40.9 s interval when the detector is facing the sun, however counts are still accumulated over thirty spins. In this mode it is possible that spectra of some sources will be obtained when the source is partially eclipsed by the satellite, with a corresponding attenuation of lower energy photons by spacecraft material.

Burst events are selected by requiring a  $25\sigma$  deviation from the steady background count rate during one integration period, and the event spectrum must be consistent with the common fit to the Imp-6 data (Cline et al. 1976). This second requirement removes spectrally steep events of magnetospheric origin. Thirty-three increases satisfying these requirements have been discovered to date, and twenty-four of these were detected in coincidence by Vela and (or) other spacecraft. The spectra of nine of these events have been analysed in detail and shown to be consistent with a common fit, after allowing for the different modes of satellite operation (Cline et al. 1975). In addition the Imp-6 spectra also adhere to this fit, after allowing for corrections applied to account for electronic imperfections which do not exist on Imp-7.

1.4. OGO-5

Two of the detectors on board the OGO-5 satellite were capable of detecting gamma bursts.

(1) A lithium drifted solid state detector of thickness  $800\mu$  and area  $10\text{ cm}^2$ , with a lower threshold of  $\sim 150\text{ keV}$  to gamma rays.

(2) A  $5\text{ cm} \times 6\text{ cm}$  CsI crystal-photomultiplier combination having a threshold of  $\sim 5\text{ MeV}$ . (L'Heureux 1974).

During the period March 1968 - July 1971 ten bursts were observed, nine of which were seen by Vela satellites and one, only by OSO-6 in addition to OGO-5.

### 1.5. OSO-6

The OSO-6 satellite also had two instruments on board with burst detection capability. These were the solar x-ray detector designed by the Naval Research Laboratory, and the Bologna wheel experiment.

The former consisted of a 1.27 diameter x 2.54 cm thick NaI crystal which was only operated in the daylight portion of each orbit. Photons in the range 23-82 keV were analysed with a six channel pulse height analyser, and an integral channel was used to measure the flux above 82 keV. Data was accumulated in 1.3 s. time bins and read out once every 2.6 s. The geometry of the system was such that photons with energy  $>80$  keV were detected with an average area of  $3 \text{ cm}^2$  over  $2\pi$  steradians. A counting rate increase was deemed to be significant, if there was a  $5\sigma$  deviation in a single 1.3 s bin in the integral channel, at the same time as an increase in the 70-82 keV channel. Six such events were discovered during the satellite's lifetime (August 1969 - June 1972) which coincided with bursts detected by other spacecraft. Five were observed by Vela detectors and one was confirmed by OGO-5 (Share 1976).

The Bologna wheel experiment was a scanning device positioned at right angles to the satellite's spin axis. It consisted of a  $5 \text{ cm}^2$  NaI crystal sensitive to photons in the range 27-189 keV, the interval being divided into four energy channels. Counts were accumulated in a 15.36 s. time bin and read out during a following 2.4 s period. This corresponded overall to  $\sim 7.5$  satellite rotations (Brini et al. 1973). One burst was observed on 7th October 1964 (Palumbo et al. 1974) in coincidence with the NRL detector and 2 Vela



satellites. The event was a particularly long one lasting well over a minute, and it was seen to consist of two distinct pulses within the wheel experiments resolving time of  $\sim 17.8$  s.

#### 1.6. Other Detectors

In addition to the systems already discussed there are several other satellites that have observed gamma bursts. The Apollo-16 space module detected a burst on 27th April 1972 during its return journey to earth (Metzger et al. 1974). The event was observed by an x-ray spectrometer and a gamma-ray spectrometer, which together provided an energy window stretching from 2 keV to 5 MeV, the widest spectral range over which a burst has been observed to date.

The SAS-2 satellite recorded increases coincident with four bursts during its operational lifetime (November 1972 - June 1973). The bursts were detected by the anti-coincidence dome of the high energy gamma-ray telescope flown on the spacecraft. The dome had an average collecting area of  $2.5 \times 10^3 \text{ cm}^2$  and was virtually an omnidirectional detector, with a lower threshold of 150 keV (Ogleman et al. 1975).

The low orbiting polar satellite 1972-076B observed two bursts, one on the 18th December 1972 and the other on the 21st July 1973 (Imhof et al. 1974). The former was observed by a plastic anti-coincidence dome, and a germanium spectrometer which was sensitive to gamma-rays in the range 50-500 keV. Due to the depletion of solid carbon dioxide the second event was only observed by the anti-coincidence system.

Detailed spectral information about a gamma burst on 14th May 1972 was provided by two x-ray telescopes on OSO-7 (Wheaton et al. 1973). One was a cosmic x-ray detector with a  $6.5^\circ$  FWHM circular aperture, and the other was a device designed to study

solar x-rays, the instrument having a  $90^{\circ} \times 20^{\circ}$  FWHM field of view. Counts in both detectors were accumulated in broad energy channels and read out once every 10.24 s. The burst was also seen by IMP-6 and three Vela satellites, the six detectors providing an energy window which went from 7-1500 keV. To date this is the only event, apart from the burst observed by Apollo-16, to be observed down to energies of a few keV.

The first burst of 1976, detected on 23rd January, was also the first to be detected by a satellite instrument specifically designed for that purpose. The detector was developed by the Goddard Space Flight Centre and is a modification to the interplanetary and solar particle experiment carried on board the Helios-B spacecraft. The device functions in a similar manner to the Vela 5 and 6 detectors, being triggered by a rapid increase in count rate and then recording the event in parallel using 4, 32, and 256 ms time bases. This ensures that good temporal resolution is achieved throughout the event, as opposed to the Vela system where the resolution deteriorates with time. Five bursts have been observed to date, four of which were independently detected by other satellites.

### 1.7. Burst Structure

The study of intensity variations as a function of time is of interest, because such variations allow limits to be placed upon the size of the emitting region responsible for a burst. The varying temporal nature of gamma bursts makes it impossible to talk about a typical event. Burst durations measured by the Vela detectors are found to vary from 0.1-100 s, with an average length of  $\sim 6$  s. The event observed on 17th October 1969 by Vela 5A and which has a duration of only 0.1 s, is illustrated in Figure 1.1. It is evident that there are significant variations at the start of the event, not fully resolved by the 16 ms resolution available immediately after commencement of the data record. An event is usually seen by the Vela satellites to consist of a number of distinct pulses. In contrast the longest duration single pulse, which formed the whole of the event observed on 15th March 1971 by Vela 6A, is shown in Figure 1.2. The duration is  $\sim 10$  s and no appreciable detail is obvious.

The loss of resolution as a function of time following the initiation of a record, as well as the general absence of recoverable data previous to the start of the recording sequence, are shortcomings of the Vela detection system. Other experiments have recorded responses to bursts with constant resolution. The two bursts observed with detectors on board 1972-076B are illustrated in Figure 1.3. The count rates plotted refer to data obtained from one of the two anti-coincidence shields employed on the spacecraft, and represent accumulations during alternate 32 ms intervals. It is immediately apparent that narrow "micro-bursts" exist throughout the event, the

Fig 1.1: Event 69-03  
As Recorded By Vela  
5A.

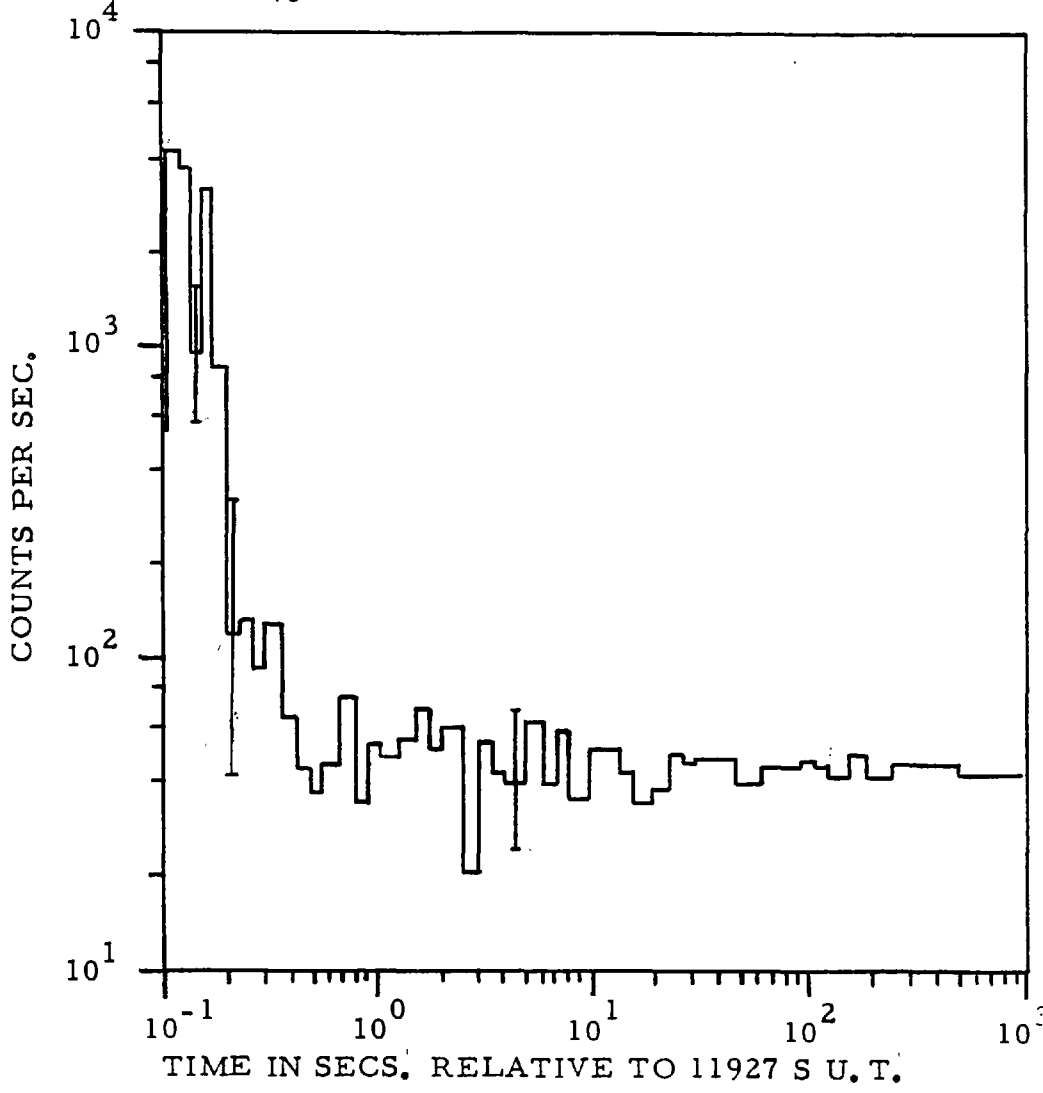
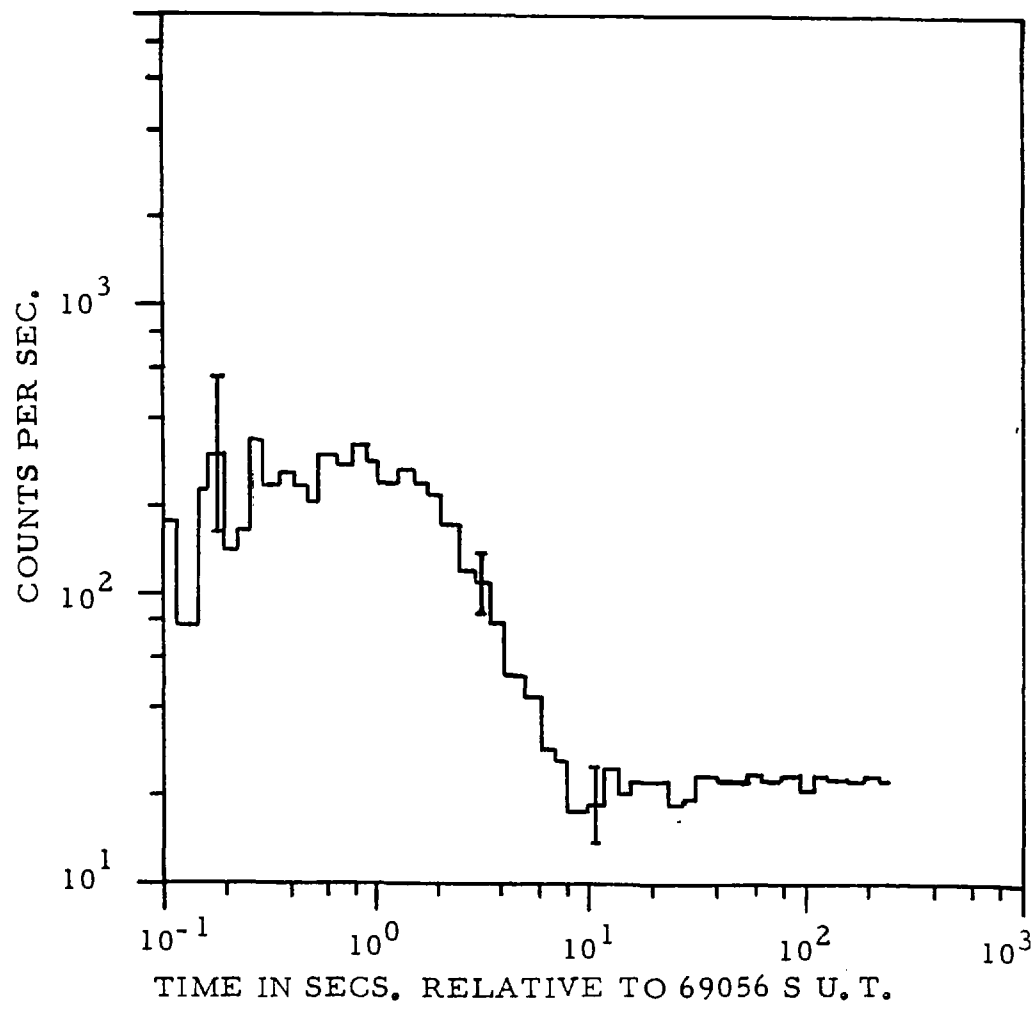


Fig 1.2: Event 71-01  
As Recorded By Vela  
6A.



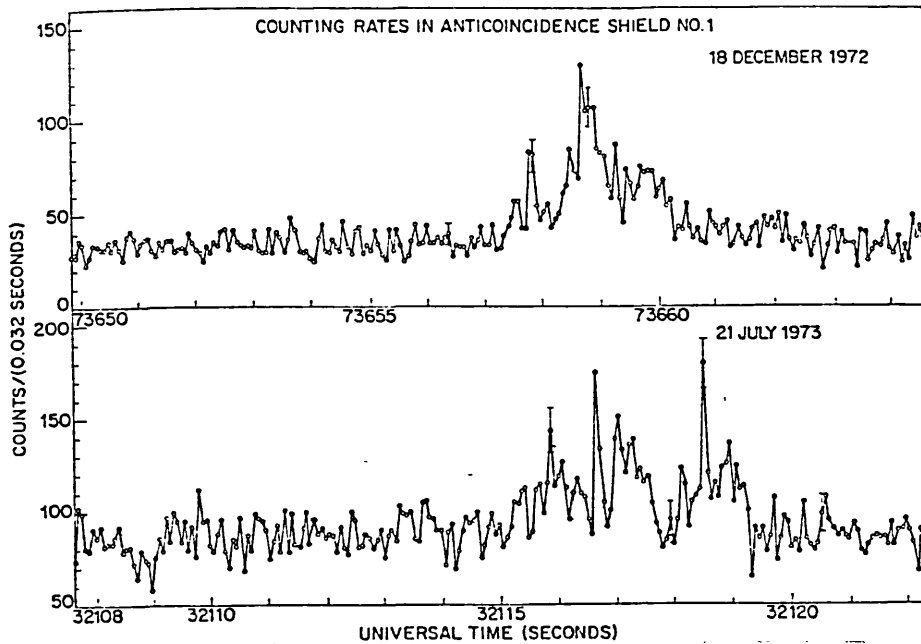


Fig 1.3: Events 72-7 And 73-5 As Observed By Anticoincidence Shield No. 1 On The Satellite 1972-076B.

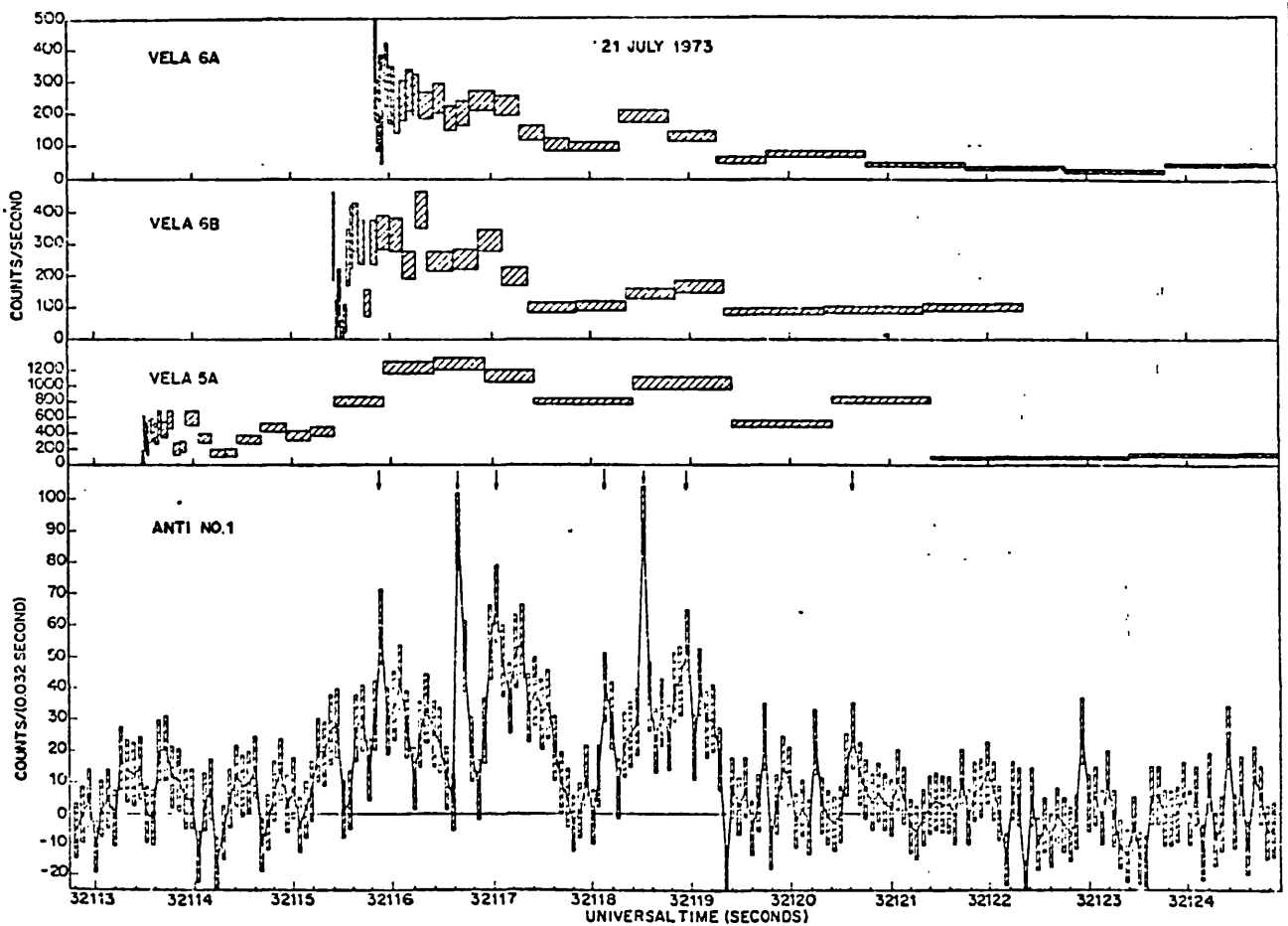


Fig 1.4: Event 73-5 Showing How The Burst Was Recorded By Three Vela Spacecraft. The Error Bars Are 1 Sigma Limits.

widths of which are found to vary between 0.03-0.1 s. There is statistical evidence that there are no pronounced micro-bursts present with widths between 0.007-0.016 ms (Imhof et al. 1976).

The event on 21st July was also recorded by three Vela spacecraft whose count rates as a function of universal time are shown in Figure 1.4, together with the anti-coincidence dome counting rate for comparison. Only the Vela 5A detector recorded the event from the start and it can be seen that the pulse structure present in the various Vela records, actually consists of a series of micro-bursts, not resolved by the timing available on the Vela spacecraft.

More information regarding the fine structure of bursts was obtained from the Apollo-16 gamma-ray spectrometer, which observed the burst on 27th April 1972 over the spectral range 0.067-5 MeV. The count rate is shown in Figure 1.5; the width of the time bins corresponds to the 328 ms integration time of the spectrometer. The event has a very distinct onset and decay phase with the period of maximum intensity inbetween. Several distinct pulses are displayed together with a statistically significant precursor ( $3.1\sigma$ ). Examination of the data stream reveals that after reaching a peak intensity of more than  $1000 \text{ cts s}^{-1}$ , the count rate actually fell to zero for 18 ms and then returned almost, to its previous level. The existence of narrow micro-bursts with widths of  $\sim 50 \text{ ms}$  is also evidenced in the data (Metzer et al. 1974).

Micro-bursts with a width of 2 ms have been observed by the Helios-B satellite. Figure 1.6 illustrates the first second of the event detected on 23rd January 1976, the width of the data bins is 4 ms. The very pronounced spike consists of twenty-three counts in one bin

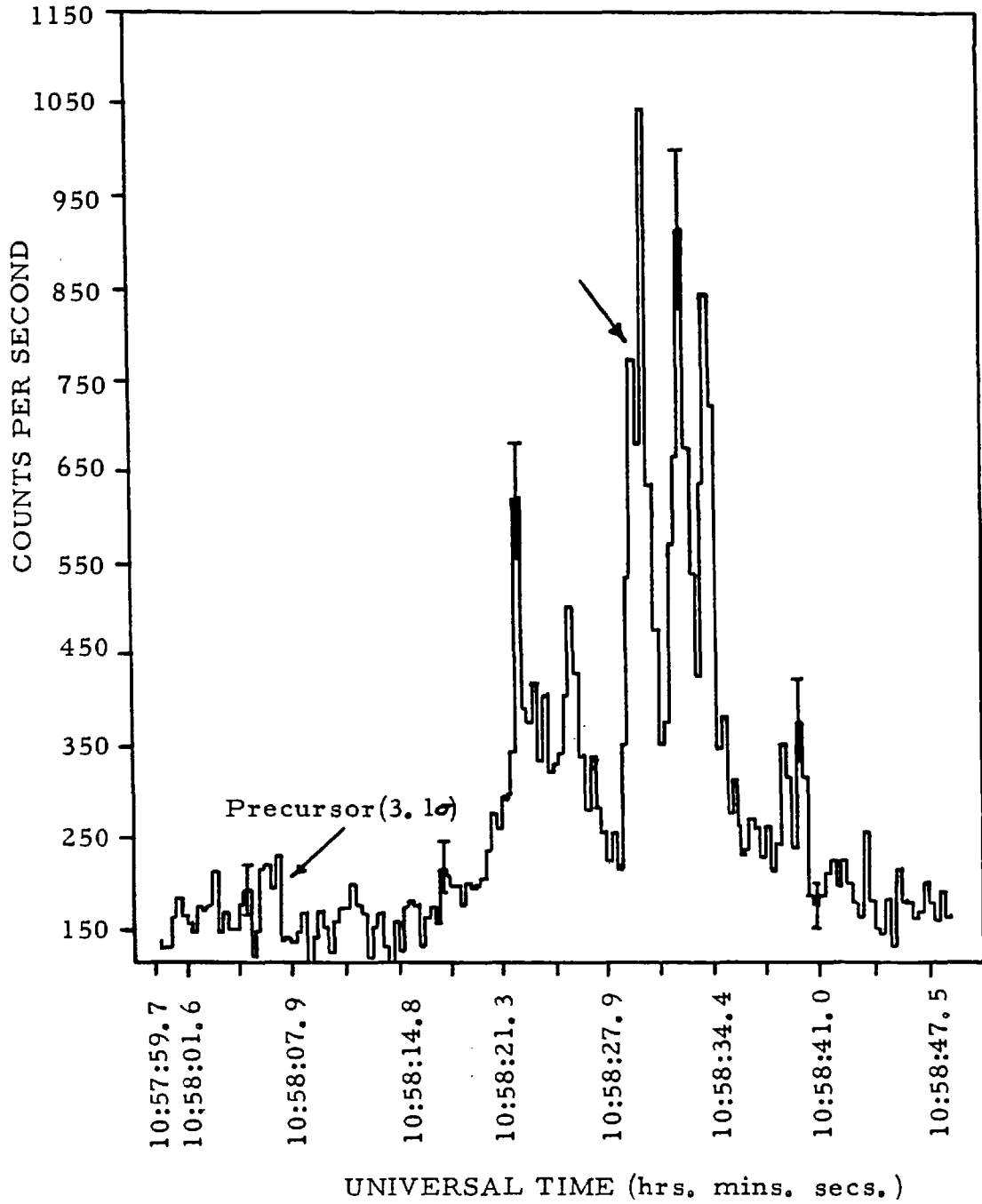


Fig 1. 5: Time Structure Of The Event Recorded By The Apollo 16 Gamma Ray Spectrometer. At The Point Arrowed The Count Rate Fell To Zero For 15 Consecutive Milliseconds.



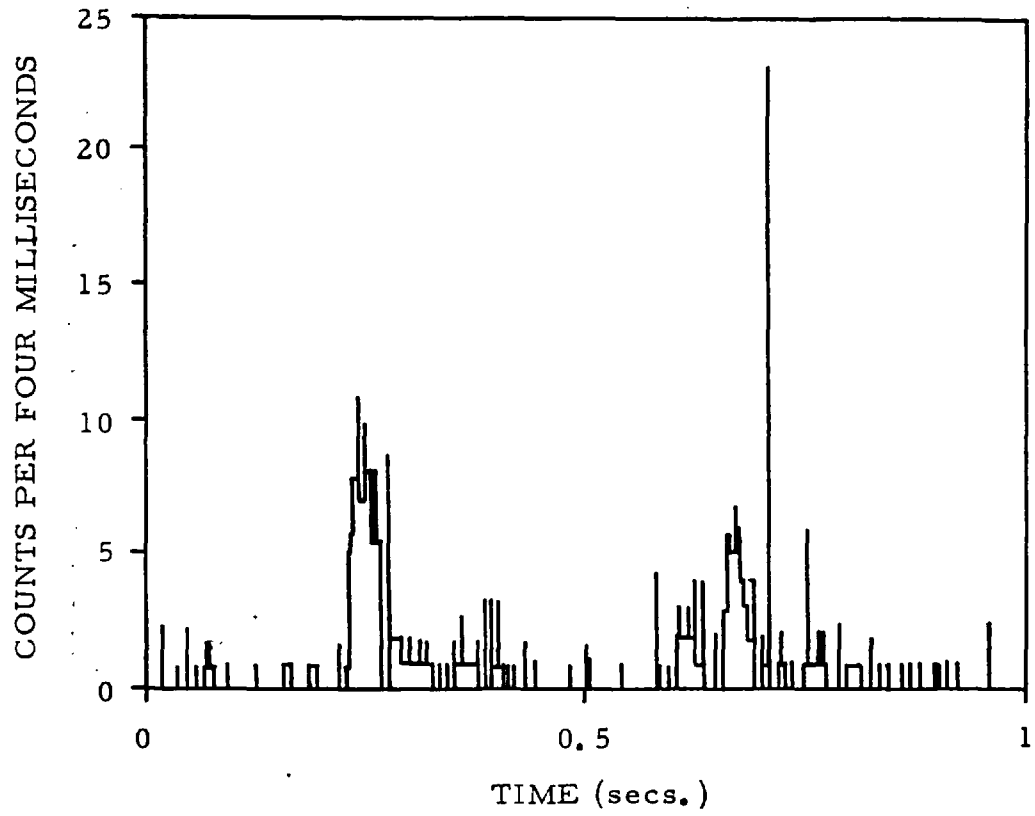


Fig 1.6: Time Structure Of The Event Recorded By The Helios -B  
Spacecraft. Only The First Second Of The Burst Is Shown.

with no more than a single count in adjacent time slots. This indicates that the duration of the spike was no more than  $\sim 2$  ms including both rise and fall. These data display the most rapid variations in intensity recorded to date, and imply a source emitting region of no more than 300 km diameter.

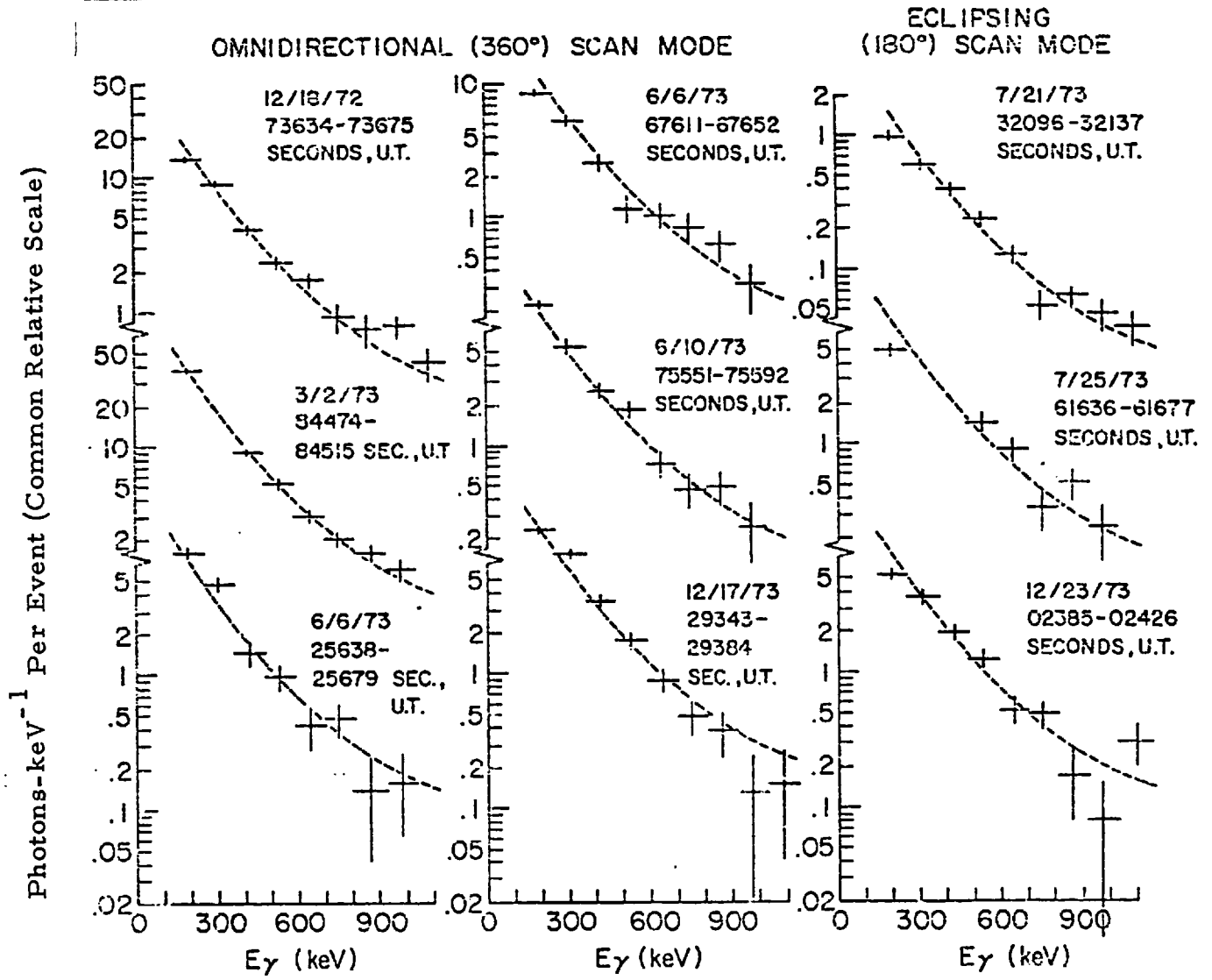


Fig 1.7: Nine Event Average Burst Spectra As Recorded By Imp-7.

### 1.8. Energy Spectrum

Several gamma-bursts have been detected by instruments with intrinsic spectral resolution. Figure 1.7 illustrates nine event average spectra measured by the Imp-7 satellite. Six of these were obtained during the continuous scan mode of operation, and three during the eclipsing mode, already referred to. All the spectra are consistent with a common fit in the range 100-1000 keV which consists of a 150 keV exponential curve, tangent to a power law of index -2.5 at  $\sim 400$  keV. Two of the eclipsing scan mode spectra are deficient at the bottom end, due to attenuation of the softer gamma-rays by spacecraft material. The spinning of the satellite introduces some spectral distortion, as the viewing angle increases with photon energy. However, the distortion is more or less the same for each event which means that the true spectra are also indistinguishable.

The spectrum of the burst observed by Apollo-16 is shown in Figure 1.8. The photon number spectrum is best fitted by a power law of index -1.38 from 2-250 keV, and a power law of index -2.63 from 300-3000 keV. An exponential shape of the form

$$\frac{dN}{dE} = \frac{8.15 e^{-E/325}}{E} \quad \text{photons cm}^{-2} \text{ s}^{-1} \text{ keV}^{-1}$$

is also a reasonable fit in the range 100-1000 keV, as is the standard Imp-7 event average spectrum.

The event observed on 14th May 1972 by the x-ray telescopes on OSO-7, (resolving time 10.24 s) consists of two distinct pulses. The spectrum obtained of the second pulse is shown in Figure 1.9; the shape is identical to the Apollo-16 and Imp-7 spectra.

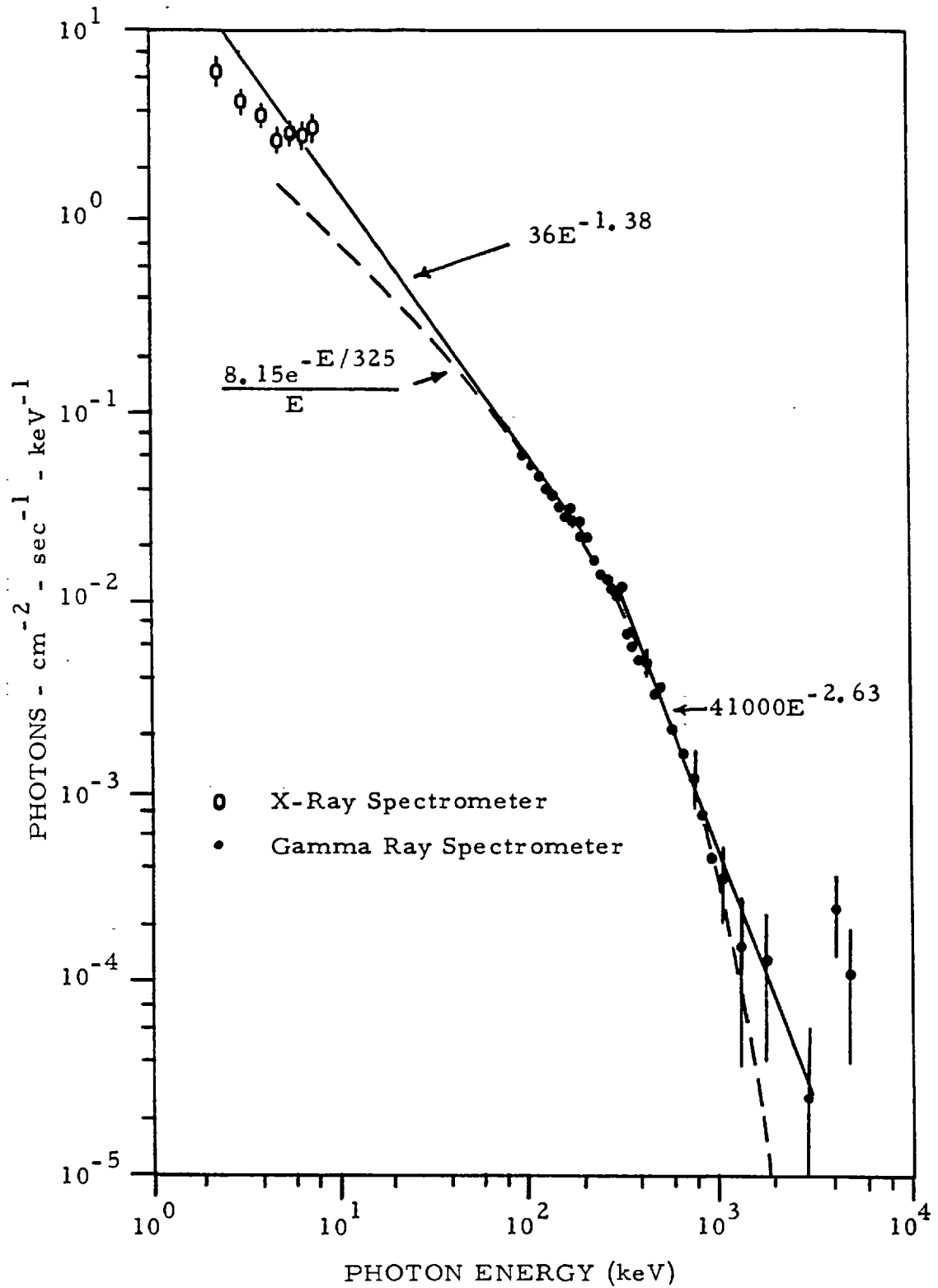


Fig 1.8: The Event Average Spectrum Of The Burst Observed On The 27 April 1972 By The X And Gamma-Ray Spectrometers On Apollo 16.

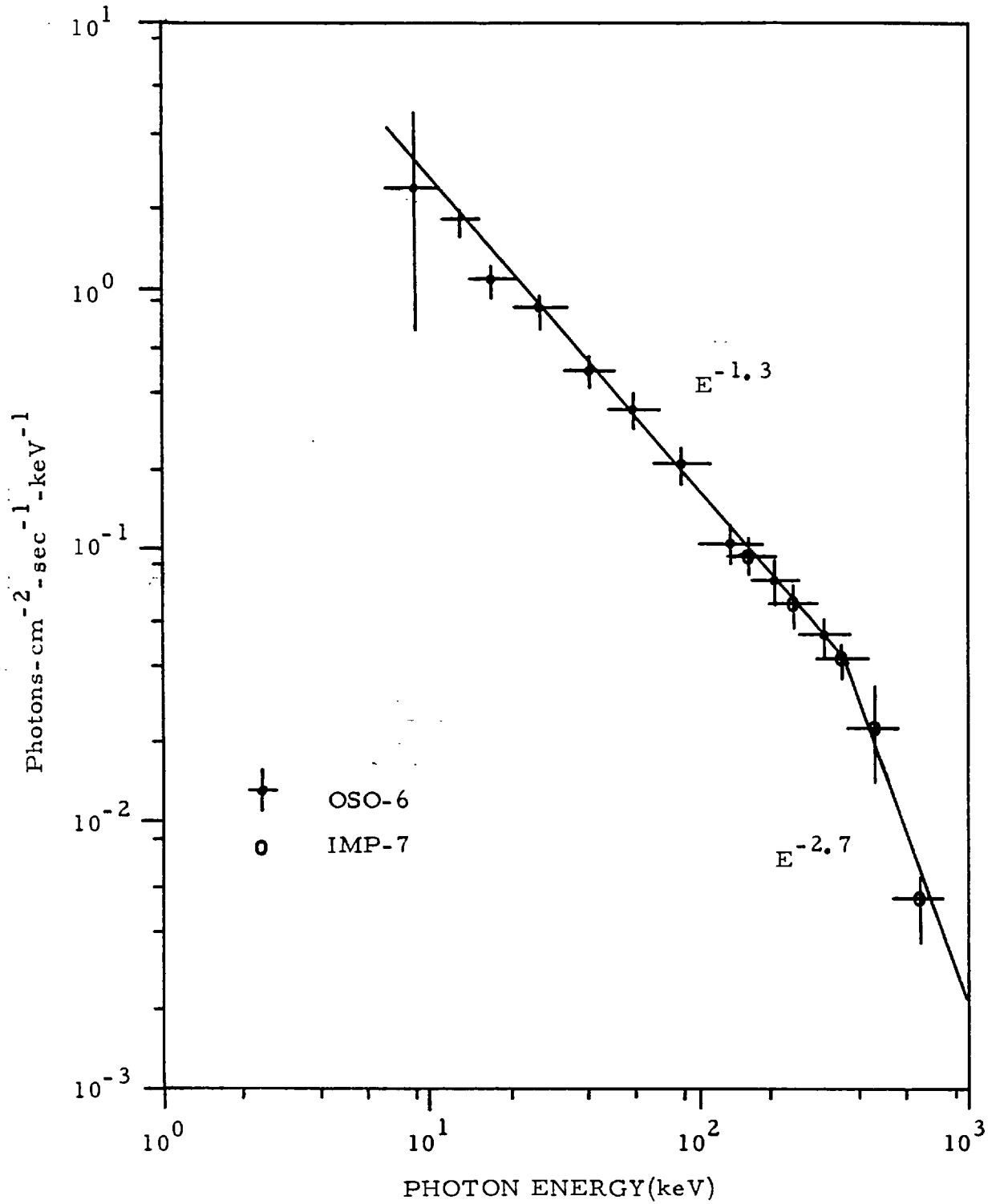


Fig 1. 9: Spectrum Of The Second Pulse Of The Event Observed By OSO-6 And IMP-7 On 14 May 1972. The Spectrum Is Best Fitted By Two Intersecting Power Laws And Is Identical To The Spectrum Of The Burst Observed By Apollo-16.

Spectral variations also seem to be a characteristic feature of gamma-bursts. Throughout the whole of the event on the 27th April 1972 the flux above 1 MeV, as measured by Apollo-16, stayed virtually constant. However, the more impulsive regions of the burst were accompanied by an increase in the flux below this energy; the overall spectrum therefore softened at these time. Such variations have also been observed by the Vela satellites. Figure 1.10 compares the count rates of Vela 5B and COSMOS-461 during a burst on the 17th June 1972. The COSMOS-461 detector had a lower threshold of 50 keV as opposed to the 150 keV threshold of Vela 5. The softening during the more active burst periods is readily apparent.

The nature of the spectral variations at the lower end of the spectrum is indicated by data obtained from the Apollo-16 x-ray spectrometer (Trombka et al. 1974). Figure 1.11. displays four spectra obtained from this instrument during the 27th April 1972 event; the integrating time was 8 s. The spectra a and d correspond to the onset and decay phases of the burst, shown in Figure 1.5, whilst b and c were obtained during the intense main burst period. The latter are considerably flatter, indicating spectral hardening at lower photon energies (<10 keV) during more active burst periods. The combined data for the event suggest that the spectrum can be modelled as a relatively hard power law, upon which is superimposed an exponential component dominant during the more intense burst period. The burst observed by OSO-7, previously referred to, exhibited a similar behaviour, with a noticeable hardening of the spectrum in the <50 keV range during the two main pulses of the event.

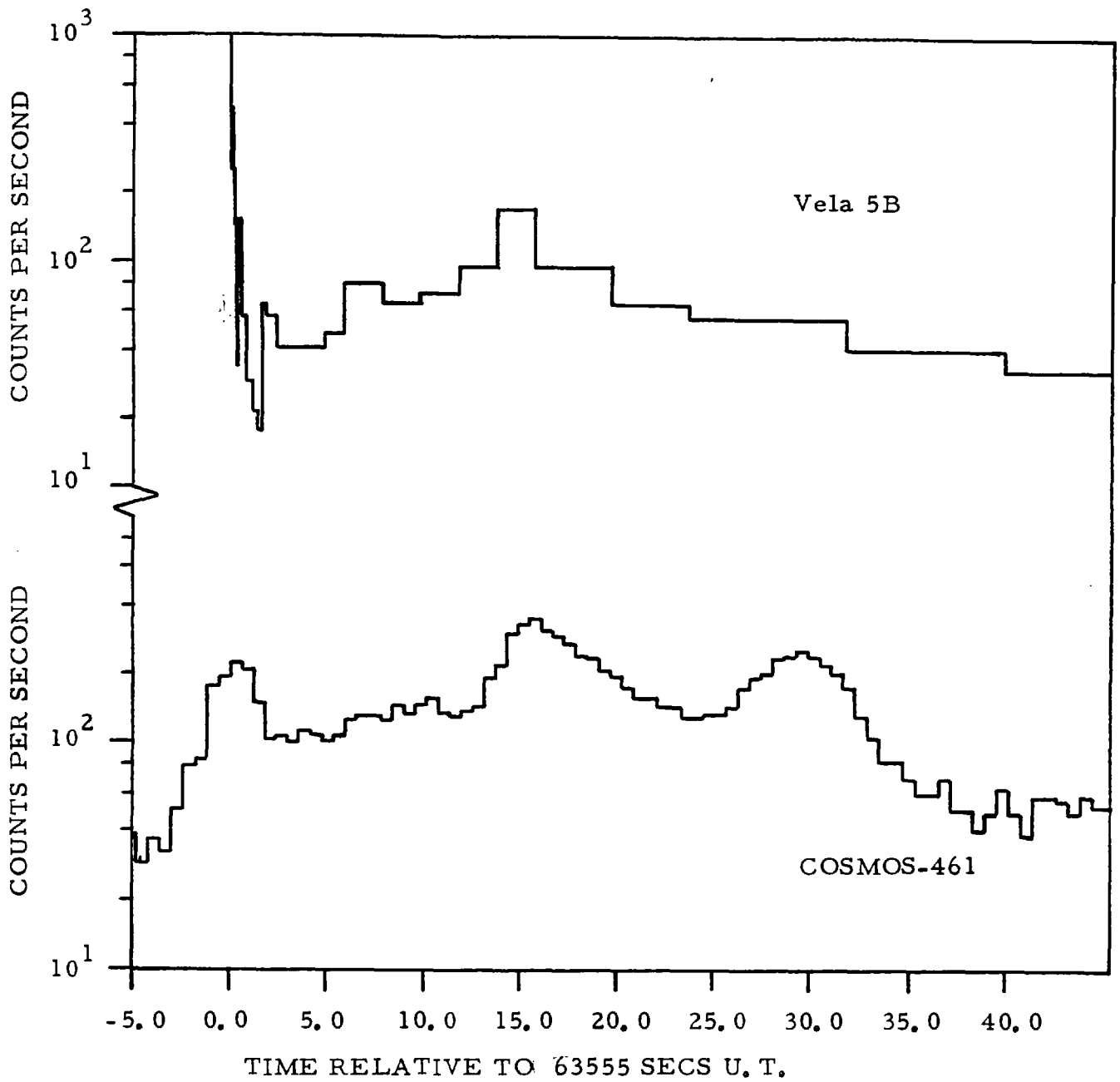


Fig 1.10: Comparison Of The Responses Of Vela 5B And Cosmos-461 To Event 72-01.



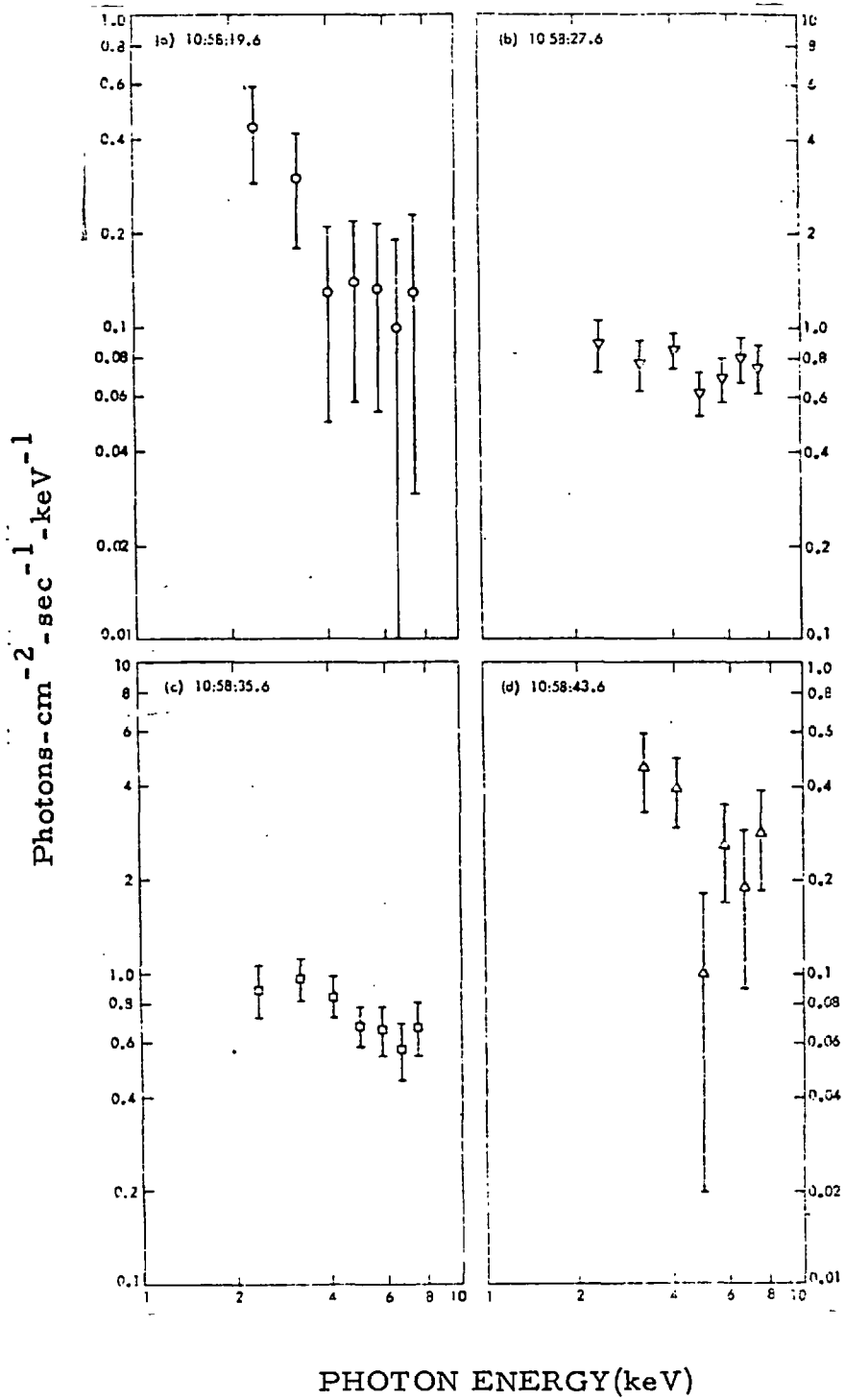


Fig 1. 11: Four Spectra Recorded During The Event 72-6 By The X-Ray Spectrometer On Apollo 16. Each Spectrum Corresponds To 8 Secs. Of Data.

The spectral behaviour can be summarized as follows:

- (1) Gamma-bursts have a standard event average spectrum which is best represented by two power laws intersecting at  $\sim 275$  keV.
- (2) During the more impulsive burst periods the flux above 1 MeV stays constant whilst the flux below 1 MeV increases i.e. the overall spectrum softens.
- (3) At the low energy end ( $< 50$  keV) the spectrum hardens during more active burst periods.

The latter two conclusions are contrary to those drawn by Imhof et al. 1975 based on data obtained during the burst on the 18th December 1972 by the germanium spectrometer on 1972-076B. They suggest that the hardness of the event increased throughout its onset independently of intensity variations. Unfortunately, the field of view of the instrument rotated beyond the source prior to the main outburst and these results are inconclusive.

### 1.9. Burst Size

All burst detectors measure a flux in terms of photons  $\text{cm}^{-2}$ , and to calculate the corresponding energy flux involves making spectral assumptions. Klebesadel et al. 1973, have previously estimated the rises of the Vela bursts by assuming a spectral shape of the form

$$\frac{dN}{dE} = I_0 e^{-E/150}$$

and then integrating from zero to infinity. With such a correction about 25% of the energy lies below the Vela 5 lower threshold, and 5% above the upper cut-off. However, Apollo-16 and Imp-7 data indicate that the spectrum has a power law tail, and correspondingly, a larger fraction of the energy is concentrated in the upper spectral region. The size of the Apollo-16 event is estimated to be  $2.2 \times 10^{-4}$  ergs  $\text{cm}^{-2}$  in the range  $0-\infty$ , assuming that the power law tail remains unchanged above 5 MeV. The Vela 5 detector has an energy window which stretches from 150-750 keV and the burst size in this range is  $0.9 \times 10^{-4}$  ergs  $\text{cm}^{-2}$ . Thus instead of missing only 30% of the energy, the Vela detectors fail to observe  $\sim 60\%$  of the incident flux.

Table 1.1 contains a list of all the confirmed Vela events. The event number refers to the order in which bursts were discovered during a particular year. The estimates of the burst sizes have been calculated by assuming that each burst had the common event-average spectrum consisting of two intersecting power laws. The burst sizes vary over three orders of magnitude, ranging from  $\sim 5 \times 10^{-6}$  to  $5 \times 10^{-3}$  ergs  $\text{cm}^{-2}$ , with an average size of  $\sim 10^{-4}$  ergs  $\text{cm}^{-2}$ . Uncertainties in the effective area and efficiency of the Vela

Table 1.1

Event Number	Date Yr Mo Dy	UT Hr Mn S	Estimated Flux Units of $10^{-5}$ ergs $\text{cm}^{-2}$ Vela/Imp	Source Position	Error Circle	Observer
67-1	67 07 02	14 19 28	17			2V
69-1	69 07 03	07 17 13	3.4			2V
69-5	69 07 19	03 46 46	17			05,1V
69-2	69 10 07	07 26 31	34	223,+79		2V,06,05
69-3	69 10 17	03 18 47	3.4	238,-12	86	2V
69-4	69 10 17	21 41 53	6.8	244,+47	83	2V,03
70-7	70 01 25	05 01 27				06,05
70-5	70 07 10	05 17 46	6.8			2V
70-2	70 08 22	16 44 31	17	153,+42		3V,05
70-2				321,+31		
70-6	70 10 01	15 42 12	17			05,06,1V
70-3	70 12 01	20 00 59	6.8	235,-27	67	2V,06,05
70-4	70 12 30	07 02 17	51	215,+21		3V
70-4				262,+20		
71-1	71 01 02	19 10 56	17	306,+67		3V,S1
71-6	71 02 27	17 27 35				2V,06
71-2	71 03 15	11 20 27	8.5	72,-80	82	4V,I6,05
71-3	71 03 18	15 28 05	17	192,-10		3V,I6,05
71-3				277,-10		06

Event Number	Date Yr Mo Dy	UT Hr Mn S	Estimated Flux Units of $10^{-5}$ ergs $\text{cm}^{-2}$ Vela/Imp	Source Position	Error Circle	Observer
71-4	71 04 21	03 18 39	0.51	235,-43	81	2V,S9
71-5	71 06 30	17 30 59	85	48,+77	67	2V,I6,S1,05
72-1	72 01 17	17 39 16	12	93,-1		3V,I6,S9
72-1				10,-10		C
72-2	72 03 12	15 53 15	8.5	277,+1		4V
72-2				71,+4		
72-3	72 03 28	13 46 28	17	52,+10		2V,I6
72-6	72 04 27	10 58 32	5.1	317,-46		A,1V
72-4	72 05 14	03 46 31	34	129,+41		3V,I6,07
72-5	72 11 01	18 56 46	1.2	100,-41		3V
72-5				357, 35		
72-8	72 11 13	16 02 38	1.7/7			17,V
72-7	72 12 18	20 27 39	17/20.4	20,-2		2V,I7,AF
73-10	73 01 25	15 15 57	0.51/7.8			17,2V
73-3	73 03 02	23 27 58	51/47.6	215,+74	82.5	3V,I7,S2
73-12	73 04 16	12 39 05	5.1/5.1			17,S2,1V
73-1	73 05 07	08 04 32	10.2	107,-3		3V
73-14	73 05 17	01 34 38	17/6.1			17
73-9	73 06 06	07 07 28	17/10.2			17,S2,1V
73-4	73 06 06	18 47 14	/12.1			S2,I7,2V
73-2	73 06 10	20 59 42	17/15.3	184,-23		3V,I7
73-2				279,-14		

Event Number	Date Yr Mo Dy	UT Hr Mn S	Estimated Flux Units of $10^{-5}$ ergs $\text{cm}^{-2}$ Vela/Imp	Source Position	Error Circle	Observer
73-5	73 07 21	08 55 18	34/20.4	300,-4		3V,I7,AF
73-5				158,-15		
73-6	73 07 25	17 07 57	34/11.1	300,-4		3V,I7
73-6				158,15		
73-15	73 08 20	16 39 16	/4.6			I7
73-11	73 09 18	05 10 34	34			2V
73-13	73 09 26	16 04 45	5.1/11.9			I7,I7
73-7	73 12 17	08 09 08	13.6/18.7			I7,I7
73-8	73 12 23	00 39 47	13.6/10.5			I7,I7
74-1	74 01 21	18 05 22	/7.1			I7,V
74-2	74 04 02	18 20 38	/7.6			I7,V
74-3	74 04 19	17 14 35	/5.1			I7
74-4	74 07 28	14 01 46	/4.6			I7
74-5	74 08 06	10 36 37	/7.1			I7,I7
74-6	74 08 23	14 35 44	/3.4			I7,I7
74-7	74 09 29	18 51 45	51			I7,I7
75-8	75 12 03	00 00 03	85			4V
76-1	76 01 23	22 14 45				4
76-2	76 01 28	07 24 30	510	138,-57	83	4V,H,I7
76-3	76 03 22	15 25 30		288,-60	65	2V,H,I7
76-4	76 04 07	02 54 26		102,-60	89	H,V,I7
76-5	76 04 19	07 26 14		125,-60	34	1V,H,I7

03 = OGO-3

05 = OGO-5

06 = OSO-6

07 = OSO-7

H = Helios

16 = Imp-6

17 = Imp-7

NV = Number of Velas

S1 = SAS 1

S2 = SAS 2

A = Apollo-16

C = COSMOS 461

AF = 1972-076B

detectors, allow the actual event sizes to be up to a factor of two greater than the tabulated estimates (Strong et al. 1974). The flux computed for the event 72-4 from OSO-7 data is  $5 \times 10^{-4}$  ergs  $\text{cm}^{-2}$  in the range 11-1500 keV, (Wheaton et al. 1973) corresponding to  $6 \times 10^{-4}$  ergs  $\text{cm}^{-2}$  in the range 0- $\infty$ . This compares well with the Vela estimate of  $\sim 4 \times 10^{-4}$  ergs  $\text{cm}^{-2}$ , allowing for efficiency uncertainties etc. in the two detector types.

The nature of the data recording procedure used on the Vela spacecraft means that some fraction of a burst is usually missed. Vela 6A did not trigger until the second of the three main pulses of event 72-6, and recorded a burst of size  $3 \times 10^{-5}$  ergs  $\text{cm}^{-2}$ , an order of magnitude smaller than the estimate based on Apollo-16 data. Such large discrepancies are exceptional however. The event 69-2 was observed to have a size of  $10^{-4}$  ergs  $\text{cm}^{-2}$  in the range 50-200 keV by the Bologna wheel experiment on OSO-6, corresponding to a total flux of  $\sim 4 \times 10^{-4}$  ergs  $\text{cm}^{-2}$ . A size estimate based on Vela data gives the flux as  $2 \times 10^{-4}$  ergs  $\text{cm}^{-2}$  which corresponds well, considering that the Vela detectors did not trigger until the second main pulse (see Figure 1.12).

Table 1.1 also contains size estimates obtained from Imp-7 data after applying a correction to the previously published sizes (Cline et al. 1976), to include energy in the lower and upper spectral regions. The values are in good agreement with the Vela data, indicating that in general the Vela detectors do observe most of the energy in a burst, noting that Imp-7 produces complete data records.

Most of the energy contained within a burst is usually concentrated in a series of pulses lasting several seconds, each of



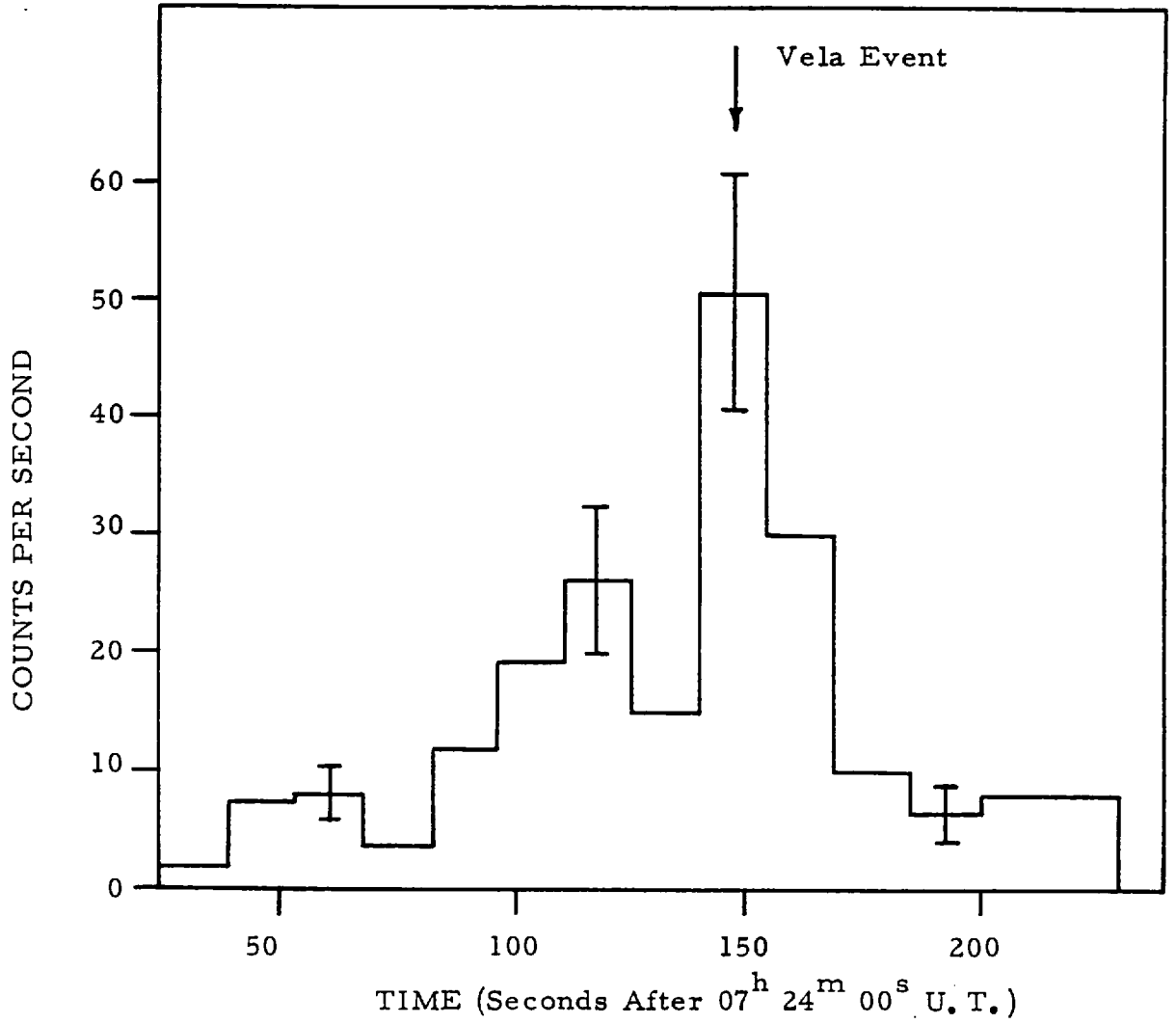


Fig 1. 12: Time Profile Of Event 69-2 As Recorded By The Bologna Wheel Experiment On OSO-6 (49-189 keV). The Vela Detectors Did Not Trigger Until The Second Main Pulse Of The Burst.

the pulses consisting of several micro-bursts. The total duration of the Apollo-16 event was  $\sim 27$  s, but as can be seen from Figure 1.5 most of the energy is concentrated in several pulses located in the centre of the record, lasting for  $\sim 5$  s. The first main pulse contains a fifth of the total flux measured above 70 keV. Figure 1.4 illustrates a similar behaviour for the burst 73-5, the event lasted  $\sim 10$  s and most of the energy is contained in micro-bursts with a total duration of  $\sim 3$  s.

Table 1.2 Burst Characteristics

<u>Parameter</u>	<u>Range of Values</u>	<u>Typical Value</u>
Duration	0.1 - 100 s	6s
Width of Micro-burst	0.002 - 0.1 s	0.05 s
Rise Time of Initial Pulse	0.002 s	
Size	$5 \times 10^{-6}$ - $5 \times 10^{-3}$ ergs $\text{cm}^{-2}$	$10^{-4}$ ergs $\text{cm}^{-2}$
Peak Intensity	$5 \times 10^{-5}$ - $5 \times 10^{-4}$ ergs $\text{cm}^{-2} \text{s}^{-1}$	$10^{-4}$ ergs $\text{cm}^{-2} \text{s}^{-1}$

### 1.10. Source Directions

If gamma-bursts are to be related to other astrophysical phenomena such as flare stars or supernovae, the establishment of the locations of their sources upon the celestial sphere is vital. To date sixteen bursts have had the positions of their sources determined. Seven events have unique locations, and for the other nine, the source could lie in one of two directions. Figure 1.13 is a map in galactic coordinates of the known positions, the error associated with each points is typically twenty square degrees.

The majority of the directions have been established by comparing arrival times at three or more satellites of the onset of the burst, or of some salient feature. Three of the events were observed with inherently directional instruments, which enabled the source directions to be determined uniquely (Palumbo et al. 1974, Wheaton et al. 1973, Trombka et al. 1974).

Two satellites can only position the burst source upon a circle whose width depends upon the timing accuracy. If the burst is observed by three satellites, the number of possibilities is reduced to two, corresponding to the intersection of two timing circles as shown in Figure 1.14. A fourth satellite, out of the orbital plane of the other three, is required to remove the ambiguity. A total of twelve events have had their sources fixed upon circles projected onto the celestial sphere. Table 1.1 lists the centre of each circle and the radius in degrees.

The size of the error box associated with each source location, has so far prevented the definite association of a gamma-burst source with a known astronomical object.

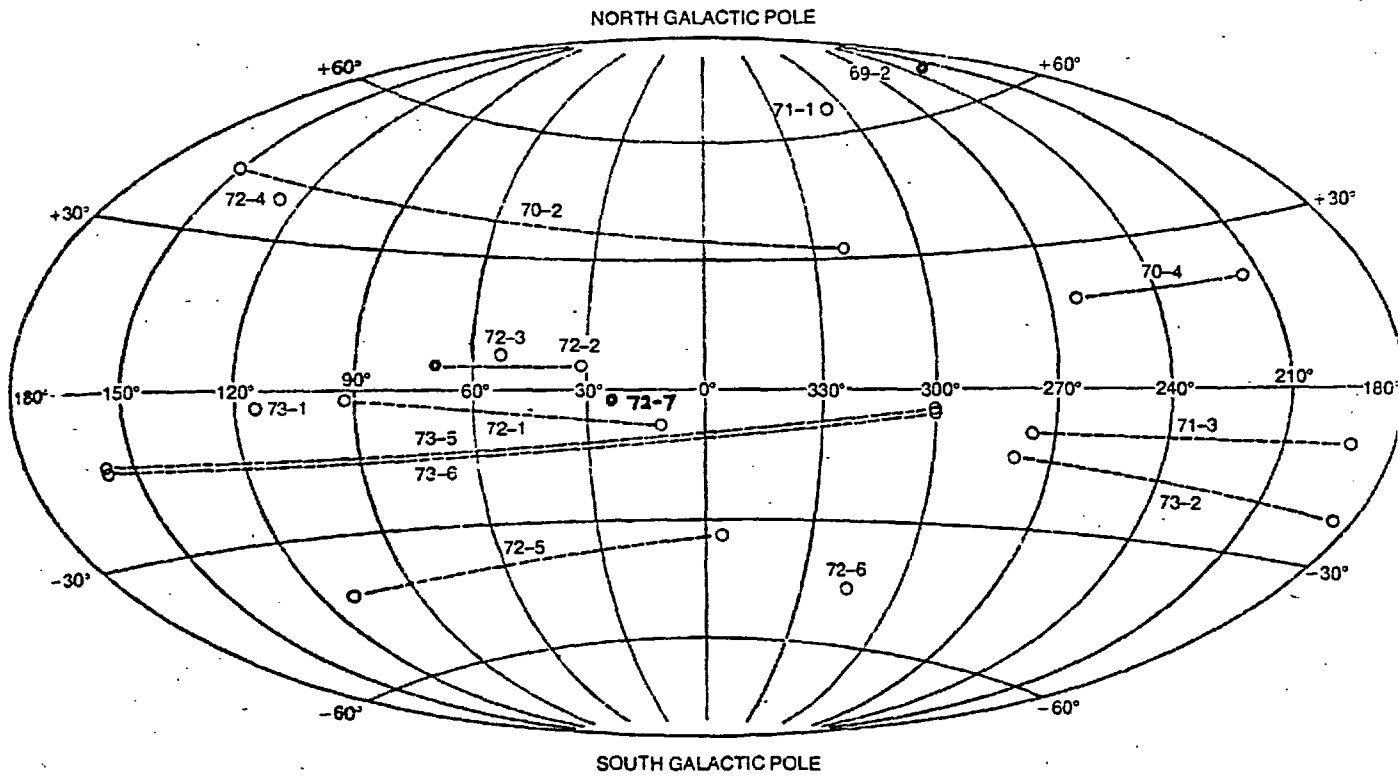


Fig 1. 13: Map In Galactic Coordinates Of The 16 Known Burst Source Positions. The Dashed Lines Refer To The 9 Bursts Whose Source Could Lie In One Of Two Directions.

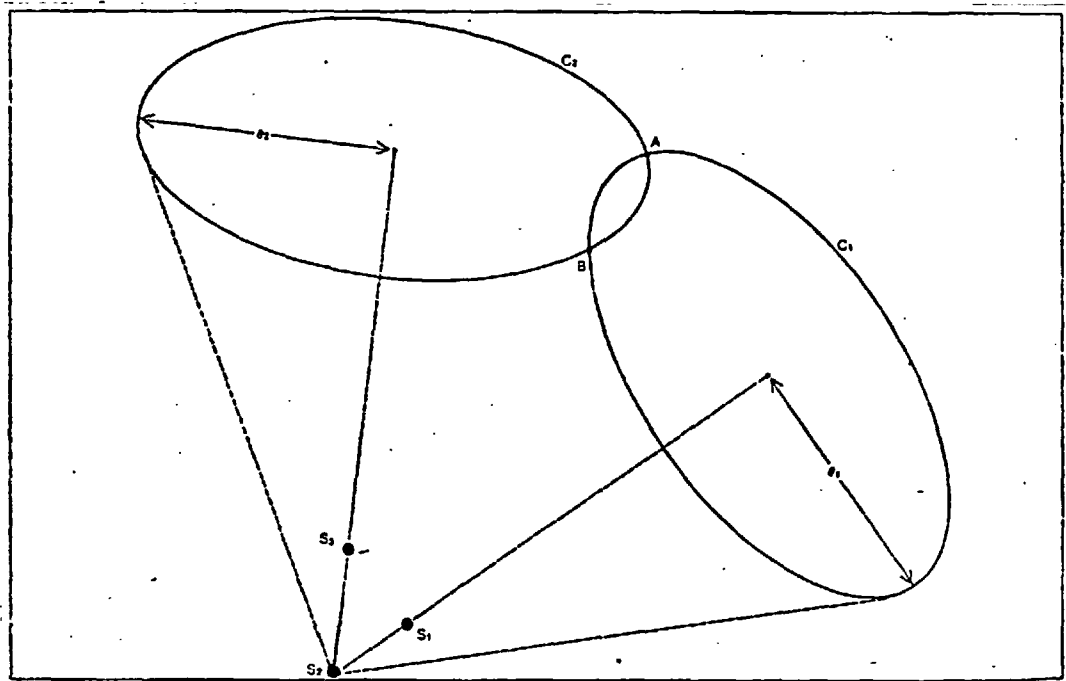


Fig 1. 14: Diagram Showing How Three Satellites Can Position A Burst Source. Comparison Of The Event Arrival Time At  $S_1$  And  $S_2$  Fixes The Angle  $\theta_1$ , And A Similar Comparison Between  $S_2$  And  $S_3$  Fixes The Angle  $\theta_2$ . A Fourth Satellite Is Required To Remove The Ambiguity.

### 1.11. Size Spectra

If the sources of gamma-bursts have a well behaved distribution about a mean strength and are uniformly distributed throughout space, it is possible to determine how the event rate is related to the detection threshold employed.

If  $N_0$  = number of sources per unit volume

$S$  = observed size of a burst

$R$  = respective source distance

Then 
$$S \propto \frac{1}{R^2}$$

And the number of events observed with size  $>S$  in unit time will be given by

$$N(>S) \propto N_0 R^3$$

Thus 
$$N(>S) \propto S^{-3/2}$$

Alternatively, if the sources are confined to an infinite thin sheet approximating the shape of the galactic disc, then  $\alpha = 1$ .

Although this argument does not require sources to have a uniform intrinsic luminosity and time behaviour, it does rely on the width of the intrinsic source distribution being small compared to the range of size values considered. In addition, the event duration must be small compared with the mean time between bursts.

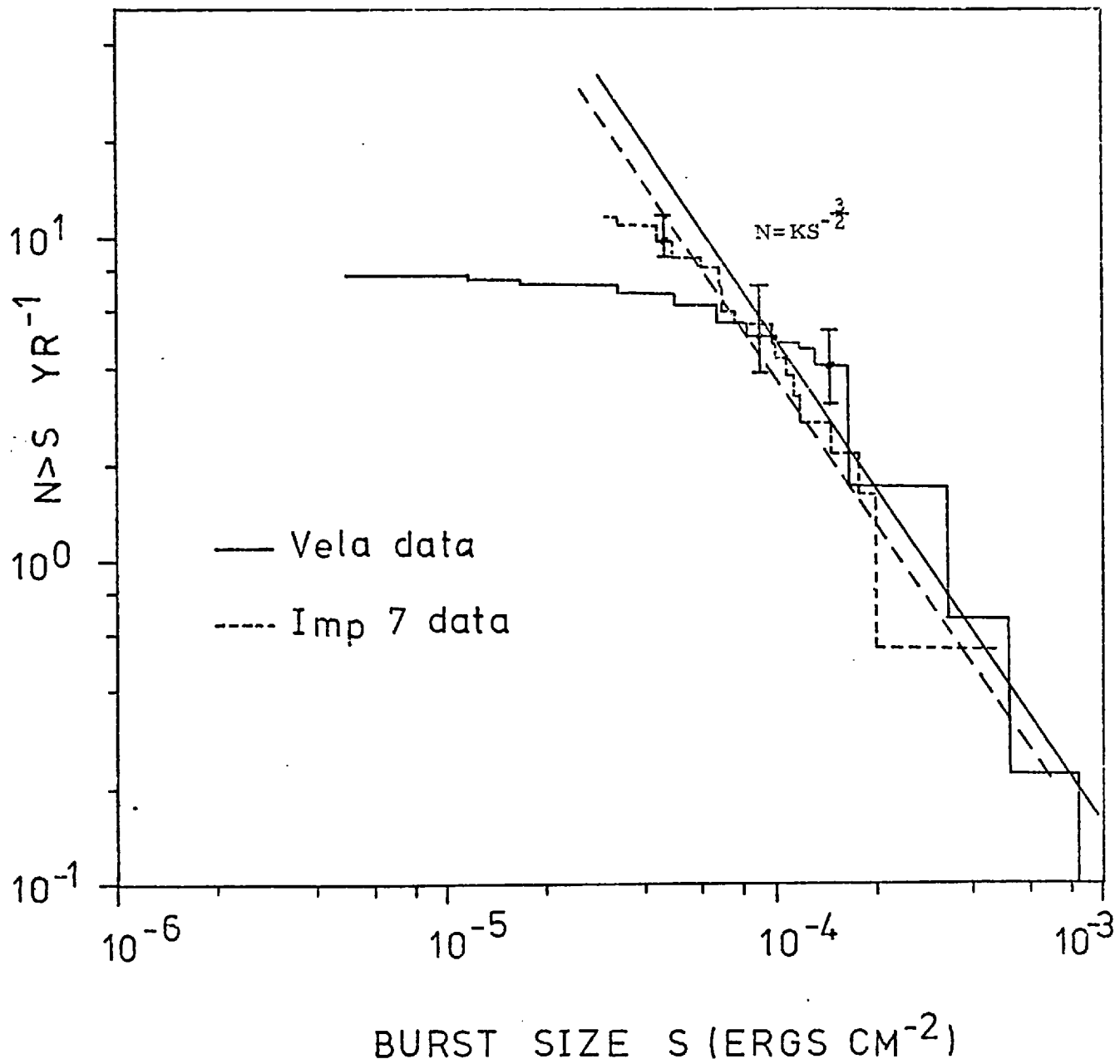


Fig 1. 15: Size Spectra Constructed From Vela And Imp-7 Data.

Size spectra constructed from Vela and Imp-7 data are shown in Figure 1.15. The burst sizes are the estimates given in Table 1.1 and the error bars are  $1 \sigma$  limits. The Vela spectrum is comprised of data accumulated during the period July 1969 - December 1973, when the satellites were in virtually continuous operation. The Imp-7 spectrum consists of bursts observed between June 1972 and August 1974 and contains several unconfirmed events. Lines with a slope of -1.5 have been drawn through both sets of points to aid the eye, they do not represent  $\chi^2$  fits. The discrepancy in the intercept of the two lines is very small, considering the spectral assumptions and efficiency approximations which were made in order to estimate the burst sizes.

Apart from a deviation at  $\sim 5 \times 10^{-5}$  ergs  $\text{cm}^{-2}$ , which is close to the lower threshold, the Imp-7 points are in good agreement with a -1.5 power law. A discrepancy is to be expected at lower energies, due to the error in determining the event size becoming increasingly large as the lower threshold is approached. The turn-over displayed by the Vela data is almost certainly due to shortcomings in the triggering of the detectors, which sometimes results in the missing of a large fraction of a burst.

Thus the size spectra are entirely consistent with a uniform distribution of the sources responsible for the observed bursts. This indicates that the sources are extra-galactic or near galactic i.e. within  $\sim 300$  pc. of the sun.

### 1.12. Discussion of Source Latitudes

Sources of gamma-bursts seem at first to be rather randomly scattered on the celestial sphere. One simple test for clustering is to ignore longitude and concentrate instead on latitude. This consideration is greatly aided by the fact that even when there are two possible source positions for an event, the two latitudes, in galactic coordinates, are usually within  $10^0$  of each other. Figure 1.16 is a plot of the number of burst sources with latitude greater than a given number of degrees  $b$ . The dashed curve shows the distribution that would be expected if the sixteen events were isotropically scattered. Although the sample of positions is too small to be conclusive, a comparison of the two curves suggests that the burst sources cluster near zero. This suggests that gamma-bursts have a galactic origin.

The combined size spectra and latitude data indicate therefore, that the observed bursts were produced by galactic sources located within 300 pc of the sun. Consequently as the size spectrum is extended to lower energies one would expect to see a change of slope as the disc like shape of the galaxy is revealed. Indeed, the latitude plot suggests that the turn-over must be starting to occur at energies around the Vela lower detection threshold. However, it is impossible to tell from the satellite data if a change of slope in this region is occurring due to the large errors associated with the sizes of small bursts. In the case of the Vela satellites, this is mainly due to the nature of the triggering system employed. In order to determine the slope of the size spectrum at energies  $< 10^{-5}$  ergs  $\text{cm}^{-2}$ , and hence the distribution of burst sources, larger detectors preferably with directional sensitivity are required.



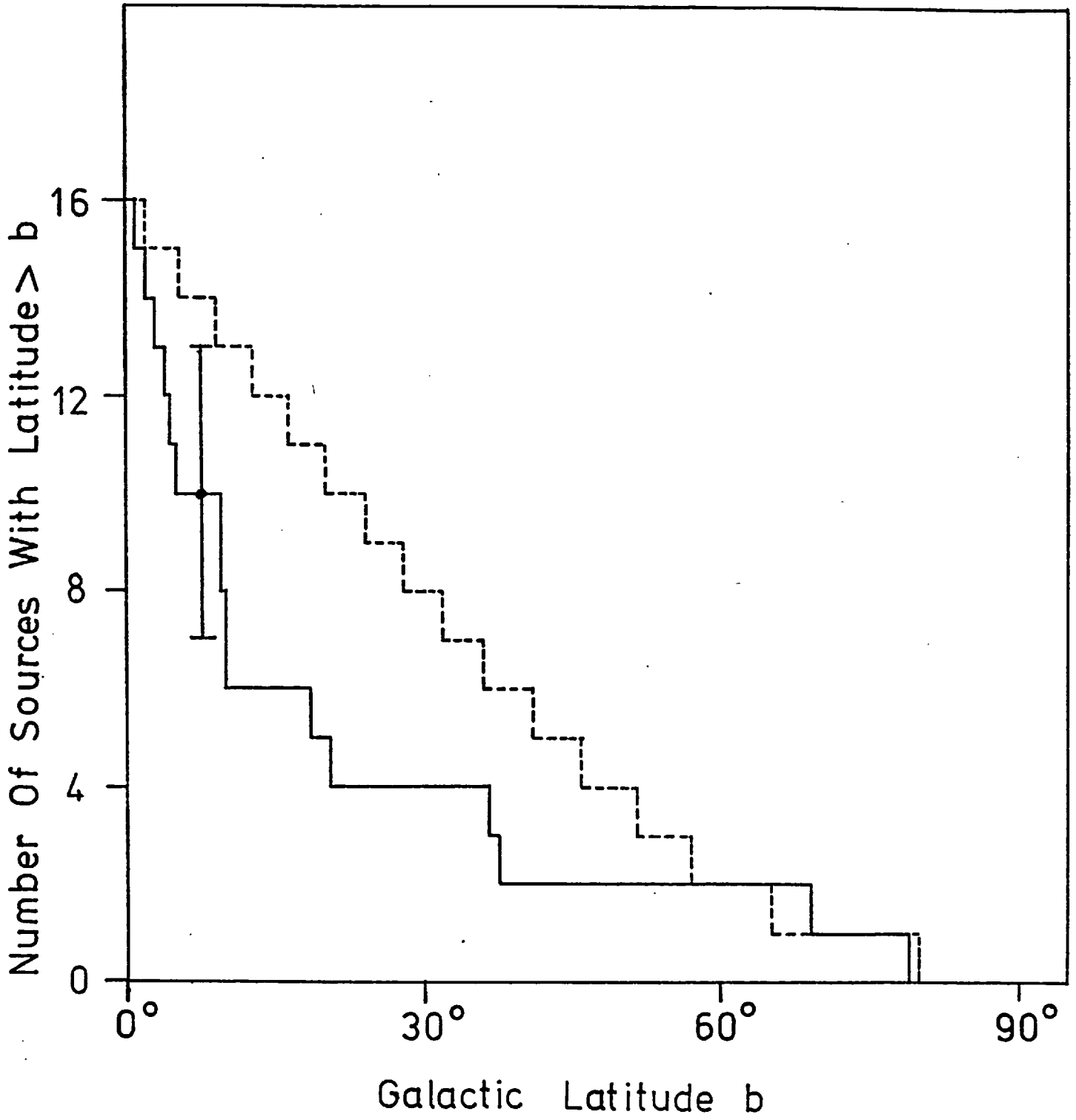


Fig 1.16: The Latitude Distribution Of The 16 Bursts Whose Sources Have Been Positioned On The Celestial Sphere.

## CHAPTER 2

### 2.1.1. Introduction

The weight restrictions imposed upon satellite borne devices allow the detectors employed to have collecting areas of only a few square centimetres. In the case of the Vela satellites, the effective area of the caesium iodide crystals is  $\sim 10 \text{ cm}^2$ , which means that gamma-bursts with a size below  $\sim 10^{-5} \text{ ergs cm}^{-2}$  cannot be seen. Balloon borne detectors on the other hand, can be very much larger with payload sizes ranging from a few kilograms up to two tons. This chapter describes the development and subsequent balloon flights of a large area scintillation counter, designed to look for bursts of gamma-rays up to two orders of magnitude smaller than the events observed by the Vela satellites.

### 2.1.2. Description of Apparatus.

The detector used in the first flight consisted of two slabs of Ne102A plastic scintillator. Each slab measured 100x50x5 cms and had three 5" photo-multipliers coupled directly to the surface with silicon fluid. The outputs of all three tubes were summed and fed into a discriminator, which produced a standard 5 volt pulse if the size of the input pulse came between an upper and lower level cut off. The two slabs were mounted adjacent to each other in the same plane and the count rates were summed. The two discriminators defined an effective energy window for x-rays with energies between 50 keV and 2 MeV.

Rechargeable silver cells producing 30 volts were used as the primary power source; low voltage converters and a corona stabilised eht converter providing the necessary power lines.

The launch site chosen was Aire Sur L'adour (Latitude =  $40^{\circ}$ ) in France, this being the most convenient and hence the cheapest of the launch sites in common use. The French organisation CNES (Centre National D'etudes Spatiales) performed the launch and provided the telemetry and tracking systems employed.

## 2.2. The Detector

### 2.2.1. Design Criteria

In order to be an efficient detector of bursts, a scintillation counter must be sensitive in the spectral range where most of the energy is concentrated. This means that a reasonable proportion of the burst photons incident must be scattered in the scintillator, and the majority of the subsequent interactions observed, otherwise some scintillator is being wasted. This involves using the correct thickness of scintillator and having good light collection from the slab. Another requirement is for accurate timing of the arrival of the burst, so that timing comparisons with a satellite enable the source direction to be determined.

### 2.2.2. Scintillator Elements

Alkyl halide scintillators, such as CsI, are far more efficient at stopping x-rays than plastic scintillators; at 100 keV, 0.17 cms of CsI is equivalent to 10 cms of Ne102A. However, if a large collecting area is required the cost of crystal scintillators becomes prohibitively expensive, and in addition large crystals cannot be grown. Therefore in practice, large area counters are made from materials such as Ne102A. Above 30 keV, the dominant interaction in plastic scintillators is Compton scattering, which means that burst spectra cannot be determined with such a detector. However, as the occurrence rate of small bursts was the main item of interest, this was considered to be of secondary importance.

One of the most important requirements for a balloon-borne burst detector is that of large area. The basic requirement is to maximise

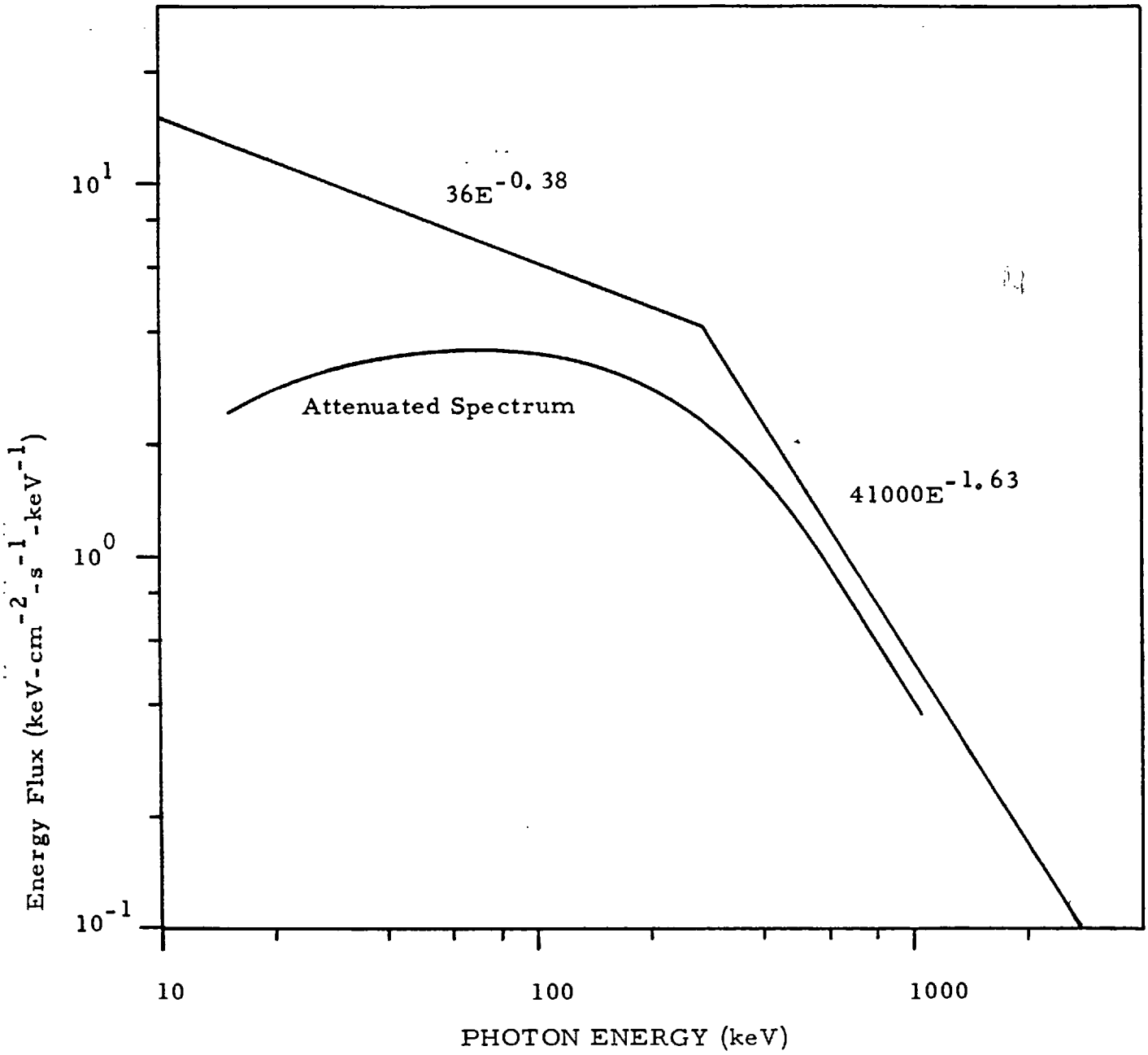


Fig 2. 1: Event Average Burst Spectrum Exponentially Attenuated By 3.5 grams Of Atmospheric Matter.

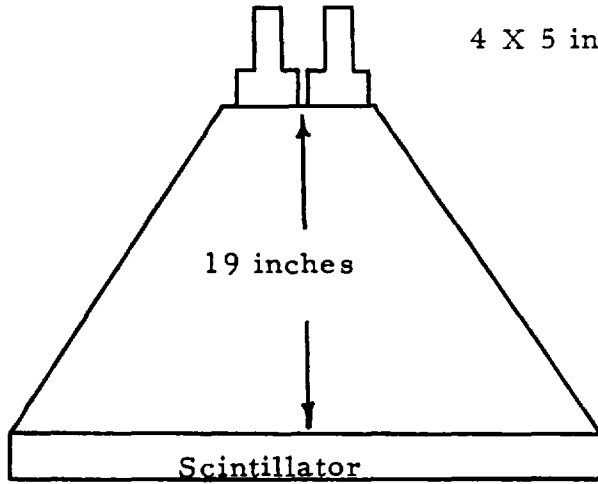
the count rate for a burst of given size, given certain constraints on the volume and weight of the scintillator. The scintillator must then be thick enough so that of the order of 50% of the x-rays passing through will interact (doubling the thickness will then only increase this percentage to  $\sim 75\%$ ). Figure 2.1 shows how the spectrum of the Apollo-16 event, already discussed, would appear to a balloon detector flying at a depth of  $3.5 \text{ grms cm}^{-2}$  after exponential attenuation by the atmosphere. It is evident that to be effective the balloon detector must be efficient in the region around 100 keV. The thickness of scintillator was therefore chosen to be 5 cms, which for 100 keV x-rays incident normally on the surface will give a 54% interaction probability (Hynds 1974), and the area was chosen to be  $1 \text{ m}^2$ .

### 2.2.3. Light Collection Efficiency

The experimental work carried out with various systems for collecting light from the scintillator elements, has already been described in detail (Wheeler 1974). Briefly, two distinct techniques were investigated:

- (i) Reflecting the light down a diffusion box to the photo-tubes.
- (ii) Coupling the photomultipliers directly onto the slab.

Two light diffusion boxes were tested, one 10" high and the other 19" high, with four 5" photomultipliers at the top in each case. Various reflecting surfaces were tried, including the special white paint developed at Imperial College, which has a reflectance of  $\sim 0.97$  (Clarke 1971). The results are summarised in Figure 2.2.



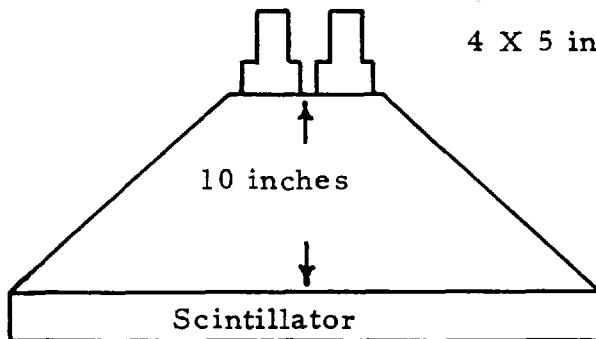
4 X 5 inch Photomultipliers

Darvic Pyramid And White Paint On Lower Scintillator Surface.

Collection Efficiency =  $3.2\% \pm 0.2\%$

Darvic Pyramid With White Paint On The Inside And Silver Foil On The Scintillator.

Collection Efficiency =  $3.8\% \pm 0.2\%$



4 X 5 inch Photomultipliers

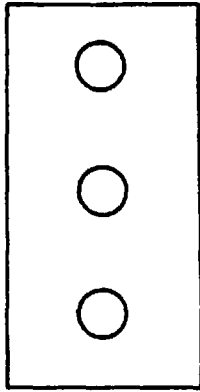
Darvic Pyramid With White Paint On The Inside And Silver Foil On The Scintillator.

Collection Efficiency =  $4.2\% \pm 0.4\%$

Fig 2. 2: Results From Light Collection Efficiency Tests Using Diffusion Boxes.

In the second instance with three 5" photomultipliers coupled directly to the slab, a substantial increase in collection efficiency was obtained, together with some loss in uniformity. Again various

reflecting coatings were applied to the surface of the slab, the results are given below, the most effective material was the shiny side of Alcan foil.



Average Collection Efficiencies Using Different Coatings

<u>Reflecting Material</u>	<u>Average Collection Efficiency</u>
Snappies Foil Shiny Side	8%
Snappies Foil Dull Side	9%
Alcan Foil Shiny Side	10%
Alcan Foil Dull Side	8%
I.C. White Paint	7.5%

With the Alcan foil it was found that the collection efficiency from 90% of the scintillator was within  $\pm 3\%$  of the average value of 10%. Only from the region directly under the photo-tubes was a marked difference found, the efficiency here being 33%.

If the object of the experiment had been to measure the spectrum

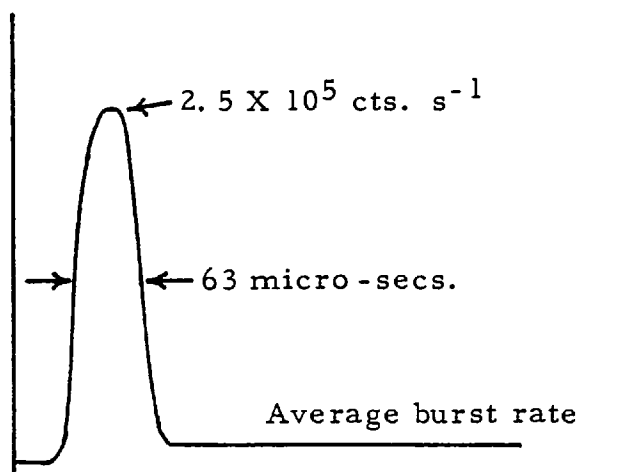


of a gamma-burst, then the light guide would have been the best collection system to use. However, as the event frequency was the point of interest, coupling the photo-tubes directly to the slab to give the highest possible collection efficiency was considered the best arrangement, with Alcan foil as the reflecting surface.

#### 2.2.4. Timing

A data encoding and transmission system which gave a maximum time resolution of 63  $\mu\text{sec}$  was used to monitor the total count rate of the detector (see section 2.2.12). Such high time resolution was used to render the detector capable of observing any short spikes which might be present in a gamma-burst. The detector was designed to look for small bursts in the range  $10^{-7}$  -  $10^{-5}$   $\text{ergs cm}^{-2}$ . Consider a  $10^{-6}$   $\text{ergs cm}^{-2}$  event.

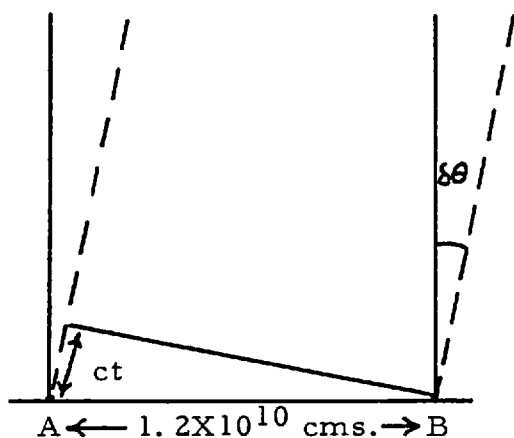
Assuming the event had a duration of 6 s (a typical burst duration), the estimated count rate produced by the burst =  $7300 \text{ cts s}^{-1}$ . The detector was capable of resolving a 63  $\mu\text{sec}$  spike with an intensity up to  $2.5 \times 10^5 \text{ cts s}^{-1}$  above the background counting rate, and thus short deviations with an intensity more than a factor of ten above the average burst counting rate would be resolvable in this case.



Timing is also important with regards to determining the arrival direction of a gamma-burst. If a burst is incident on two receiving stations, the difference in arrival times of the plane wavefront fixes the source direction within a circular band upon the celestial sphere. The width of the band depends upon the accuracy of the timing.

For timing comparisons it was hoped to use the Vela satellites which are in an earth orbit of radius  $1.2 \times 10^5$  kms. Due to the way in which data is transmitted from the satellites, the onset of a burst can only be related to Universal time with an accuracy of  $\pm 10$  ms. The balloon detector was capable of measuring the onset of a typical satellite burst to  $63 \mu\text{sec}$ , and the data base could be related to Universal time with an accuracy of  $10 \mu\text{sec}$ .

Consider the case of a burst incident normally to the baseline produced between the balloon and Vela detectors. Timing errors are dominated by the  $\pm 10$  ms Vela onset uncertainty.



$$t = \text{timing error } \pm 10 \text{ ms}$$

$$\delta\theta = \sin^{-1} \left( \frac{ct}{1.2 \times 10^{10}} \right)$$

$$= \underline{\pm 0.14 \text{ degrees}}$$

Thus the source of the burst can be localised to a circular band of width  $0.28^\circ$ . The angular resolution deteriorates as the incidence angle increases. Bursts incident at  $30^\circ$  from the normal for example, can only have their sources localised to a band of width  $3.4^\circ$ .

Three detectors allow the azimuthal angle  $\phi$  to be fixed also. The source direction must then lie somewhere inside the overlap of the two timing circles, a fourth detector being required to remove the ambiguity.

#### 2.2.5. Lower Threshold

Lower threshold discrimination was employed in order to keep noise generated by the photomultipliers at an acceptable level. It was required that the noise counting rate from the three photo-tubes should be much smaller than that generated by the x-ray background in the slab. An idea of the background count rate expected was found from data obtained by Hillier et al. (1970), during a balloon flight from Cardington designed to look for low energy  $\gamma$ -rays from the pulsar NP0532. Their detector consisted of a 110 cm diameter, 6 cm thick disc of Ne102A, viewed by two 5" photomultipliers positioned close to the centre of the disc. The output discriminator threshold was set at 2 photo-electrons, no upper level discrimination being employed. The outputs of the two tubes were summed together, which produced a background count rate of 5000 counts  $\text{sec}^{-1}$  with the balloon at an atmospheric depth of 9.5  $\text{g cm}^{-2}$ . The x-ray background in the energy range 100-250 keV, varies only by a factor of 50% in the depth range 3-10  $\text{g cm}^{-2}$  (Haymes et al. 1969). The burst detector, which had an area and thickness very similar to Hillier's detector, was designed to be flown at a depth of  $\sim 4 \text{ g cm}^{-2}$ , and therefore the background count rate was expected to be about 5000 cts  $\text{s}^{-1}$ .

The noise spectrum generated by a photomultiplier was then investigated, with particular reference to how this was affected by altering the applied eht voltage, and the nature of any temporal changes. The

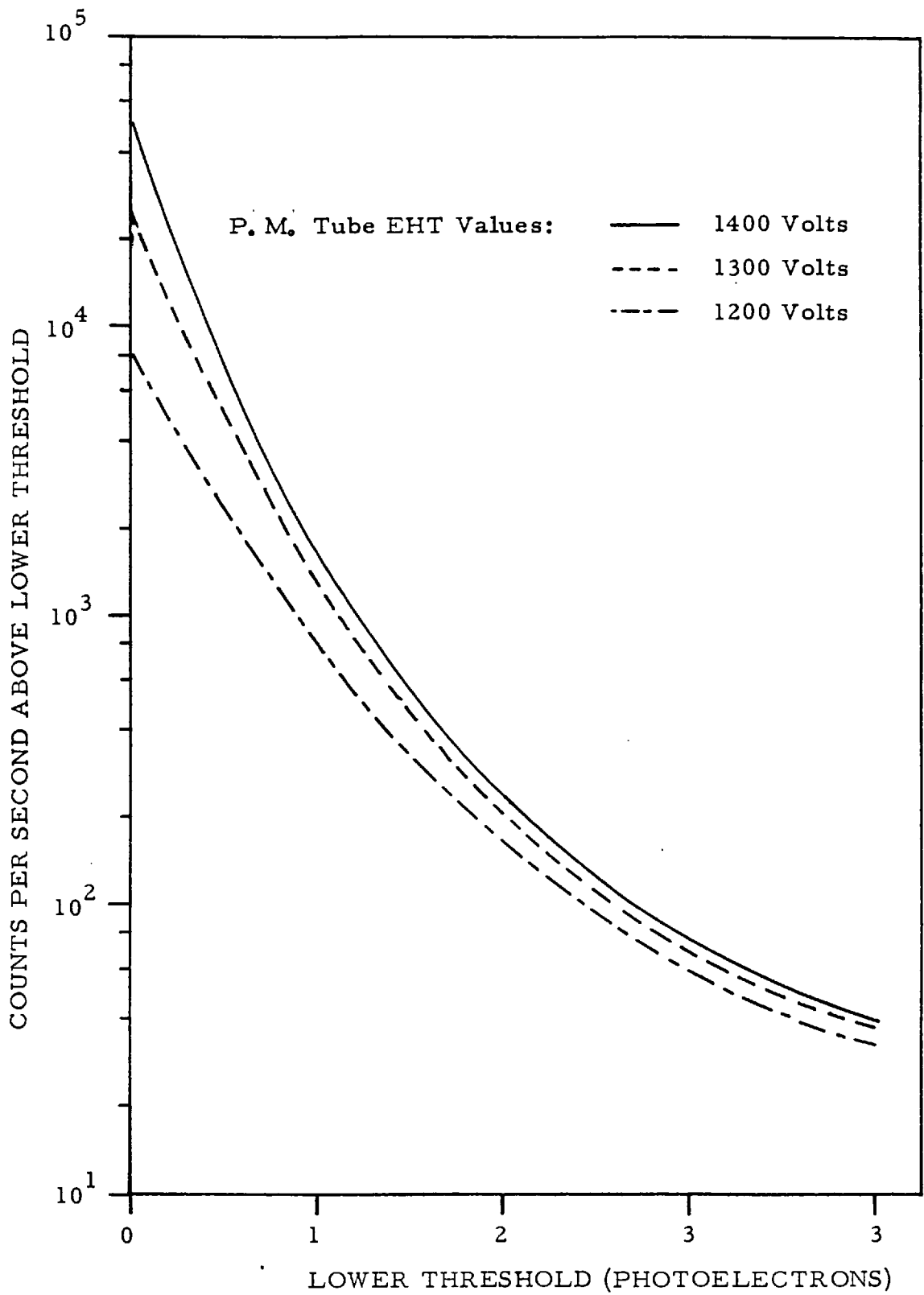
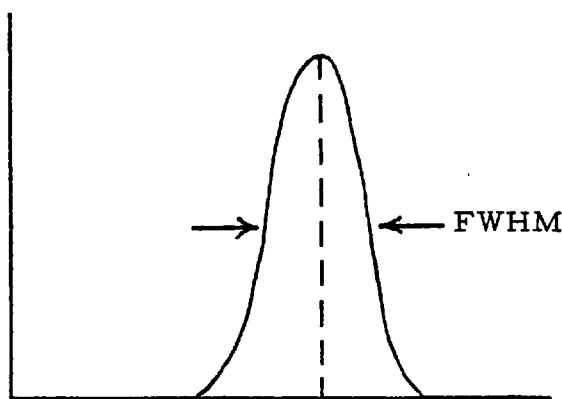


Fig 2. 3: Photomultiplier Noise Spectra

six tubes used in the detector, and the two spare units, all had noise currents below 10 nA at 200 A Lumen<sup>-1</sup> sensitivity, the average rating being 6.5 nA. The phototube used in the tests had a noise current of 6 nA at 200 A L<sup>-1</sup>. From the values of cathode sensitivity and gain given for the tube, it was estimated that an operating voltage between 1200 and 1300 volts would be required. Noise spectra were then obtained at 1200, 1300 and 1400 volts, the output of the tube being fed directly into a pulse height analyser fitted with a lower level discriminator. The number of noise counts per sec above the discriminator settings corresponding to 0, 1, 2, 3, 4 p.e. was found in each case. Calibration was carried out by positioning a photo-diode peak upon the PHA screen, noting the number of photo-electrons in the peak, and then finding the discriminator setting corresponding to half of the pulses being removed. The number of photo-electrons being produced on average was found from the formula

$$(N_{p.e.})_{AV} = 5.56 \left( \frac{\text{Max.Posn.}}{\text{FWHM}} \right)^2 \quad (\text{Wheeler 1974})$$



Thus the discriminator setting corresponding to any other value of  $N_{p.e.}$  could be found.

← Max. Position →

The results are shown in Figure 2.3.

If the lower level discriminator was set at 1 p.e., then three average tubes would produce 2460 cts sec<sup>-1</sup>, which is of the same order

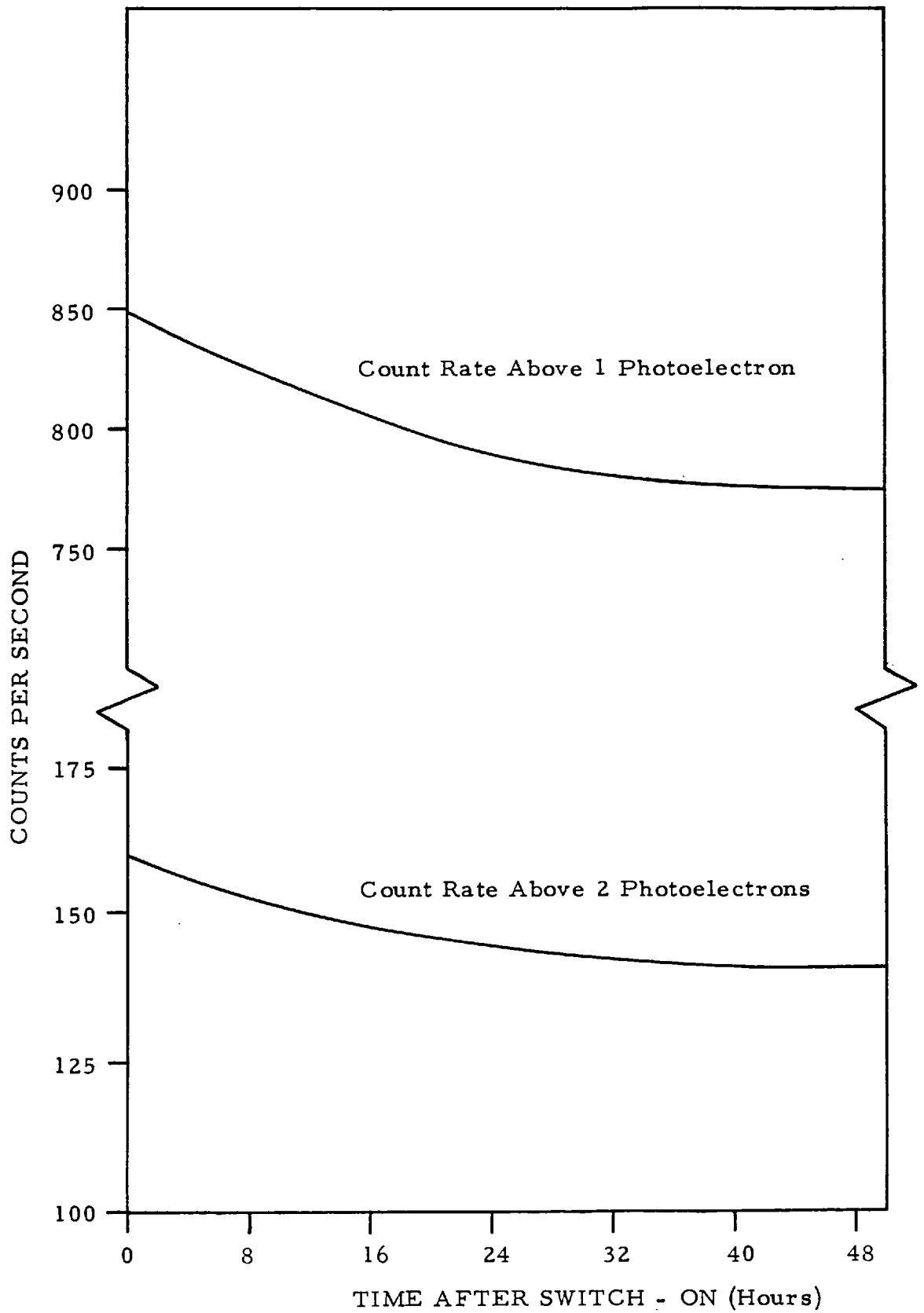


Fig 2.4: Variation Of Phototube Noise With Time

as the count rate expected from the x-ray background in each slab.

Increasing the threshold to 2 p.e. reduces the value to  $500 \text{ cts sec}^{-1}$ .

The phototube was then left running for two days at 1200 volts, and the counting rates above 1 and 2 p.e. were monitored to see how much settling down occurred. In each case the noise rate had fallen by  $\sim 10\%$  after two days, and the results indicated that further reductions were unlikely. Thus even after 48 hours of continuous operation, the noise counting rate from three such tubes would be  $\sim 2300 \text{ cts sec}^{-1}$  if the lower threshold was set at 1 p.e. It was therefore decided to set the discriminator on each slab to 2 p.e., in order to cut out most of the photo-multiplier noise.

An alternative method would have been to operate the three tubes in coincidence. However, this would have introduced large non-uniformities in the light collection efficiency and raised the lower edge of the energy window considerably.

#### 2.2.6. Upper Threshold

An upper level cut-off was employed which discriminated against all charged particles with energy above 1.7 MeV, but accepted x-rays depositing 330 keV, even if they interacted in the region directly under a phototube.

A minimum ionising single charged particle deposits  $1.8 \text{ MeV cm}^{-1}$  in Ne102A (Crispin et al. 1964), more slowly moving particles depositing energy more rapidly. Hence in 5 cms of Ne102A, all particles with energy less than 9 MeV will deposit all their energy. Considering the case of an electron of energy 1.7 MeV passing through the scintillator close to the edge, the number of fluorescent photons produced,

$$= 1700 \times \frac{200}{25} \quad (\text{a } 25 \text{ keV electron produces } 200 \text{ photons, Barnaby et al. 1961})$$
$$= 13600$$

Number of photo-electrons produced from photo-cathode

$$N_{\text{p.e.}} = 13600 \times \text{collection efficiency} \times \text{quantum efficiency}$$

$$\text{c.e.} = 0.065 \text{ at the edge}$$

$$\text{q.e.} = 0.2$$

$$\text{Thus } N_{\text{p.e.}} = 177$$

In order to reject all charged particles with energies above 1.7 MeV, the upper threshold was set at 177 photo-electrons.

In the region directly under the phototubes, the energy required to produce 177 p.e.

$$E_{\text{max}} = \frac{177}{\text{c.e.} \times \text{q.e.}} \times \frac{25}{200}$$

$$\text{c.e.} = 0.33$$

Therefore  $E_{\text{max}} \sim 330$  keV, which is the average energy deposited by 700 keV x-rays. Most of the scintillator however had a c.e. of  $\sim 10\%$  with a corresponding  $E_{\text{max}} \sim 1.1$  MeV, the average energy deposited by 2 MeV x-rays. Thus 90% of the slab was sensitive to x-rays up to 2 MeV, only the regions under the 'tubes had a cut-off at 700 keV.



### 2.2.7. Efficiency of Detector

The thickness of the scintillator was chosen to be 5 cms to optimise the detector's response at 100 keV. The efficiency at 100 keV then depends upon two parameters.

- (i) The fraction of incident photons which interact
- (ii) The percentage of these interactions actually seen above the lower threshold.

To determine the latter involves knowing the spectrum of energy deposited for a mono-energetic input of  $\sim 100$  keV. The spectrum obtained from the photomultipliers then depends upon the statistics governing photo-electric emission from the tube face, and upon the light collection efficiency from the region of scintillator being irradiated. As the light collection efficiency from 90% of the scintillator is close to the average value, a good approximation is to assume a uniform efficiency of 10%.

The spectrum of energy deposited in the scintillator by 100 keV photons was determined using a Monte Carlo Program (Hynds 1974). This traced the histories of  $10^4$  100 keV x-rays incident normally on a slab of Ne102A, measuring 100x50x50 cms. The average number of photo-electrons produced for a particular energy deposition is given by

$$(N_{p.e.})_{AV} = E_D \times c.e. \times q.e. \times \frac{200}{25}$$

$E_D$  = energy deposited

(A 25 keV electron produces 200 photons). The output from the phototubes will be a poisson distribution with a mean of  $\mu = (N_{p.e.})_{AV}$ .

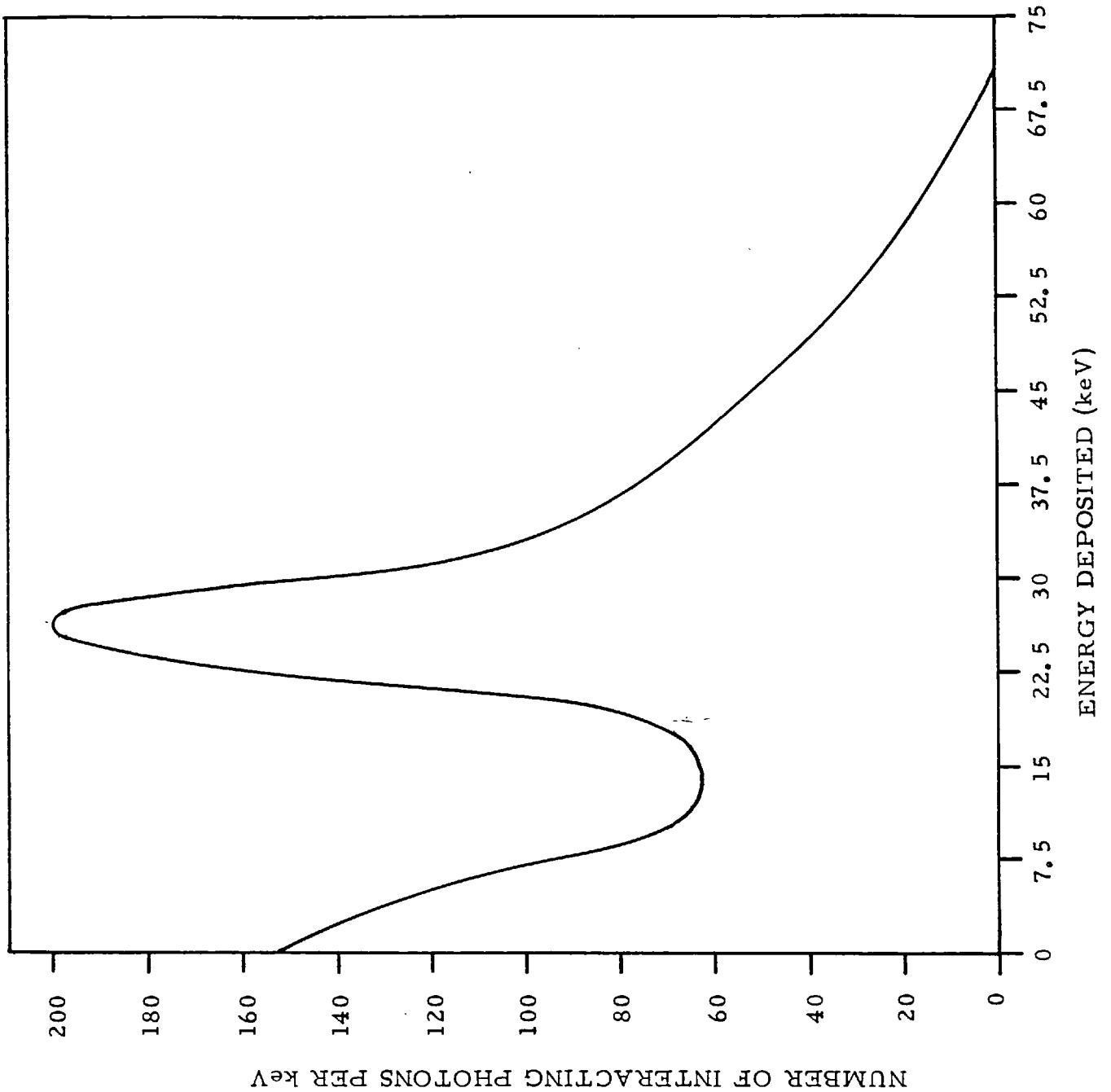


Fig 2. 5: The Spectrum Of Energy Deposited By 100 keV Photons In 5 cms. Of Ne102A. The Vertical Scale Gives The Number Of Photons Interacting Per keV, Assuming That  $10^4$  Photons Were Incident On The Scintillator.

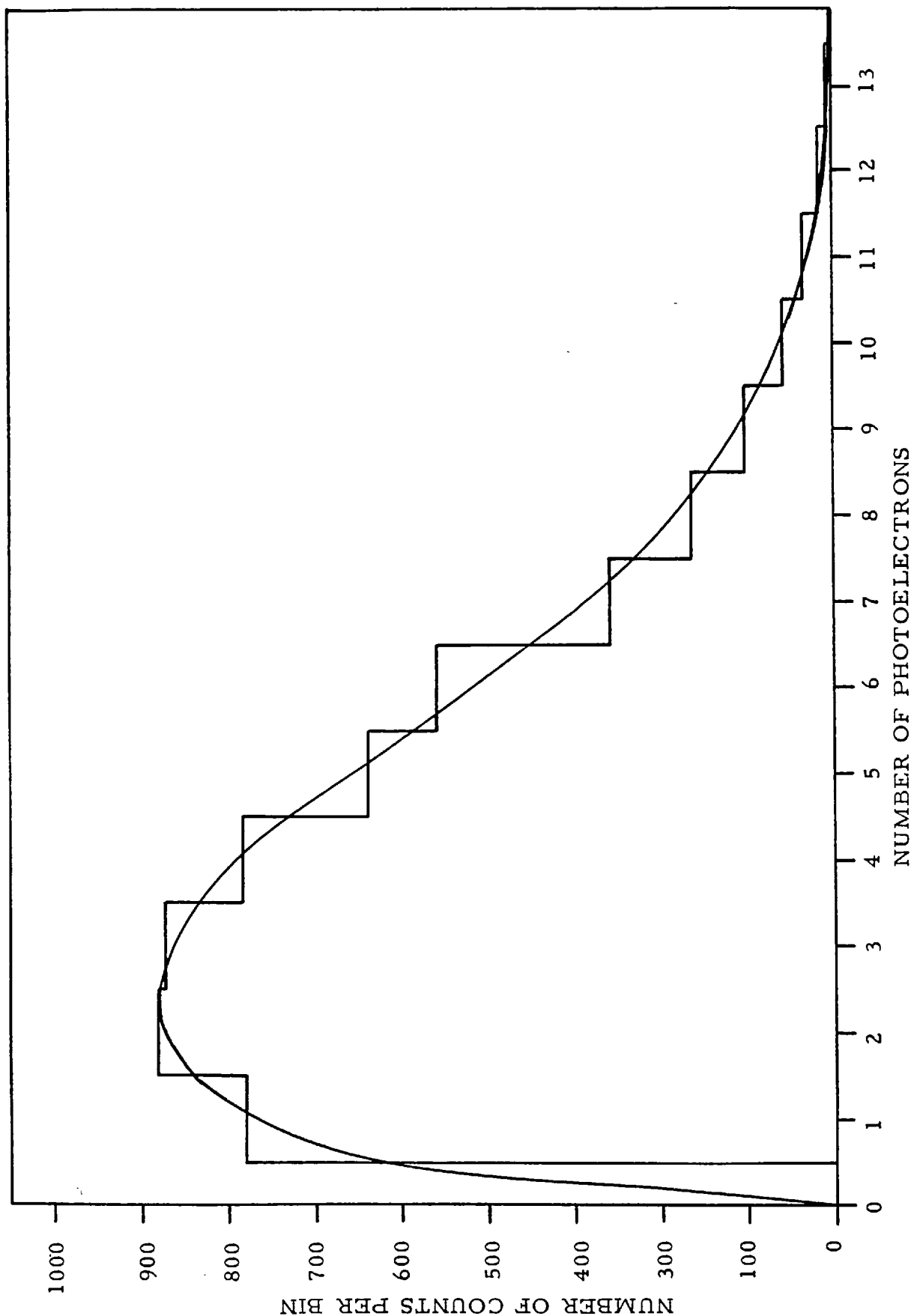


Fig 2.6: The Photomultiplier Pulse Spectrum Produced By 100 keV Photons, Each Bin Is One Photoelectron Wide. The Spectrum Is Not Quantised Due To The Nature Of The Dynode Multiplication Process. The Vertical Scale Gives The Number Of Counts Per Bin Assuming That  $10^4$  Photons Were Incident Upon A Point Where The Light Collection Efficiency Was 10%.

Each value of  $E_D$  will produce such a distribution and the resulting spectrum obtained from the phototubes is shown in Figure 2.6.

In order to check the accuracy of the computer model a spectrum was obtained from a  $^{60}\text{Co}$  source, which emits 84% of its radiation at 122 keV and 10% at 136 keV. The source was placed in a position on the scintillator, where the collection efficiency from one photomultiplier was equal to the overall average value of 10%. This simulated the real situation where the three tube outputs were summed. The output from the tube was fed into a pulse height analyser, whose screen had been calibrated in terms of photo-electrons by using a photo-diode. With the  $^{60}\text{Co}$  source placed directly on the slab, photons will be travelling through the scintillator at all angles. However, most interactions will occur in a region where the collection efficiency of the one tube is  $\sim 10\%$ , and the resulting spectrum should be very similar to that produced by x-rays incident normally. The theoretical and  $^{60}\text{Co}$  spectra are compared in Figure 2.7a. Despite the slight discrepancy in incident energy, an excellent agreement exists. The theoretical efficiency can be found as follows. Out of  $10^4$  incident photons, 5440 interacted in the scintillator, of which 64% produced output pulse sizes above the lower threshold of 2 p.e. Therefore the detection efficiency at 100 keV =  $54 \times 64 = \underline{35\%}$ .

If the lower threshold had been set at 0 p.e., 84% of the interactions would have been observed, the missing 16% corresponding to zero photo-electrons being produced. This would have given an efficiency of  $\sim 45\%$ , but would have allowed an unacceptable amount of photomultiplier noise inside the energy window.

The program was run for several other incident energies namely, 30, 50, 200, 500, 1300 keV. The next table gives the total number

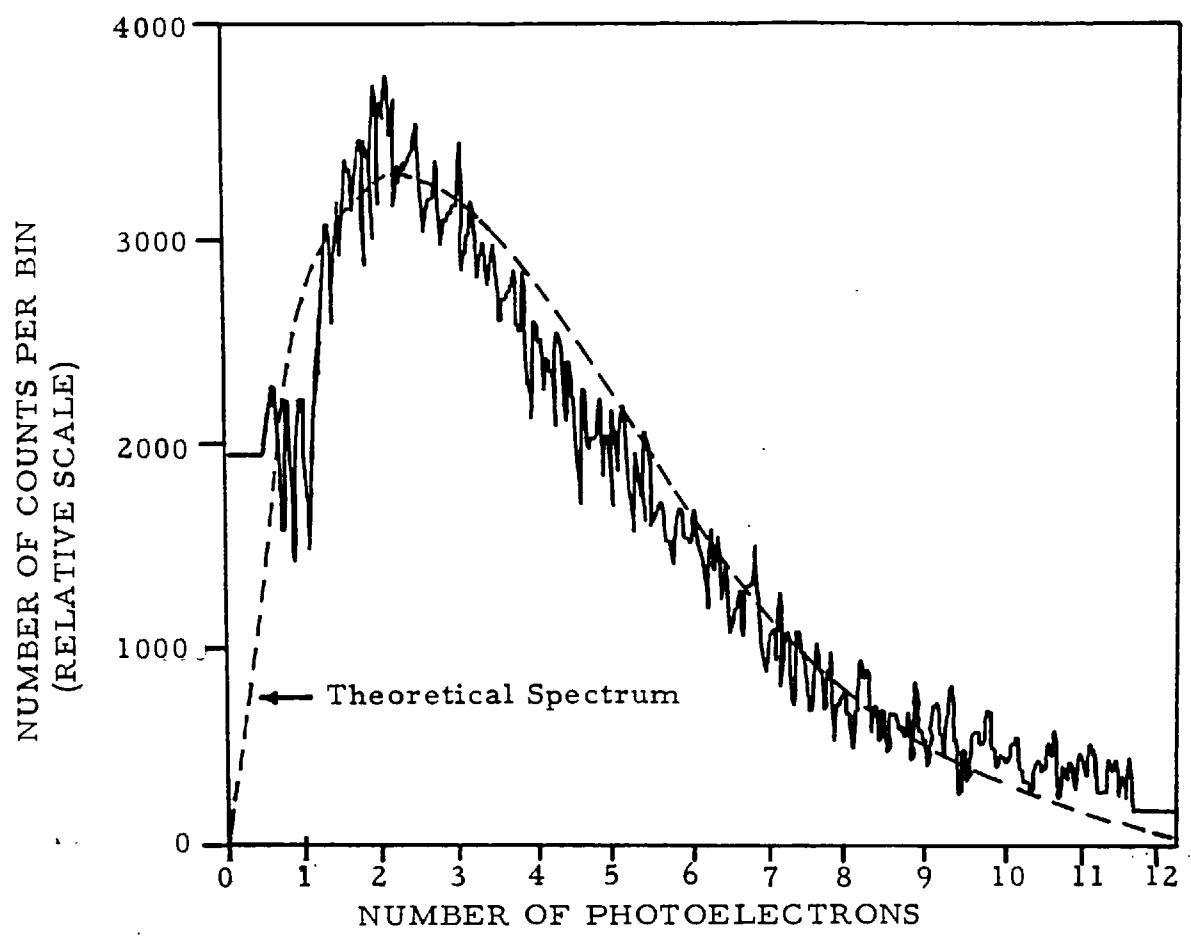


Fig 2.7(a) : A Comparison Of The Photomultiplier Pulse Spectrum Produced By 122 keV Photons With The Spectrum Theoretically Produced By 100 keV Photons.

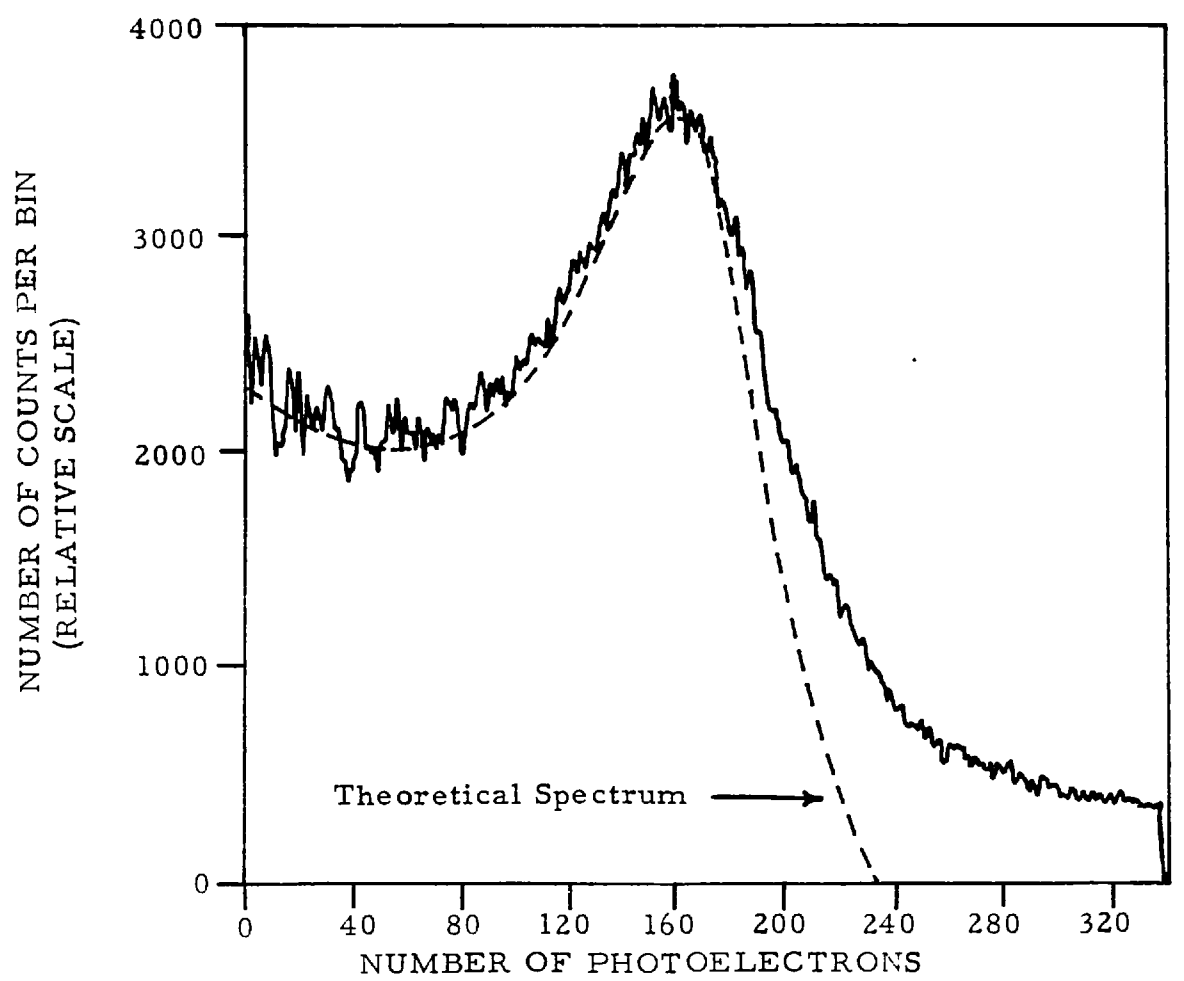


Fig 2.7(b): A Comparison Of The Photomultiplier Pulse Spectrum Produced By 1.25 MeV Photons With The Spectrum Theoretically Produced By 1.3 MeV Photons.

of interactions and the percentage seen, assuming an incident intensity of  $10^4$  photons per slab and a lower threshold of 2 p.e.

Table 2.1

<u>Incident Energy</u>	<u>Number Interactions</u>	<u>% seen</u>	<u>Overall Efficiency</u>
30 keV	7769	8%	6%
50 keV	7330	26%	19%
100 keV	5440	64%	35%
200 keV	5051	81%	40%
500 keV	3397	96%	33%
1300 keV	2953	100%	29%

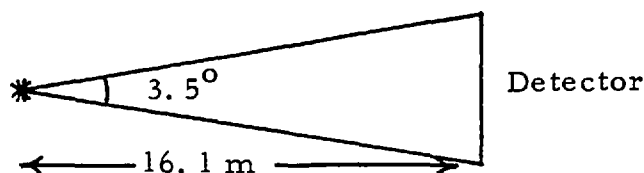
The predicted response of the scintillator is very flat for photons between 100-1100 keV. Below 100 keV a rapid fall off occurs, giving an effective lower threshold of  $\sim 50$  keV.

A spectrum was also obtained from a CO-60 source which emits most of its energy at  $\sim 1.25$  MeV, the curve is compared to the theoretical 1300 keV spectrum in Figure 2.7b. Again excellent agreement exists except at the high energy end, where the model predicts a more rapid fall off. This is ascribable to a certain amount of double counting in the PHA sampling period, and to interactions in scintillator regions with a higher collection efficiency than 10%.

### 2.2.8. Calibration

In order to determine its sensitivity to 122 keV x-rays, the detector was set up on a playing field and illuminated with a CO-57 source. This particular location was chosen in order to minimise scattering. First of all the spectrum of x-rays incident on the detector was found using a caesium iodide scintillator. This was 9.5 cms in diameter and 10 cms deep, the crystal being viewed by a  $3\frac{1}{2}$ " photo-multiplier. The source was placed 16.1 metres away and the crystal exposed to its radiation for 2000 secs, the background counts being subtracted after integration. With such a system all the photons incident from the source are stopped, and spectral broadening, due to variations in light collection efficiency, are kept to a minimum. The spectrum obtained is shown in Figure 2.8. The presence of a signal at low energies is probably due to Compton scattering of the 122 keV photons by air molecules and by the ground. However, more than 90% of the counts accumulated in 2000 secs are contained within the photo-peak, the position of which corresponds to 122 keV of energy being deposited in the crystal. Thus illuminating the burst detector with such a spectrum was a good approximation to using a mono-energetic 122 keV input.

The crystal scintillator was then replaced by the burst detector. Both the background count rate and the subsequent increase produced by the radioactive source were noted; the background rate remained invariant throughout the experiment.



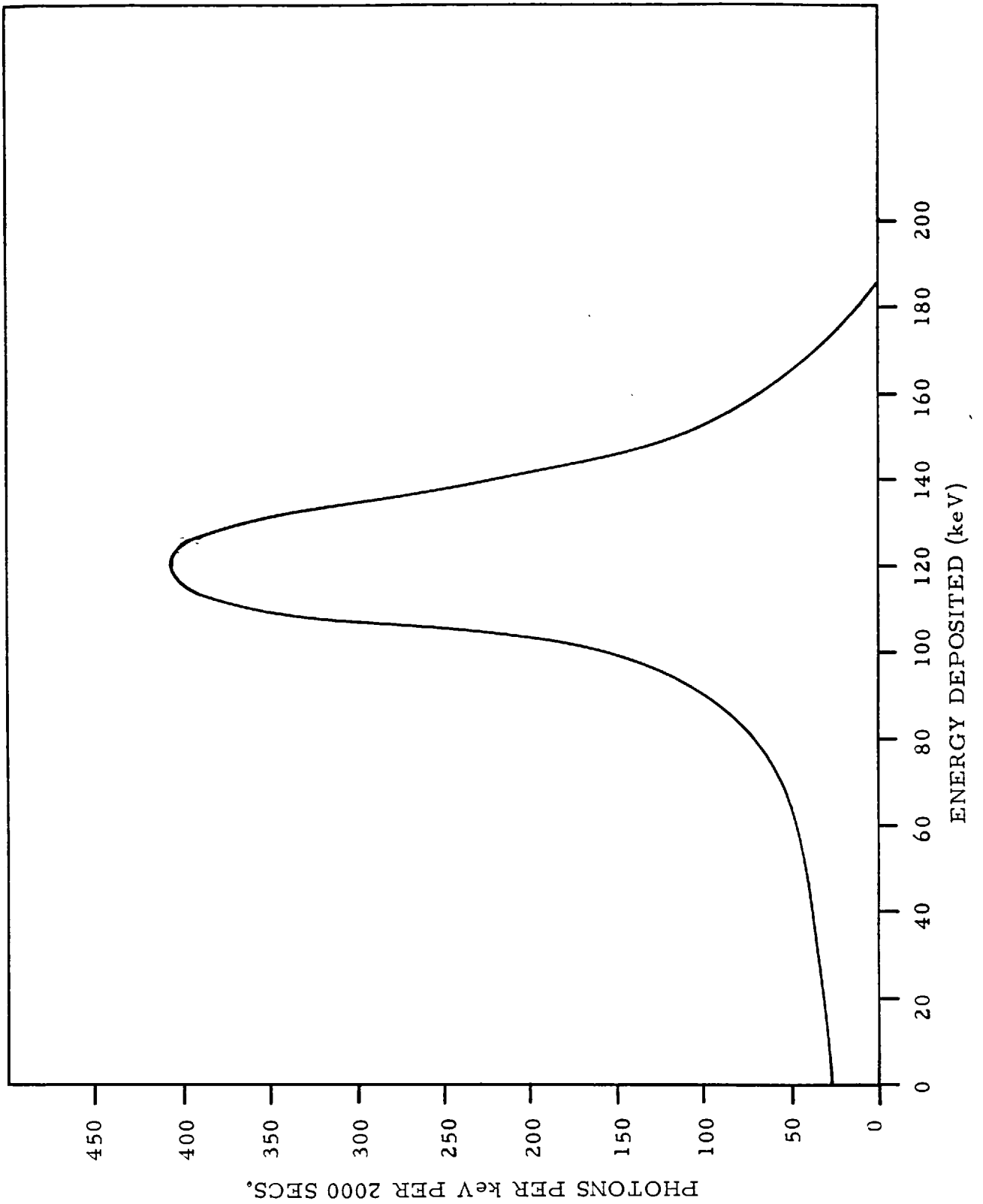


Fig 2.8: Spectrum Produced In The CsI Crystal By The CO-57 Source Placed 16.1 m Away.



Background count rate  $\sim 12500$  cts  $\text{sec}^{-1}$

Increase in count rate when source was exposed =  $467 \pm 2$  cts  $\text{sec}^{-1}$

Under these conditions the detector was essentially illuminated by a plane wave. The efficiency at 122 keV at normal incidence is therefore

$$E = \frac{\text{Source Count Rate}}{\text{Number of photons Incident per sec}}$$

The CsI detector accumulated 18403 counts in the photo-peak in 2000 secs. The number incident per sec on the burst detector is therefore given by

$$N = \frac{18403}{2000} \times \text{Area ratio of two detectors}$$

$$N = \underline{1300 \pm 7 \text{ ph sec}^{-1}}$$

Thus 
$$E = \frac{467}{1300} \times 100 = \underline{36\% \pm 0.3}$$

This value is very close to the theoretical efficiency of 35%. The slight discrepancy is partially due to the burst detector responding to the low energy tail of the incident spectrum which represented  $\sim 9\%$  of the counts accumulated by the CsI detector.

The excellent agreement between the theoretical spectra and efficiency, and the spectra and efficiency measured using the burst detector, gave confidence in the predicted efficiencies listed in Table 4.1.

### 2.2.9. Background Count Rate

The main sources of the background count rate present in all balloon borne x-ray detectors are (a) charged particles depositing energy in the scintillator and (b) the atmospheric x-ray background. The effect of the former was largely removed by using an upper threshold discriminator, but the effect of the latter could not be eliminated.

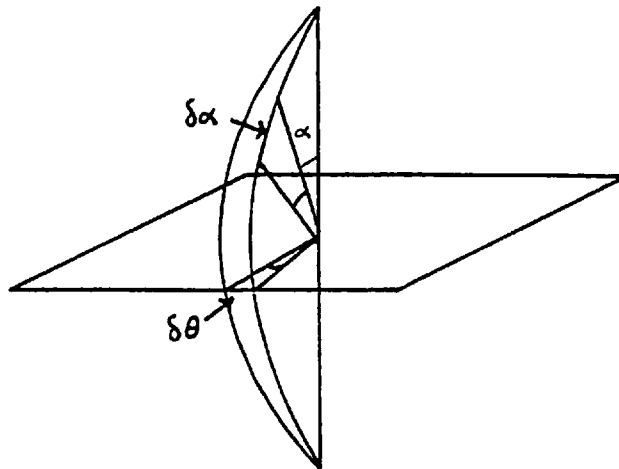
Results obtained by Peterson et al. (1973a), and Ling (1975) from balloon flights over Palestine (lat = 40°), show that the isotropic background spectrum at a depth of 3.5 grms is well fitted by a single power law

$$\frac{dN}{dE} = 1.0 E^{-1.39} \text{ photons cm}^{-2} \text{ sec}^{-1} \text{ MeV}^{-1}$$

from 80 keV-10 MeV. The horizontal intensity of the earth's magnetic field is approximately the same at Aire Sur L'adour and Palestine, and so a similar spectrum was expected for the isotropic background observed by the burst detector.

As the burst detector consisted of a 1m<sup>2</sup> flat slab of scintillator, the projected area at some angle  $\alpha$  was  $\cos\alpha$  m<sup>2</sup>.

$$\text{Average projected area} = \frac{\int \text{Projected area} \times \text{solid angle}}{\int \text{Solid angle}}$$



$$= \frac{2 \int_0^{2\pi} d\theta \int_0^{\pi/2} \cos\alpha \sin\alpha d\alpha}{4\pi}$$

$$= \underline{\underline{\frac{1}{2} \text{ m}^2}}$$

The response of the detector in the range 100-1300 keV was very flat, the average efficiency being 35%. Below 100 keV the efficiency fell rapidly the lower edge of the energy window being  $\sim 50$  keV. The average efficiency in the range 50-100 keV was 27%.

In order to estimate the background count rate expected, it was assumed that the detector behaved with a uniform efficiency of 35% in the range 50 keV to 2 MeV, for all angles of incidence. All photons with energies outside this range were assumed to be outside the energy window.

Then count rate in detector = effective area x isotropic flux  
x efficiency.

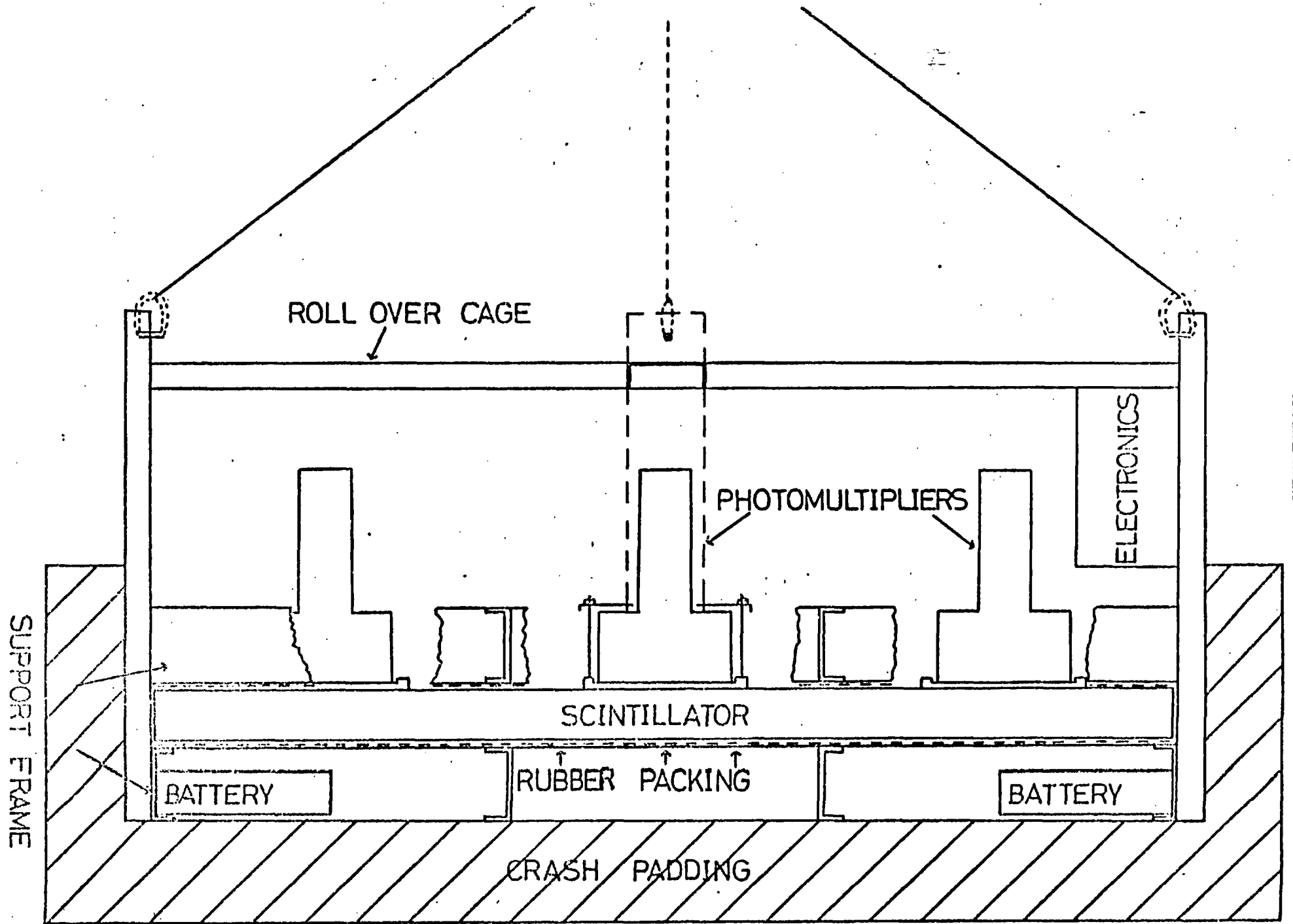
$$\text{In the range 50-2000 keV isotropic flux} = \int_{0.05}^2 E^{-1.39} dE$$

$$= \underline{\underline{6.3 \text{ photons cm}^{-2} \text{ sec}^{-1}}}$$

$$\therefore \text{Count rate} = 5000 \times 6.3 \times 0.35 = \underline{\underline{11025 \text{ cts sec}^{-1}}}$$

This predicted rate is a factor of two greater than the result obtained by Hillier previously referred to. However, using six phototubes rather than two lowers the detection threshold, and as the background flux is governed by a power law, such variations produce large changes in the observed flux. Thus the two results can be consistent.

Fig 2.9 : Sectional Diagram Of Detector



#### 2.2.10. Mechanical structure and thermal shielding

The scintillators were mounted on rubber blocks inside an aluminium framework constructed out of 3" channelling, and designed with an integral roll-over cage. The framework was completely covered with aluminium sheeting in order to screen the electronics systems from the CNES radio transmitter and to provide a firm base for attaching expanded polystyrene. This was required to prevent large temperature variations during flight, in particular during ascent through the Tropopause, where external temperatures<sup>s</sup> of  $\sim -60^{\circ}$  exist. The thickness of polystyrene used was 2", and the outer surface was painted black and white in the ratio 3:2 to maintain some sort of thermal equilibrium during flight. Nine inches of foam rubber was fastened to the underside of the payload to cushion the impact of the 120 kg detector landing at  $\sim 10$  m.p.h.

#### 2.2.11. Environmental checks

The main causes of failure of balloon detectors when at float altitude are

- (i) Coronal discharging from high voltage connectors, starting at  $\sim 20$  mbars.
- (ii) Failure of electronic components when faced with extremes of temperature.

To guard against the former, all the photo-multipliers and eht power converters were encased in Silastic RTV Rubber potting material. All units were then operated under vacuum conditions for several hours,

and the phototube outputs checked for spikes and other evidence of coronal discharge. No such evidence was produced.

The detector was also operated in a large thermal chamber at 0°C for twelve hours, and the background count rate examined for non-statistical behaviour. During the experiment, the mean of the count rate rose by ~2%, which was expected due to the photo-multiplier gain having a negative temperature coefficient. There was no evidence of non-statistical deviations from the average count rate.

The successful completion of the two tests produced confidence that the detector would perform satisfactorily at float altitude.

#### 2.2.12. Data encoding and transmission

(a) The count rate from the detector was fed into a data-flag system. This could occupy either of two possible states, "up" or "down", the level changing every time eight counts were received. The state of the flagging system was indicated by a level sensor, whose output was transmitted back in the form of a stream of eight bit binary words. These were arranged in a data frame with 256 such words to a frame. Each bit could be 0 or 1, 0 corresponding to the flag being in the "down" state and 1 when in the "up" state.

Thus the level was sensed

$$256 \times 8 = 2048 \text{ times sec}^{-1}$$

and sixteen frames were transmitted every second, thus

$$\text{total sampling rate} = 16 \times 2048 = 32768 \text{ times sec}^{-1}.$$

Assuming the background rate =  $10^4$  cts  $\text{sec}^{-1}$ ,

Max. observable burst flux =  $2.5 \times 10^5$  cts  $\text{sec}^{-1}$

Corresponding to a  $3 \times 10^{-5}$   $\text{erg cm}^{-2}$  burst

The time resolution of such a system is essentially limited by the rate at which the level sensor operates, two level changes being required to signal the onset of a burst.

Thus max. resolution =  $\frac{2}{\text{sampling rate}} \sim \frac{1}{16000}$  sec.

The time resolution for a particular event being dependant upon its size.

(b) In addition to the 256 words devoted in each frame to monitoring the count rate, eight words were used to transmit analogue information from the detector. Each channel was read out sixteen times a second.

<u>Analogue Channel Number</u>	<u>Content</u>
1	Electronics Thermistor
2	Battery Thermistor
3	P.M. Thermistor
4	+ 12v Line
5	+ 5v Line
6	+ 15v Line
7	EHT Monitor
8	Analogue Ratemeter

Three channels monitored the outputs of thermistors measuring the

temperature in various parts of the detector, and four channels were used to keep a check on the power lines. The last channel was an analogue representation of the total count rate.

The encoded data was transmitted on a carrier wave of frequency  $\sim 400$  MHz and recorded on an Ampex tape recorder running at  $32'' \text{ sec}^{-1}$ . Absolute timing was provided by a Rubidium frequency standard whose output was recorded simultaneously with the data stream.



## 2.3. Flight and Results

### 2.3.1. Flight details

The detector was launched from Aire Sur L'adour on 27th September, 1974. A flight duration of 4.25 hours at a float altitude of 4.6 mbars was achieved, cut down being at 12H 58 UT. During the flight the eight analogue channels were displayed on a chart recorder, the results from two of the temperature monitors are shown in Figure 2.10. The temperature of the batteries, located beneath the scintillator, stabilised at  $\sim 16^{\circ}\text{C}$  whereas the thermistor coupled to one of the photo-tubes, indicated a rapid fall in temperature during ascent followed by a steady rise at float altitude. The initial fall was due to the effect of the Tropopause, already discussed, the gradual rise being brought about by solar heating. The batteries, having a larger thermal capacity, followed these variations less closely. All the power lines remained invariant throughout the flight.

### 2.3.2. Results

(a) The analogue ratemeter permitted the count rate to be observed in real time. Immediately after launch the rate dropped by a factor of ten, and then exhibited a gradual rise to a peak value at 100 mbars, where the ratemeter saturated (known as the Pfozter maximum). The steady background count rate at 4.6 mbars was  $\sim 10,800 \text{ cts sec}^{-1}$  (c/f to the predicted value of  $\sim 11,000$ ). At 10.21.57. UT, a slight increase in the count rate was observed which lasted for  $\sim 5$  secs before the ratemeter returned to its original value. This was the only significant deviation observed in the whole of the analogue data

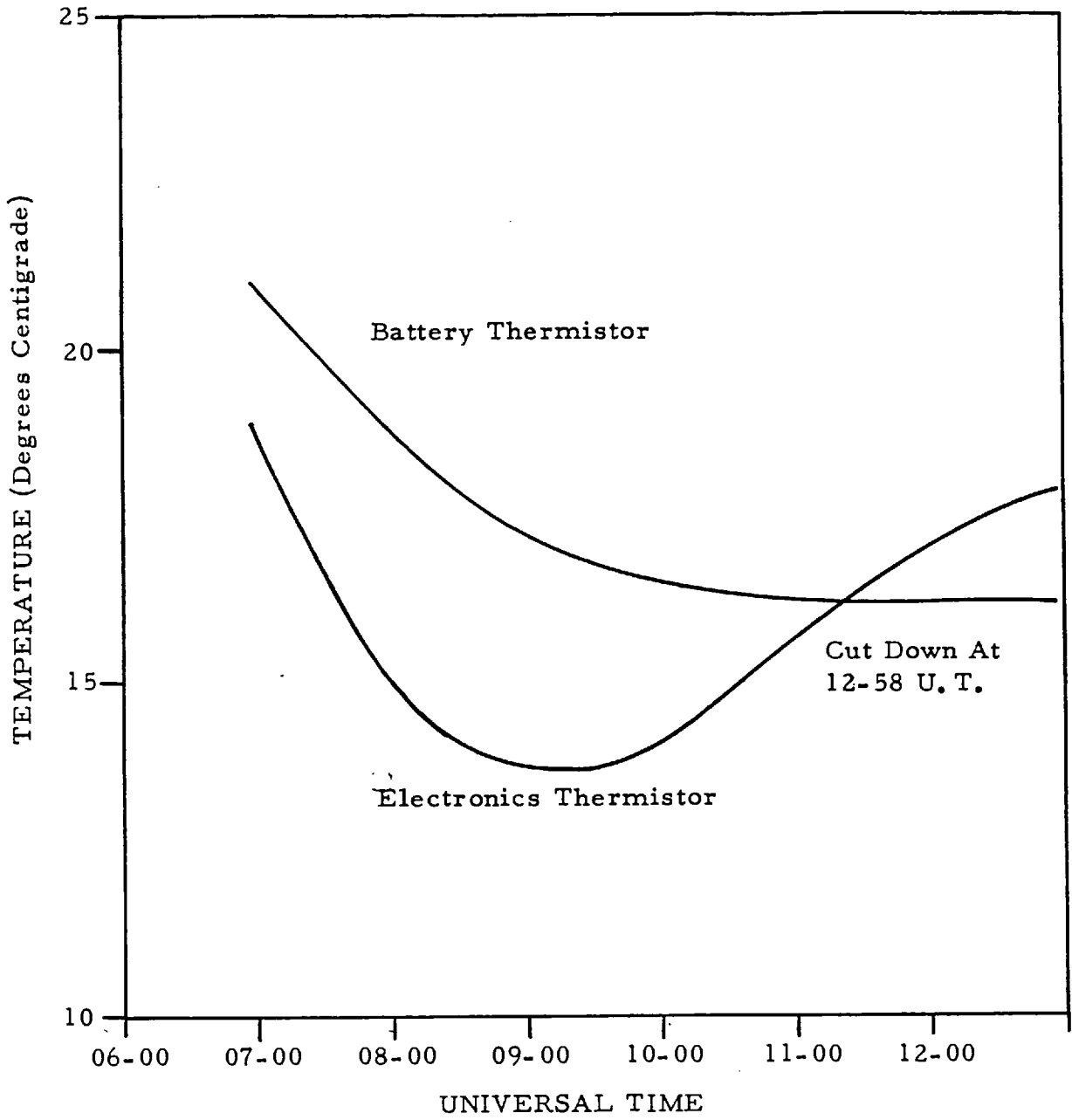
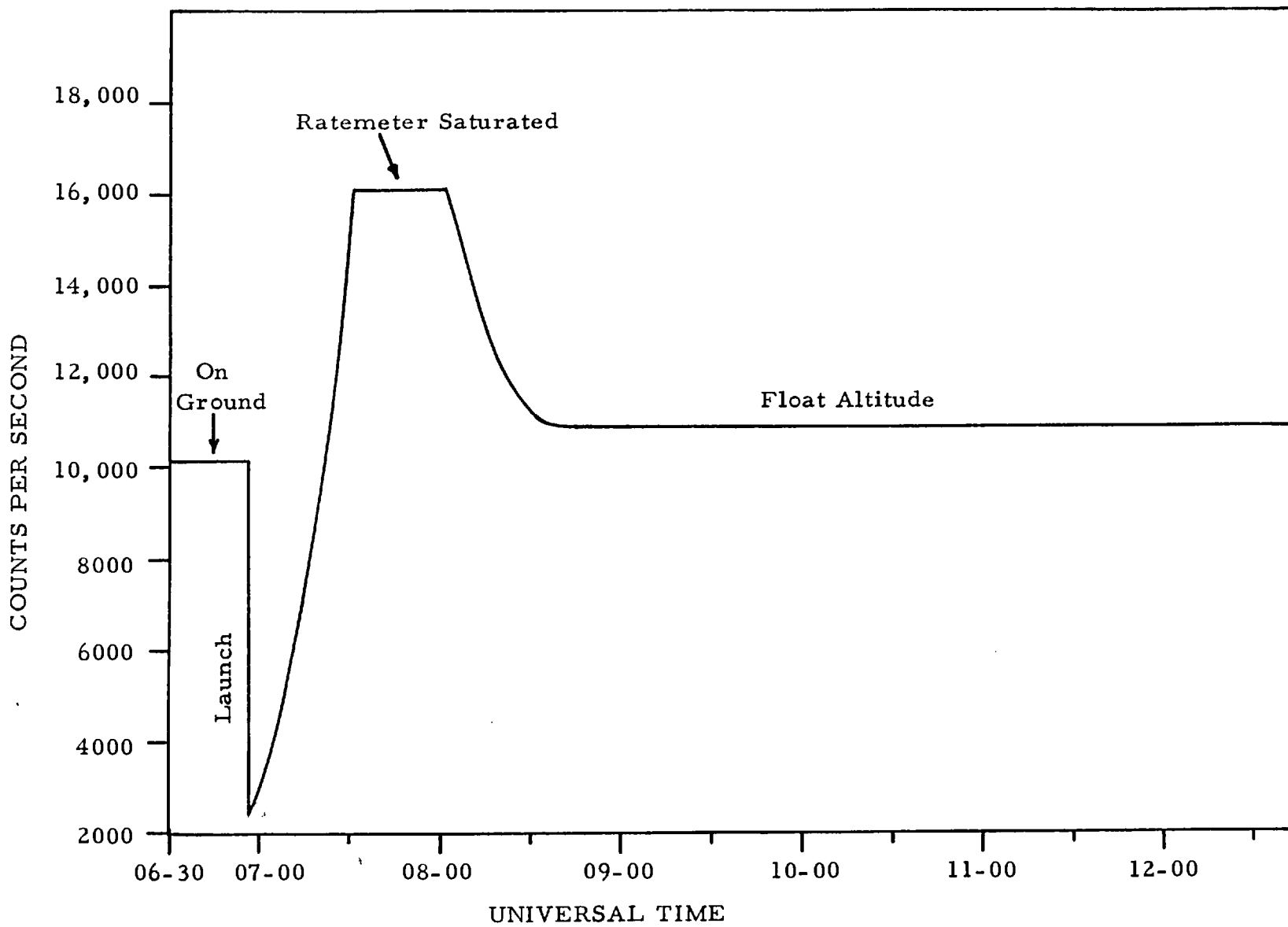


Fig 2.10: Temperatures During Flight

Fig 2. 11: Output Of The Analogue Ratemeter.



produced at float altitude.

(b) The digital data was punched out on papertape and analysed on an interdata 70 computer. A search for significant increases in the count rate was carried out using  $\frac{1}{16}$ ,  $\frac{1}{4}$ , 1, 8 sec integration times, a deviation being classified as significant if the count rate rose above  $3\sigma$  and remained at this level for three successive integration periods. The only instance of this coincided with the increase observed from the analogue ratemeter. Figure 2.12 illustrates the light curve of the event using 1 and 0.25 sec integration times. In the first instance, it can be seen that four points during the event are more than  $4\sigma$  above the average background rate. The 0.25 sec plot indicates the presence of fine structure, and the duration and general shape of the pulse are typical to those of the gamma-ray bursts observed by satellites.

(c) The total number of counts accumulated in the period 10.21.51 - 10.27.02 =  $56540 \pm 238$ .

The mean background rate prior to and following the event =  $10850 \text{ cts sec}^{-1}$ .

Thus increase above background =  $2290 \pm 238 \text{ cts sec}^{-1}$ .

The integrated flux is  $\sim 10\sigma$  above the average background count rate. The probability of a statistical excursion of this size in 4.25 hours of operation is less than  $10^{-10}$ .

(d) The statistical nature of the counting rate was also examined, during the event, and from a one minute period following the increase. The two distributions are shown in Figure 2.13 together with the

Fig 2.12 (a): Plot Of  
Burst Count Rate Using  
1 Second Time Bins

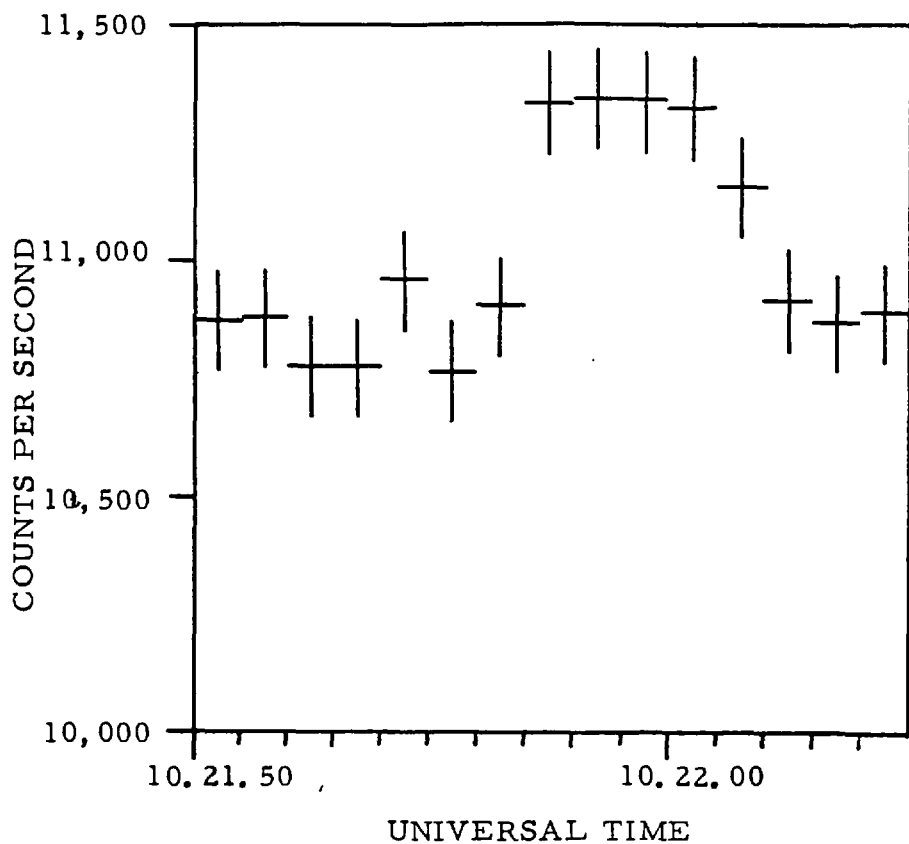
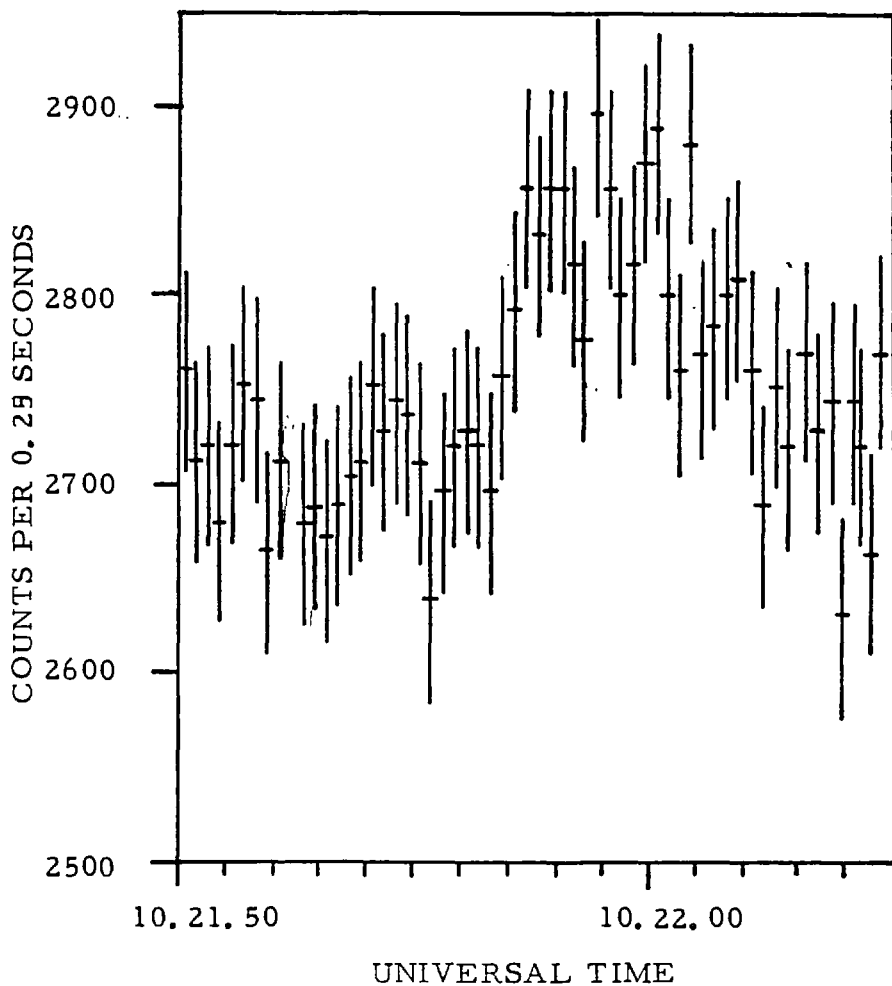


Fig 2.12 (b): Plot Of  
Burst Count Rate Using  
 $\frac{1}{4}$  Second Time Bins



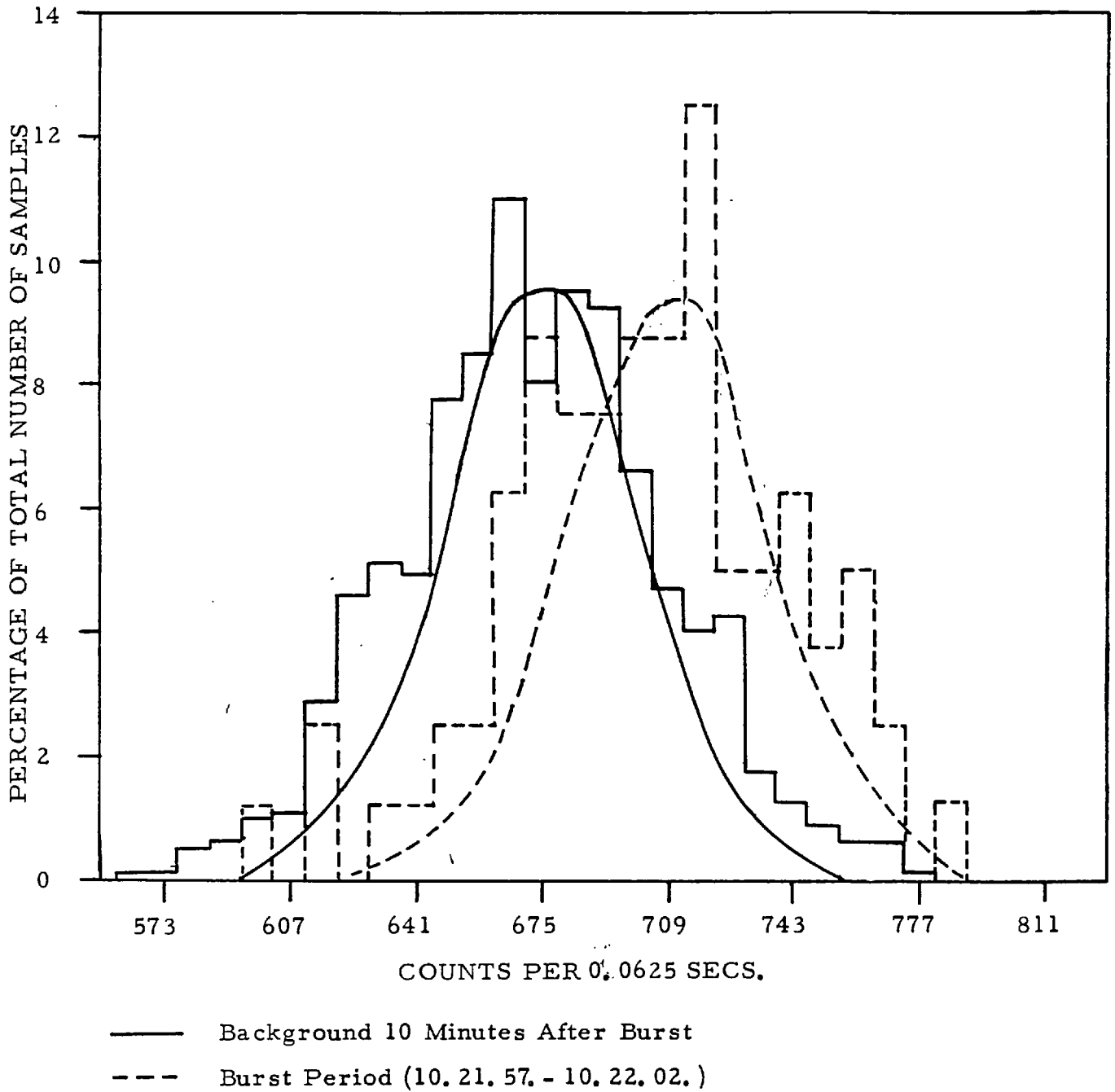


Fig 2.13: Burst And Background Count Rate Distributions. The Smooth Curves Are The Theoretical Distributions. The Bins Are 8.5 Counts Wide.

gaussian curves corresponding to the individual means. It is clear that although some evidence is present in each case of non-statistical deviations, both distributions are essentially gaussian. In the case of the sample taken during the event period, a wider distribution is expected due to the mean changing, as illustrated in Figure 2.12. A small amount of noise in the data stream can cause occasional losses of synch at the receiving station. The effect of this is to cause a broadening of the count rate distribution, which could explain why the two histograms are not quite gaussian.

(e) The possible causes of the increase observed are,

- (1) Detector Malfunction
- (2) Solar Activity
- (3) Charged Particle Dumping
- (4) Detection of a Gamma-burst

Detector malfunction can be eliminated as all the power lines remained invariant during the event period and throughout the rest of the flight. The good approximation of the event histogram to a gaussian fit also confirms that the detector was functioning normally.

There were no solar flares on 27th September and only one small subflare preceded the event, occurring at 03.13 UT, seven hours before the onset of the event. A solar origin can therefore be ruled out.

Dumping of large numbers of charged particles from the radiation belts normally occurs at the time of a geomagnetic storm. There were no such disturbances on 27th September. Several satellite x-ray detectors have observed small spikey increases in the background

counting rate which have been ascribed to charged particle dumping on a small scale, below the threshold of normal Van Allen belt particle detectors. However, these events occur mainly over the Atlantic anomaly and the Eastern Pacific, and are much less likely to be detected over France as the radiation belts are higher than over the U.S.A.

The pulse observed by the balloon detector had very similar temporal characteristics to the known gamma-bursts. Unfortunately it was too small to register on any satellite detectors, and thus its exact nature and the location of the source cannot be determined. However, out of the four possible causes of the rise in counting rate, the detection of a gamma-burst is the most likely.

### 2.3.3. Analysis of Results

Assuming that the pulse observed was produced by a gamma-burst, the size of the burst must have been  $\sim$  two orders of magnitude smaller than the average events detected by satellites. In order to determine if the occurrence rate implied at this level is consistent with a  $\frac{3}{2}$  power law extrapolation of the satellite data, the following considerations must be taken into account.

(a) If the sources of bursts are distributed isotropically, a detector with a uniform angular response positioned above the atmosphere will observe an event rate given by

$$N(>S) = kS^{-3/2} \quad N(>S) \text{ is the number of events seen with size } >S \text{ counts cm}^{-2}.$$

However, the response of a flat slab of scintillator distorts the size spectrum as follows.

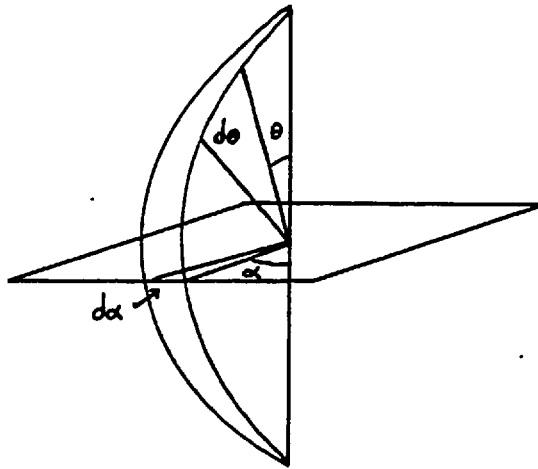


Let  $N(S) dS$  = number of bursts with size  $S \rightarrow S + dS$  incident isotropically.

$$\text{Then } N(S) dS = CS^{-5/2} dS \quad C = \frac{3}{2} k.$$

The number incident within the solid angle  $d\Omega$  inclined at an angle  $\theta$

$$= \frac{CS^{-5/2} \sin\theta d\theta d\phi ds}{4\pi}$$



If the detector has an efficiency  $E$  at all angles, the burst will have an apparent size  $Z = SE \cos\theta$  cts  $\text{cm}^{-2}$ .

Integrating over all  $\phi$  gives

$$N(Z) dZ = \frac{CZ^{-2.5} E^{1.5}}{2} \int_0^\theta \cos^{1.5}\theta \sin\theta d\theta dZ$$

i.e. the number of bursts observed with sizes  $Z - Z + dZ$ .

Therefore the number of bursts observed with a size  $>Z$ ,  $N(>Z)$ ,

$$= \int_0^\infty N(Z) dZ = \frac{CZ^{-1.5} E^{1.5}}{2} \int_0^\theta \cos^{1.5}\theta \sin\theta d\theta$$

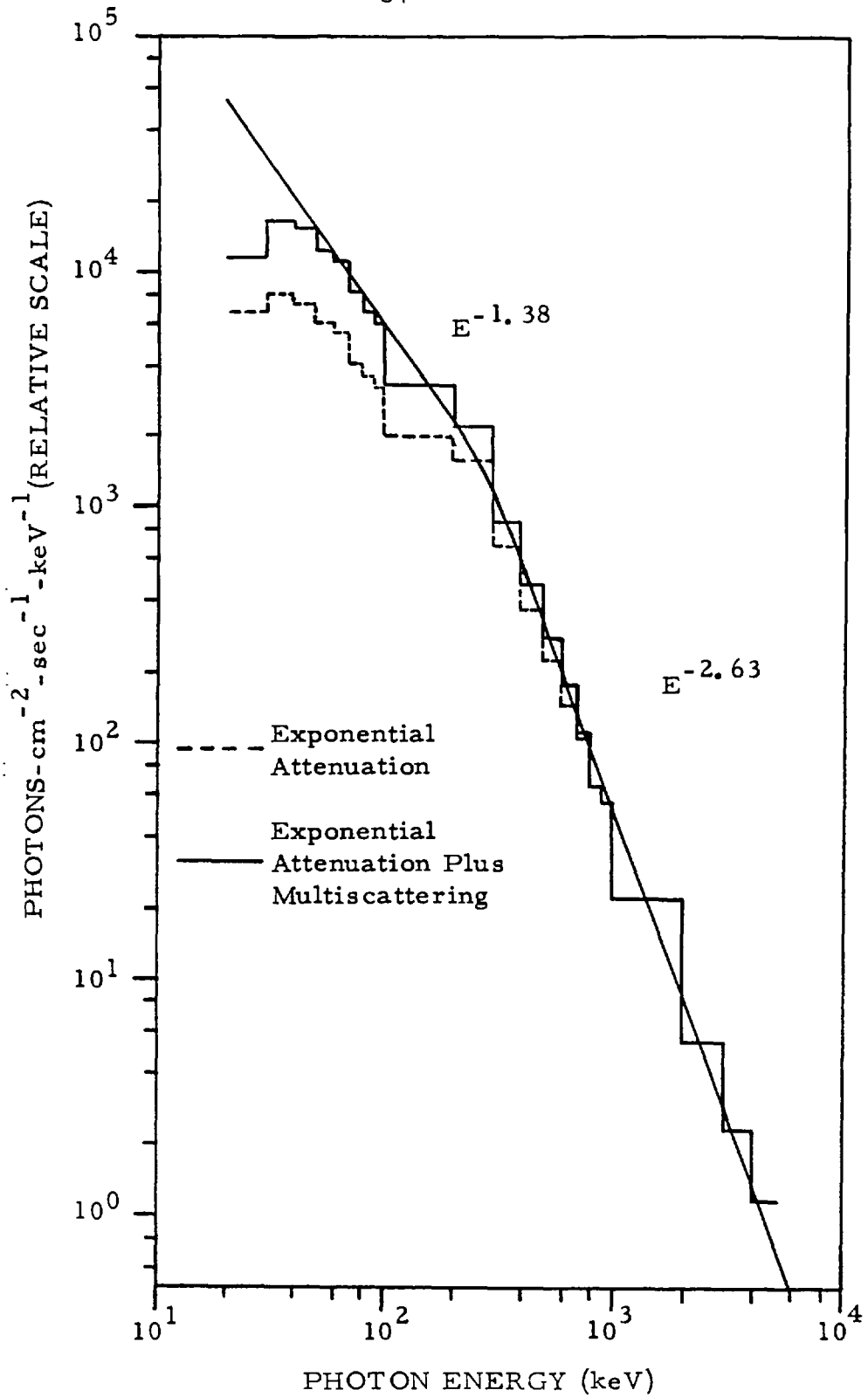


Fig 2. 14: How The Standard Event Average Burst Spectrum Is Affected By Atmospheric Scattering.

This calculation has so far ignored the effect of atmospheric attenuation on the burst. Manchanda (1975) has considered the case of a burst with the standard intersecting power law spectrum incident in the zenith direction, and calculated how the spectrum would appear to a burst detector at a float altitude of  $4 \text{ grms cm}^{-2}$ . He considers two cases, the second one being the most realistic.

- (1) Pure exponential attenuation.
- (2) Exponential attenuation plus multi-scattering effects.

As can be seen in Figure 2.14, the latter case yields a spectrum which is virtually unchanged above 50 keV. However, as the zenith angle  $\theta$  increases so does the amount of attenuation, becoming large for bursts with  $\theta$  values  $>60^\circ$ .

In view of these considerations the effect of the atmosphere has been approximated as causing no attenuation for incidence angles up to  $60^\circ$ , and total attenuation after that point.

$$\text{Thus } \int_0^\theta \cos^{1.5} \theta \sin \theta \, d\theta = \int_0^{60} \cos^{1.5} \theta \sin \theta \, d\theta = \underline{0.33}$$

Computer studies indicate that the detection efficiency  $E$  averaged over all angles = 45% for a standard burst spectrum. Therefore

$$E^{1.5} = \underline{0.3}$$

$$\text{Thus } \underline{N(>Z)} = 0.05 \times KZ^{-1.5}$$

(b) The event observed had a size of  $2290 \pm 238$  cts. This corresponds to  $5.2 \pm 0.54 \times 10^{-8}$  ergs  $\text{cm}^{-2}$  in the range 0.05-2 MeV, assuming that the spectrum was not significantly altered by the atmosphere from the standard form.

(c) The best estimate of the event rate is one burst every 4.25 hours. If the true mean =  $\mu$ , the probability of observing such an event rate is,

$$P = \frac{e^{-\mu} \mu^r}{r!} \quad \text{where } r = 1.$$

Error bars were assigned to the event rate by determining the two values of  $\mu$  corresponding to a P value of 0.05. Values of  $\mu$  satisfying this condition are

$$\begin{aligned} \mu_1 &= 4.5 \\ \mu_2 &= 0.045. \end{aligned}$$

The probability of observing one event from a distribution with a mean inside these two limits is  $>0.05$ . Thus assigning the above limits to the mean of the event rate represents placing 95% confidence levels on the event frequency.

(d) One burst of size  $5.2 \times 10^{-8}$  ergs  $\text{cm}^{-2}$  was observed in 4.25 hours, which corresponds to an isotropic incidence rate of

$$\begin{aligned} \frac{1}{0.05} &= 20 \text{ bursts of this size every 4.25 hours.} \\ \text{i.e. } N(>S) &\text{ where } S = 5.2 \times 10^{-8} \text{ ergs } \text{cm}^{-2} \end{aligned}$$

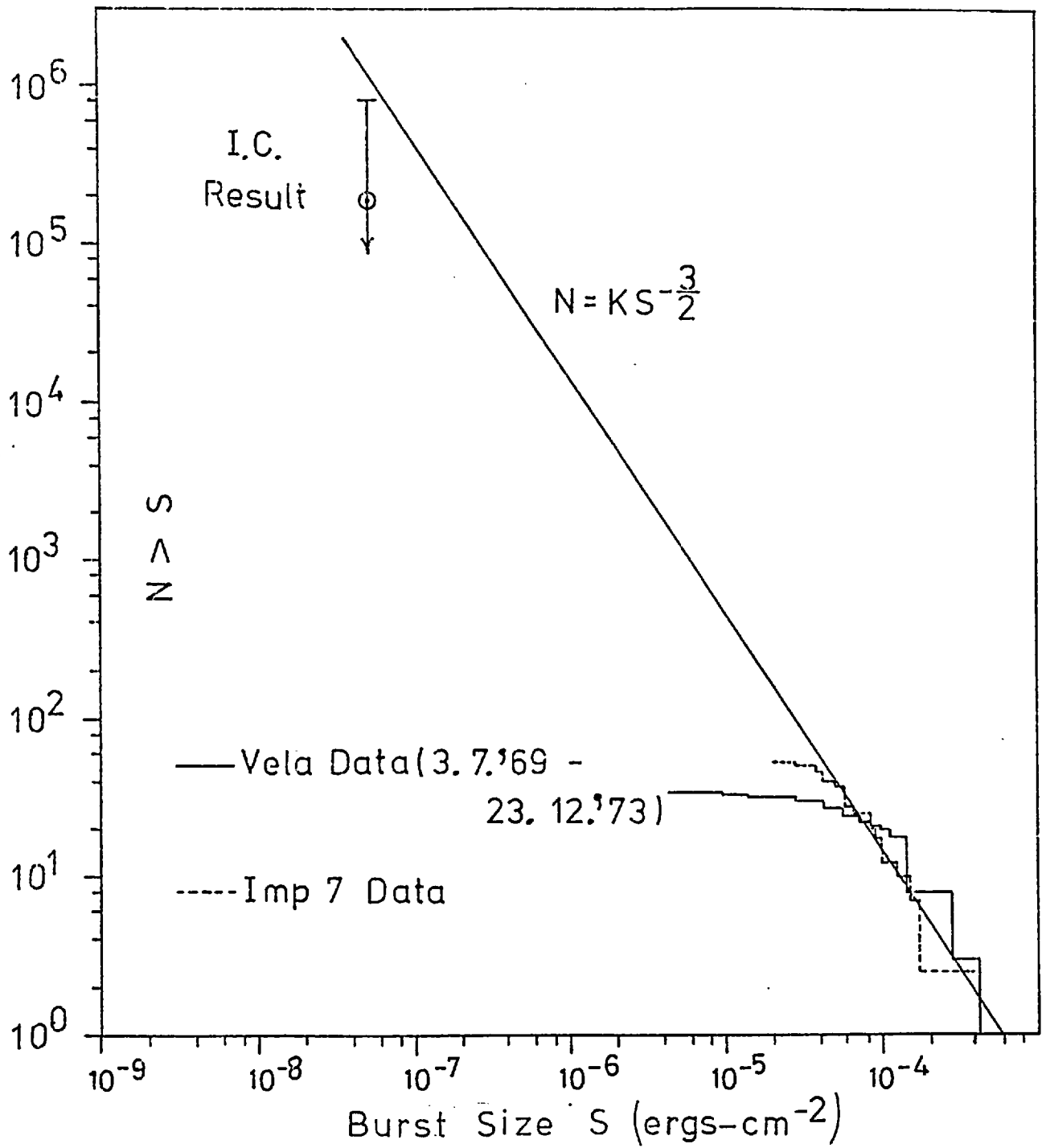


Fig 2. 15: Comparison Of The Event Rate As Given By The Imperial College Result With A Size Spectrum Constructed From Satellite Data. All The Event Rates Have Been Normalised To The Vela Exposure Period.

This result is compared with Vela and Imp 7 size spectra in Figure 2.15. The balloon data has been corrected to cover the same exposure period, and the satellite burst sizes multiplied by a factor of two to account for the different energy windows of the two detector types. The  $\frac{3}{2}$  power law extrapolation lies just outside the 95% confidence limits imposed upon the balloon point, indicating that the results are inconsistent with an isotropic distribution of burst sources.

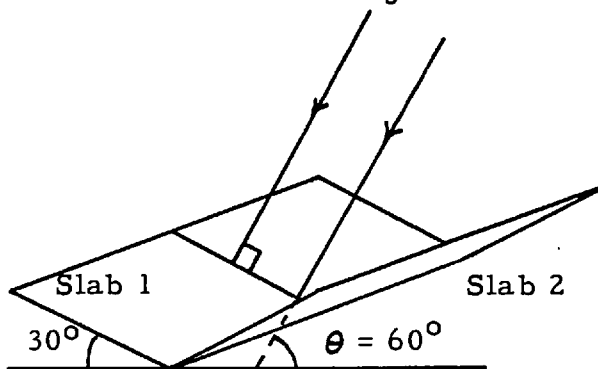
Horstman et al. (1977), have used a more sophisticated model to account for atmospheric scattering. They consider the case of a flat, unshielded detector with a lower threshold of 50 keV, operating at an altitude of 4 mbars, and calculate that the isotropic incidence rate is thirteen times greater than the detected rate above some particular size  $S$  ergs  $\text{cm}^{-2}$ , for a detection efficiency of  $\sim 0.45$ .

This compares well with the simple model used to analyse the balloon data, the effect however is to cause the result to be even more inconsistent with the  $\frac{3}{2}$  power law extrapolation. In order to discover if the discrepancy implied is real, it was decided to fly the detector again to increase the total exposure time.

## 2.4. The Modified Detector

### 2.4.1. Configuration

Originally, it was intended to obtain directional information about a burst by comparing the arrival times measured by the balloon detector and one or more satellites. However, the event observed was too small to trigger any of the satellite systems in use. Furthermore, the low event rate meant that it was unlikely that a burst large enough to register on both detector types would be observed in a flight of similar duration to the first. The two slabs of scintillator were therefore arranged in such a configuration, that the comparison of their individual outputs was sensitive to the angle of incidence of a burst. The slabs were mounted so that they were both inclined to the horizontal at an angle of  $30^\circ$ .



Thus a burst incident normally upon slab 1 strikes slab 2 at an angle of  $60^\circ$  from the normal. As the projected area in this direction is half the

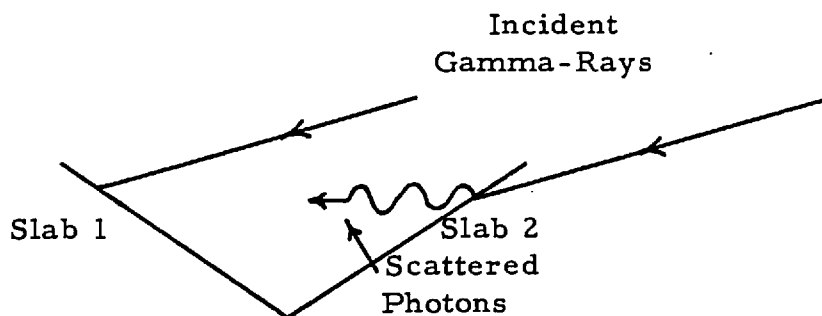
total area of  $0.5 \text{ m}^2$ , slab 2 will produce a lower count rate than slab 1, and the possible source locations lie upon a circle whose plane is inclined in the direction  $\theta = 60^\circ$ . This is the best that can be done with two slabs; four slabs are required to limit the number of source directions to two, corresponding to the intersections of the two respective circles.

The width of the circle  $\delta\theta$  is essentially fixed by the counting statistics obtained from the slabs, which in turn are dependent upon the burst size; greater precision corresponding to larger size.

The angle of inclination to the horizontal of the two slabs was chosen to be  $30^\circ$  for two reasons.

(a) Although the angular sensitivity of such a device increases with inclination, the effective area is reduced. The chosen configuration represents a reasonable compromise, the effective area being  $\sim 0.87 \text{ m}^2$  at normal incidence.

(b) Bursts incident with angles  $> 60^\circ$  from the zenith can only be seen by multiple scattering, due to atmospheric attenuation. Therefore with an inclination of  $30^\circ$ , there will be no events where appreciable scattering from one scintillator into another can occur. This would be plausible if the inclination was increased, thereby complicating the angular response.

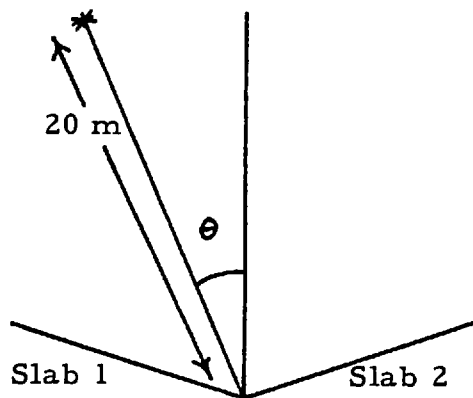


Apart from the alteration to the configuration, the only change introduced was to arrange for the two slab counting rates to be monitored separately, before being summed. The upper and lower thresholds remained unchanged.



#### 2.4.2. Angular Response.

The angular dependence of the detection efficiency was determined for each slab by illuminating the detector with 122 keV x-rays from a calibrated CO-57 source. The survey was conducted on a playing field, previous experiments having shown that in such an environment scattering effects are small. The detector was stood edge on and the source positioned 20 m away at a height of 50 cms. The azimuthal angle  $\theta$  was varied from  $-60^{\circ}$  to  $+60^{\circ}$ , the number of counts accumulated by each slab in 30 secs being determined at each source position.

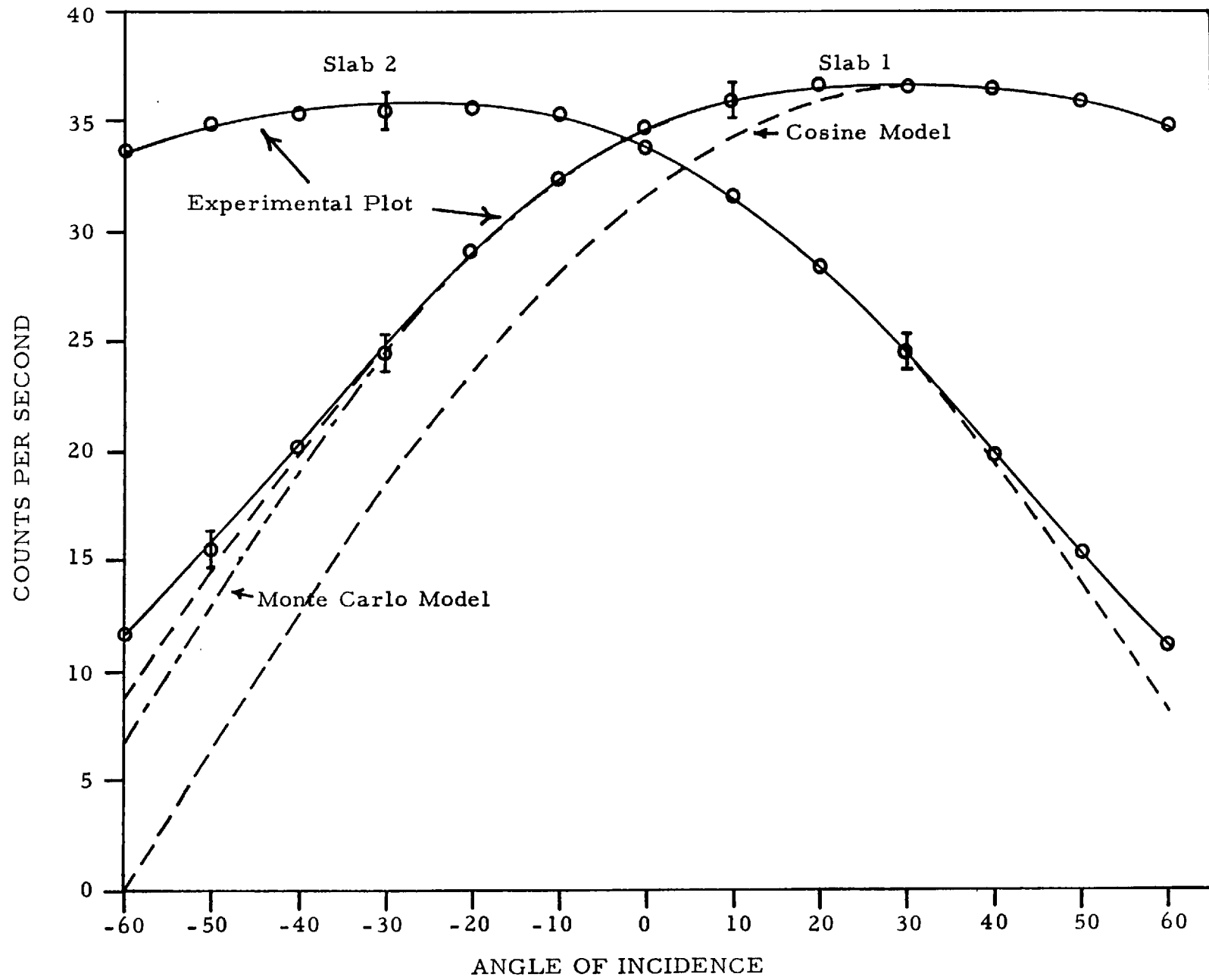


The two background count rates were taken before and after the survey and found to be invariant.

The results are illustrated in Figure 2.16 together with theoretical models of the angular efficiency. The number of cts  $\text{sec}^{-1}$  is normalised to an incidence rate of  $0.02 \text{ photons cm}^{-2} \text{ sec}^{-1}$ . i.e. 100 photons per slab per sec at normal incidence. The response functions of the two slabs are in excellent agreement, a slight discrepancy in the two efficiencies at normal incidence being ascribable to marginally different lower threshold settings. The average of the two efficiencies at normal incidence is equal to 36% as measured for the first detector.

The simple cosine model, which only considers the change in effective area with angle, predicts too sharp a fall off in efficiency as increases in path length are not accounted for. The Monte Carlo

Fig 2.16: A Comparison Of The Angular Response Of The Detector With A Monte Carlo Model.



model on the other hand, is in excellent agreement up to angles of incidence to a slab of  $70^{\circ}$ , after which an excess of counts is evident in the experimental calibration. This was probably caused by Compton scattering of 122 keV photons off the ground and by air molecules.

The configuration chosen for the detector ensures that when the angular efficiency is varying slowly for one slab, the rate of change is virtually a maximum for the other. Figure 2.17 illustrates how the ratio of the two count rates varies with the source direction. It has been assumed that the experimental responses would have followed the projected line had it not been for scattering effects.

The precision with which the arrival direction of a burst can be determined depends upon its size. Considering the case of a burst equal in magnitude to the one previously observed.

Size observed by detector = 2290 cts.

Actual size at detector =  $\frac{\text{size observed}}{\text{efficiency} \times \cos\theta}$

Average efficiency 0.05 - 2 MeV  $\sim$  0.35

Assume normally incident

Size  $\sim$  6500 cts. = S

If the same event was incident on the modified detector at  $30^{\circ}$  to slab 1,

Count rate in slab 1 =  $\frac{S}{2}$  x angular efficiency.

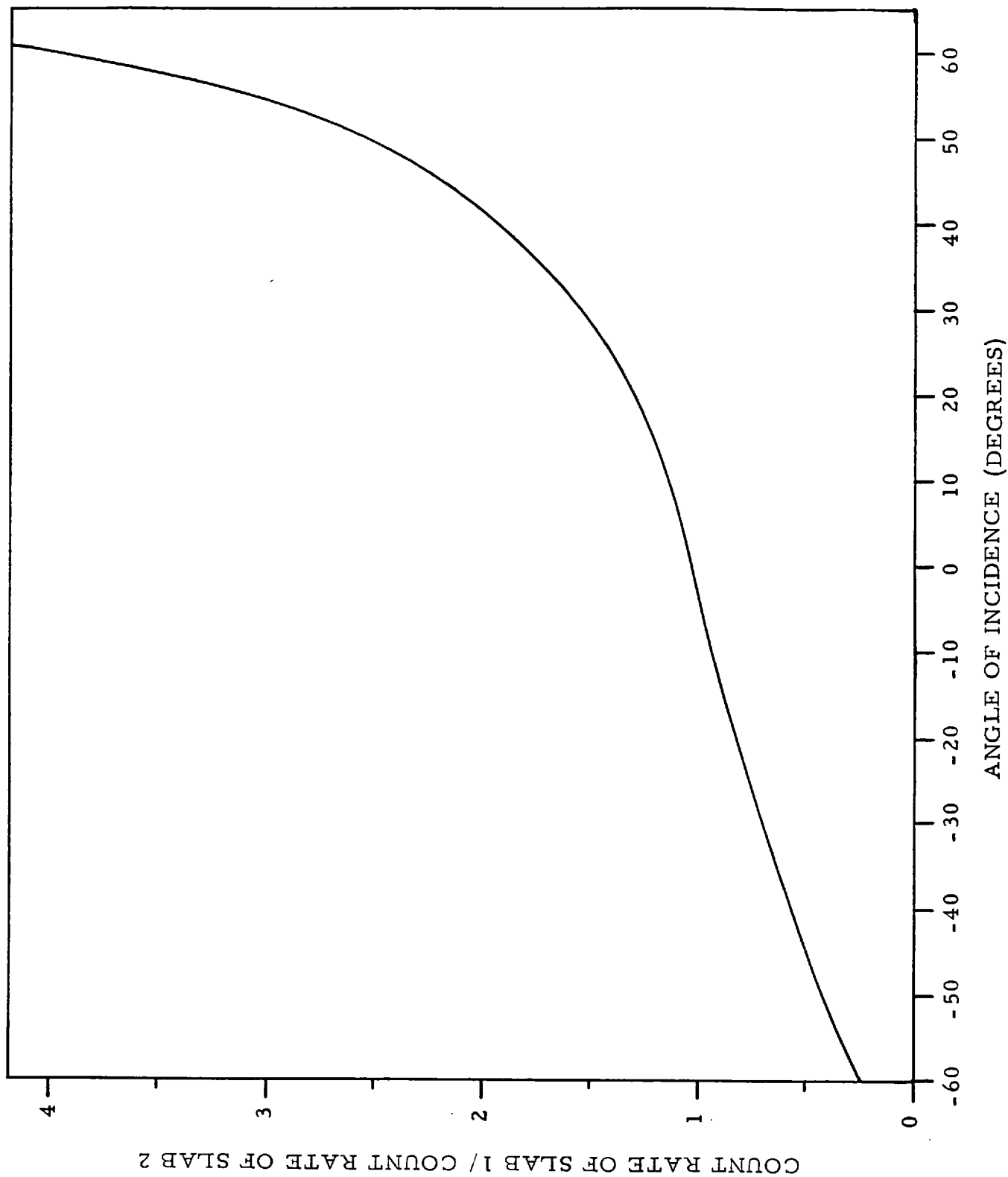
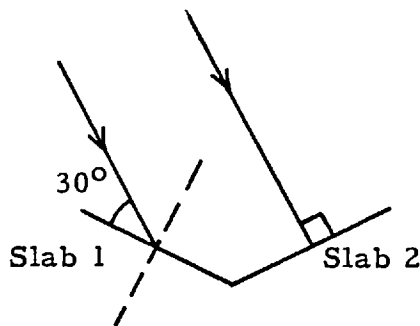


Fig 2. 17: Variation Of The Slab Count Rate Ratio With The Angle Of Incidence.

Assuming that the efficiency in the range 0.05 - 2 MeV is equal to the efficiency as measured at 122 keV the number of counts obtained from,

$$\text{slab 1} = 810 \pm 160$$

$$\text{slab 2} = 1164 \pm 162$$



$$\text{Ratio} = 0.7 \pm 0.17$$

$$\text{which gives } \theta = 30^\circ \pm 12^\circ$$

$$\underline{\underline{\delta\theta \sim 24^\circ}}$$

The errors assume a burst duration of 5 secs and a background rate in each slab of  $5000 \text{ cts sec}^{-1}$ .

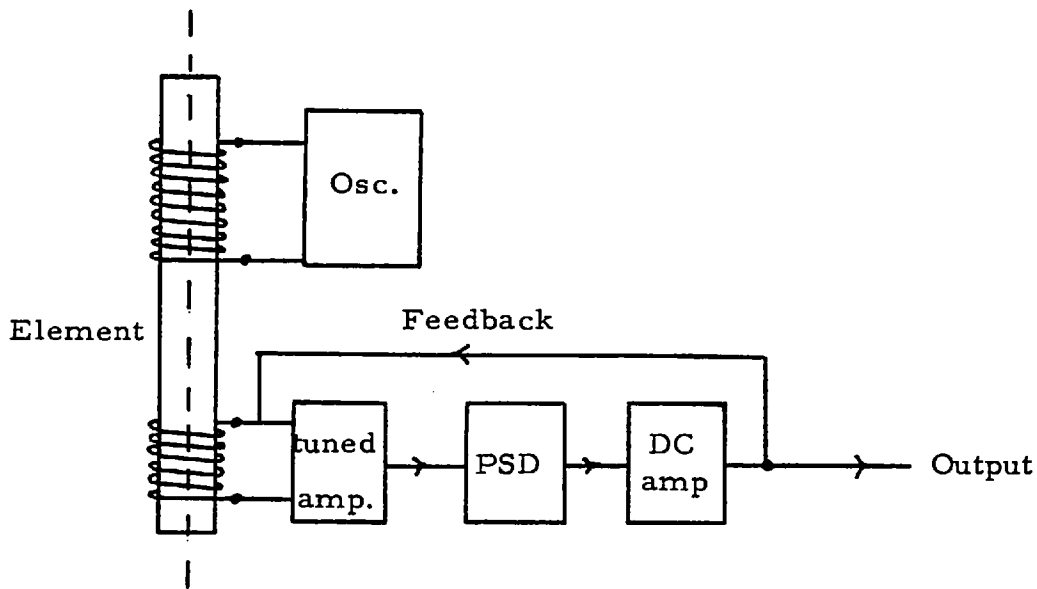
In order to obtain a  $\delta\theta$  of  $\sim 1^\circ$  requires a burst of size  $\sim 45,000 \text{ photons cm}^{-2} \text{ sec}^{-1}$ , if it is of 5 secs duration. A burst of the same size but with a shorter duration produces a smaller value of  $\delta\theta$ . Thus to determine the source direction reasonably accurately requires a burst seven times larger than the one previously observed. If the  $\frac{3}{2}$  power law holds then a burst of this size should be seen  $\sim$  once every ten hours.

#### 2.4.3. Detector Orientation

In order to determine the arrival direction of a burst, it is necessary to know the detector's orientation with respect to the celestial sphere. To achieve this, a two axis fluxgate magnetometer

was attached to the framework in order to fix the payload's orientation with respect to the Earth's magnetic field; and hence to the universe at large. A block diagram of the system is shown in Figure 2.18, for simplicity only one axis is illustrated.

Figure 2.18. Magnetometer Layout



An oscillator drives the fluxgate element at 1 kHz with sufficient power to drive it into saturation. The output from the element is an a.c. signal with a component at 2 kHz, the amplitude of which depends upon the magnetic field along the axis. The signal is amplified, filtered and then fed into a phase sensitive detector. The d.c. voltage from the detector is amplified and then fed back to the element as negative feedback. Thus the magnetometer essentially operates as a null seeking device, the amount of negative feedback required being a measure of the field along the element's axis.

The two elements were mounted at  $90^{\circ}$  to each other in a non-magnetic framework. The device measured the payload orientation with  $1^{\circ}$  accuracy.

#### 2.4.4. Data Encoding

The outputs from the magnetometer, and the two slab count rates, were placed into analogue locations in the data format and read out sixteen times a second. Another analogue channel was used to monitor the total count rate from the two slabs above the upper thresholds, thus enabling a check to be kept of the charged particle flux. The total counting rate of the two slabs and the house-keeping sensors' outputs, were encoded and transmitted in the same way as for the previous flight.

#### Analogue Channels Used

<u>Channel Number</u>	<u>Function</u>
1	+5 V line
2	+12 V line
3	+15 V line
4	-6 V line
5	-15 V line
6	EHT monitor
7	P.M. Thermistor
8	Battery Thermistor
9	Electronics Thermistor
10	Mag. X axis
11	Mag. Y axis
12	Slab 1 Ratemeter
13	Slab 2 Ratemeter
14	Upper Threshold Ratemeter

## 2.5. Flight and Results

### 2.5.1. Flight Details

The modified detector was launched by CNES from Gap Tallard (France) at 05.26 UT on 11th June, 1975. The flight duration at float altitude (3-4 mbars) was six hours, but owing to transmitter failure only three hours of data were received. A second launch was performed at 04.51 UT on 21st June, and a flight of 6.25 hours at an altitude between 3 and 4 mbars was achieved, the absence of transmitter problems ensuring good data reception. During both flights the low and high voltage lines remained steady, thermal behaviour being similar to that displayed during the original flight.

### 2.5.2. Results

(a) During both flights the two analogue ratemeters behaved in a similar manner to the count rate monitor used on the first detector. The average count rates at altitude were,

$$\begin{aligned}\text{slab 1} &\sim 5500 \text{ cts sec}^{-1} \\ \text{slab 2} &\sim 5400 \text{ cts sec}^{-1}\end{aligned}$$

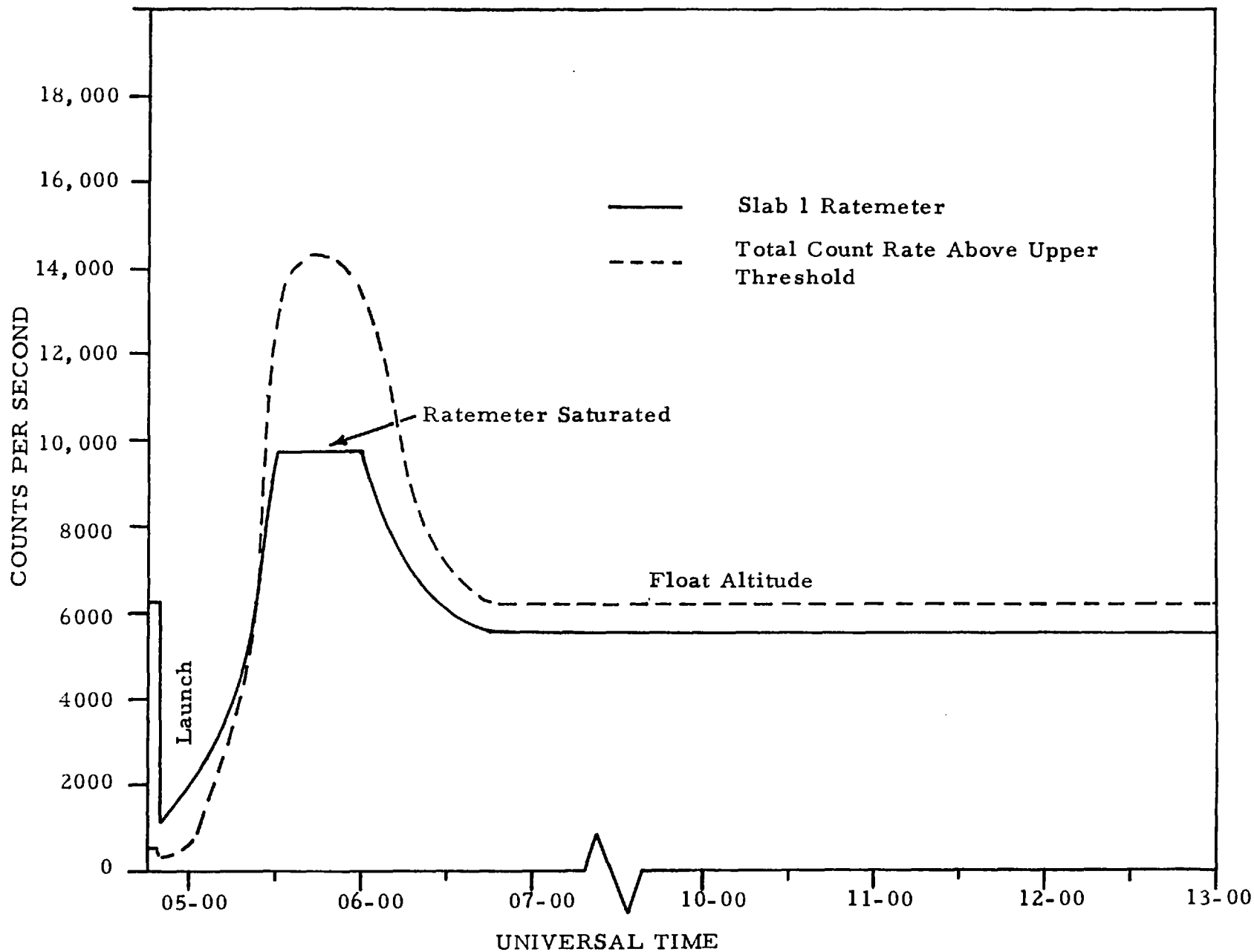
The difference is in the same sense as the one observed during the angular survey.

During the whole of the nine hours of observations, neither ratemeter displayed statistically significant deviations from the average background counting rate.

(b) The count rate above the upper threshold increased sharply after lift off, peaking at the Pfozter maximum together with the two back-



Fig 2. 19: Outputs Of The Slab 1 And Upper Threshold Ratemeters.



ground count rates. The final rate at float altitude was 6300 cts sec<sup>-1</sup>, a factor of ten higher than the corresponding figure at ground level.

(c) The digital data, which comprised the total count rate, was analysed as before using  $\frac{1}{16}$ ,  $\frac{1}{4}$ , 1, 8 sec integration times. A search was carried out for significant deviations from the steady background signal, employing the criterion that a deviation was significant if a  $3\sigma$  rise was present for at least three successive integration periods. No such increase was discovered with any of the four integration times used.

### 2.5.3. Analysis of Results

Only one statistically significant rise above the steady background counting rate was present in 13.5 hours of data. The burst occurrence rate implied by this result is plotted in Figure 2.20, together with results from several other balloon groups. The event rate given by each experimental point is the burst occurrence rate predicted assuming a uniform source distribution, after correcting the raw data for a flat detector's response to such a distribution.

i.e. If the size spectrum is given by

$$N(>S) = kS^{-1.5}$$

A flat detector actually observes a size spectrum of the form

$$N(>Z) = AkZ^{-1.5}$$

"A" depends upon the efficiency of the detector and upon the effect of the atmosphere. Knowing A and the occurrence rate of bursts observed with size  $>Z$ , enables k to

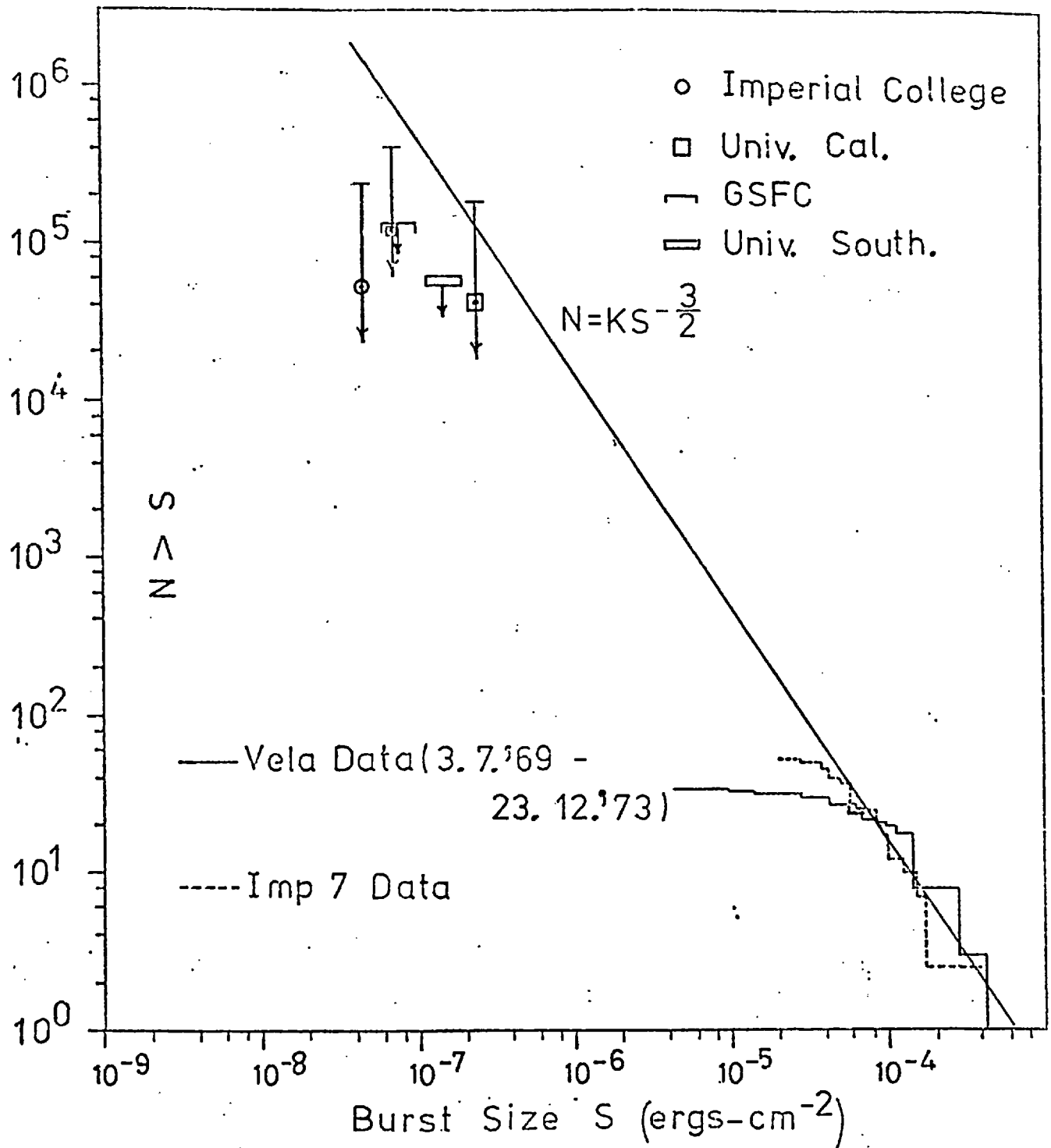


Fig 2. 20: Event Frequencies As Given By Results From Several Balloon Groups, Compared To The Theoretical Rate From A Uniform Source Distribution.

be found. Once  $k$  has been found, the actual incidence rate of bursts with size  $>Z$  can be determined and compared with the rate predicted by extrapolating the satellite data. As the satellite detectors are virtually isotropic, they do not distort the size spectrum and hence form a standard to which other results can be compared. The following corrections and considerations have been taken into account.

- (1) All error bars and limits represent 95% confidence levels.
- (2) All burst sizes and lower limits where no bursts were observed, have been corrected to give the corresponding size in the range 0.05-2 MeV, the energy window of the Imperial College detector. This was done by taking each burst or lower limit as given in the relevant reference, noting the energy range of the detector and its efficiency, and hence calculating the actual burst size as observed by the detector in question in the required energy range. This is important as the efficiency of the detector is accounted for by the constant  $A$ , and should not be used to estimate the size of the burst actually incident on the detector. Cline et al. (1977) have used a similar treatment to the one described here to correct the Southampton result. However, they have made the mistake of using the efficiency of the detector to calculate the actual size of the burst (lower limit in this case) observed. Hence the result has been over-corrected.

When calculating the burst sizes, it was assumed that the bursts had the standard intersecting power law spectrum.

- (3) The effect of the atmosphere has been approximated as causing no attenuation for angles of incidence within  $60^\circ$  of the zenith, and total attenuation for larger angles.

(4) The occurrence rates have been adjusted to an exposure period equal to that over which the Vela data was accumulated, i.e. (3.7.'69 - 23.12.'73).

(5) The efficiency of each detector has been accounted for by the factor "A".

(6) The satellite data were obtained using isotropic detectors, and therefore only the burst sizes need adjusting to account for the 0.05-2 MeV energy window assumed in this treatment of the data.

Then from section 2.3.3.

$$N(>Z) = \left[ \frac{k}{2} E^{1.5} \int_0^{60} \cos^{1.5}\theta \sin\theta \, d\theta \right] Z^{-1.5}$$

E represents the efficiency of the detector in question.

$$\int_0^{60} \cos^{1.5}\theta \sin\theta \, d\theta = 0.33 \text{ in each case.}$$

Figure 2.23 lists the corrections applied to each balloon result and gives the corresponding A values. The correction factors have been evaluated using the information given in Figure 2.22. The event frequency as given by each balloon result is compared with a  $3/2$  power law in Figure 2.20. As can be seen, only the University of California result is consistent with a uniform source distribution, and even then only just. These results strongly indicate that burst sources are not distributed uniformly throughout all space.

If instead of being uniformly distributed throughout all space burst sources follow the distribution of galactic matter, then an omnidirectional burst detector flown above the atmosphere will observe a size spectrum of the form:

$$N(>S) = kS^{-1} \quad (\text{see section 1.11})$$

Of course a flat detector flown in the atmosphere will not observe this spectrum. Horstman et al. (1977) have considered the case of a flat detector with a lower threshold of 50 keV, flying at a depth of 4 grms  $\text{cm}^{-2}$  at a latitude of  $40^{\circ}$ . They have shown by detailed computation, that if a disc population of sources exists the detector will observe a size spectrum of the form:

$$N(>Z) = 0.13 k Z^{-1}$$

assuming that the detector is unshielded and has an efficiency of 0.45 averaged over all angles. The calculation takes multi-scattering by the atmosphere into account, and it is assumed that bursts have an intersecting power law spectrum.

Applying this result to the Imperial College data.

1 burst was observed in 13.5 hours and the event had a size of  $5.2 \times 10^{-8}$  ergs  $\text{cm}^{-2}$ .

From the results of Bassani this corresponds to an incidence rate of  $\frac{1}{0.13} \sim 7.7$  bursts of size  $> 5.2 \times 10^{-8}$  ergs  $\text{cm}^{-2}$  in 13.5 hours, assuming that burst sources follow a disc distribution.

Applying similar corrections to the GSFC and Southampton experiments results in these detectors seeing size spectra of the form,

$$N(>Z) = 0.09 kS^{-1} \quad (\text{GSFC detector})$$

$$N(>Z) = 0.13 kS^{-1} \quad (\text{Southampton detector})$$

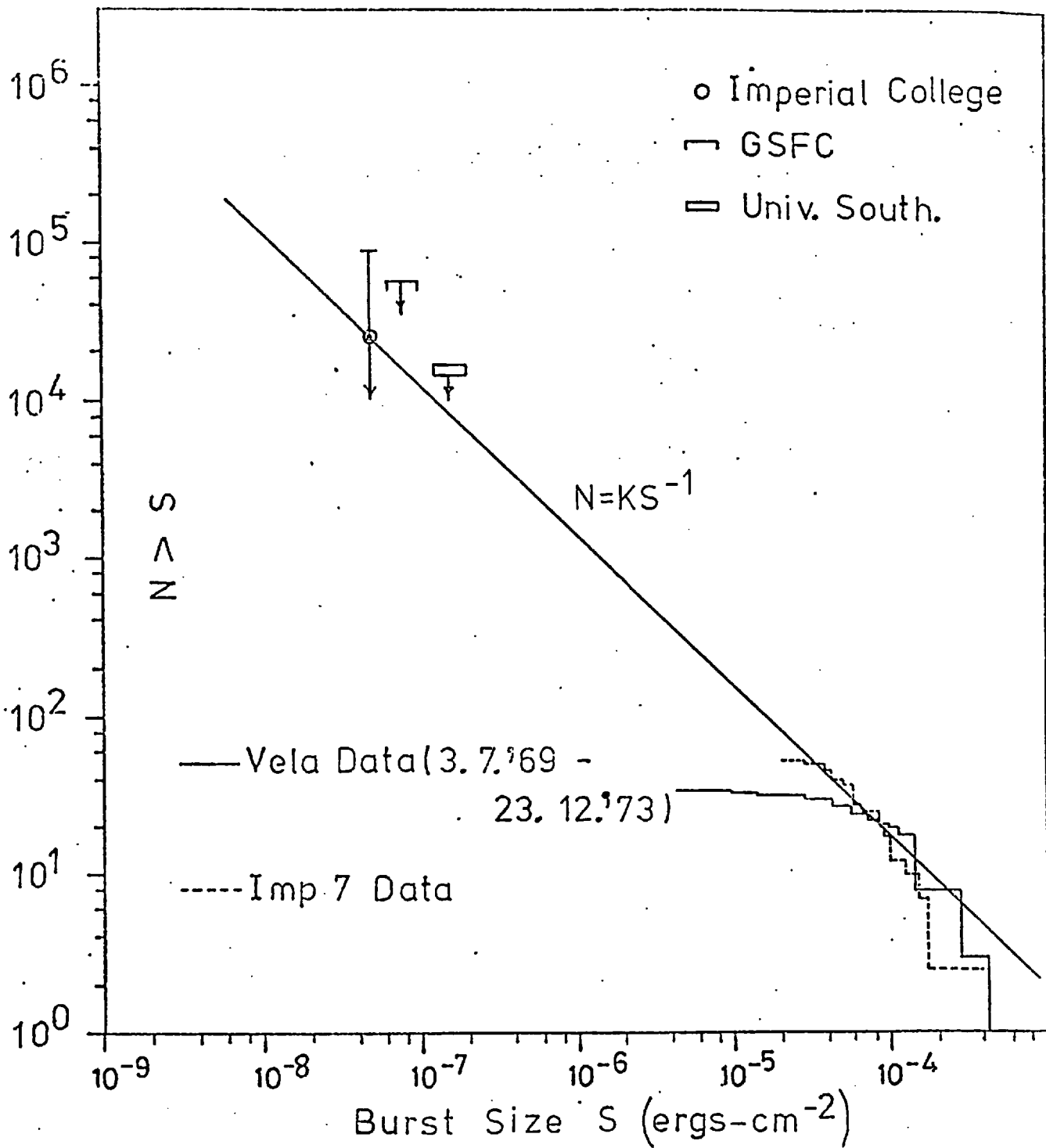


Fig 2. 21: Burst Frequencies As Given By Results From Several Balloon, Compared To The Theoretical Rate From A Galactic Disc Source Distribution.

Fig. 2. 22: Details of Balloon-Borne Burst Detectors

<u>Organisation Involved</u>	<u>Scintillator Elements</u>	<u>Energy Window</u>	<u>Average Efficiency</u>	<u>Total Flying Time</u>	<u>Number Of Bursts Seen</u>	<u>Burst Size Or lower Limit</u>	<u>Reference</u>
Imperial College	$10^4$ cms <sup>2</sup> Ne102A 5 cms thick	0.05-2 MeV	0.45	13.5 hrs.	1	$5.2 \times 10^{-8}$ ergs cm <sup>-2</sup>	
University of Southampton	125 mm diameter NaI(Tl) crystal 1 cm thick	100-1000 keV	0.70	55 hrs.	0	$1.3 \times 10^{-7}$ ergs cm <sup>-2</sup>	Carter et al (1976)
GSFC	2 detectors flown in coincidence Each 0.89 m <sup>2</sup> 5 cms thick	0.3-2.5 MeV	Estimated as 0.4	20 hrs simultaneous observations	0	$4.2 \times 10^{-8}$ ergs cm <sup>-2</sup> (300 keV-2.5 MeV)	Cline et al (1977)
University of California	$10^4$ cms <sup>2</sup> liquid scintillator	500 keV upwards	0.19	65 hrs.	2X	$3.5 \times 10^{-8}$ ergs cm <sup>-2</sup>	Herzo et al (1976)
					1X	$1.4 \times 10^{-7}$ ergs cm <sup>-2</sup> (500 keV upwards)	White et al (1978)



Fig. 2.23: Correction Factors Applied To Balloon Data

<u>Organisation Involved</u>	<u>Corrected Burst Size (Z) 0.05-2 MeV</u>	<u><math>A = \frac{E^{1.5}}{2} \int_0^{60} \cos^{1.5} \theta \sin \theta d\theta</math></u>	<u>Event Rate As Observed By An Isotropic Detector. N(&gt; Z) (normalised to Vela period 3.7.1969 - 23.12.1973)</u>
Imperial College	$5.2 \times 10^{-8}$ ergs cm <sup>-2</sup>	0.05	$5.9 \times 10^4$ bursts
University of Southampton	$1.8 \times 10^{-7}$ ergs cm <sup>-2</sup> (lower limit)	0.10	$2.2 \times 10^4$ bursts
GSFC	$8.6 \times 10^{-8}$ ergs cm <sup>-2</sup> (lower limit)	0.04	$1.5 \times 10^5$ bursts
University of California	$7 \times 10^{-8}$ ergs cm <sup>-2</sup> (2 events)	0.013	$1.4 \times 10^5$ bursts
	$2.8 \times 10^{-7}$ ergs cm <sup>-2</sup> (1 event)		$4.8 \times 10^4$ bursts

The burst incidence rates for a disc-like source distribution, as predicted by the results given in Figure 2.22, are shown in Figure 2.21. The rates are compared with a  $-1$  index size spectrum constructed from satellite data. The three balloon points are all consistent with the  $-1$  index power law and hence with a disc-like distribution of burst sources

#### 2.5.4. Conclusions

One event was observed by the Imperial College detector in 13.5 hours of operation. The event had temporal characteristics typical of gamma-ray bursts. The occurrence rate of small bursts inferred from this result favours a disc-like source distribution and is incompatible with a uniform source distribution. Data from two other balloon groups suggest a similar conclusion. Thus it seems very likely that the sources of the observed gamma-bursts are located within the galaxy.

## CHAPTER 3

### 3.1. Experimental Aim

The results obtained from the flights of the one square metre burst detector, strongly suggest that gamma-bursts have a galactic origin. If the burst sources follow the distribution of galactic matter, then the occurrence rate of small bursts should be consistent with the rate as given by the  $-1$  index power law shown in Figure 2.21. An event rate significantly below this theoretical rate, will indicate that the only gamma-bursts are large local events, most of which are detected by satellites.

In order to determine more accurately the frequency of small bursts and hence differentiate between the above two cases, it was decided to fly a large balloon borne burst detector from Alice Springs in Central Australia (latitude =  $-23^{\circ} 42'$ ). This location was chosen to maximise the probability of observing bursts from a galactic disc population, as  $\sim 95\%$  of galactic matter can be viewed over a twenty-four hour exposure period compared to  $\sim 30\%$  from Northern Hemisphere launch sites. To further maximise the probability of observing small bursts, it was decided to fly the largest possible detector compatible with the equipment available in Australia, and aim for a flight with the longest possible duration. In the past, flights of up to three days duration have been obtained in Australia and it was hoped to achieve a similar flight with the large detector.

### 3.2. The Dectector

#### 3.2.1. General Description

The detector consisted of eighteen slabs of Ne102A plastic scintillator and had a total collecting area of  $6.75 \text{ m}^2$ . The slabs were grouped together in three's (each group being referred to as a tray) and were mounted as shown in Figure 3.1. Using this arrangement, it was hoped to be able to determine the incidence directions of any gamma bursts observed, by comparing the various tray count rates produced by the events.

Each slab measured 75 x 50 cms and was 5 cms thick. Two 5" photomultipliers were coupled directly to the surface of the slab using silicon fluid as a coupling agent. The outputs of the two tubes were inputed in parallel into a head amplifier and discriminator circuit. The discriminators defined an energy window of 50 keV - 2 MeV as with the small detector, and the circuit produced a standard 5 volts pulse every time a photon with an energy inside this range interacted in the scintillator. The outputs from the eighteen head amplifiers were then fed into a data handling box.

The power source consisted of six parallel stacks of lithium organic primary cells. Each stack produced 24 volts and had a capacity of 10 ampere hours. These cells were used because of their very high power to weight ratio (total mass of the cells was only 4 kgs). Six power converters were then used to produce the required voltage lines. The high voltage needed to run the photomultipliers was provided by a separate eht converter on each slab. This ensured that each slab was able to operate as an independent unit.

The framework consisted of eight aluminium sections which when bolted together formed a 10' x 10' raft. The scintillators were mounted

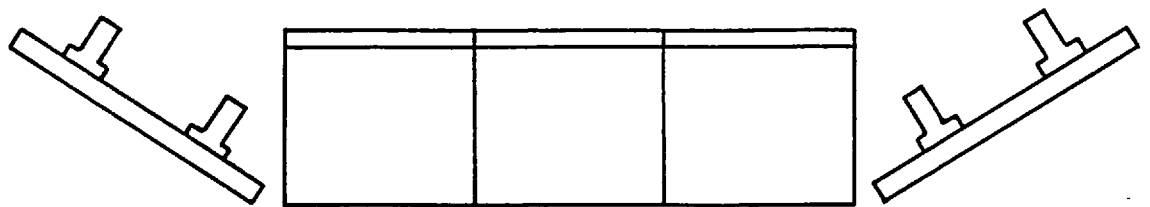
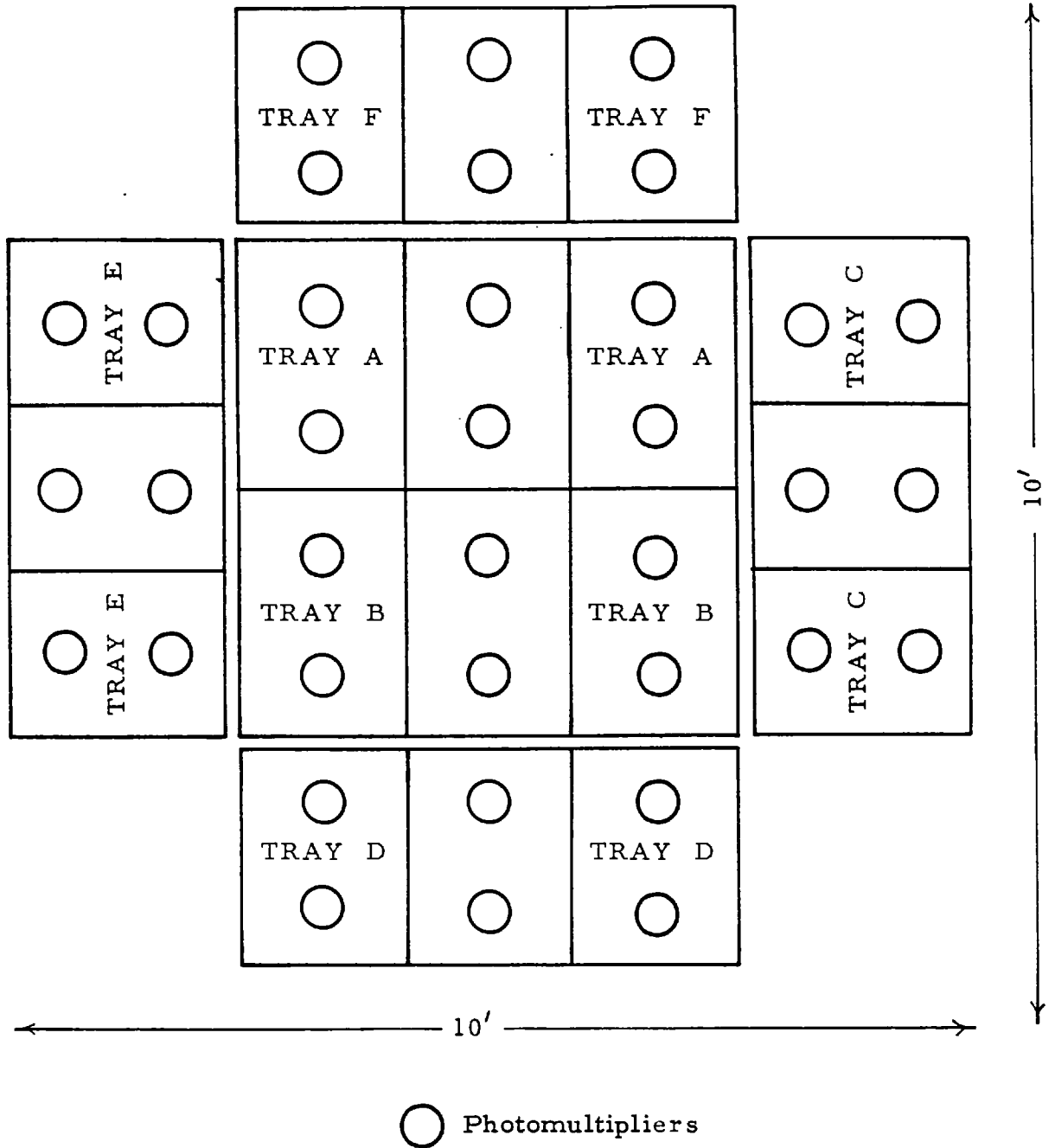


Fig 3.1 : Schematic Diagram Of The Large Burst Detector

in aluminium trays which bolted directly onto the raft. This made the detector easy to assemble at the launch site. The framework and suspension were designed to withstand forces of 20 g. The necessary thermal insulation was provided by an 8" layer of expanded polystyrene which completely covered the detector. Corrugated cardboard crash-padding was attached to the underside of the detector, and the total weight of the device was 700 kgs.

In order to facilitate a long flight, 450 kgs of ballast were carried in a container suspended underneath the crash-padding. The ballast was in the form of lead shot and radio commands were used to release the required amount.

### 3.2.2. Scintillator Elements

In view of the discussion of design criteria in the previous chapter and the successful flights of the  $1 \text{ m}^2$  detector, it was decided that the large detector should simply be a scaled up version of the  $1 \text{ m}^2$  detector. However, although the scintillators had the same width and depth (50 cms and 5 cm respectively) as the slabs used in the previous experiment, it was necessary to make them 25 cms shorter in order that they would fit into a new environmental chamber which had been installed at Imperial College. In order to keep the ratio of photocathode to scintillator area approximately the same, it was decided to view the slabs with two 5" phototubes instead of three as with the small detector. The shiny side of silver foil was again used as a reflecting layer around each scintillator. To prevent light entering the slab, two layers of black tape were wrapped over the foil and a black plastic bag was placed over each photomultiplier.

The light collection efficiency from a completed slab was measured as follows. A grid of small holes to accept a photodiode were drilled in the underside of the slab; the holes were separated by 2" and the grid covered half the slab. The two phototubes were operated at the same voltage from an external eht supply and a photodiode, installed in one of the holes using optical grease as a coupling agent, was used to generate pulses from the photomultipliers. The outputs of the two tubes were fed separately into a pulse height analyser and displayed. The photodiode output was set sufficiently high to ensure that the resulting distribution was gaussian; the positions of the two photopéaks were noted. Keeping the diode setting constant, this procedure was repeated as the diode was moved over the slab. A  $\mu$ - meson telescope was used to measure the absolute collection efficiency from each photomultiplier at two diode locations, using the technique described by Wheeler (1974). The collection efficiency from each photomultiplier from each diode position (n), could then be found by finding the ratio of the position of the photopeak produced when the diode was in one of the two calibrated positions, and then multiplying by the absolute collection efficiency measured from the latter position. As there were two calibrated positions, the average efficiency from each point (n) was determined. The variation in the total collection efficiency is shown in Figure 3.2, where the summed efficiency from the two phototubes is plotted as a function of distance along the line whose position is shown in the insert. The average collection efficiency was 9.5% (cf. to 10% using three tubes on a 100 x 50 cm slab) and the efficiency from 90% of the slab was within  $\pm 3\%$  of this value, i.e. between 6.5 and 12.5%.

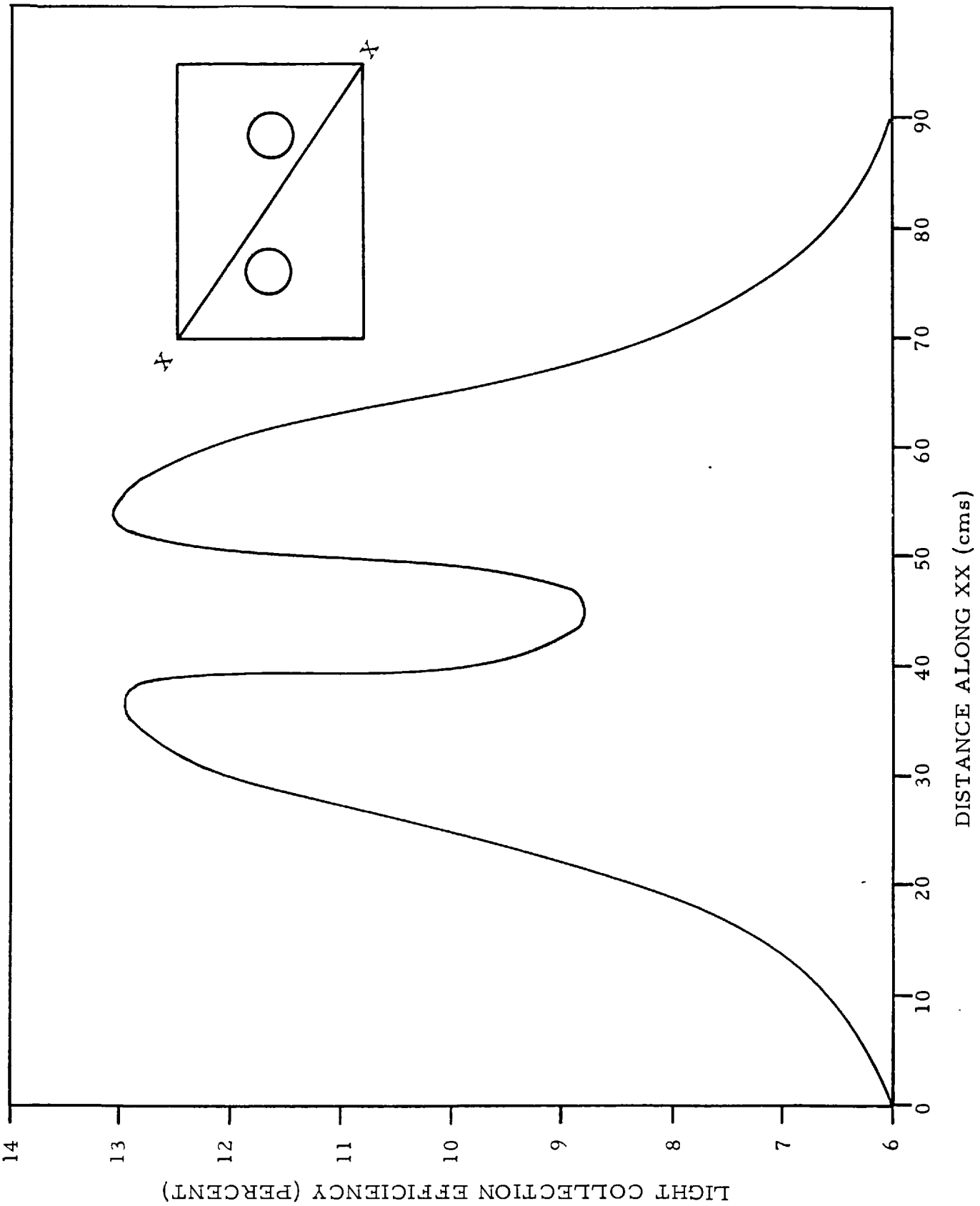


Fig 3. 2: The Variation In Light Collection Efficiency From A Slab.



As the geometry of light collection was virtually identical to that from the slabs used in the small detector, it was decided to use the same upper and lower thresholds, to reduce photomultiplier noise to an insignificant level and to reject all charged particles with energies  $>1.7$  MeV. It is evident from the above discussion that the theoretical efficiency of the 75 x 50 cm slabs, will be almost identical to the theoretical efficiency computed for the 100 x 50 cm slabs. It was expected that the measured efficiency would also be very similar.

### 3.2.3. Slab Calibration

The lower threshold of each slab was set at 2 p.e. as follows. One of the photomultipliers on the slab was connected to the slab's eht supply, and the tube's output was fed into a PHA, whose screen was calibrated in terms of photoelectrons using the method described in Chapter 2. A photodiode, driven at 5 kHz, was then used to produce pulses from the photomultiplier. The photodiode output was adjusted until the pulse height distribution corresponded approximately to a poisson distribution with a mean of 2 p.e. The percentage of pulses with size greater than 2 p.e. was then noted (theoretically 46% if the distribution is perfectly poissonian with a mean of 2 p.e.). The tube's output was then fed into the slab's amplifier and discriminator circuit, and the eht supply was adjusted until the same percentage of the output pulses appeared above the lower threshold discriminator. The eht to the second photomultiplier was then adjusted until the two tubes were balanced, and the balance was checked using radioactive sources. The two phototube outputs were then connected in parallel into the head amplifier which produced the required lower threshold of 2 p.e. The upper threshold was set at 177 p.e. by scaling the upper discriminator

setting accordingly.

The efficiencies of the eighteen slabs at 122 keV were then measured by exposing them to a Co-57 source, using the method detailed in section 2.2.8. The average efficiency of the eighteen slabs was found to be 36% (cf. the theoretical value of  $\sim 35\%$  and the value of 36% as measured for the small detector). However, it was found that the individual efficiencies varied between 31% and 41%. This was due to differences in the average light collection efficiency from the slabs, brought about by differences in optical coupling and of the efficiency of the reflecting layer of silver foil. The eht supplies were adjusted until all the slabs had an efficiency of 36% at 122 keV. This ensured that the main design criterion was satisfied, i.e. the large detector was simply a scaled up version of the  $1 \text{ m}^2$  detector, with an energy window of 50 keV-2MeV.

#### 3.2.4. Angular Resolution

The layout of the detector was chosen as a compromise between the conflicting requirements of:

- (i) maximising the angular resolution.
- (ii) restricting the overall size of the detector.

To maximise the angular resolution would have meant placing all the slabs in the inclined side arms, but unfortunately this was not possible as the detector would then have been too large to launch.

The angular variation of the detection efficiency of a single slab at 122 keV was determined as for the small detector (see section 2.4.2), and is illustrated in Figure 3.3. The experimental curve is compared with

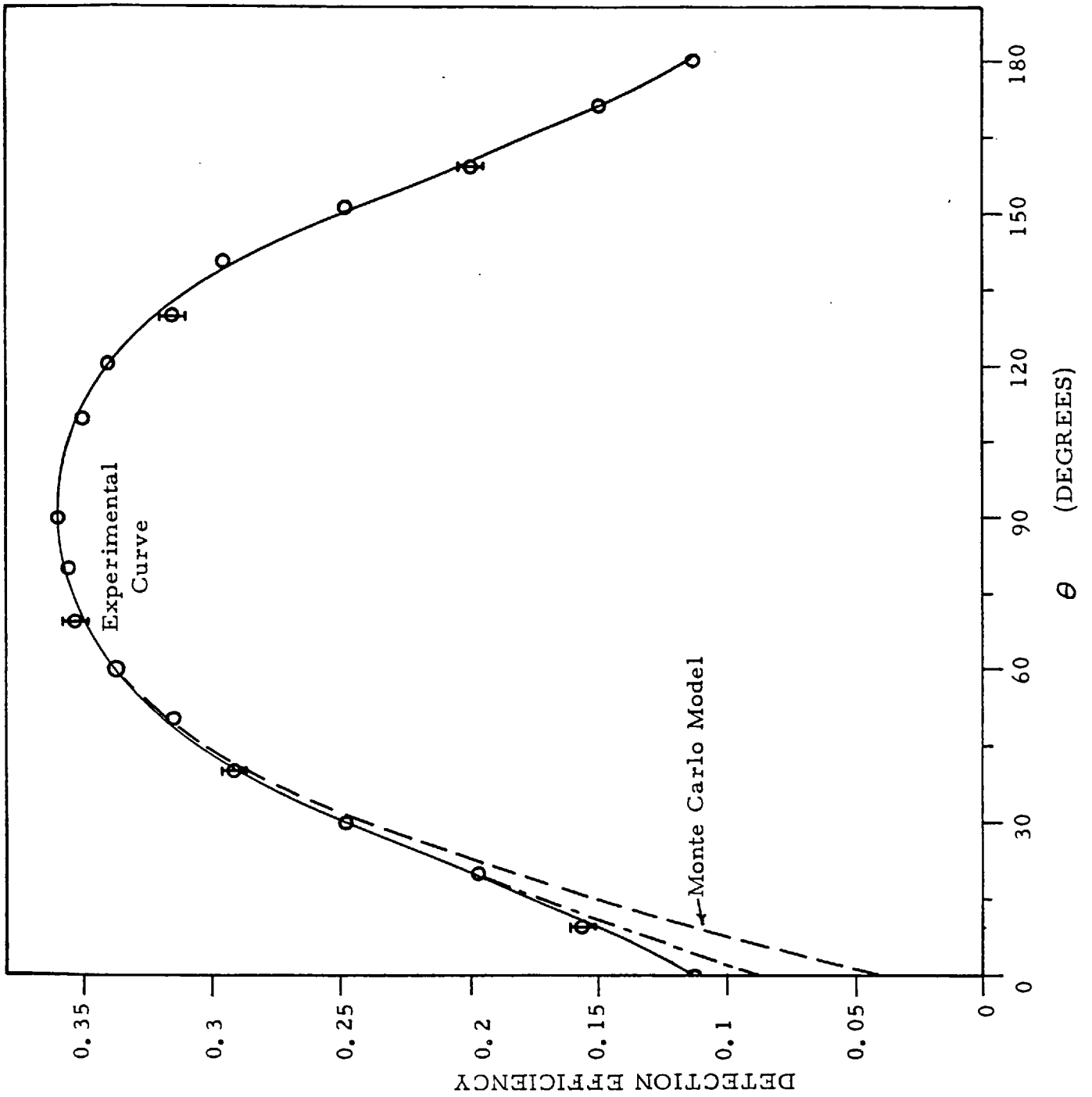


Fig 3. 3: Variation Of The Detection Efficiency With The Angle Of Incidence  $\theta$ .  $\theta = 90$  Represents Normal Incidence. The Detection Efficiency At Angle  $\theta$  Is The Ratio Of The Count Rate To The Number Of Photons Incident Per Second At Normal Incidence.

the theoretical function obtained from a Monte Carlo computation. The two curves are in good agreement up to large incidence angles where experimentally, an excess of counts was obtained, presumably due to the effects of ground scattering.

It is possible to estimate the potential angular resolution of the large detector from these results. Referring to Figure 3.4, there are two possible ways of determining the incidence angle  $\theta$  of a burst in the  $x = 0$  plane.

- (i) By comparing the count rates of trays D and F.
- (ii) By comparing the count rate of tray D or F to the combined count rate of trays A and B.

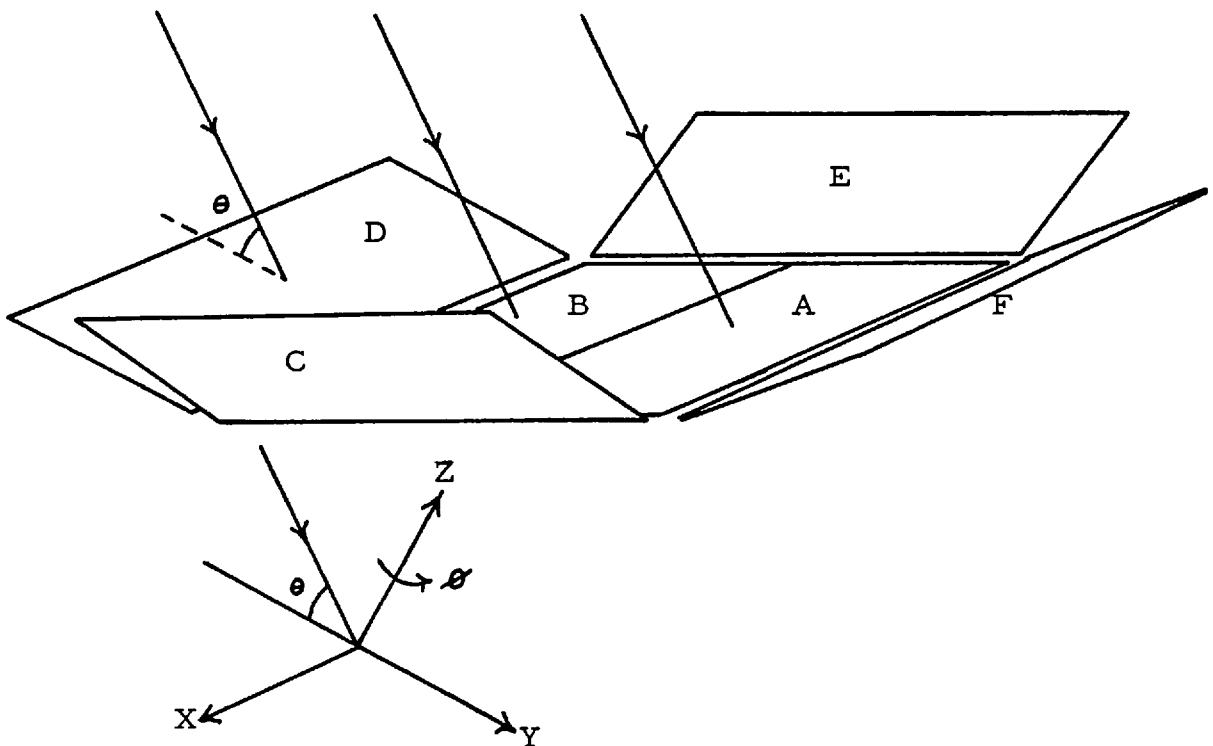


Fig 3. 4: Determination Of The Arrival Direction Of A Burst.

Fig 3. 5: Variation In The Count Rate Ratios With The Angle Of Incidence.

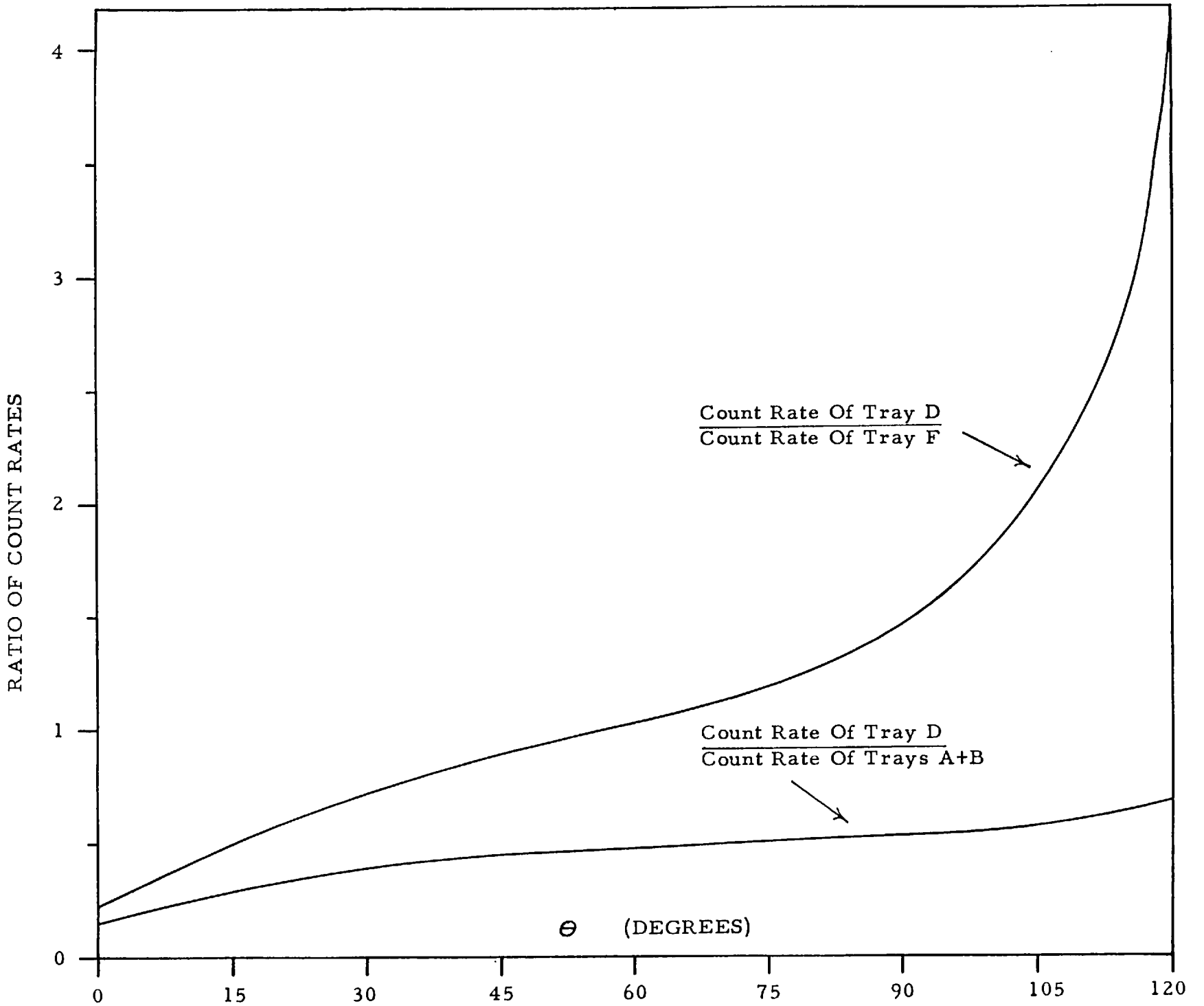


Figure 3.5 shows how these ratios will vary with  $\theta$ , assuming that the angular response curve would have followed the projected line were it not for the effects of scattering. The angular resolution of the detector will be symmetric about  $\theta = 60^\circ$ . If method (ii) is used to determine the angle of incidence, the best resolution for  $\theta$  values greater than  $60^\circ$  will be obtained by comparing the count rate of tray F to the combined count rate of trays A and B.

Consider a burst equal in size and duration to the one observed by the small detector incident at  $\theta = 30^\circ$  where the angular resolution will be about average.

Burst size  $\sim 6500$  photons  $\text{cm}^{-2}$  (assuming it was incident normally on the small detector. See section 2.4.2.)

Burst duration  $\sim 5$  s.

Total number of counts produced in any tray (S)

$$= 6500 \times A \times \epsilon(\theta)$$

A = area of tray (S) in meters.

$\epsilon(\theta)$  = detection efficiency.

The burst will produce the following tray counts:

Tray D	:	$1828 \pm 240$ cts
Tray F	:	$2632 \pm 243$ cts
Tray (A+B)	:	$4943 \pm 343$ cts

The errors assume a background counting rate of  $1 \text{ ct cm}^{-2} \text{ s}^{-1}$ .

(i) Comparing the count rates of trays D and F gives the incidence angle  $\theta$  as  $30^{\circ} \pm 8.5^{\circ}$ .

(ii) Comparing the count rate of tray D to the combined rate of Trays A and B,  $\theta = 30^{\circ} \pm 10^{\circ}$ .

Noting that the above results represent the average situation it is evident that in general, comparing the rates of the inclined side arms produces the smallest error.

Thus the burst source must lie somewhere on a circular band of width  $17^{\circ}$ . A comparison of the count rates of Trays C and F will produce a similar band which will intersect the first at two points. The burst source must lie inside one of the two areas of intersection whose size will be  $\sim 300$  square degrees. It is impossible to determine from the burst detector data alone in which of the two areas the source is located.

The small detector could only have positioned the source to a circular band of width  $24^{\circ}$ , and thus the large detector represents a big improvement in terms of angular resolution.

### 3.2.5. Housekeeping and attitude monitors

A pressure transducer was used to determine the altitude of the detector. This consisted of a reference oscillator and an oscillator whose frequency was pressure dependent. Monitoring the difference between the two frequencies enabled the pressure to be determined to within 0.1 mbars; the frequency difference went to zero at zero pressure.

A three axis fluxgate magnetometer gave the detector's orientation with respect to the earth's magnetic field and hence to the celestial

sphere. Like the instrument used on the small detector, the magnetometer operated as a null seeking device. However, the electronics of the two magnetometers were quite different - as the device used on the large detector relied on logic circuitry and did not require any tuned circuits; this greatly simplified construction. The fluxgate elements were mounted in a non-magnetic framework, and aligned with each other and with the detector to within  $1/10^{\circ}$ . The magnetometer was able to determine the orientation of the payload to within  $0.5^{\circ}$ .

To monitor the temperature inside the detector, six thermistors were distributed over the apparatus. These were designed to operate down to  $-40^{\circ}\text{C}$ . To monitor the temperature on the outside of the detector, four diodes were coupled just beneath the outer layer of the polystyrene insulation. One diode on each of the top and bottom surfaces and two diodes on the sides. Using the diodes, temperatures in the range  $-140^{\circ}\text{C}$  -  $+140^{\circ}\text{C}$  could be measured.

The battery voltage and the voltages on all the power lines were monitored.

To relate the detector's output to Universal time, a quartz controlled clock was included in the payload.

In order to keep a check on the charged particle flux, the total count rate of each tray above the upper thresholds of the three slabs in the tray was recorded.

### 3.2.6. Commands

Six commands were used to control the status of the detector during flight. These commands enabled the whole detector to be switched



on or off and individual slabs to be similarly switched. This latter facility was included so that in the event of a slab malfunctioning due to coronal discharging or some other fault, the slab could be switched off, allowing the remaining slabs to continue operating without interference.

Table 3.1. Commands

<u>Number</u>	<u>Function</u>
1	All slabs on
2	All slabs off
3	Slab n on
4	Set
5	Reset
6	Slab n off

Due to telemetry limitations, it was not possible to address each slab with individual on and off commands. Instead, the eighteen slabs were arranged electrically in a continuous loop, only one slab being addressed at any one time. In order to step the address to the next slab in the loop, command 4 and then command 5 had to be sent. This enabled the eighteen slabs to be individually switched on or off using only four commands rather than thirty-six.

### 3.2.7. Data Encoding and Transmission

The outputs from the eighteen slabs and the house-keeping monitors etc., were fed into a data handling and encoding box. The signals from the slabs were treated as follows:

(i) The data handling system summed the eighteen slab counting rates in time bins of  $1/256$  s to give the total count rate. The resulting signal was then scaled by a factor of eight and encoded as an 8-bit binary word. The 256 words representing one second of data, were then placed into a telemetry format as shown in Figure 3.6. One format was transmitted every second.

(ii) The count rate from each tray was sampled sixteen times a second and scaled by sixteen before being placed into the format.

(iii) The outputs from the individual slabs were sampled once a second and scaled by a factor of sixty-four. This was simply to check that all the slabs were functioning correctly and that any event was not ascribable to just one slab.

(iv) The total count rate from each tray above the upper threshold was scaled by 256 and read out once a second.

From the above discussion it is apparent that the time resolution of the detector was  $1/256$  s. With the scaling factors chosen, the detector was capable of observing bursts with sizes  $\leq 3 \times 10^{-5}$  ergs  $\text{cm}^{-2}$  before saturating. If the -1 power law holds, the detector should observe one event with size  $\geq 10^{-5}$  ergs  $\text{cm}^{-2}$  every sixty-five days. Thus the probability of observing one such event in a sixty hour flight is small.

The outputs of the house-keeping and attitude monitors were converted into digital form before being transmitted; all the monitors were sampled once a second.

S <sub>0</sub>	S <sub>1</sub>	T	T	P15	SL0	T	T	AP0	API	T	T	T	TRATRI	T	T	TRC	TRRI	T	T	TRF	TRF	T	T	T	T
S <sub>0</sub>	S <sub>1</sub>	T	T	P0	SL1	T	T	AP2	AP3	T	T	T	TRATRI	T	T	TRC	TRRI	T	T	TRF	TRF	T	T	T	T
S <sub>0</sub>	S <sub>1</sub>			P1	SL2			AP4	AP5																
				P2	SL3			M0	M1																
				P3	SL4			M2	N						V <sub>0</sub>	V <sub>1</sub>									
				P4	SL5			B0	B1						V <sub>2</sub>	V <sub>3</sub>									
				P5	SL6			CL <sub>0</sub>	CL <sub>1</sub>						V <sub>4</sub>	V <sub>5</sub>									
				P6	SL7			CL <sub>2</sub>	CL <sub>3</sub>																
				P7	SL8										A <sub>0</sub>	A <sub>1</sub>									
				P8	SL9			E <sub>0</sub>	E <sub>1</sub>						A <sub>2</sub>	A <sub>3</sub>									
				P9	SL 10			E <sub>2</sub>	E <sub>n</sub>						A <sub>4</sub>	A <sub>5</sub>									
				P10	SL 11			θ <sub>0</sub>	θ <sub>1</sub>																
				P11	SL 12			θ <sub>0</sub>	θ <sub>1</sub>																
				P12	SL 13																				
				P13	SL 14																				
				P14	SL 15			SL 16	SL 17																
S <sub>0</sub>	S <sub>1</sub>	T	T	T	SL 15	T	T	T	SL 16	SL 17	T	T	T	TRATRI	T	T	TRC	TRRI	T	T	TRF	TRF	T	T	T

Fig 3.7: Telemetry Format Layout.

Table 3.2. Telemetry Format Symbols

<u>Symbol</u>	<u>Definition</u>
T	Total count rate (per $1/256$ s)
SL(N)	Count rate from slab N (per s)
TR(X)	Count rate from tray X (per $1/16$ s)
AP(X)	Count rate above upper threshold of tray X
$E_0, E_1, E_2$	Status of the eighteen slabs (on or off)
$E_n$	The slab being addressed
$M_0-M_2$	Magnetometer Outputs
$B_0-B_1$	Barometer Outputs
$CL_0-CL_3$	Clock Outputs
$\theta_0-\theta_5$	Thermistor Outputs
$\theta_6-\theta_9$	Diode Outputs
$V_0-V_5, AS_5$	Voltage Monitors
N	The number of the frame
$P_0-P_{15}$	Polarity check, i.e. number of "ones" in the preceding frame
$A_0-A_5$	Outputs from NaI detector described in Chapter 5.

The layout of the telemetry format is shown in Figure 3.6. The format consisted of 512, 8-bit binary words, and as one format was transmitted every second, the data rate was  $\sim 4 \text{ k-bits sec}^{-1}$ . At the start of each format, or subframe, a synch pattern was sent which consisted of two words  $\bar{S}_0 \bar{S}_1$

$$\begin{aligned}\bar{S}_0 &= 11101011 \\ \bar{S}_1 &= 10010000\end{aligned}$$

Then at the beginning of each line or frame, another synch pattern was sent which was just the inversion of  $\bar{S}_0, \bar{S}_1$ .

$$\begin{aligned}S_0 &= 00010100 \\ S_1 &= 01101111\end{aligned}$$

The meanings of the various symbols in Figure 3.6 are listed in Table 3.2.

The encoded data was transmitted on a 136 MHz carrier wave. The received signal was passed through a bit synchroniser and recorded on magnetic tape. A decoder, connected in parallel with the tape recorder, enabled any part of the format to be sampled during data recording.

It was hoped to achieve a flight of about sixty hours duration. With a flight of this length, the balloon might well drift a thousand miles from the point of launch. To receive data throughout the whole of such a flight, two receiving stations are required. A duplicate set of ground equipment was therefore assembled, and arrangements were made to establish a roving receiving station utilising a light aircraft.

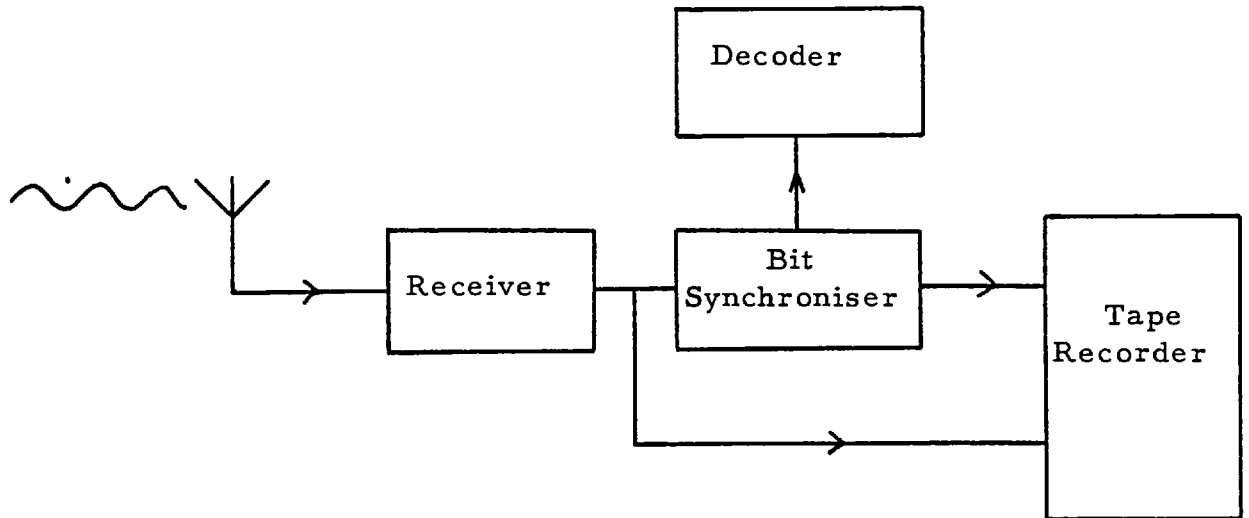


Fig 3. 7: The Data Receiving And Recording System.

### 3.2.8. Thermal Insulation

It was decided to fly the detector during the October/November wind turn-around period at Alice Springs. At this time of year, the galactic centre is directly overhead at  $\sim 15$ -30 local time, and it was hoped that a three day observation of this region would be possible. Commencing with a morning launch, this would involve the detector being in operation for  $\sim 60$  hours, spending two nights at altitude before being cut down in the early evening of the third day's operation.

During the day, it is relatively easy to keep a balloon payload warm due to the effects of solar heating. However, once the sun has set the temperature on the outer surface of the payload falls rapidly, and

a considerable amount of thermal insulation is required to prevent the temperature of the detector going too low. The insulation normally used is expanded polystyrene, and to avoid using an excessive thickness it is common practice to paint some of the outer surface black. These areas then become good absorbers of solar radiation and consequently help to warm the payload up during the day. One problem with this technique is that when the sun is directly overhead, the black polystyrene gets so hot that it begins to melt. It was envisaged that over three days of operation, this would cause a serious reduction in the thickness of the insulation. It was therefore decided to paint the outside surface of the insulation with a paint whose absorptivity was sufficiently smaller than the absorptivity of black paint to ensure that serious melting would not occur.

Several shades of grey paint were produced by mixing together black and white emulsion paint. To measure the various absorptivities, a small piece of aluminium sheet was painted in each colour, and the sheets were then exposed to intense solar radiation under conditions of enforced cooling. A piece of black painted sheet was similarly exposed for comparison. All the sheets were the same size. The temperature of each sheet was measured using a thermistor coupled to the rear surface, away from the sun. Under these conditions, it is a reasonable approximation to use Newton's Law of Cooling, and say that the rate of heat loss from each sheet is proportional to the temperature difference between the sheet and its surroundings.

$$W a_n \propto (T_n - T_o)$$

W = intensity of solar radiation  $\text{wm}^{-2}$

$a_n$  = absorptivity of paint n

$T_n$  = temperature of sheet n

$T_o$  = ambient air temperature,

As all the sheets had the same dimensions the ratio of the absorptivity of the respective paint to the absorptivity of black is simply given by

$$\frac{a_n}{a_b} = \frac{T_n - T_o}{T_b - T_o}$$

knowing  $a_b \sim 0.95$  (Lichfield et al. 1967) enabled the various values of  $a_n$  to be determined.

Table 3.3. Paint Absorptivities

<u>Paint No.</u>	<u>% Black</u>	<u>% White</u>	<u>a</u>	<u>T<sub>max</sub></u>
1	90	10	0.90	118 <sup>o</sup> C
2	75	25	0.85	113 <sup>o</sup> C
3	50	50	0.80	107 <sup>o</sup> C
5	25	75	0.65	88 <sup>o</sup> C

Tests indicate that polystyrene begins to melt at  $\sim 115^{\circ}\text{C}$ . When the sun is directly overhead, the upper surface of a balloon payload receives  $1400 \text{wm}^{-2}$  of solar radiation. Assuming that the surface is in radiative equilibrium, the temperature is given by



$$1400 a = \sigma \epsilon T^4$$

$$\therefore T = \left( \frac{1400a}{\sigma \epsilon} \right)^{\frac{1}{4}}$$

$\epsilon$  = emissivity of surface (0.95 for most paints)

$\sigma$  = Stefan's constant.

A black surface with an emissivity of 0.95 attains a temperature of  $123^{\circ}\text{C}$  and the polystyrene therefore melts. The corresponding maximum temperatures of the various grey paints are listed in Table 3.3. (Previous page). It has been assumed that the emissivity of each paint = 0.95. In view of the need to keep the temperature of the polystyrene below  $115^{\circ}\text{C}$ , it was decided to paint the detector overall with paint number 3 which has an absorptivity of 0.8.

In order to estimate the thickness of polystyrene required, it is necessary to calculate what the outside temperature of the payload will be.

(i) During the night

(a) The top surface will receive deep space radiation at a rate of  $20 \text{ W m}^{-2}$ . Assuming the surface is in radiative equilibrium, the temperature is given by

$$T = \left( \frac{20a}{\sigma \epsilon} \right)^{\frac{1}{4}}$$

$$a = 0.8$$

$$\epsilon = 0.95$$

$$\therefore T = -142^{\circ}\text{C}$$

(b) The sides receive radiation from the ambient air which is at  $-40^{\circ}\text{C}$ . Their temperature will be  $-50^{\circ}\text{C}$ .

(c) In the event of high cloud cover, the lower surface will receive  $\sim 167 \text{ W m}^{-2}$ , whereas if there is no cloud cover the surface will receive radiation directly from the ground, which will be at  $\sim 20^{\circ}\text{C}$ . Assuming there is cloud cover for half the night, the average temperature of the lower surface will be  $-16^{\circ}\text{C}$ .

The average temperature of the outer surface

$$T_A = \frac{\sum_1^n T_n A_n}{A} = -68^{\circ}\text{C}$$

A = total surface area of insulation.

(ii) During the day.

(a) The upper surface will now receive solar radiation in addition to deep space radiation. The average flux will be equal to half the flux with the sun directly overhead (average projected area =  $\frac{1}{2}$  total area), i.e.  $700 \text{ W m}^{-2}$ . The average temperature of the surface will be  $46^{\circ}\text{C}$ .

(b) The sides will also receive solar radiation, in this case at an average intensity of  $350 \text{ W m}^{-2}$ , assuming that the payload is swinging. There will still be an input from the ambient air giving an average temperature of  $23^{\circ}\text{C}$ .

(c) The lower surface will receive radiation from the ground, or reflected solar radiation in the event of high cloud cover. The average temperature will be  $\sim 20^{\circ}\text{C}$ .

The average temperature of the whole of the outside surface =  $29^{\circ}\text{C}$ .

Assuming that heat is lost only by conduction through the polystyrene, the rate of change of the internal temperature of the detector is given by

$$\frac{dT_i}{dt} \cdot H = \frac{-kA(T_i - T_o)}{dx} + P$$

$T_i$  = internal temperature

$T_o$  = average temperature of outside surface

$H$  = heat capacity of detector ( $5.7 \times 10^5$  joules $^{\circ}\text{C}^{-1}$ )

$k$  = conductivity of polystyrene ( $0.035$  joules  $\text{m}^{-1} \text{ }^{\circ}\text{C}^{-1} \text{ s}^{-1}$ )

$A$  = average area over which heat flows ( $31.3 \text{ m}^2$ )

$dx$  = thickness of polystyrene

$P$  = power dissipated inside detector (25 watts)

The heat capacity of the detector is mainly provided by the 338 kgs of scintillator, which has a specific heat of  $1680 \text{ joules kg}^{-1} \text{ }^{\circ}\text{C}^{-1}$ .

In order to solve the equation for the temperature of the detector as a function of time, it was assumed that the value of  $T_o$  during the day and night were simply equal to the values as given by the radiative equilibrium conditions. The temperature variation was then calculated for a number of different values of  $dx$ . The plots for  $dx = 6''$  and  $8''$  are shown in Figure 3.8. It was required that at no time would the temperature of the detector fall below  $-20^{\circ}\text{C}$ . To satisfy this condition, it was decided to make the polystyrene  $8''$  thick, which allowed a small margin for error in the preceding calculations.

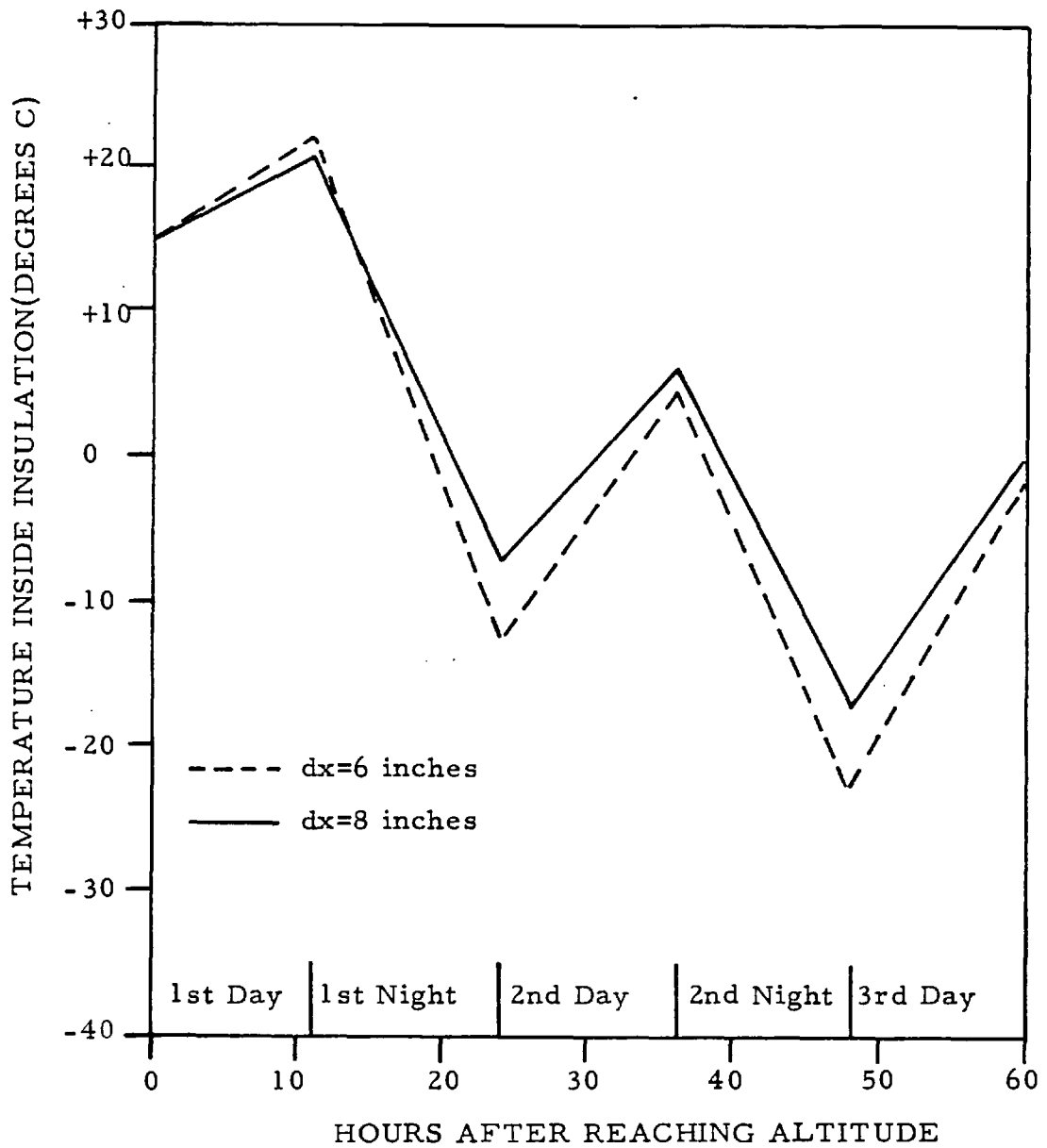


Fig 3. 8: Schematic Diagram Showing The Theoretical Temperature Variation Of The Detector With Time. It Has Been Assumed That The Detector Has A Temperature Of 15 Degrees When Altitude Is Reached.

### 3.2.9. Environmental Tests

By providing each slab with a separate eht unit, it was possible to seal all the high voltage connections with silastic rubber before dissembling the detector to ship it to Australia. This enabled us to vacuum test the detector by testing the slabs individually. Each slab was run in an environmental chamber at a pressure of 2 mbars for two days, and a check was kept on the count rate to ensure that coronal discharging was not occurring.

Ideally, the thermal tests should also have been conducted under vacuum conditions, but unfortunately the environmental chamber proved unsuitable for thermal testing equipment as large as the scintillators. The tests were therefore done in an ordinary thermal chamber at atmospheric pressure. It was originally planned to temperature test the slabs by thermally cycling them over the predicted temperature cycle; however, problems arose with this method. When the slabs were being brought up from a low temperature, condensation tended to form on the scintillator's surface underneath the silver foil. This had the effect of causing the count rate to drop by 25% and the affected slabs had to be recovered with foil. This problem will not arise when the payload is at altitude due to the absence of moisture. Each slab was therefore tested by simply operating it at  $-20^{\circ}\text{C}$  for a day, and then slowly bringing it up to room temperature whilst monitoring the count rate. By raising the temperature slowly, it was possible to eliminate the problem of condensation. The count rate at  $-20^{\circ}\text{C}$  was about 4% higher than the count rate at room temperature. This result is consistent with results obtained from thermal testing the  $1\text{ m}^2$  detector.

In addition to testing the slabs, all the electronic circuitry was thermally tested by running the equipment for several days at  $-20^{\circ}\text{C}$ .

### 3.3. Flight and Results

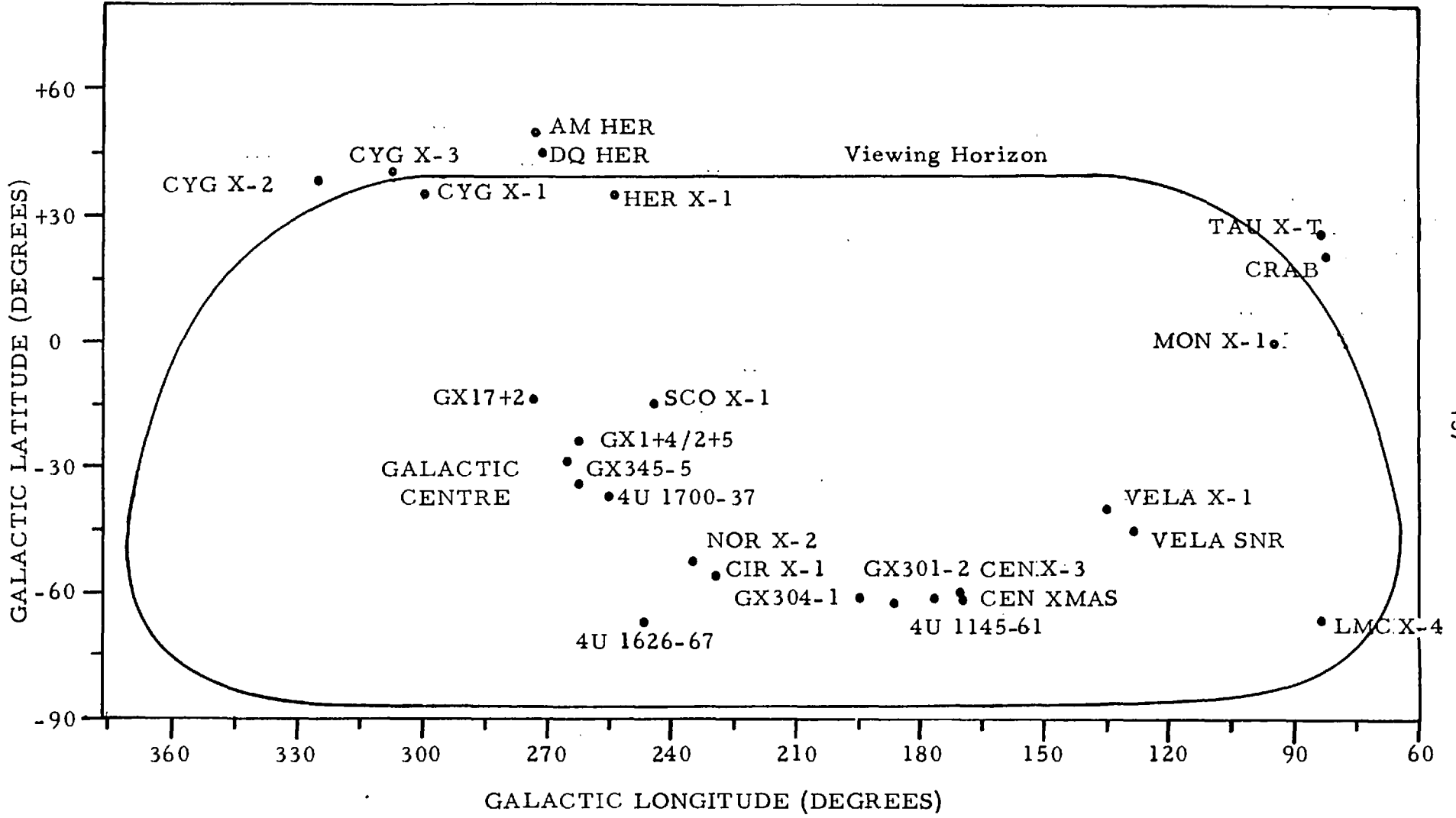
#### 3.3.1. Flight Details

The detector was successfully launched from AliceSprings at 05-30 local time on 3rd November 1977 using a 20.9 MCF balloon. The payload reached altitude at 07-00 local time and remained at 3.5 mbars throughout the flight, which was unfortunately of only  $10\frac{1}{2}$  hours duration. At around 17-00, the detector began to lose height whilst over a severe electrical storm, and attempts were made to drop ballast to keep the payload at altitude. One of the ballast drop commands must have been interfered with as a result of the storm and misinterpreted as a cut down command, causing the flight to be prematurely terminated. However, the detector performed perfectly whilst at altitude.

The region of the sky scanned during the flight is shown in Figure 3.9, assuming that only sources within  $60^{\circ}$  of the zenith could be observed due to the effects of atmospheric attenuation. The galactic centre rose above the detector's horizon at 11-00 and remained in view throughout the rest of the flight. MonX-1 and the Vela pulsar were both visible when the detector reached altitude, although the Crab Nebulae was just outside the field of view. Immediately before the flight was terminated, HerX-1 was visible and CygX-1 could just be seen.

The temperature of the detector dropped to a minimum of  $13^{\circ}\text{C}$  during the ascent and then gradually rose throughout the flight, reaching a maximum of  $21^{\circ}\text{C}$  just before shutdown. This behaviour was consistent with the theoretical prediction. When the payload was recovered, it was evident from the condition of the insulation that some melting had occurred, although the melting was much less severe than has previously been obtained with black surfaces. It would however be advisable in future experiments to use a paint with a lower absorptivity than 0.8.

Fig 3. 9: Map In Galactic Coordinates Showing The Region Of The Sky Viewed By The Large Burst Detector.



### 3.3.2. Results and Conclusions

The data that was recorded on magnetic tape during the flight has not yet been analysed. However, it was possible using the decoder, to monitor the total count rate of the detector during the flight. The decoder was set so that every word representing the total count rate in  $1/256$  s, was extracted from the telemetry format at the same time as the data was being recorded. The resulting signal was fed through a digital to analogue converter, integrated using  $1/16$  s time bins, and plotted on a chart recorder. The average background counting rate at altitude was  $84000 \text{ cts s}^{-1}$ , which is equivalent to  $12500 \text{ cts s}^{-1} \text{ m}^{-2}$ . This latter value is close to the background rate observed over France (c/f.  $10800 \text{ cts s}^{-1} \text{ m}^{-2}$ ), and in good agreement with the theoretical rate of  $11025 \text{ cts s}^{-1} \text{ m}^{-2}$  based on Ling's semi-empirical model (Ling 1975).

The burst observed by the small detector appeared quite clearly on the chart recording of the total count rate. This event had a duration of 5 s and in total was  $10 \sigma$  above the mean background count rate. The chart recording produced by the large detector was examined for statistically significant rises in the background count rate. A burst with an overall significance of  $10 \sigma$  would have been quite easy to detect by eye; however, no such events were found in the data. Although a computer study of the data may reveal the presence of smaller events, the fact that there are no  $10 \sigma$  bursts in the data allows further limits to be placed on the occurrence rate of small bursts.

A  $10 \sigma$  event is equivalent to  $960 \text{ cts m}^{-2}$  assuming a background rate of  $88400 \text{ cts s}^{-1}$  and a burst duration of 5s. The corresponding burst size =  $2.2 \times 10^{-8} \text{ ergs cm}^{-2}$ , assuming that the spectrum is not



significantly altered by the atmosphere. No bursts of this size were present in 10.5 hours of data.

(i) This result allows an upper limit to be placed on the event rate. The best estimate of the burst frequency is 0 bursts in 10.5 hours. If the true mean is  $\mu$ , the probability of observing such an event rate is

$$P = \frac{e^{-\mu} \mu^r}{r!} \quad \text{where } r = 0$$

The upper limit was fixed at the value of  $\mu$  which gave a probability  $P$  of 0.05. The value satisfying this condition was  $\mu = 3$ . Any distribution with a mean greater than 3 gives a smaller probability of seeing 0 events. This limit therefore represents the 95% confidence level. From the discussion in Chapter 2, if burst sources are isotropically distributed throughout all space, then every burst observed with size  $>s$  by the balloon detector is equivalent to twenty such events being observed by an isotropic satellite detector. Applying these considerations to the result from the large detector allows an upper limit to be placed on the event rate as shown in Figure 3.10. The point lies more than a factor of twenty below the  $3/2$  power law, and further confirms that burst sources cannot be uniformly distributed throughout all space.

(ii) It is also possible to place an upper limit on the event rate assuming that burst sources follow the distribution of galactic matter. As discussed in chapter 2, Horstman and Bassani's calculations show that every burst of size  $>s$  as observed by a flat detector at a latitude of  $40^\circ$ , is equivalent to an isotropic satellite detector observing 7.7 such events. In the Southern hemisphere at a latitude of  $-23^\circ$ , about three times more galactic matter is viewed over a twenty-four hour

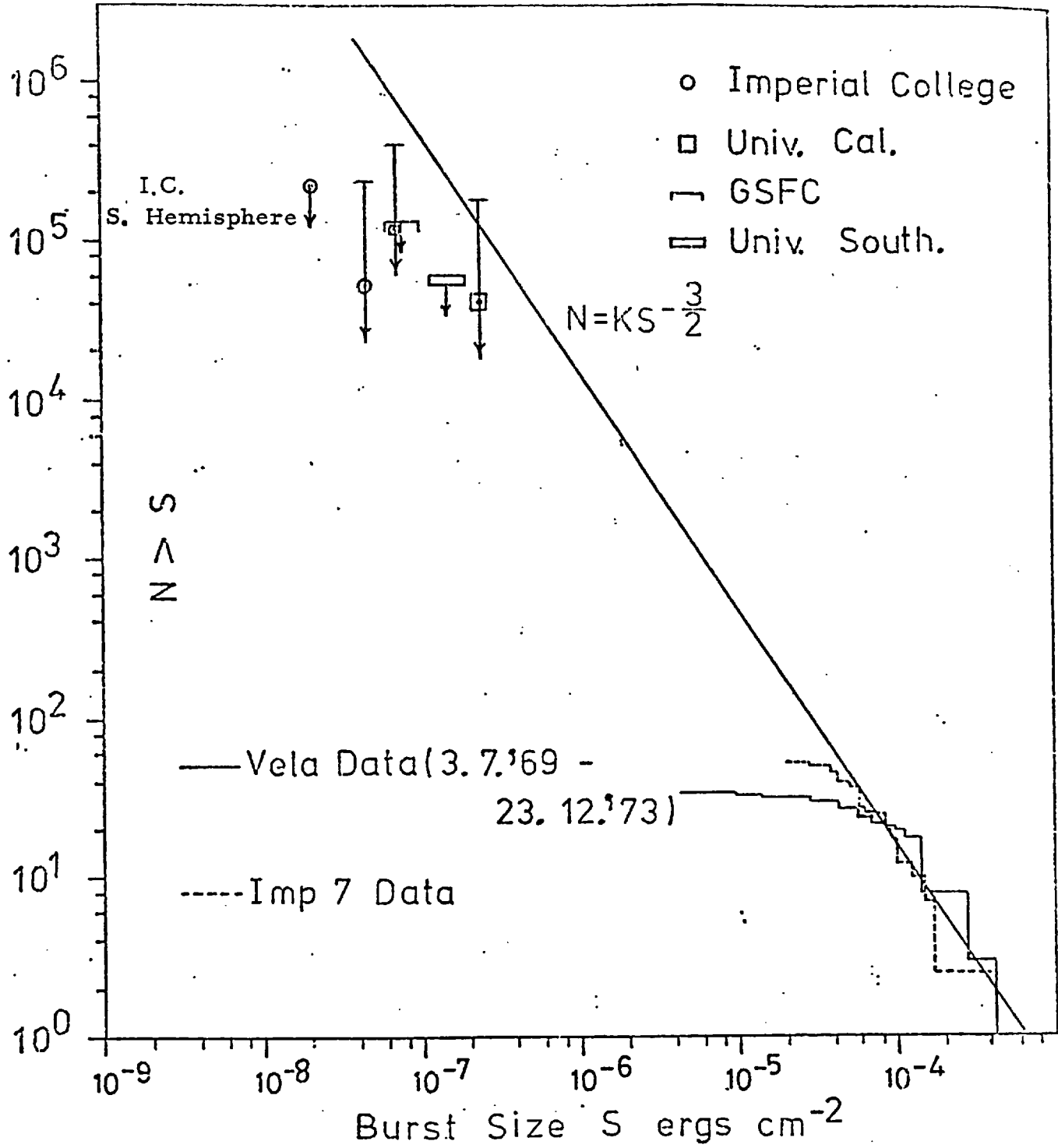


Fig 3. 10: The Event Rate As Given By The Results From The Large Detector Compared With The Theoretical Rate From A Uniform Source Distribution.

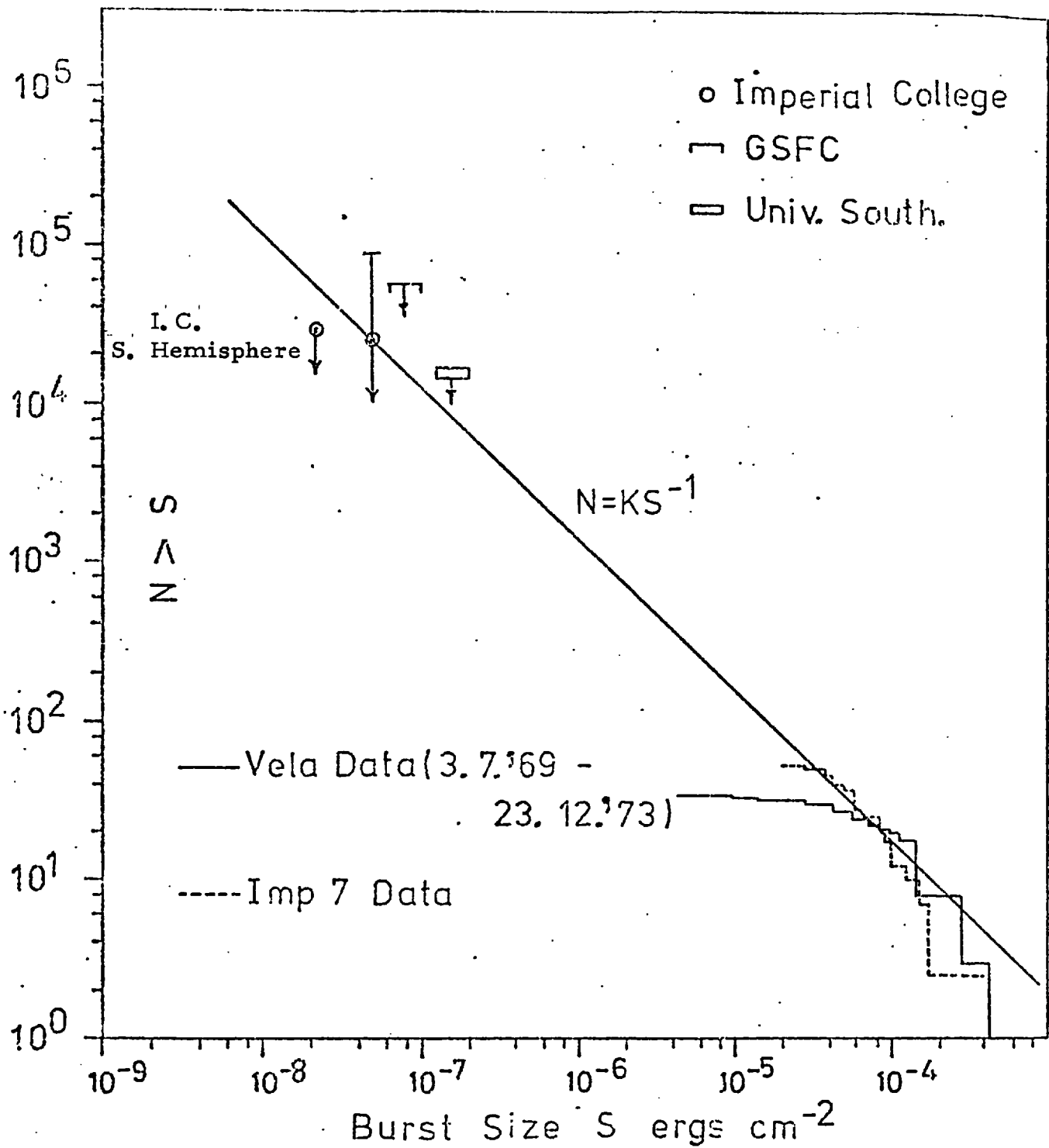


Fig 3. 11: The Event Rate As Given By The Results From The Large Detector Compared With The Theoretical Rate From A Galactic Disc Source Population.

exposure period than is observed from a latitude of  $40^{\circ}$ . If burst sources follow the distribution of galactic matter, the event rate will increase accordingly. As the galactic centre region was in view of the large detector for well over half the flight, to a first approximation Horstman's results can be scaled by a factor of three, i.e. every burst observed by the balloon detector with size  $> 2.2 \times 10^{-8}$  ergs  $\text{cm}^{-2}$  is equivalent to a satellite detector observing  $\frac{7.7}{3}$  such events.

The event rate as given by this result is shown in Figure 3.11, together with results from several other balloon groups, as described in chapter 2. The result from the large detector is a factor of two below the -1 index power law. This indicates that the event rate at low energy may be inconsistent with even a galactic disc source population. However, due to uncertainties inherent in the various correction factors applied to it, the result from the large detector cannot be said to be inconsistent with any degree of certainty.

The detector is to be flown again from Alice Springs to increase the exposure time, hopefully by a factor of six. If no  $10\sigma$  bursts are observed, then the frequency of  $2.2 \times 10^{-8}$  ergs  $\text{cm}^{-2}$  events will lie more than an order of magnitude below the -1 index power law. This will indicate that gamma-bursts are produced by some class of local source within a few hundred parsecs of the sun.

### 3.4. Source Models

#### 3.4.1. Introduction

The results presented in this and in the preceding chapter, almost certainly confirm that gamma-bursts are produced by sources located within the galaxy. Although it is still unclear as to whether the  $-1$  power law governs the event rate at low energies, it is very likely that the large satellite bursts are produced by sources within 300 pc of the sun. Any source model must be able to explain the following observed properties.

(i) Bursts have an average duration of about 6 s and normally consist of several distinct pulses. At least one burst has been observed with significant structure on a time scale of 1 ms.

(ii) Taking an average burst size of  $10^{-4}$  ergs  $\text{cm}^{-2}$  and a mean source distance of 200 pc, gives an average total luminosity of  $5 \times 10^{38}$  ergs, assuming that the source radiates isotropically.

(iii) In order to produce the standard burst spectrum requires a source temperature of the order of  $10^9$  k.

There have been almost as many source models suggested as there have been bursts observed. These models can be split into two groups, galactic and extragalactic source models. I shall concentrate on the former and discuss three of the most plausible production mechanisms.

### 3.4.2. Stellar Flare Model

The time structure of the hard (>10 keV) impulsive x-ray emission which is sometimes observed in solar flares, is similar to the structure of gamma-bursts (e.g. Frost, 1969); although the spectrum of this emission is usually considerably softer than the standard burst spectrum, being given by

$$\frac{dN}{dE} = CE^{-\gamma} \text{ photons cm}^{-2} \text{ s}^{-1}$$

$2.5 < \gamma < 5.0$  for energies up to 60 keV.

Above 60 keV, the spectrum is much steeper (Kane 1973, Peterson et al. 1973b). It was originally proposed by Brecher et al. (1974), that gamma bursts are produced by solar type flares on stars with similar properties to the sun. That is stars with convective surface layers, slow rotation and modest magnetic fields ( $B < 10^3$  gauss), such as the F and G main sequence stars in the solar neighbourhood.

The total energy required to produce a burst depends upon how the burst photons are produced. Assuming that these photons are generated by fast electrons, then the total energy required is given by

$$E = \frac{W}{\eta \epsilon}$$

$W$  = total burst luminosity ( $5 \times 10^{38}$  ergs)

$\eta$  = fraction of flare energy going into fast electrons

$\epsilon$  = efficiency of conversion of this energy to gamma rays.

If the radiation is produced by bremsstrahlung emission

$$\epsilon \approx \frac{10^{-4} E}{m_e c^2} \quad (\text{Blumenthal et al. 1970})$$

$E_\gamma$  = gamma ray energy (assume 100 keV), which gives  
 $\epsilon \approx 2 \times 10^{-5}$ .

Even if  $\eta = 1$ , the amount of energy required

$$E \sim 10^{43} \text{ ergs}$$

about  $10^{10}$  times larger than the largest solar flares seen this century. Assuming that the prime energy source is magnetic energy, then if the burst is produced inside a sphere of radius  $R$ , the total available energy is given by

$$E = \frac{B^2 R^3}{6} \text{ ergs}$$

The 1 ms time variations which have been observed mean that  $R < 1.5 \times 10^7$  cms. Thus  $B$  must be of the order of  $10^{11}$  gauss, about  $10^8$  times greater than fields commonly present in solar flares. It is very unlikely that such conditions will be obtained on stars with similar properties to the sun.

Another possibility is that the burst is produced by inverse compton scattering of stellar photons by fast electrons. Brecher et al. (1974) postulate that more energetic flare processes in more luminous main sequence stars, especially those of spectral type F, can accelerate electrons to an energy between 50-500 MeV, instead of 0.1-1 MeV as in solar flares. They suppose that a pulse of these electrons propagates outwards along a curved magnetic tube through the stellar radiation field, the electron motion being confined to a cone of a few degrees. The directed beam pulse will then sweep over a fixed direction in several seconds. The electrons with energy  $E_e = \gamma m_e c^2$ , will collide with the numerous stellar photons of mean energy  $E \approx 1 \text{ eV}$  to produce inverse

compton photons with energy

$$E_{\gamma} \approx \gamma^2 E \approx 250 \text{ keV}$$

i.e. the burst photons.

The efficiency of this process

$$= \frac{\gamma^2 E}{n m_e c^2} \approx 10^{-3}$$

assuming  $\eta = 1$

In the case of bremsstrahlung the energy is emitted over  $4\pi$ , but in this situation, since an individual electron radiates in a solid angle,

$$\Omega \approx \frac{\pi}{\gamma^2}$$

the burst in principal is emitted in a solid angle of only  $10^{-5}$  str.

Thus the total energy required

$$E = \frac{5 \times 10^{38}}{10^{-3}} \times \frac{10^{-5}}{4\pi} \sim 4 \times 10^{35} \text{ ergs}$$

This requires a magnetic field of the order of  $10^7$  gauss.

The density of F and G stars in the solar neighbourhood is about  $10^{-2} \text{ pc}^{-3}$  (Allen 1964), and thus within 300 pc there are  $\sim 10^6$  such objects. Satellites observe ten bursts a year, and thus the number of flares required per object

$$N = \frac{10}{10^6} \times \frac{\Omega}{4\pi} \sim 10 \text{ yr}^{-1}.$$

This high event rate is due to the small solid angle  $\Omega$  in which the burst



is emitted. Considering the size of the flares which are about a hundred times larger than the greatest solar flares seen in a century, such a high event rate seems very unlikely.

### 3.4.3. Accreting Compact Objects

The compact x-ray sources listed in the 4U and Ariel V catalogues have the following general properties.

(i) A luminosity in the soft x-ray region ( $<10$  keV) in the range  $10^{36} - 10^{38}$  ergs  $s^{-1}$ .

(ii) Membership of binary systems as evidenced by eclipses or association with binaries.

(iii) A flat spectrum similar to that produced by radiation from a hot gas with a temperature of  $50-1000 \times 10^6$  K.

(iv) Fast, and in some cases periodic, variations on a time scale of 1 s or less. In particular the black hole candidate CygX-1, exhibits variations on a time scale of 1 ms. The emission from these sources is thought to be produced by matter accreting onto the compact member of the binary system from the more massive companion star.

Several of the properties listed above, in particular the luminosity and temporal behaviour, are very similar to the properties required of burst sources. Lamb et al. (1973a) have suggested that gamma-bursts may be produced by fleeting episodes of accretion onto compact objects located in binary systems in the solar neighbourhood. The compact object could be a degenerate dwarf, a neutron star or a black hole.

### 1. Degenerate dwarf

An estimate of the amount of matter required to produce the burst can be found from equation (1), assuming an efficiency of 100% in the conversion of gravitational energy into radiation.

$$\Delta m = \frac{WR}{GM} \quad (1)$$

$W$  = total burst luminosity ( $5 \times 10^{38}$  ergs)

$R$  = radius of star

$M$  = mass

The radius of a degenerate dwarf of mass  $M$  is given by

$$R = 10^{-2} R_{\odot} \left(\frac{M_{\odot}}{M}\right)^{1/3} \quad (2)$$

(Landau et al. 1958)

Assuming  $M = M_{\odot}$        $\Delta m \sim 10^{21}$  grms.

Lamb et al. (1973a) postulate that the source of this matter is a large solar type flare on the massive companion star. Only a fraction of the ejected matter  $m$  will actually accrete onto the compact object, i.e.

$$\frac{\Delta m}{m} = \frac{\Omega a}{\Omega m} \quad (3)$$

$\Omega a$  is the solid angle over which accretion occurs.

$\Omega m$  is the solid angle into which the flare material is ejected.

In solar flares matter is ejected with velocities up to  $1500 \text{ km s}^{-1}$

(Sweet 1969). If this is assumed to be the velocity of the matter ejected by the companion star, then an accretion disc is unlikely to form around the compact object, and the accretion cross-section will be  $\pi r_a^2$ , where

$$r_a \approx \frac{2GM}{V^2} \quad (4)$$

(Bondi et al. 1944)

Thus

$$\Omega a = \frac{\pi r_a^2}{R_b^2} = \frac{\pi}{R_b^2} \left( \frac{2GM}{V^2} \right)^2 \quad (5)$$

$R_b$  is the binary separation.

In the case of solar flares  $\Omega_m = 1$  str. (Tandberg-Hanssen 1967).

Assuming  $V = 1500 \text{ km s}^{-1}$  and  $R_b = 10 R_\odot$

$$m \sim 10^{24} \text{ grms.}$$

This is a factor of  $10^8$  greater than the amount of matter ejected during the larger solar flares (importance classes 3 and 4), which have a frequency of  $5\text{-}20 \text{ yr}^{-1}$ .

Rough estimates (Weidemann 1968), give a white dwarf birth rate in the solar neighbourhood of  $2 \times 10^{-12} \text{ pc}^{-3} \text{ yr}^{-1}$ , or after  $12 \times 10^9$  years a local white dwarf space density

$$n_{\text{wd}} \sim 2.5 \times 10^{-2} \text{ pc}^{-3}.$$

White dwarfs are expected to occur fairly frequently in close binary systems and assuming that 10% do, there will be  $\sim 3 \times 10^5$  white dwarf

close binary systems within 300 pc. The burst frequency per compact object  $V_b$  will be given by

$$V_b = \frac{f}{3 \times 10^5} \approx 3 \times 10^{-5} \text{ yr}^{-1} \quad (6)$$

$f$  is the observed burst frequency (10 events per year)

The flare frequency  $V_f$ , in any one system is

$$V_f = \frac{V_b}{P_a} \quad (7)$$

$P_a$  is the probability that a flare will accrete onto the compact object.

$$P_a \approx \frac{\Omega_a}{4\pi} \sim 10^{-4} \quad (8)$$

Therefore  $V_f \sim 0.3 \text{ yr}^{-1}$ .

Thus although a large flare is required, there only has to be one such flare every  $\sim 3$  years.

In this model, one would expect the duration of the burst to be comparable to the free fall time from  $r_a$  onto the surface of the star. With the above choice of parameters this will be  $\sim 50$  s, which is long compared with typical burst durations. In addition, the dynamical time scale on the surface of the dwarf

$$\tau \approx \left(\frac{R^3}{GM}\right)^{\frac{1}{2}} \sim 1 \text{ s} \quad (9)$$

much longer than the 1 ms variations which have been observed.

It is also difficult to see how accretion onto a white dwarf can produce the required temperature of  $10^9$  k. The temperature  $T$  produced by thermalisation of the flow is

$$T \approx \frac{\alpha m_p GM}{kR} \quad (10)$$

$m_p$  = proton mass

$k$  = Boltzman's constant

$\alpha$  is an efficiency factor which depends on how the matter is heated. For adiabatic heating in a strong shock wave  $\alpha \sim 0.1$  (Landau et al. 1959). For slower heating processes, such as viscous heating in a disc, radiation losses are important and the temperature is determined by the balance between radiative losses and heating. In this case,  $\alpha$  can be as small as  $10^{-5}$  -  $10^{-6}$  (Pringle et al. 1972, Shakura et al. 1973).

From equation (10)

$$\alpha \left(\frac{M}{M_{\odot}}\right) \left(\frac{R_{\odot}}{R}\right) \geq 40$$

and from equation (2)

$$\alpha 100 \left(\frac{M}{M_{\odot}}\right)^{4/3} \geq 40$$

Thus if  $M = M_{\odot}$ ,  $\alpha \geq 0.4$  in order to produce the required temperature. Therefore, even if the matter is heated adiabatically, it is difficult to see how a temperature of  $10^9$  k can be produced. Both the structure and temperature requirements suggest that the accreting object is more

compact than a degenerate dwarf.

## 2. Neutron star

In neutron stars the degenerate pressure of the nucleons stabilises the star against gravitational collapse, and the mass radius relationship is

$$\frac{R}{R_{\odot}} \approx 10^{-5} \left(\frac{M_{\odot}}{M}\right)^{1/3} \quad (11)$$

$$\text{Assuming } M = 1.4 M_{\odot}, \quad R \sim 6 \text{ km.}$$

Studies of accretion by neutron stars (Lamb et al. 1973b, Pringle et al. 1972, Davidson et al. 1973) render plausible an efficiency of 100% in the conversion of gravitational energy into radiation. Thus the amount of matter which has to be accreted to produce a burst is given by equations (1) and (11).

$$\Delta m \sim 10^{18} \text{ grms.}$$

From equations (4) and (5), the solid angle in which accretion occurs

$$\Omega_a \sim 0.02 \text{ str.} \quad (12)$$

assuming a binary separation of  $10 R_{\odot}$  and that the flare material is ejected with a velocity of  $1500 \text{ km s}^{-1}$ .

From equation (3) the amount of matter which actually has to be ejected to produce the burst

$$m \sim 5 \times 10^{19} \text{ grms.}$$

assuming  $\Omega_m = 1 \text{ str.}$

From equations (8) and (12), the probability that the flare will actually accrete onto the neutron star is

$$P_a \sim 10^{-3} \quad (13)$$

Because the evolutionary processes which lead to the formation of neutron stars are so poorly understood, it is difficult to make a meaningful estimate of their density in the galaxy. From our present limited knowledge a local space density of

$$n_{ns} \sim 4 \times 10^{-3} \text{ pc}^{-3} \quad (\text{Lamb et al. 1973a})$$

is a reasonable estimate. Thus within 300 pc there will be  $5 \times 10^5$  such objects. The fraction of neutron stars in close binary systems is also difficult to estimate, but values considerably higher than one in fifteen have been suggested (Davidson et al. 1973, Gott et al. 1970). As a lower limit, this gives the number of neutron stars  $N$  within 300 pc in close binary systems

$$N \sim 10^5.$$

Thus from equation (6) the burst frequency per compact object

$$V_b \sim 10^{-4} \text{ yr}^{-1} \quad (14)$$

From equations (7), (13) and (14), the required flare frequency in each binary system

$$V_f \sim 10^{-1} \text{ yr}^{-1}$$

Thus to produce the observed burst frequency, each binary system has only to produce one flare every ten years with a size  $10^3$  times larger than typical class 3 or 4 solar flares. This requirement does not appear to be excessive.

From equation (10), the temperature produced by thermalisation of the flow

$$T \approx \frac{\alpha \mu p GM}{kR}$$

$$M = 1.4 M_{\odot}, \quad R = 6 \times 10^5 \text{ cms}, \quad T \geq 10^9 \text{ k}$$

$$\therefore \alpha \geq 2.5 \times 10^{-4}.$$

Thus the accreting material could be heated adiabatically or by a slower process. The free fall time from  $r_a$  will be  $\sim 10$  s, and the dynamical time scale on the surface of the neutron star will be  $\sim 10^{-4}$  s.

This model is therefore capable of explaining all the observed burst properties. In addition, the required flares on the companion star do not have to be excessively large or occur very often.



### 3. Black hole

It is difficult to construct a meaningful model where the accreting object is a black hole as very little is known about these objects. However, for comparison consider the situation where the compact object is a 5 solar mass black hole. The effective radius of the black hole will be of the order of the Schwartzchild radius

$$R = \frac{2GM}{c^2} \sim 10 \text{ kms.}$$

The amount of matter which has to be accreted to produce a burst

$$\Delta m \sim 10^{18} \text{ grms.}$$

assuming a 100% conversion efficiency. However, in the absence of an accretion disc a black hole is thought to be very inefficient at converting gravitational energy into radiation (Pringle et al. 1972), and  $\Delta m \geq 10^{21}$  grms. is a more realistic estimate. The amount of matter which needs to be ejected in the flare is then

$$m \geq 5 \times 10^{22} \text{ grms.}$$

Neither the spatial density of black holes or the fraction occurring in binary systems is known. Assuming that the density is equal to the density of neutron stars, and that 1% of black holes occur in binary systems, the burst frequency per system

$$V_b \sim 10^{-3} \text{ yr}^{-1}.$$

To produce this frequency requires one flare every year with a size of  $\geq 5 \times 10^{22}$  grms.

As with neutron stars the black hole model can easily satisfy the necessary heating and structural requirements. However, to satisfy the observed event rate, there must be one flare every year in each system with a size more than a million times greater than typical large solar flares. This makes the neutron star model a much more attractive proposition.

#### 3.4.4. Thermonuclear Flash Model

Woosley et al. (1976) have proposed that gamma-bursts are produced by the rapid burning of degenerate carbon on neutron stars. They consider a  $1.4 M_{\odot}$  neutron star accreting hydrogen and helium at a rate of  $10^{-10} M_{\odot} \text{ yr}^{-1}$  from a companion star. If the star has a strong magnetic field, the material is not accreted spherically symmetrically but instead accumulates in polar caps of  $\sim 10^{10} \text{ cm}^2$  (Rosenbluth et al. 1973). As material is accreted compression occurs and nuclear fusion reactions commence. Hydrogen burns to helium and helium to carbon and oxygen. Hansen et al. (1975) have found that the density of the helium burning shell on a neutron star is  $\sim 10^6 \text{ g cm}^{-3}$ , and thus the carbon formed will be relativistically degenerate. Because of the high conductivity of degenerate matter, the carbon will be maintained at a temperature close to that of the helium burning shell. Woosley et al. (1976) calculate that the temperature of the carbon layer will be  $\sim 4 \times 10^8 \text{ k}$ .

They consider the state of the carbon layer after  $4 \times 10^{22} \text{ gm}$  of matter has accumulated; the density at the base of the carbon shell

will then be  $\sim 2 \times 10^9$  gm.  $\text{cm}^{-3}$  (calculated from the hydrostatic equilibrium equation with pressure support from degenerate electrons). This layer of carbon, about 50 m thick, will be topped by one or two metre layers of helium and hydrogen, containing  $10^{17}$  and  $10^{18}$  grms respectively, both with active burning shells. Once the carbon reaches a density of  $2 \times 10^9$  gm.  $\text{cm}^{-3}$ , the nuclear energy generated from carbon burning dominates energy loss by neutrino emission which cools the carbon at lower densities. Any increase in density above this value will lead to a thermonuclear runaway (Arnett 1969), which is expected to be quite violent due to the high degree of degeneracy. Not only will the carbon burn but also oxygen and their products as well, and ultimately species in the iron group are formed, the total energy release being  $7.6 \times 10^{17}$  erg  $\text{g}^{-1}$ . In the model discussed here, complete combustion of all available carbon releases  $3 \times 10^{40}$  ergs, heating the carbon up to a temperature of  $5 \times 10^9$  k. It appears very likely that convective over-shoots and instabilities will develop, and hot blobs of burning carbon will break through the thin covering layers of hydrogen and helium to the surface of the star. These incandescent blobs, having dimensions of only a few meters and temperatures in excess of  $10^9$  k, will cool by emitting gamma rays and neutrinos, hence producing a gamma-burst. The fast time structure is related to the cooling time of these blobs which is expected to be  $< 1$  s. It is expected that the whole process will last several seconds. Only 2% of the total energy released is required to be emitted as gamma rays to produce a  $10^{-4}$  ergs  $\text{cm}^{-2}$  burst, assuming a source distance of 200 pc.

In section 3.4.3, the number of neutron stars with 300 pc in close binary systems was estimated to be  $\sim 10^5$ . What fraction of these binaries are accreting matter at the required rate? Suppose the mode of mass transfer is a stellar wind emanating from a massive companion star.

If the wind has a velocity of  $500 \text{ km s}^{-1}$ , then from equation (5) the solid angle in which accretion occurs  $\Omega_a \sim 0.14 \text{ str}$ . Thus the total mass loss rate is

$$m = \frac{4\pi}{0.14} \times 10^{-10} M_{\odot} \sim 10^{-8} M_{\odot} \text{ yr}^{-1}$$

which is typical for supergiant stars with mass  $\sim 20 M_{\odot}$ . However, as the duration of this mass loss phase is  $< 10^5 \text{ yr}$  (Van den Heuvel 1975) there will be

$$10^5 \times 10^{-5} < 1$$

objects at this phase of evolution within 300 pc, which is clearly not in accordance with observations.

Consider instead mass transfer via a Roche lobe overflow; a mass loss rate of  $10^{-10} M_{\odot}$  a year might be typical for a main sequence star less massive than the neutron star. One then expects  $10^5 \times (0.01 - 0.1) \sim 100-1000$  such objects within 300 pc. Since the critical mass of carbon will accrete each year, the event frequency will be  $100-1000 \text{ yr}^{-1}$ . Even allowing for many bursts that go undetected, this can easily explain the observed event frequency of ten burst per year.

This model gives rise to the possibility of observing repeated bursts from a particular source. As can be seen in Figure 1.13, there is some evidence in the Vela data that bursts 73-5 and 73-6 were produced by the same source. Although each burst had two possible source positions, there is quite a high probability that the events had a common source because both sets of alternative positions overlap.

Of the various models discussed, accretion onto neutron stars,

and thermonuclear explosions on neutron stars are the most attractive. As neutron stars are distributed throughout the galaxy, it is a direct consequence of both models that balloon detectors should observe an event rate that is consistent with the  $-1$  power law. If the event rate at low energy is shown to be significantly below this theoretical rate, then both the models based on neutron stars must be rejected and others considered.

## CHAPTER 4

### 4.1. Introduction

X-ray bursts were discovered by Babuskina et al. (1975) and independently by Grindlay et al. (1976). A transient event is normally classified as an x-ray burst if it has a risetime  $< 2$  s, a duration of several seconds to tens of seconds, a large fraction of its energy in the form of soft and medium energy x-rays (i.e.  $< 50$  keV), and recurs on a time scale which may vary from seconds to months. To date twenty-three independent sources producing such events have been discovered. Several other sources which produce bursts (flares) with durations of the order of 100 s have also been discovered (Heise et al. 1975, Fuligni et al. 1976, Swank et al. 1977 and Markert et al. 1976). However, as risetime information is not available for these events it is unclear if they are simply long x-ray bursts or whether they are a different phenomenon.

It is important to know if x-ray bursts and gamma-bursts have a common origin. Share (1976) and Babuskina et al. (1975) have reported events which could be described as hard x-ray bursts or soft gamma-bursts. Quenby et al. (1976) report that the Ariel V satellite seems to have detected enhanced fluxes of hard x-rays which may be from the burst source MXB 1730-335, following the production of normal x-ray bursts. The relationship between these phenomena is discussed in section 4.10.

Before discussing the general nature of x-ray bursts a brief description of the systems which have featured in their detection is in order.

#### 4.2. Detection Systems

(a) SAS-3. The M.I.T. detectors on board the SAS-3 satellite have provided a large fraction of the information accumulated to date on x-ray bursts. The satellite carries six detectors suitable for observing rapidly varying phenomena. Three of these are proportional counters collimated by etched wire grids which provide long fields of view. These intersect on the Y-axis of the satellite coordinate system at right angles to the spin axis (Z-axis) and the detectors are usually designated right, left and centre slat. The former devices have fields of view of  $0.5^\circ \times 32^\circ$  (FWHM) inclined at  $\pm 30$  degrees to the YZ plane of the system, and the centre slat is collimated to  $1^\circ \times 32^\circ$  with the long axis parallel to the YZ plane. Each detector consists of an argon filled proportional counter of area  $75 \text{ cm}^2$ , sensitive to x-rays in the range 1.5 - 15 keV. Counts are accumulated in two energy channels, namely 1.5 - 6 keV and 6 - 15 keV, using an integrating period of 0.416 s. The centre slat also collimates a xenon filled proportional counter located behind the argon detector, and this extends the energy range up to 60 keV.

The fourth instrument comprises a horizontal tube system sensitive in the range 1.3 - 50 keV and the energy interval is split into six channels. The detector points along the Y-axis and has a  $1.7^\circ$  (FWHM) field of view. These four detectors have an area in common of  $1.1 \text{ deg.}^2$  and sources can be positioned to a few minutes of arc by comparing the individual responses.

The other two detectors are identical rotation modulation collimated devices which point along the Z-axis. Each one has a

field of view of  $12^{\circ} \times 12^{\circ}$  and is sensitive to x-rays in the range 2 - 11 keV, counts being accumulated in 2-6 and 6 - 11 keV bins.

(b) ANS. Instruments carried on board the ANS satellite were among the first to detect x-ray bursts. The soft x-ray experiment, which operates in the range 0.2 - 0.28 keV, consists of a grazing incidence parabolic reflector (effective area  $144 \text{ cm}^2$ ) with a small area proportional counter situated in the focal plane. The sensitivity is such that  $1 \text{ ct s}^{-1} \equiv 0.53 \text{ photons cm}^{-2} \text{ s}^{-1}$  at 0.28 keV.

The medium energy detector is a proportional counter which is sensitive to 1 - 7 keV x-rays. Pulse height analysers divide the detector's energy range into five channels whose addresses are read out once every 5 s. The field of view is collimated to  $32' \times 82'$  FWHM.

The hard x-ray detector consists of two large area collimated ( $10' \times 3^{\circ}$  FWHM) proportional counters sensitive in the range 1 - 30 keV. Counts are accumulated in fifteen logarithmically spaced channels over this range. The two fields of view are separated by  $3.7'$  and sources can be positioned to a few minutes of arc (in one dimension) by comparing the individual responses.

(c) Ariel 5. Three of the pointing experiments on this satellite have been used to search for bursts. Experiment A, which was designed by the Mullard Space Science Laboratory and Birmingham University, is a proportional counter with an effective area of  $102 \text{ cm}^2$  and an energy window from 2 - 19 keV. The device can be rotation modulation collimated which enables the position of a source to be determined to within fifteen minutes of arc if there is a known x-ray source within  $17^{\circ}$ , and to  $0.5^{\circ}$  if not. Charged particles are rejected by a pulse shape discriminator.



Experiment C, which was also designed by MSSL, is a honey-comb collimated proportional counter which is designed to study x-ray spectra. The experiment operates in the range 2 - 30 keV and has an effective area of  $100 \text{ cm}^2$ .

Experiment F, designed at Imperial College, is an actively collimated CsI(Na) crystal of effective area  $8 \text{ cm}^2$ . The instrument has an opening angle of  $8^\circ$  (FWHM) and is offset from the spin axis of the satellite by  $3^\circ$ . The pulsar mode of operation is used to study potential bursts sources. In this mode counts are accumulated in a broad energy channel stretching from 70 - 280 keV. The onset of a burst can only be measured to 24 s.

(d) In addition to gamma-ray detectors, the Vela-5 satellites also carry x-ray detectors sensitive to photons in the range 3 - 12 keV. Each instrument is used as a scanning device and has its  $6^\circ \times 6^\circ$  (FWHM) field of view aligned perpendicular to the satellite spin axis. The spatial coverage of the system is not uniform, and observations are concentrated towards the poles of the satellite centred coordinate system located at  $l'' = 149^\circ$ ,  $b'' = +5^\circ$  and  $l'' = 329^\circ$ ,  $b'' = -5^\circ$ .

(e) In addition to the satellites mentioned above, x-ray bursts have been observed by detectors on board COSMOS-428, OSO-7, OSO-8 and UHURU.

Table 4.1  
X-Ray Burst Source Positions

<u>Source Name</u>	<u>Position</u>		<u>Positional Accuracy</u> (Degrees <sup>2</sup> )
	<u>Galactic Longitude</u> (Degrees)	<u>Galactic Latitude</u> (Degrees)	
XB 1608-52	331.0	-1.0	0.5x6
MXB 1728-34	354.33	-0.13	0.05
MXB 1730-335	354.838	-0.141	0.003
KGX 345-6	345.4	-6.9	1.5
MXB 1742-29	359.5	-0.4	0.34
MXB 1743-28	0.5	+0.0	0.28
MXB 1743-29	359.98	-0.16	0.09
or	359.67	-0.17	0.09
KGX 349-11	348.1	-11.4	8
[ NGC6624 ]	2.79	-7.91	0.03
[ 3U1820-30 ]			
MXB 1837+05	36.21	4.86	0.09
MXB 1906+00	35.12	-3.75	0.09
Aql MXB	36.1	-3.3	1.2
or	38.7	-3.1	1.2
MXB 1659-29	353.8	+7.3	0.006
MXB 1637-53	332.9	-4.9	0.03
MXB 0512-40	244.5	-34.9	2
MXB 1735-44	263.8	-44.4	0.09
MXB 1916-05	288.9	-5.28	0.07
Unnamed Sources			
1	263	-14	12 x 12
2	11	-8	8 x 8
3	176	+0	2 x 120
4	344	-1.8	Several Deg. <sup>2</sup>
5	4	-4	"
6	26	-3.8	"

#### 4.3 Burst Source Locations

Table 4.1 lists the best available positions of the twenty-three known x-ray burst sources, together with the sizes of the associated error boxes. All these positions have been determined by instruments with intrinsic directional sensitivity, as opposed to the case of gamma-bursts where only crude directional information has been obtained, usually from timing comparisons between satellites. Several of the x-ray burst sources have associated steady x-ray sources. These are either objects that were known to exist before a burst was discovered from that location, or objects that have been found as a result of a specific search once a burst has been observed.

(a) XB 1608-52. The large error box associated with this burst source, which is located in the constellation Norma, prevents a definite association with any other object. There is an approximately steady x-ray source present within the error box which was observed by UHURU (designated 4U 1608-42, Tananbaum et al. 1977) and OSO-7 (designated MX 1608-52, Li 1976). Also present in the vicinity is the hard x-ray source GX 331-1 as observed by Ricker et al. (1976a) and Guo et al. (1975). In addition, the region has yielded a bright transient source which was detected by Ariel 5 (Kaluzienski et al. 1975) and which persisted for at least three days. The relationship between these sources is still rather unclear.

(b) MXB 1728-34. The burst source is almost certainly associated with the steady source MX 1728-34. The latter object has been observed by the RMC systems on SAS-3 (Hoffman et al. 1976) and Ariel 5 (University of Birmingham 1976) and found to lie within the error

circle of the burst source. The previously reported position of 3U 1721-33 has been shown to be incorrect and the new location is consistent with the position of MX 1728-34. A specific search for a globular cluster within the error box by Liller, failed to produce a positive result (Hoffman et al. 1976).

(c) MXB 1742-29, MXB 1743-28 , MXB 1743-29. These three burst sources, which lie within  $0.7^{\circ}$  of the galactic centre, were discovered by the SAS-3 satellite (Lewin et al. 1977 a). The extended galactic centre source, GCX (3U1743-29), covers the area occupied by all three sources and it has already been suggested that this object could consist of at least three discrete sources (Kellogg et al. 1971). The region also contains the transient source A 1743-29 which was discovered by the Ariel V group. This transient lies within the error circle of MXB 1742-29. Finally, the SAS-3 data indicates that the region contains at least one more burst source (Lewin et al. 1977 a). Again the exact relationship between the burst sources and the steady sources is unknown, the association will become clearer when the nature of the GCX source is more fully understood.

(e) MXB 1906+00. The RMC system on SAS-3 has detected a steady source with a one minute radius error circle which lies within the error box of the burst source (Doxsey 1976). The x-ray source A 1905+00 (Seward et al. 1976) lies very close to the burst source, and it is very likely that these three sources are the same.

(f) The burst source MXB 1735-44, which was discovered by the SAS-3 group (Lewin et al. 1977 b), is almost certainly the burst

source KGX 345-6 which was discovered by COSMOS-428 (Babuskina et al. 1975). The error circle for the burst source, which has a radius of  $\sim 10'$ , includes 3U 1735-44 and there is little doubt that this strong x-ray source produced the observed bursts.

(g) The extremely high value of the time averaged burst luminosity from the rapid burster MXB 1730-335, enabled the source position to be found using the RMC detectors on SAS-3 and Ariel 5 (Carpenter et al. 1976a). The associated error circle, which has a radius of  $2'$ , is consequently the smallest reported to date for a burst source. An object which may well be a globular cluster is located inside the error box (Liller 1976) but as yet, no associated steady x-ray source has been discovered.

(h) The burst sources MXB 1837+05 (Li et al. 1977), MXB 1637-53 (Hoffman et al. 1977), MXB 1916-05 (Lewin et al. 1977 c), MXB 0512-40 (Clark et al. 1977 a), have very probable associations with steady x-ray sources. The other sources listed in Table 4.1 have yet to be identified with steady x-ray sources. Figure 4.1 is a map in galactic coordinates of the more accurately known source positions. The clustering towards the galactic plane is readily apparent. This clustering, together with the association of burst sources with known galactic objects, is sufficient to confirm that x-ray bursts are a galactic phenomenon.

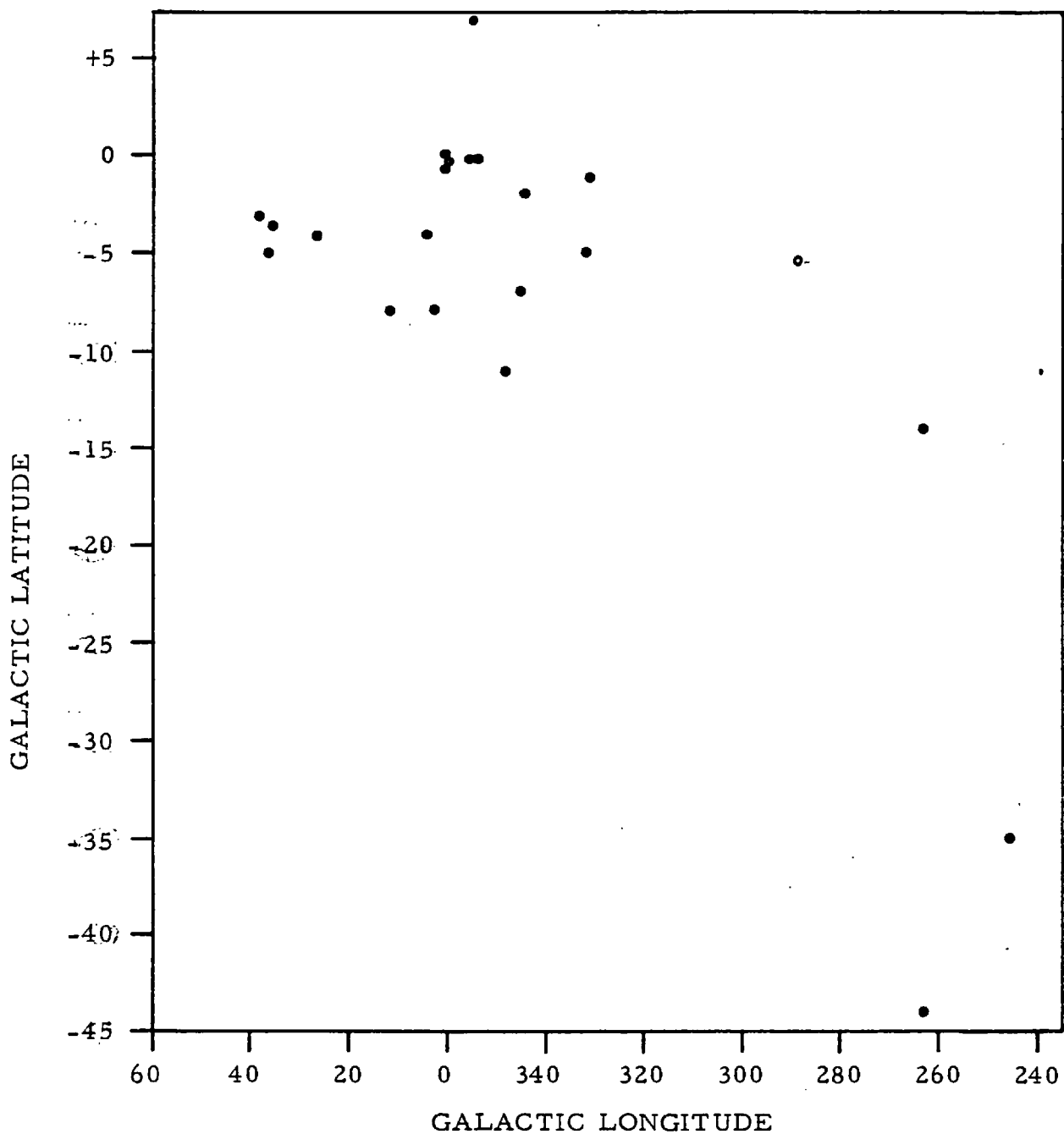


Fig 4. 1: Map In Galactic Coordinates Showing The Positions Of 22 Burst Sources. The Size Of The Error Box Associated With Each Point Is Given In Table 4. 1

#### 4.4. Burst Structure

X-ray bursts are at least as varied as gamma-bursts in their temporal nature. However, variations within particular bursts are characterised by a time scale of seconds as opposed to the milli-second variations displayed by many gamma-bursts. The risetime of the initial pulse is typically  $\sim 1$  s but this may vary with energy. During a particular burst from NGC 6624, which was observed by SAS-3 (Clark et al. 1976), the 2 - 6 keV flux peaked in  $\sim 1$  s whereas the 6 - 11 keV flux took 2 s to reach its maximum value. The spectrum consequently hardened with time. However bursts from other sources, e.g. MXB 1837+05 (Li et al. 1977), have been found to have spectra which soften with time.

Bursts can be single, double or even triple peaked, the peak widths varying from 0.8 - 8 s. The overall duration can be anywhere in the range 0.8 - 50 s but most of the energy is usually emitted within 10 s of the onset of the burst. (see Figure 4.2 for examples). The decay of many bursts is roughly exponential, 3 s being a typical time constant. Figure 4.3 shows the composite light curves of six bursts detected from MXB 1728-34 by SAS-3 in March 1976 (Hoffman et al. 1976). The time constant of the decay portion increases with energy which implies spectral softening with time. A weak flux is still present after 20 s in the lower energy channels.

Bursts from a particular source are often very similar. Figure 4.4 shows two bursts from MXB 1743-29 which were detected by SAS-3 (Lewin et al. 1977 a). All other bursts from this source have a similar structure:

- (i) The bursts rise simultaneously in all energy channels (within the 0.8 s resolving time).
- (ii) They show a double peak structure which is more prominent at higher energies.
- (iii) The peak separation increases with energy.
- (iv) The second peak has a higher maximum than the first.
- (v) Following the fast decay there is a slow decay which lasts 30 - 40 s in the 3 - 6 keV channel.
- (vi) The spectrum softens during decay.

However, the nature of bursts from other sources has been found to alter significantly in a time scale which varies from seconds to weeks. Bursts from MXB 1730-335 for example, are known to vary in duration by up to two orders of magnitude in less than 10 s, and multiple peaks are observed in almost all the larger events.



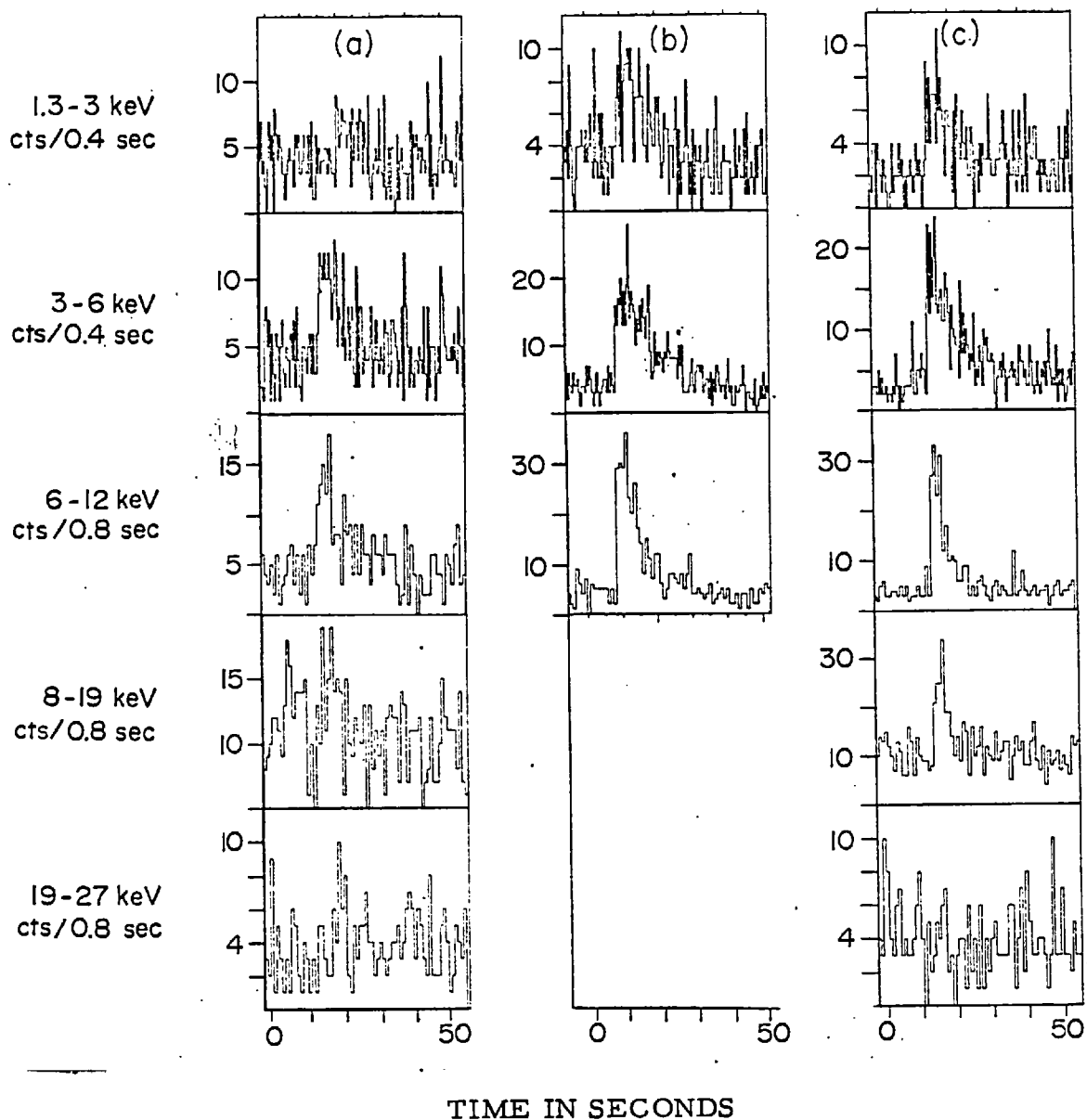


Fig 4. 2: Three Bursts From MXB1906+00 As Recorded By SAS-3. Each Event Has A Duration Of About 10s And A Pulse Structure Which Is Energy Dependant.

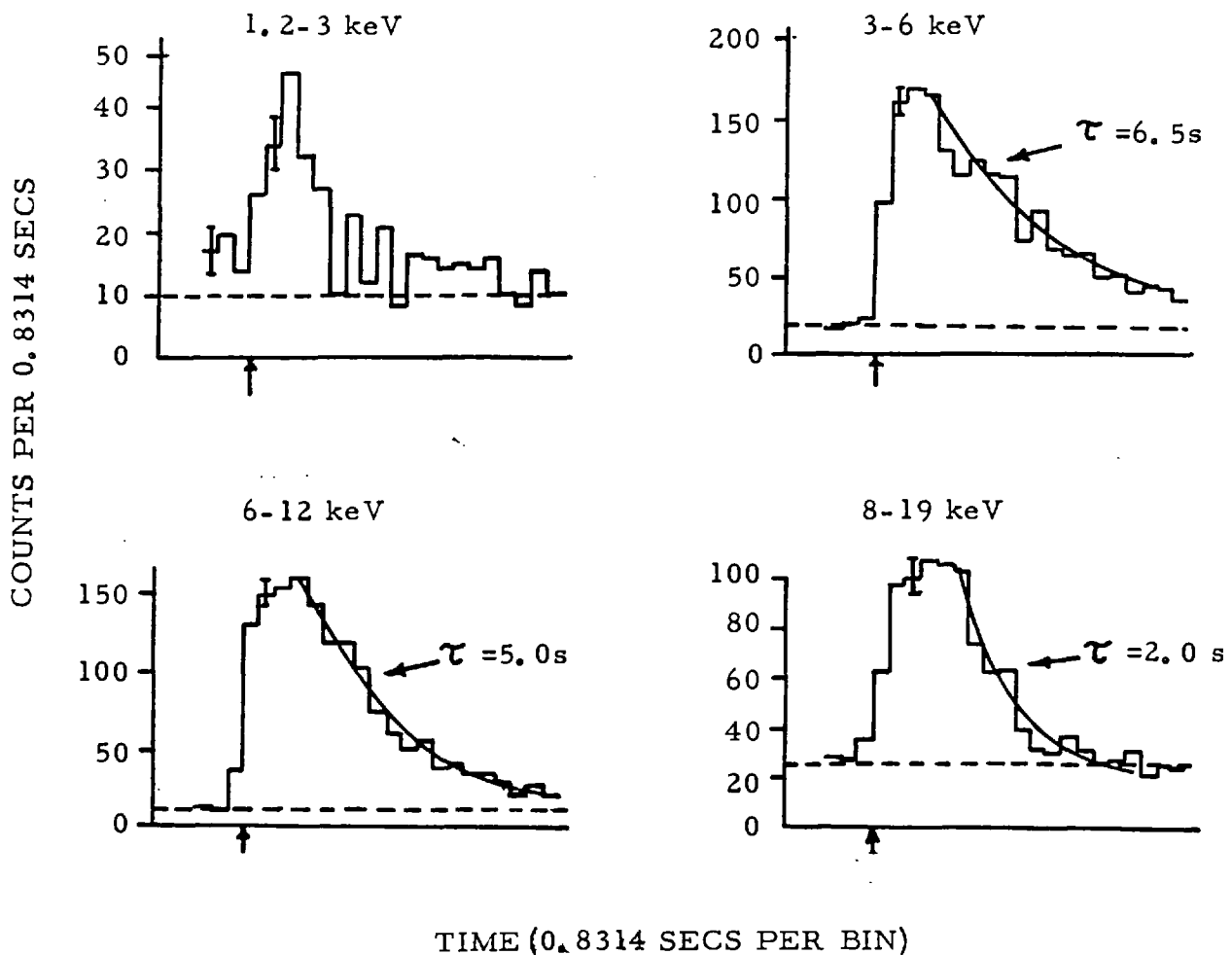


Fig 4.3: Composite Light Curves Of Six Bursts From MXB 1728-34 As Recorded By The Horizontal Tube System On SAS-3.

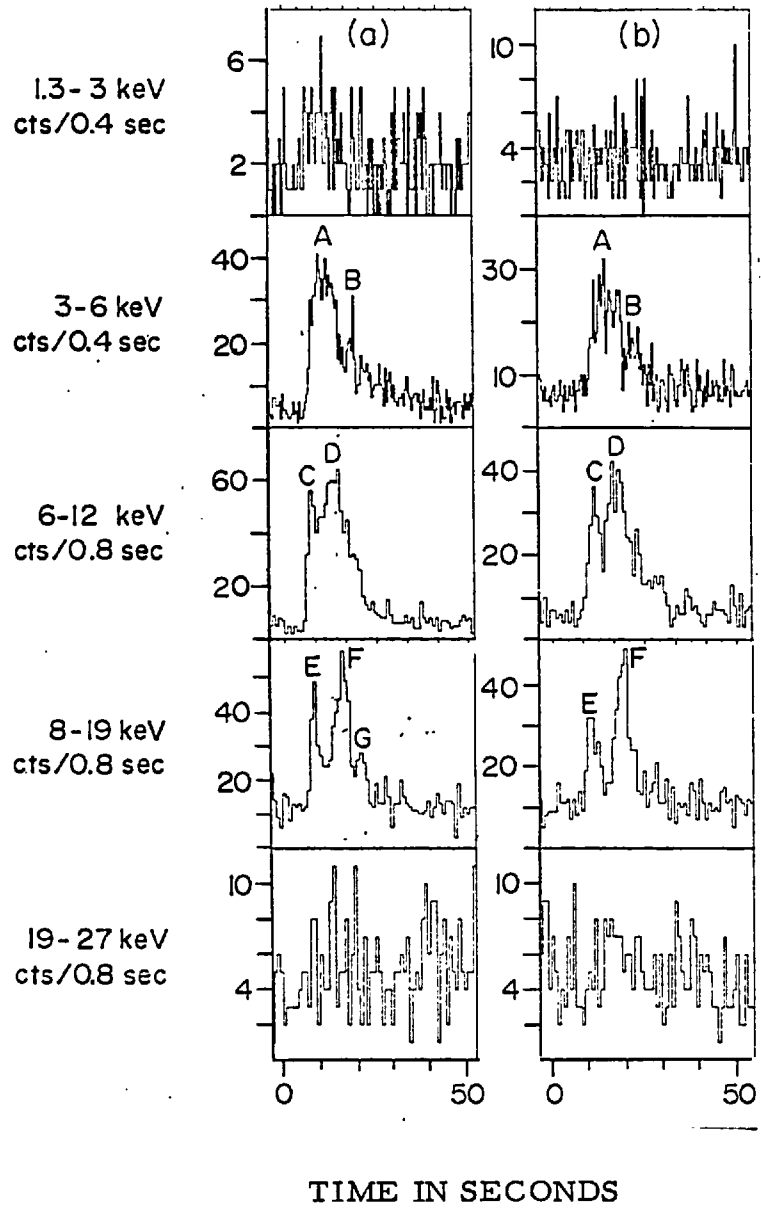


Fig 4.4: Two Bursts From MXB 1743-24 As Recorded By SAS-3. All Bursts From This Source Have A Similar Structure.

#### 4.5. Burst Sizes and Burst Separation

The association of x-ray bursts with known celestial objects has enabled the bursts' sizes to be determined, knowing the photon fluxes at the earth. The sizes are found to vary over three orders of magnitude, ranging from  $10^{37}$  -  $10^{40}$  ergs (1 - 19 keV), and the peak intensities are usually in the range  $5 \times 10^{37}$  -  $5 \times 10^{38}$  ergs  $s^{-1}$ . As yet no burst has been observed with a measurable flux above 19 keV except for the very hard bursts already referred to.

Several sources emit bursts at regular intervals. MXB 1728-34 was observed on three separate occasions in March 1976 (Hoffman et al. 1976), and the mean burst separation times during the individual periods were 4.6 hr (0.5 hr rms Jitter), 3.0 hr (0.5 hr Jitter) and 7.8 hr (0.1 hr Jitter). The burst sizes remained constant to within 20% throughout each observation. The galactic centre source MXB 1743-29 was observed continually for twenty-three days in February and March 1976 by SAS-3 (Lewin et al. 1977a). The bursts had a mean separation time of thirty-five hours (5.9% Jitter) and their sizes stayed more or less constant. A similar behaviour has also been reported for MXB 1906+00 (Lewin et al. 1977c). As yet no highly periodic burst source has been discovered. Such a source was reported by Carpenter et al. (1976b), but the discovery was refuted by Lewin et al. (1976b), who proved that the bursts were from MXB 1730-335 and that several periodicities could be made to fit the data.

This burst source, often referred to as the "rapid burster", is the most prolific source discovered to date. Figure 4.5 displays data produced by the four Y-axis detectors on SAS-3 during a four

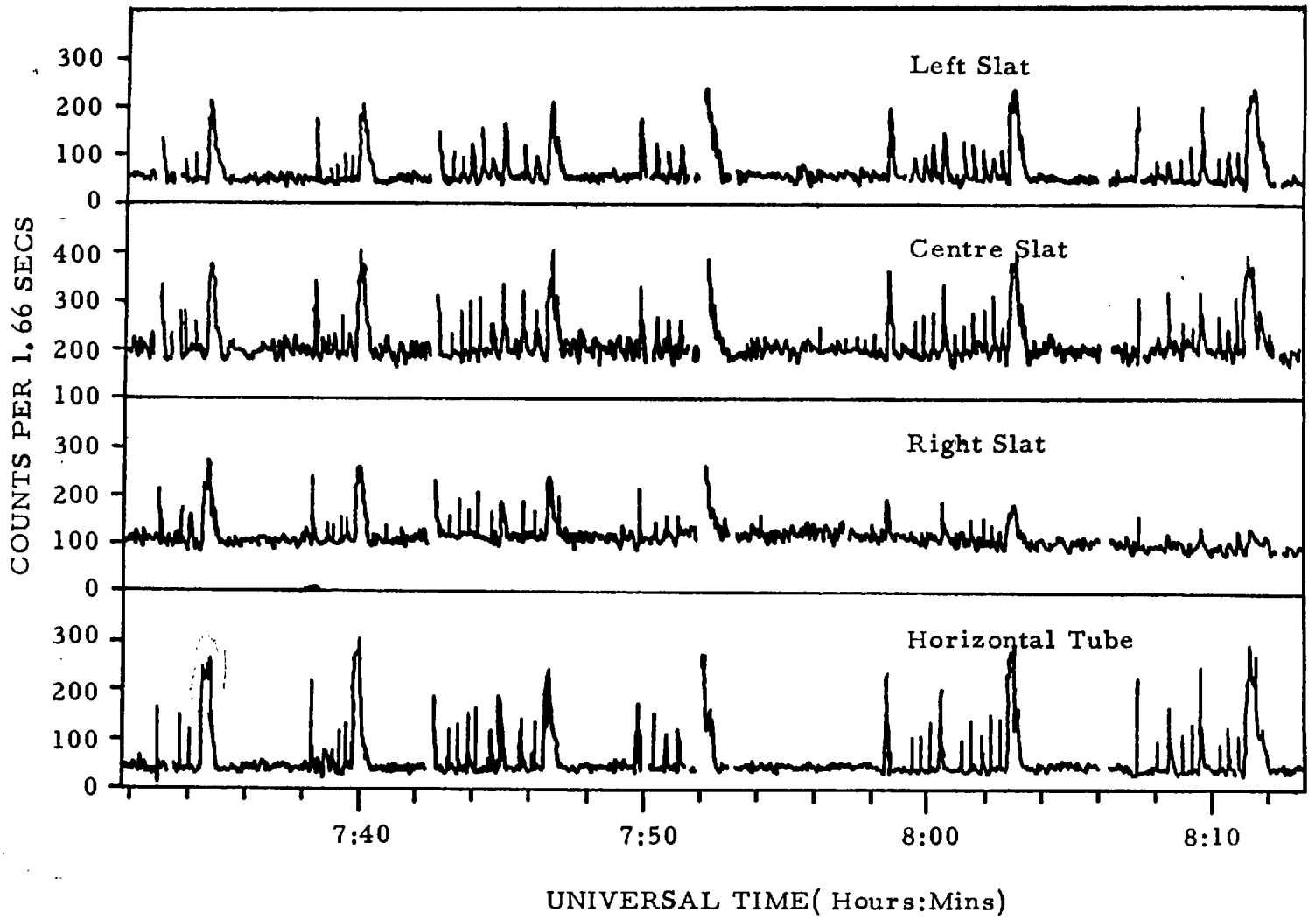


Fig 4.5: Bursts From MXB 1730-335 As Recorded By SAS-3  
 On 2 March 1976. Many Small Bursts Are Displayed  
 Together With Several Larger Events.

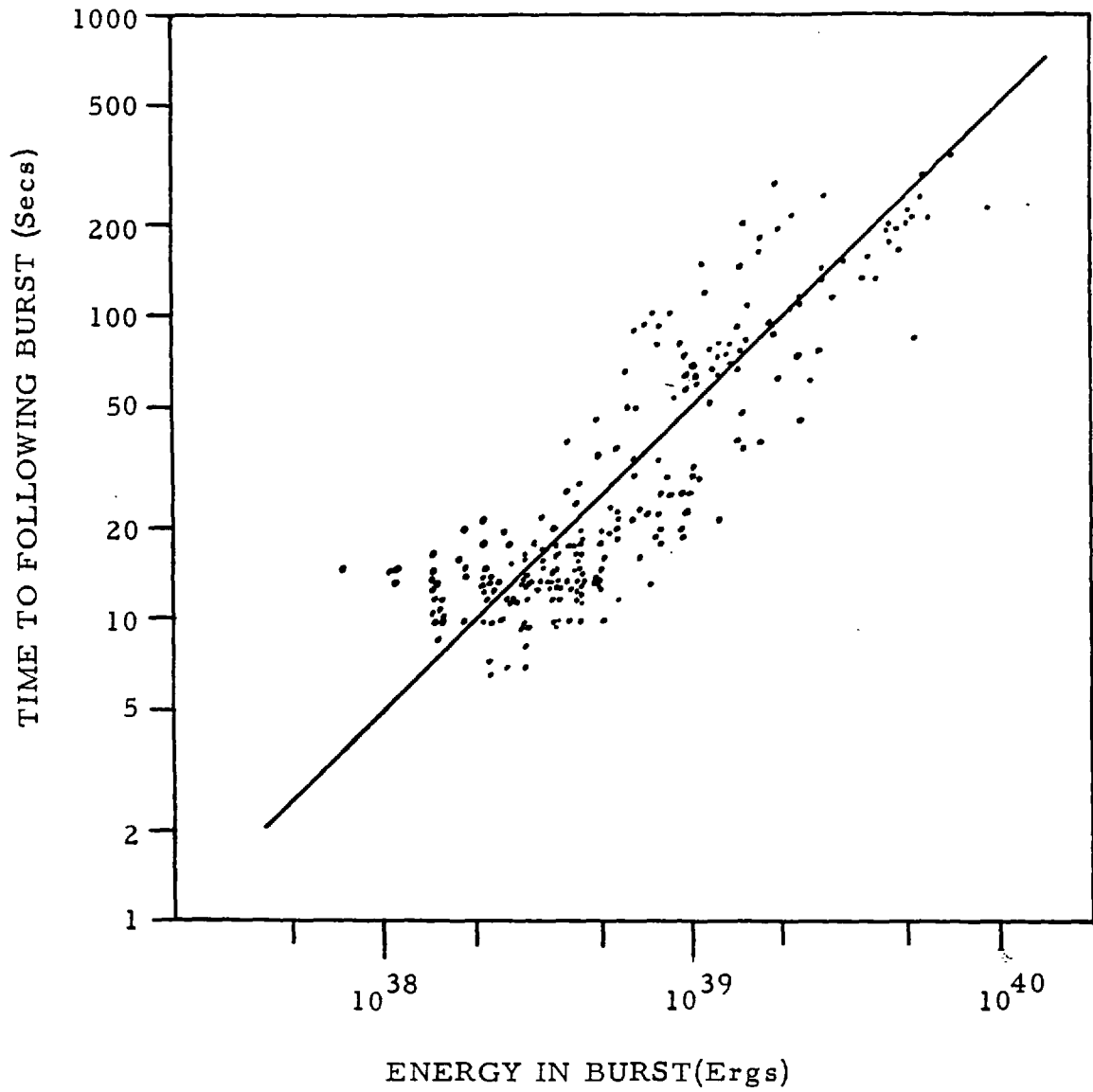


Fig 4.6: Plot Of Energy In Burst (1.5-10 keV) Versus The Time Separation To The Following Burst For 250 Events From MXB 1730-335.

day observation in March 1976. During the observation, the burst separation times were found to vary between 6 s - 450 s, and the burst sizes ranged from  $\sim 10^{38}$  -  $10^{40}$  ergs (1.5 - 10 keV) for an assumed source distance of 10 kpc. The sizes could vary by two orders of magnitude in the space of one interval. Figure 4.6 is a plot of the time interval to the following burst versus burst size for 250 events. If the energy in a given burst is linearly proportional to the separation between it and the following event, the points should lie on a straight line inclined at  $45^\circ$  (one such line is drawn). As can be seen, an approximate linear relationship holds for bursts in the range  $\sim 2 \times 10^{38}$  ergs to  $\sim 6 \times 10^{39}$  ergs; the error in size is  $\sim 40\%$  at the bottom end of the graph. Another interesting feature displayed by the bursts is that the intensity appears to have a threshold level which cannot be exceeded, no matter what the burst size may be. This source has also been observed in a state where it produces bursts of more or less constant size at regular intervals (Lewin et al. 1976 a).

When the source MXB 1837+05 was observed by SAS-3 in July 1976 the burst intervals were highly irregular, varying by a factor of 25, whereas the burst sizes were constant to within a factor of 2 (Li et al. 1977). This type of behaviour is unique amongst burst sources. However, when the source was re-examined in August 1976, it was found to be emitting bursts of almost constant size at regular intervals of 6.3 hr (6.2% Jitter).

The behaviour of several other sources is worthy of note. The galactic centre source MXB 1742-29 emitted bursts at regular intervals of 13 hr (3.4% Jitter) during the whole of the SAS-3 twenty-

three day observation period in 1976 (Lewin et al. 1977 a). However, the burst sizes varied by up to a factor of five from one event to the next. NGC 6624 on the other hand was observed by SAS-3 to be emitting bursts of a constant size at a time when the mean separation was varying slowly from 3.4 hr to 2.2 hr (Clark et al. 1977 b).

Thus although the behaviour pattern appears to vary considerably from object to object, several of the observations mentioned above indicate that a particular source can emit bursts in several different ways. Each burst source may be capable of producing all the different emission patterns described here and more information is required to clarify the matter.



#### 4.6. Burst Spectra

It was pointed out in Chapter 1 that gamma-bursts have a well established event average spectrum. Despite the fact that the vast majority of x-ray bursts have been observed by instruments with intrinsic spectral resolution, very little is understood about the nature of their spectral behaviour. Satisfying fits to the data have yet to be achieved using conventional spectra such as thermal bremsstrahlung, blackbody or power law. One of the reasons for this is that the instantaneous burst luminosity can change rapidly and differently in different energy channels. In addition, many of the bursts which have been observed by SAS-3 have only had a measurable flux in the three channels of the horizontal tube system which cover the range 1.3 - 12 keV. The statistical errors associated with each of the three points, make it very difficult to achieve a satisfying spectral fit to the data produced by a single burst.

The rapid burster was observed by the hard x-ray detector on the ANS satellite in March 1976 (Heise et al. 1976). This detector has a better spectral resolution than the SAS-3 devices and spectra were obtained of twenty bursts. The best fit to the composite data produced by the twenty events is a thermal bremsstrahlung spectrum, plus absorption by cold matter i.e.

$$\frac{dN}{dE} \propto \frac{e^{-E/KT}}{E} e^{-\sigma N_H} \text{ photons cm}^{-2} \text{ s}^{-1} \text{ keV}^{-1}$$

$$KT = 10 \pm 4 \text{ keV}$$

$$N_H = 5_{-1}^{+2} \times 10^{22} \text{ atoms cm}^{-2}. \text{ This value of } N_H \text{ is consistent with}$$

the interstellar absorption measured for the globular cluster which is

known to exist within the error box of the burst source.

Observations of NGC 6624 indicate that the event average spectrum remained unaltered over a period of several months. When the source was observed by SAS-3 in May 1975 (Clark et al. 1976), the data were consistent with a thermal fit with  $kT \gtrsim 20$  keV and a low energy cut-off at 3 keV. When the cluster was observed by ANS in September 1975 (Grindlay et al. 1976a) two bursts were detected. The spectra of these events are best represented by thermal fits with  $kT = 17 (+13, -10)$  and  $kT = 16 \pm 8$  keV and low energy cut-offs in the 1 - 3 keV region.

However, several sources exhibit spectral variations in time scales which range from one burst interval to several months. Four bursts were detected from the Norma source XB 1608-52 by UHURU, two in December 1971 and two in May 1972. Data from the former events are consistent with a thermal fit, which has a  $kT$  value  $>18$  keV and a low energy cut-off at  $\sim 3$  keV. The May events had considerably softer spectra, best fitted by thermal spectra with  $kT$  values of 4 and 8 keV and low energy cut-offs at  $\sim 3$  keV. The spectra of the December events hardened with time, but there was no evidence of spectral change during the May bursts. Table 4.2 lists the hardness ratios of twenty-two bursts from MXB 1837-05 which were detected by SAS-3. It is readily apparent that there are significant spectral changes between bursts which do not appear to be related to the bursts' sizes, or the separation between them. Bursts 5 and 12 have hardness ratios which are low compared to the average value. It appears that burst 12 was cut off at low energies, and burst 5 had a relatively soft spectrum.

Burst Number	Separation From Previous Burst (in days)	Integrated Intensity (total counts 1.3-12 keV)	Ratios Of Counts Of 1.3-3 keV To 3-6 keV Channel	Ratios Of Counts Of 6-12 keV To 3-6 keV Channel
1		*		
2	0.18	*		
3	0.75	860	0.26	0.55
4	0.58	760	0.43	0.38
5	1.57	500	0.38	0.23
6	0.52	520	0.43	0.65
7	0.063	500	0.72	0.88
8	0.54	540	0.36	0.71
9	0.11	490	0.35	0.68
10	0.39	**		
11	0.14	860	0.39	0.88
12	0.28	390	0.07	0.44
13	0.25	530	0.38	0.49
14	0.14	590	0.46	0.41
15	0.19	720	0.36	0.69
16	0.4	520	0.32	1.00
17	0.19	530	0.4	0.77
18	0.39	460	0.86	0.40
19	***	660	0.54	0.35
20	0.26	620	0.44	0.66
21	0.23	733	0.27	0.76
22	0.83	570	0.21	0.68
		Typically $\pm 120$	Typically $\pm 0.15$	Typically $\pm 0.2$

\* Only seen in centre slat system

\*\* Only the decay portion of the burst was observed

\*\*\* Observing gap of 35 days

Table 4.2: Hardness Ratios Of 22 Bursts from MXB 1837-05

Most x-ray bursts exhibit spectral variations throughout their duration. Some sources produce events whose spectra harden during onset, whereas others emit bursts whose spectra soften during the initial rise. At least one source, MXB 1837+05, produces both types of events. Figure 4.3 illustrates the spectral behaviour displayed by many bursts during their decay phase using MXB 1728-34 as an example. The softening of the composite spectrum with time is readily apparent. Only bursts from NGC 6624 have been found to harden during decay.

#### 4.7. Source Activity Periods

It is well established that four sources have burst inactive states (XB 1608-52, MXB 1730-335, MXB 1743-28 and NGC 6624). Bursts from the last source have only been observed when the steady source is in a "low" state. When the cluster was observed by SAS-3 in March 1976 (Clark et al. 1977 b), the steady luminosity was gradually increasing. During the observation twenty-two bursts were observed in four days. As the steady flux increased, the burst separation time decreased, but the burst sizes remained constant (to within 20%). When the steady flux reached a critical level the source stopped producing bursts. No burst activity has been detected from this source when it is in its "high state". A similar behaviour by another source has yet to be reported.

#### 4.8. Long x-ray bursts (flares).

At least six long x-ray bursts (or flares) have been observed to date. The events all originated at different sources and their risetimes have only been crudely determined ( $<10$  s). It is therefore unclear if they are simply long x-ray bursts, or if they are a different type of event. To avoid confusion the events will be referred to as x-ray flares from here on.

Two of the flares were produced by UVCeti flare stars (Heise et al. 1975). During October 1974 and January 1975, the flare stars UVCeti and YZCMi were observed by the x-ray telescopes on the ANS satellite. A total of  $\sim 300$  minutes of good quality low background data was obtained on each object. On 9th October a flare was observed on YZCMi by the soft and medium energy x-ray detectors (see section 4.2). The duration of the flare was  $\sim 6$  minutes in the soft energy range, (0.2 - 0.28 keV) and 1.5 minutes in the medium energy range (1 - 7 keV). Both these durations are considerably longer than the duration of a typical x-ray burst, which is  $\sim 20$  s. The total energy release from YZCMi, known to be at a distance of 6.06 pc., between 0.2 and 0.28 keV was  $4.2 \pm 0.3 \times 10^{31}$  ergs, and the peak luminosity was  $2.5 \pm 0.4 \times 10^{29}$  ergs  $s^{-1}$ . In the medium energy range the corresponding values were  $1.9 \pm 0.4 \times 10^{32}$  ergs and  $3.6 \pm 0.7 \times 10^{30}$  ergs  $s^{-1}$ . The event was therefore six orders of magnitude smaller than a typical x-ray burst ( $\sim 10^{38}$  ergs).

The flare from UVCeti itself was observed on 8th January by the soft x-ray detector only. The event had a duration of  $\sim 48$  s, and the x-ray luminosity at the source was at least  $6.1 \pm 1.3 \times 10^{28}$  ergs  $s^{-1}$ , giving a minimal total energy release of  $2.9 \pm 0.6 \times 10^{30}$

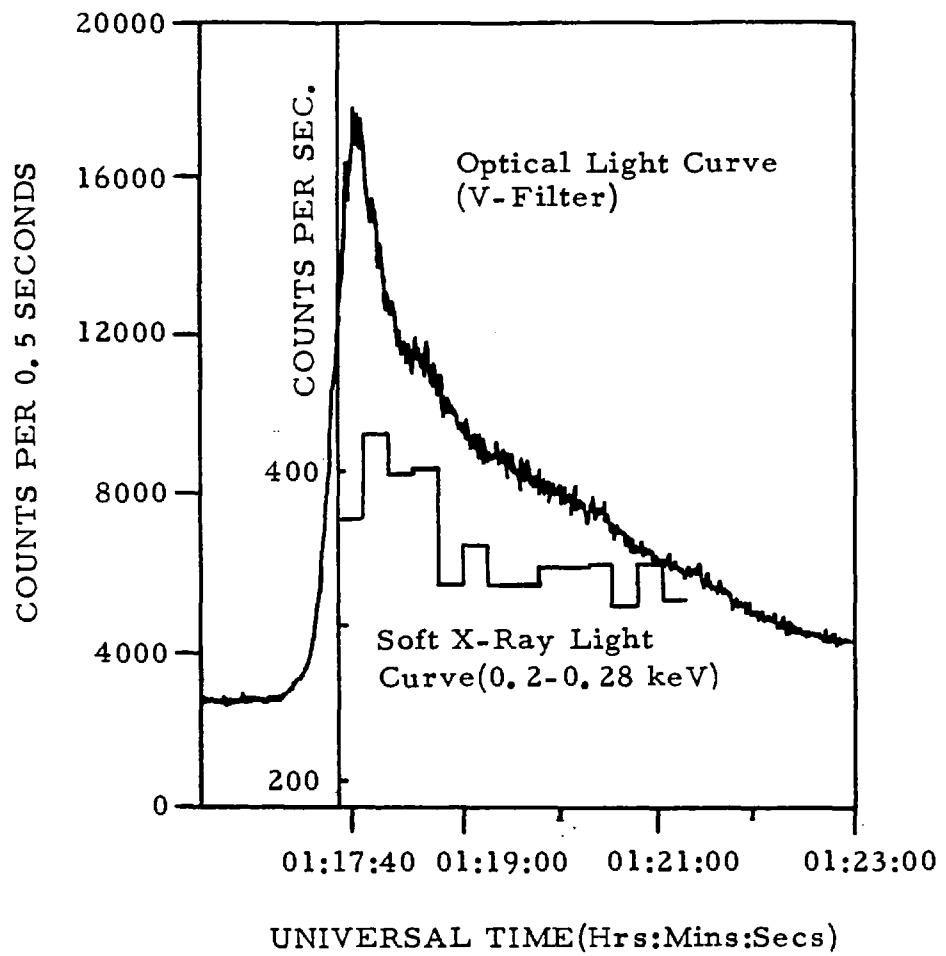


Fig 4. 7: Optical And Soft X-Ray Flare From UV Ceti.

ergs. A large optical flare was observed in coincidence with the soft x-ray increase, and Figure 4.7 shows the two light curves superimposed. The peak flux in the optical (U-band) flare was greater than  $2 \times 10^{30}$  ergs  $s^{-1}$  ( $\Delta M_U > 6$ ). The ratio of x-ray to optical flare luminosities at the peak was therefore  $L_x/L_{opt} \leq 3 \times 10^{-2}$ . There are several models which predict x-ray emission from flare stars in coincidence with the commonly observed optical and radio flares (Cranell et al. 1974, Grindlay 1970 and Kahler et al. 1972). The observed ratio during the UVCeti flare of  $L_x/L_{opt}$  is significantly below all predictions, but closest to that of Kahler et al. They assume that a UVCeti flare is analogous to a solar flare, and use the observed ratio of solar x-ray to solar optical flare luminosities to predict a corresponding ratio of  $\sim 10^{-1}$  for a UVCeti flare. It is perhaps significant to note when considering the nature of the flares, that no x-ray burst has been observed in coincidence with an optical or radio flare.

Another flare was observed by detectors on board OSO-8 on the 11th September 1975 (Swank et al. 1976, Bunner 1976). The source of the event was found to be located at  $l'' = 356.4^0$ ,  $b'' = +2.3^0$ , and several days later a steady source was discovered within the error box. The flare was detectable for  $\sim 50$  satellite rotations of 10.7 s each, and the light curve is shown in Figure 4.8. During the event the spectrum varied considerably, as illustrated in Figure 4.9 where the spectral hardness (ratio of 6 - 11 to 2 - 6 keV fluxes) is plotted as a function of time. During the peak, the spectrum was very soft and then it hardened rapidly during decay, only to soften during the later stages of the decay phase. The



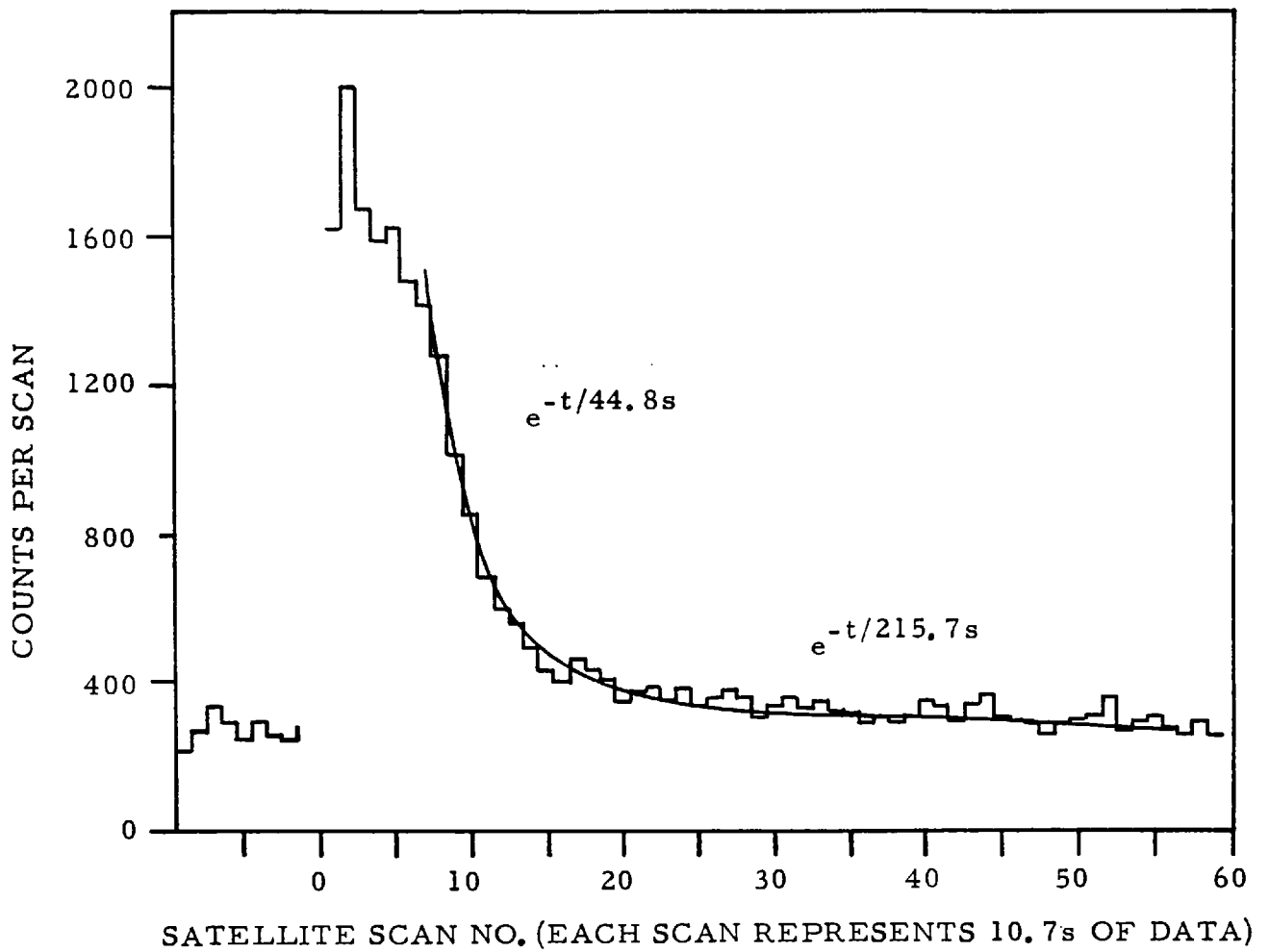


Fig 4. 8: Light Curve Of The Flare Observed By OSO-8. The Decay Portion Of The Event Is Well Fitted By Two Exponential Functions.

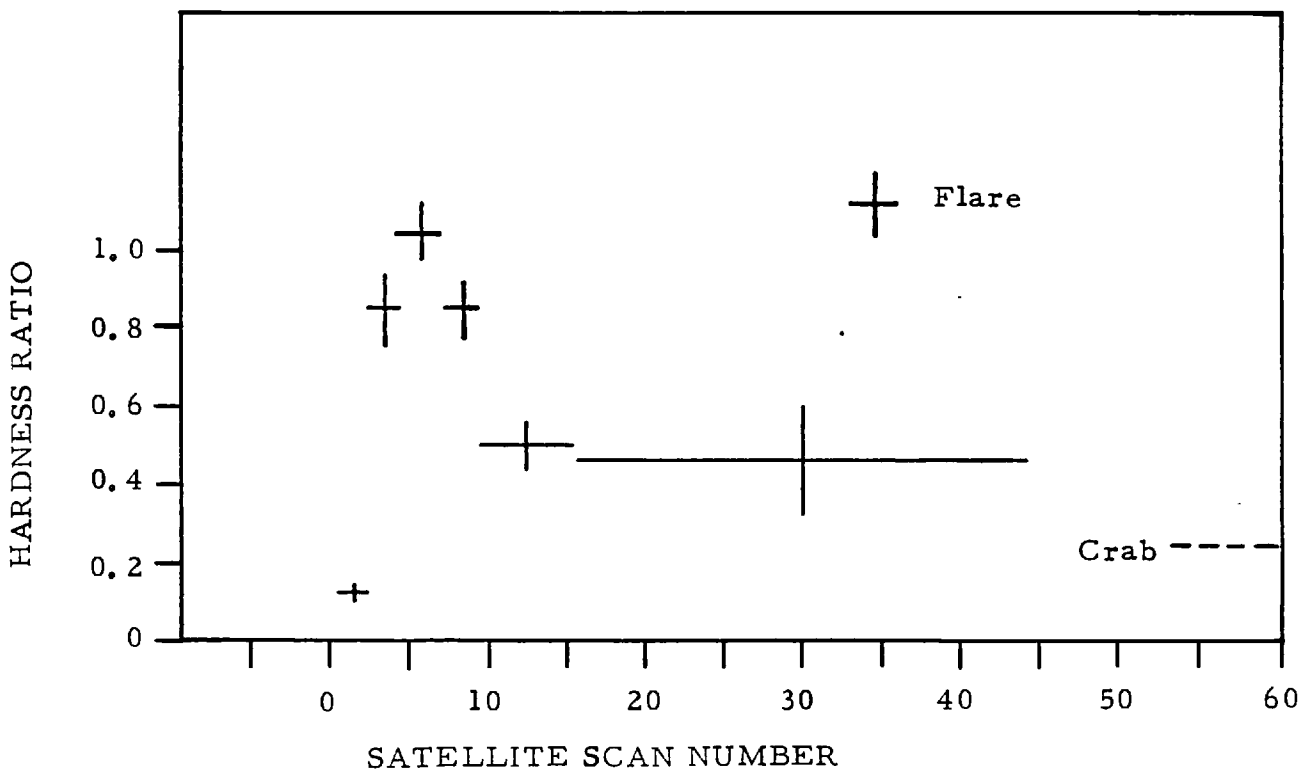


Fig 4. 9: Hardness Ratio (6-11/2-6 keV Fluxes) Of The OSO-8 Flare. The Hardness Of The Crab Spectrum Is Shown For Comparison.

individual spectra, obtained at various times during the event, are best fitted by a blackbody emission model with absorption by cold matter.

i.e.

$$\frac{dN}{dE} \propto \frac{E^2}{e^{E/KT} - 1} e^{-N_H \sigma} \text{ photons cm}^{-2} \text{ s}^{-1} \text{ keV}$$

KT varies from 0.87 - 2.33 keV

$N_H \sim 3 \times 10^{22} \text{ atoms cm}^{-2}$

$\sigma$  = cross-section for photoionisation of neutral material with abundancies as used by Fireman (1974). The value of  $N_H$  is virtually the same for all spectra taken during the event, and only falls to  $10^{21} \text{ atoms cm}^{-2}$  for spectra taken during the later stages of decay. This latter value is consistent with the absorption measured from the steady source ( $N_H = 1.8 \pm 1.8 \times 10^{21} \text{ atoms cm}^{-2}$ ) whose spectrum is well fitted by a thermal bremsstrahlung law with  $KT = 10 \pm 2 \text{ keV}$ .

Although the duration of the flare was long compared to that of an x-ray burst, the event does exhibit certain similarities to the shorter bursts. In particular, the intensity rose relatively fast compared to the life-time of the event, and the major part of the decay was exponential. The changes in spectral hardness are similar to those displayed by NGC 6624, and the low energy cut-off at 2 - 3 keV is commonly exhibited by burst spectra.

Before it can be decided whether or not these flares, and the similar events referenced in section 4.1, are x-ray bursts, more observations of their sources are required to see if the events recur; and if so, to measure their risetimes. If the UVCeti flares are shown to be examples of x-ray bursts, then their known flare origin and small size has important consequences for burst production theories.

4.9. The association of x-ray bursts with gamma-bursts

Because of the general similarity in time scales, the question of a possible connection between x-ray and gamma-ray bursts arises. The obvious association is to assume that gamma-bursts are simply the high energy tail of x-ray bursts. The fact that the two burst types have not been observed in coincidence does not preclude this association, when one considers the sizes of the observed x-ray bursts. Apart from the very hard bursts reported by Baburskina et al. (1975) and Share (1976), there have been no x-ray bursts detected with a size  $> 0.7 \times 10^{-6}$  ergs  $\text{cm}^{-2}$  in the range 0 - 20 keV. If such a burst was the low energy portion of a gamma-burst, the integrated burst size (0 -  $\infty$ ) would be  $\sim 10^{-5}$  ergs  $\text{cm}^{-2}$ , which is below the Imp-7 detection threshold and close to the Vela threshold. However, there are other factors which point to the two burst types being unrelated phenomena.

(i) X-ray bursts normally consist of one or two distinct pulses which have a total duration of  $\sim 50$  s, most of the energy being emitted within the first 10 s. The risetime of the initial pulse is usually 1 s and the final decay is often exponential. Although gamma-bursts have a not dissimilar duration (typically  $\sim 6$  s), they usually consist of a series of very short pulses or micro-bursts (width  $\sim 50$  ms) which contain most of the energy. Even when viewed with detectors which have a similar resolution to the SAS-3 detectors (0.4 s), they display more fine structure than typical x-ray bursts. The risetime of the initial pulse is sometimes as short as 2 ms and the decay is rarely exponential. Thus apart from their durations, the two burst types are rather different in temporal nature.

(ii) In the first part of this section the assumption that gamma-bursts and x-ray bursts had identical spectra was used. In actual fact the two burst types have rather different spectra. X-ray burst data are quite often best fitted by a thermal bremsstrahlung law of the form

$$\frac{dN}{dE} \propto \frac{e^{-E/KT}}{E} \text{ photons cm}^{-2} \text{ s}^{-1} \text{ keV}^{-1}$$

with a  $KT$  value somewhere between 10 and 20 keV.

Only two gamma-bursts have been observed at x-ray energies (Metzger et al. 1974 and Wheaton et al. 1973). Both sets of data are consistent with a power law fit in the range 0 - 250 keV of the form

$$\frac{dN}{dE} \propto E^{-1.38} \text{ photons cm}^{-2} \text{ s}^{-1} \text{ keV}^{-1}$$

As Figure 4.10 illustrates, the gamma-burst spectrum is somewhat harder than the x-ray burst spectrum.

Both types of burst display spectral variations throughout their duration. In the case of x-ray bursts the variations are quite often unrelated to intensity changes, whereas gamma-bursts frequently display spectral softening during intense burst periods (see section 1.8). In addition, gamma-bursts have a well established event average spectrum, but x-ray bursts exhibit a great variety of spectra.

(iii) Many x-ray bursts are thought to be produced by objects located within the galaxy, and the distribution of their sources is similar to the distribution of galactic matter. Although size spectra

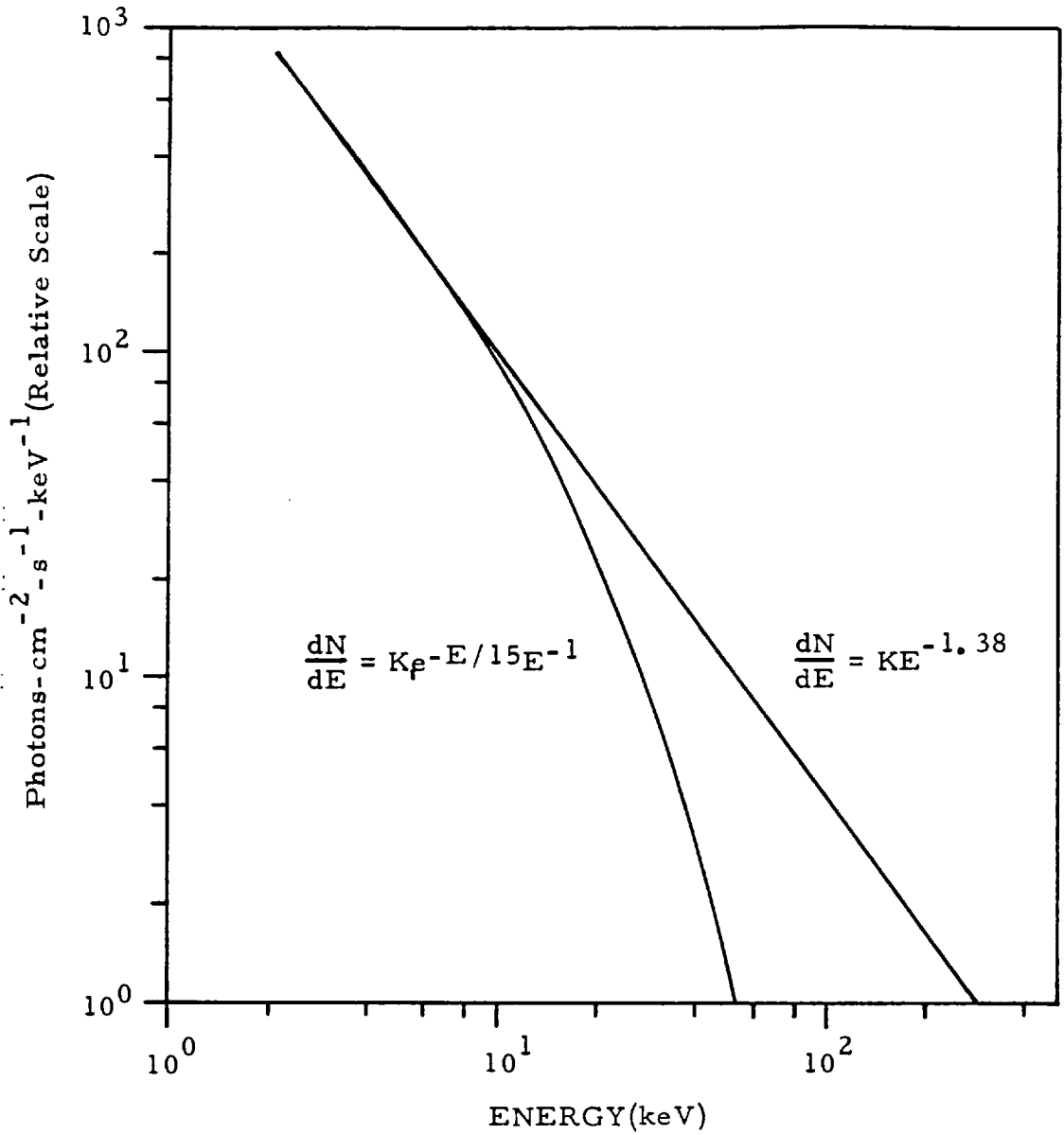


Fig 4. 10: A Typical X-Ray Burst Spectrum Compared With The Standard Event Average Gamma Burst Spectrum.

and latitude data indicate that gamma-bursts are also a galactic phenomenon, the actual distribution of their sources is very different to the distribution of x-ray burst sources, as Figures 4.1 and Figures 1.13 illustrate. In particular, there are several gamma-burst sources at high galactic latitude.

(iv) Virtually all x-ray burst sources are recurrent. The existence of a recurring gamma-burst source has yet to be proved.

The evidence presented in this section argues strongly against the association of the two burst types, particularly against the idea that gamma-bursts are the high energy tail of x-ray bursts.

#### 4.10. Hard X-ray Bursts

##### 4.10.1. COSMOS-428 and OSO-6 Results

The first x-ray bursts were detected by COSMOS-428 (Babuskina et al. 1975) which observed eight events from two distinct sources, designated KGX 345-6 and KGX 349-11. The bursts were called x-ray bursts because they were considerably softer than the gamma-bursts which had already been reported. However, the events had rather different properties to the other x-ray bursts which have since been observed, and whose characteristics have already been described.

(i) Their event average spectra were much harder than typical burst spectra, hard enough to register on the COSMOS-428 detectors which have a lower threshold of 40 keV.

(ii) The bursts were very energetic and had sizes which varied between 10 and  $80 \times 10^{-7}$  ergs  $\text{cm}^{-2}$ , much greater than the typical burst size of  $\sim 2 \times 10^{-7}$  ergs  $\text{cm}^{-2}$ .

(iii) Their durations were of the order of 10 s more than a factor of two smaller than the duration of typical x-ray bursts.

The NRL solar x-ray detector (described in section 1.5) on OSO-6 detected six burst-like events in coincidence with other satellites during its lifetime. Five of the bursts were confirmed by the Vela satellites. All these bursts were originally classified as gamma-bursts but as Table 4.3 shows, three of the events were considerably softer than the gamma-burst detected by Apollo-16 on

Table 4.3

Spectral Hardness of Gamma-bursts Observed  
by OSO-6

Yr	Date		Hardness Ratio $\frac{\text{counts } 30 \leq E \leq 82 \text{ keV}}{\text{counts } E > 30 \text{ keV}}$	Observers
	Mo.	Day		
69	10	07	$0.31 \pm 0.06$	06, 05, 2V
70	12	01	$0.31 \pm 0.08$	06, 05, 2V
70	01	25	$0.63 \pm 0.24$	06, 05
70	10	01	$0.79 \pm 0.11$	06, 05, 1V
71	03	18	$0.32 \pm 0.04$	06, 05, I6, 3V, S1
71	02	27	$0.73 \pm 0.07$	06, 2V
72	04	27	0.4 (Estimated response of OSO-6)	A16, 1V

06 = OSO-6

05 = OSO-5

NV = Number of Velas

I6 = Imp-6

A16 = Apollo-16

S1 = SAS-1



the 27th April 1972. The "hardness" of this burst is estimated because OSO-6 did not observe the event. The six bursts form two distinct groups, three of the bursts had hardness ratios of  $\sim 0.31$  which almost certainly confirms them to be gamma-bursts. The other three events, which had hardness ratios of  $\sim 0.7$ , are more aptly classified as hard x-ray bursts. These latter events had durations of the order of 10 s and sizes of  $\sim 3 \times 10^{-5}$  ergs  $\text{cm}^{-2}$ . The similarity in duration and size to the COSMOS-428 bursts suggests that the bursts are further examples of the same phenomenon.

At least one hard x-ray burst source, KGX 345-6, is thought to be capable of producing normal x-ray bursts. In May 1977 the SAS-3 observatory detected twenty-six bursts from a source later designated MXB 1735-44. The error box for the source has a radius of  $\sim 10'$  and includes the steady source 3U 1735-44 (Lewin et al. 1977 b). The error circle also lies within the  $1.5 \text{ deg.}^2$  error box of KGX 345-6. The bursts were very short in duration (3 - 7 s) although they had a similar size and spectrum to typical x-ray bursts. There was no detectable signal above 20 keV. The short duration and positional coincidence suggest that KGX 345-6 was responsible for the bursts, which also implies that 3U 1735-44 is the steady source associated with this burst source.

#### 4.10.2. Coincident Observations of Hard and Soft Bursts

During the period 8th-11th March 1976, the Ariel V satellite was used to search for burst activity from the region of the sky centred on the rapid burster MXB 1730-335. To facilitate this search, experiments C (proportional counter) and F (scintillation telescope) were operated for most of the observation in the pulsar mode, in which counts from  $\frac{1}{2}$  s intervals are stored sequentially in sets of sixteen locations (bins). Each set is scanned four times before proceeding to the next set. As it is impossible to tell during which scan a particular count was placed into one of the sixteen bins, the time resolution of the system is 24 s. For the remainder of the observation the two detectors were operated in the pulsar mode which scans each data set for 20 s, rather than 32 s as in the first instance, before proceeding to the next set. The field of view of experiment C is collimated to  $3.5^\circ$  FWHM, but as the detector is offset by  $1.75^\circ$  from the satellite's spin axis, the effective field of view is a Gaussian-like curve of  $5.0^\circ$  FWHM centred on the spin axis. In the pulsar mode counts are accumulated in one energy channel stretching from 2 - 7 keV. The effective field of view of experiment F is  $11^\circ$  FWHM, and counts are accumulated in one broad channel stretching from 70 - 280 keV when the experiment is operated in pulsar mode. Absolute timing is known to  $\pm 30$  s. Figure 4.11 shows the fields of view of the two experiments at the time of the observation. The only known burst sources in the field of view of the proportional counter were the rapid burster and MXB 1728-34. The field of view of experiment F encompassed two of the galactic centre burst sources in addition to the two sources mentioned above.

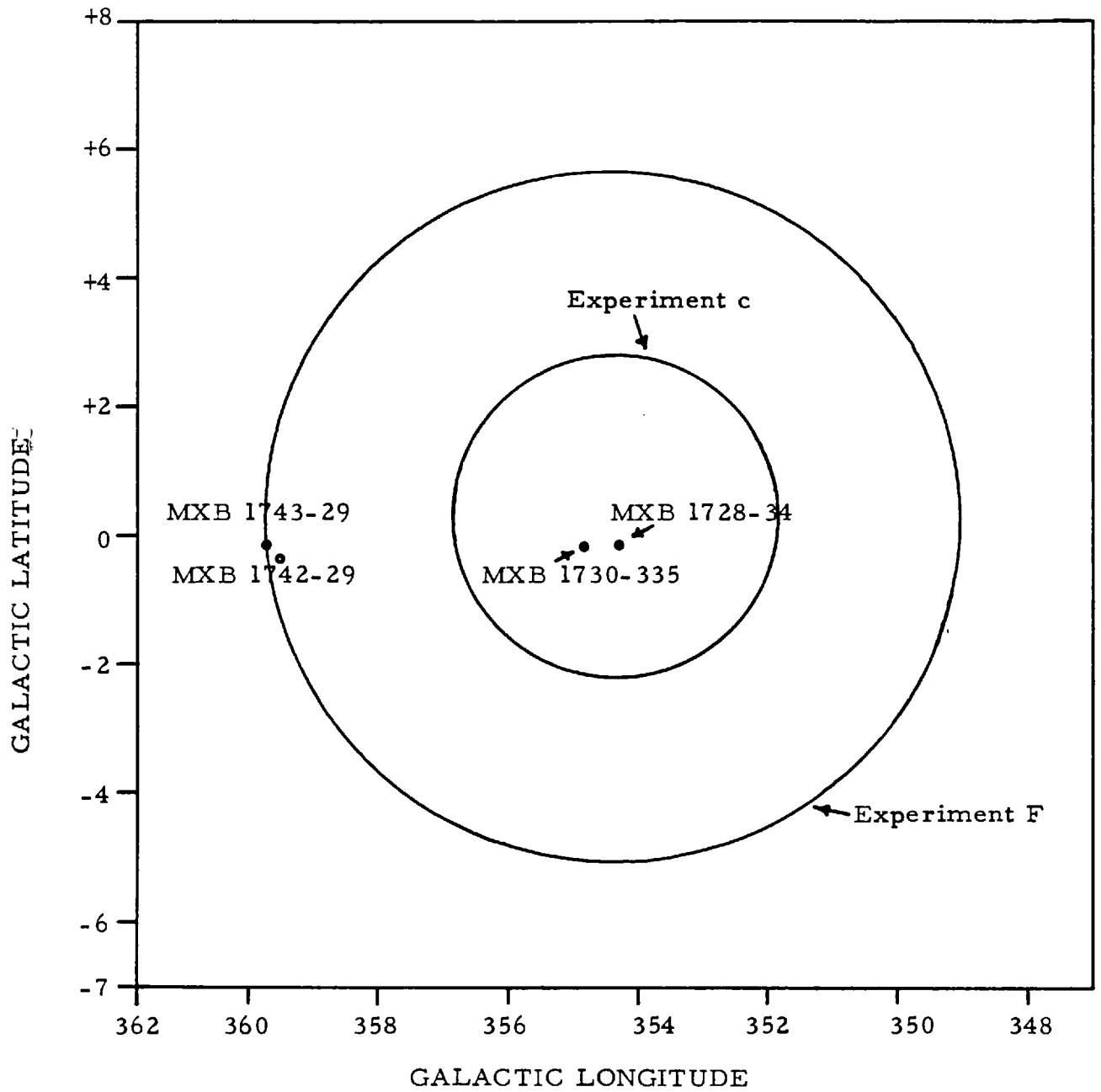


Fig 4. 11: The Fields Of View Of Experiments F And C During The March 8-11 Observation Period.

During the observation the proportional counter detected a large number of small bursts (Mason et al. 1976). Most of these had durations of only a few seconds, but a few lasted for about 20s. Many of the bursts were separated by  $\sim 15 - 20$  s and it was found that the larger the event the longer the time interval to the next burst. This type of behaviour is typical of MXB 1730-335, and the phase of the modulation of the larger bursts confirms that this source was indeed responsible for the bursts.

In addition to the small bursts described above, seven very large events were detected by experiment C. The phase of the modulation of these bursts also confirmed MXB 1730-335 as the source. Experiment F data was searched for prominent increases in the counting rate around the occurrence times of the large "C" bursts. Three such increases were identified, labelled as A, E and F in Table 4.4, together with a smaller ( $3.3\sigma$ ) increase which is associated with burst C. It was found however that the bursts in the 70 - 280 keV channel were not coincident with the soft bursts, the hard emission occurred after the soft burst. Following the discovery of the hard bursts, the whole of the "F" data was searched for statistically significant increases in the counting rate. Two such events were found, labelled as B and D in Table 4.4, but these are not associated with any of the seven large bursts in the "C" data. There are however smaller increases in the proportional counter data which precede events B and D, and which are likely candidates for the associated soft bursts.

Figure 4.12 shows "C" and "F" counting rates during bursts E and F; the counting rates plotted are the counts per time bin,

Table 4.4

		2 → 7 keV Channel		50→190 keV Channel			Delay (s)	
Event	Time at Start of bin (U.T.)	Width (s)	erg/cm <sup>2</sup>	Width (s)	erg/cm <sup>2</sup>	Significance (σ)	Min.	Max.
A	8.7765	8→32	2 10 <sup>-7</sup>	2.5	2.4 10 <sup>-7</sup>	3.7	11.5 1.5	59.5
B	8.9544	4	2.3 10 <sup>-8</sup>	3.5	4.1 10 <sup>-7</sup>	5.4	2.5	26.5
C	9.1656	8→32	1.8 10 <sup>-7</sup>	3.0	2.2 10 <sup>-7</sup>	3.3	0	28
D	9.4869	3	2.5 10 <sup>-8</sup>	6.5	4.3 10 <sup>-7</sup>	6	3.5	27.5
E	10.9419	4.5	5.2 10 <sup>-8</sup>	2.5	2.7 10 <sup>-7</sup>	5	3→4	34.3
F	11.0819	3.2	1.4 10 <sup>-7</sup>	1.6	2.9 10 <sup>-7</sup>	6.5	7.2 3.8	37.2

Table 4.4: Details Of The Six Hard X-Ray Bursts Observed By Experiments F And C On Ariel 5.

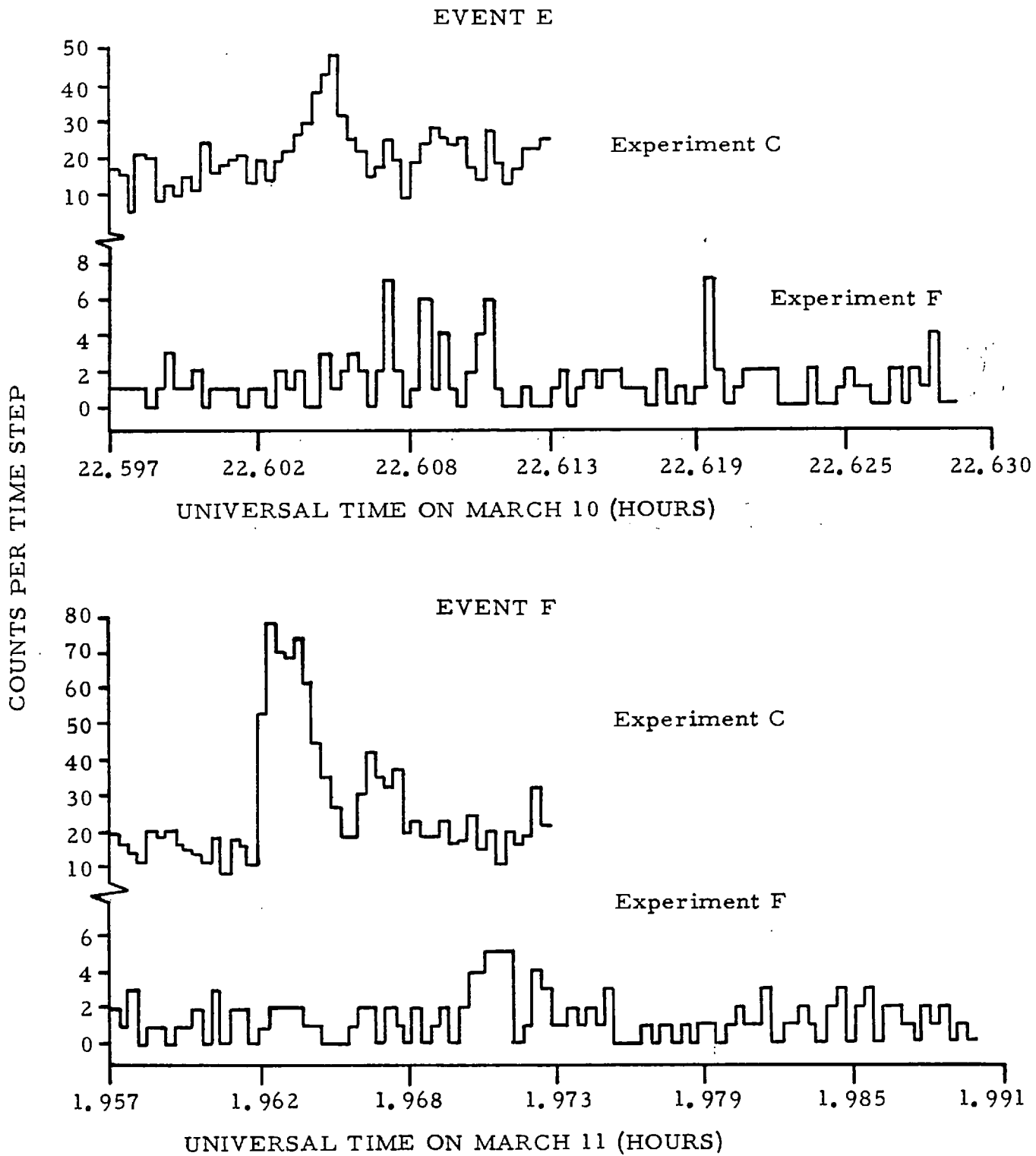


Fig 4.12: Events E And F As Observed By Experiments C And F On Ariel 5. The Time Bins Are 0.5s Wide And Each Bin Is A Superposition Of Four Scans.

i.e. a superposition of four scans. Assuming that the bursts are only present for one scan, the significances of bursts E and F are  $5\sigma$  and  $6.5\sigma$  respectively in the 70 - 280 keV channel. Experiment C data indicate that the duration assumption is a reasonable one. The burst sizes, as given in Table 4.4, were estimated by assuming that all the counts corresponded to 70 keV photons and therefore represent lower limits. Due to the way in which data was accumulated, the delays between "C" and "F" bursts cannot be unambiguously determined, but limits can be set. In the case of events A and F the larger of the two values for the lower limit is the most probable; the smaller figure results from taking secondary peaks in the "C" data as the associated events.

It is possible that the "F" data contains more bursts which are lost in the statistics of the background counting rate. Assuming that these bursts are all associated with proportional counter bursts and that there is a fixed delay between the two burst types, folding techniques can be used to reveal the presence of bursts in the scintillation telescope data. Such a technique was investigated. The "F" and "C" data sets from a particular orbit ( $\sim 40$  minutes of good data), were aligned with each other and the corresponding bin counts multiplied together. The exercise was repeated with the F data set displaced by  $\pm \frac{1}{2}$  s (1 bin) and thereafter at increasing displacements up to a maximum value of  $\pm 8.3$  minutes. Corresponding displaced data set products from different orbits were then multiplied together, and the resulting product examined for significant deviations from the mean product of all the displacements. No such deviation was found over the whole of the  $\pm 8.3$  minute range. This lack

of a spike at a particular displacement indicates that either a unique delay between the two burst types does not exist, or that there are so few hard bursts in the data that statistical fluctuations are masking any spike in the data set product. The lack of data prevents a definite conclusion being drawn.

A similar observation was carried out in April 1977. Experiment C detected several large bursts from the rapid burster which was active at the time. However, there were no statistically significant increases in the scintillation telescope data around the occurrence times of these large bursts. In addition, folding the two data sets together again failed to produce a spike at a particular displacement. This indicates that either MXB 1730-335 was not responsible for the original hard bursts, or that the source does not always produce such bursts (c.f. MXB 1735-44).

These data present another instance of a "normal" x-ray burst source producing hard x-ray bursts of short duration, in this case in near coincidence with soft x-ray bursts. Whether or not these bursts are of a similar nature to the bursts detected by COSMOS-428 and OSO-6 cannot be determined, as neither of these satellites carried detectors capable of detecting soft bursts. The small number of hard x-ray bursts which have been observed to date, indicates that special conditions are required at the burst source before production can be initiated. Any theory which attempts to explain how x-ray bursts are produced must also be capable of explaining the hard x-ray emission described in this section.



#### 4.11. Burst Production Mechanisms

The fact that there are no periodic x-ray burst sources rules out any form of production model which is based on an orbital or rotational mechanism. The most likely explanation is that bursts are produced by the conversion of gravitational potential energy due to mass accretion onto a compact object, as is thought to be the case with many variable x-ray sources. Lewin et al.(1976a) have used the concept of a relaxation oscillator to explain the behaviour of the rapid burster. In their model, matter is accreted onto a magnetised neutron star and the source of the matter is a massive binary companion. Matter falling onto the compact object is held in a plasma reservoir at a distance from the surface which is large compared to its radius, and hence only a small fraction of the gravitational energy is converted at this stage. The matter builds up in the reservoir until the mass exceeds some critical level, whereupon the reservoir springs a leak and allows some fraction, which can vary, of the matter to fall upon the neutron star and produce a burst. Assuming that the mass outflow rate from the massive object is constant, then the interval to the next burst will be directly proportional to the size of the burst just produced. This is known to be the case with MXB 1730-335.

In common with several other burst sources, the rapid burster has been observed in a state where it produces bursts of constant size at regular intervals. In such a situation the accretion rate must stay constant, and the reservoir must allow the same amount of matter to leak away to produce each burst. In the case of sources such as MXB 1837+05 where there is no correlation between burst size and

separation, a plasma reservoir fed by a star with a variable mass outflow rate could be the mechanism whereby bursts are produced.

The majority of burst sources have associated "steady" x-ray sources and at least four burst sources have inactive states. In particular, bursts from NGC 6624 have only been observed when the associated steady source 3U 1820-30 is in a "low" state. Baan (1976) has developed a qualitative theory, based on a relaxation oscillator mechanism, which attempts to explain these observations. In this theory, the steady x-ray luminosity is produced by controlled accretion from a binary companion onto a compact object via a plasma reservoir. Baan suggests that instabilities occur when the plasma temperature drops below a critical value, initiating burst production. Thus the cessation of burst activity when the persistent intensity exceeds a certain value, as with NGC 6624, may be the result of plasma stabilisation due to an increase in the plasma temperature caused by radiative heating.

The majority of the twenty-three known burst sources do not lie in globular clusters, and therefore burst production cannot be attributed to objects which might be found only in such clusters. Such a model was suggested by Grindlay et al. (1976a) who proposed that burst sources were associated with super massive black holes located in the centres of globular clusters. This model was primarily devised to explain the spectral hardening exhibited during decay by bursts from NGC 6624. In this model, the spectral hardening results from the scattering of the initial pulse by a  $10^9$  °K gas cloud, which could only be bound by an object such as a super-massive black hole. However, Canizares (1976) has shown that spectral

hardening does not require the presence of such a cloud. In addition, further observations have shown that spectral hardening is not a unique feature of bursts and the softening during decay, which is exhibited by many bursts, excludes the presence of a surrounding  $10^9$  °K gas cloud. Thus there is no argument for burst production by super-massive black holes. However, at least three burst sources, NGC 6624, NGC 1851, NGC 6441 and quite possibly the rapid burster, are located in globular clusters. These sources represent about 15% of the total number of known burst sources and as only 0.01% of all known stars exist in globular clusters, such an environment must be particularly suitable for burst source production. The same could be said of variable x-ray sources as about 5% of these are known to be located in globular clusters. It has been proposed by Clark (1975) that globular cluster x-ray sources are close binary systems, formed not by the evolution of short lived massive binary systems as in the spiral arms, but by the capture of low mass nuclear-burning field stars by the compact remnants of the original cluster stars. Hills (1976) has shown that capture by exchange collisions between heavy remnants and primordial low mass close binaries, may be sufficiently frequent to produce the observed number of variable x-ray sources located in clusters. It is reasonable to suppose that a certain number of the close binary systems will also be capable of burst activity, by the relaxation oscillator method already referred to. If this is indeed the case it is tempting to explain the steady or rather persistent luminosity of 3U 1820-30, which is associated with NGC 5524, in terms of controlled accretion between a binary pair.

Quenby et al. (1976) have suggested a mechanism to explain

the observation of hard x-ray bursts in near coincidence with soft bursts. It is assumed that the bursts are caused by accretion of material onto a neutron star. Initially, the magnetosphere of the neutron star is penetrated by the enhanced mass of transferring material by some convection process.

This is followed by gravitational fall onto the neutron star's atmosphere where a shock occurs, resulting in energy transfer to the stellar atmosphere, which then emits an x-ray burst by the process of thermal bremsstrahlung. One must suppose that the delayed hard x-ray emission results from a deeper penetration of the stellar atmosphere at later times. Different atmospheric conditions are then required to ensure that the shock energy gets shared amongst fewer particles, which therefore attain a higher temperature and produce a hard x-ray burst. The fact that hard x-ray bursts are not often observed suggests that the conditions described above are infrequently obtained in practice.

## CHAPTER 5

### 5.1. Introduction

#### 5.1.1. Need for correlated hard and soft x-ray measurements with high time resolution

Observations of the variations of source intensity with time have been shown to be the best way of understanding the dynamics of x-ray sources. Up until now, only proportional counter measurements, mainly in the 1-20 keV band, have been able to reveal the fast time variations with fluctuations in the few secs. range exhibited by binary sources, or follow spectral changes with a time scale of ~one hour. However, many important x-ray sources have appreciable emission extending to 200 keV. To fully understand the nature of such sources, requires making measurements with high time resolution of intensity and spectral variations in the 20-200 keV band, as well as in the 1-20 keV band. This chapter describes the development of a large area hard x-ray detector (LAD) designed to fulfil these requirements. The device is designed to be used in conjunction with a proportional counter operating in the 1-20 keV range, and is suitable for use on vehicles such as spacelab.

The detector is particularly suitable for studying x-ray phenomena which vary in a time scale of one hour or less. Such phenomena include, x-ray bursters, x-ray binaries, x-ray pulsars, solar fluxes and the nuclei of active galaxies.

X-ray burst sources provide a strong broadband energy signal, with a complicated time structure extending over several seconds and a variable energy dependence. One key question is the nature of the hard x-ray emission which has been observed from several bursters. To

investigate the phenomenon requires simultaneous observations of the hard ( $>50$  keV) and soft (1-20 keV) x-ray fluxes. To date, time variations studies of x-ray bursts have only been performed down to 0.4 s. Faster time resolution can probe such questions as the relation of the event rise time to the typical gravitational fall time of material from the magnetosphere of a neutron star onto the star's atmosphere. This time, typically  $\sim 0.2$  s, may set a limit to the scale of the source variability on the neutron star model. The smaller dimensions of the black hole Schwarzschild radius, may allow faster variations if these objects are indeed the source.

Several x-ray sources exhibit large and irregular intensity fluctuations in time scales of minutes, seconds and milli-sec in the case of CYGX-1. It has been suggested that rapid fluctuations (e.g. Shakura et al. 1973) are a distinguishing feature of black hole x-ray sources, and indeed CYGX-1 and VELAX-1 are black holes candidates on mass grounds. Fast time resolution (1-10 ms) of intensity variations and discovering how these variations are related to energy (1-200 keV), is necessary to understand the emission mechanism of such sources. Correlated hard and soft x-ray observations have already been useful in establishing the nature of the two steady states of CYGX-1, (Coe, et al. 1976).

Nine well established binary x-ray pulsars are known: SMC X-1, HER X-1, CEN X-3, A0535+26, GX1+4, 3U0900-40, A1118-61, GX301-2 and XPER. Most have relatively hard spectra and as a class they produce a variety of pulse shapes as a function of pulsar period. Some, but not exhaustive, studies of the variation of pulse shape with energy have been carried out (e.g. A053+26, Ricker et al. 1976b). It is generally believed that most of the emission comes from accretion

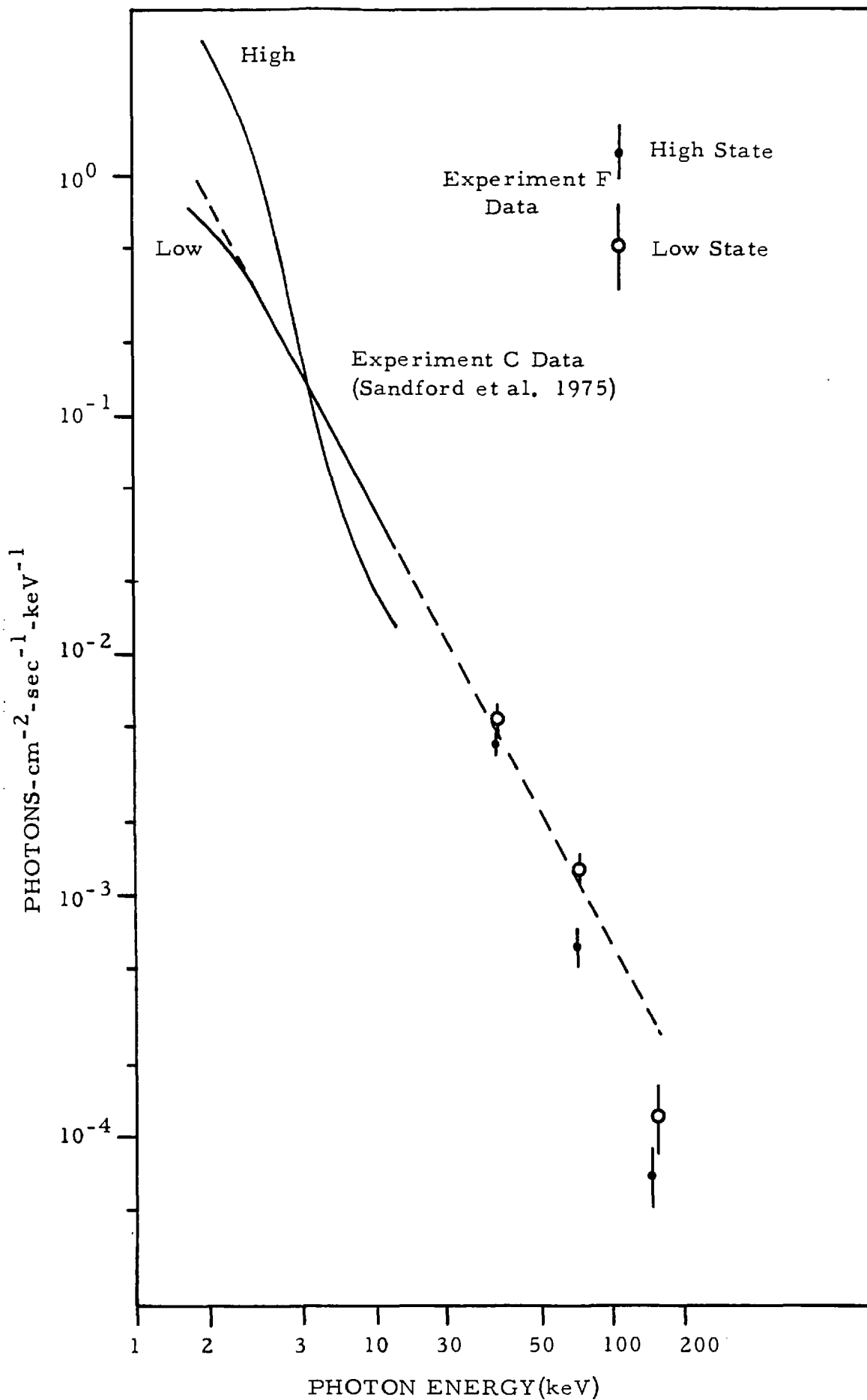


Fig 5. 1: The Two States Of CYG X-1 As Observed By Experiments F And C On Ariel V.

funnels deep in the pulsar magnetosphere but no details are settled. For example cyclotron radiation could dominate. Alternatively heating by Comptonisation in the neutron star atmosphere followed by preferential emission along directions where the Thomson scattering is least, due to the strong magnetic field, is another model. Further high resolution time variation studies as a function of energy (1-200 keV), should help distinguish between the various possibilities.

#### 5.1.2. Description of the detector.

The detector is designed to be built in modular form, and have a total effective area up to one square meter. Each module is sensitive to x-rays with energies in the range 20-200 keV and can operate with a time resolution down to 1 ms. The module consists of a NaI(Tl) crystal measuring 20 x 10 cms (200 cm<sup>2</sup> effective area) by 2 mms thick. The crystal is viewed by two 3" photomultipliers connected to the scintillator by means of a perspex "light pipe". The outputs of the two tubes are summed, amplified and fed into a sixty-four channel pulse height analyser which only accepts x-rays with energies between 20 and 200 keV. The large number of PHA channels ensures that instrument resolution, rather than data handling, is the factor which limits the energy resolution. The crystal is sealed on top by a 0.05 mm Al window, and collimated with a passive tantalum honeycomb collimator which defines an approximately triangular field of view with a FWHM of 2<sup>0</sup>.

Methods of reducing the counting rate produced by the diffuse background, charged particles and thermal neutrons are currently being investigated. These include:



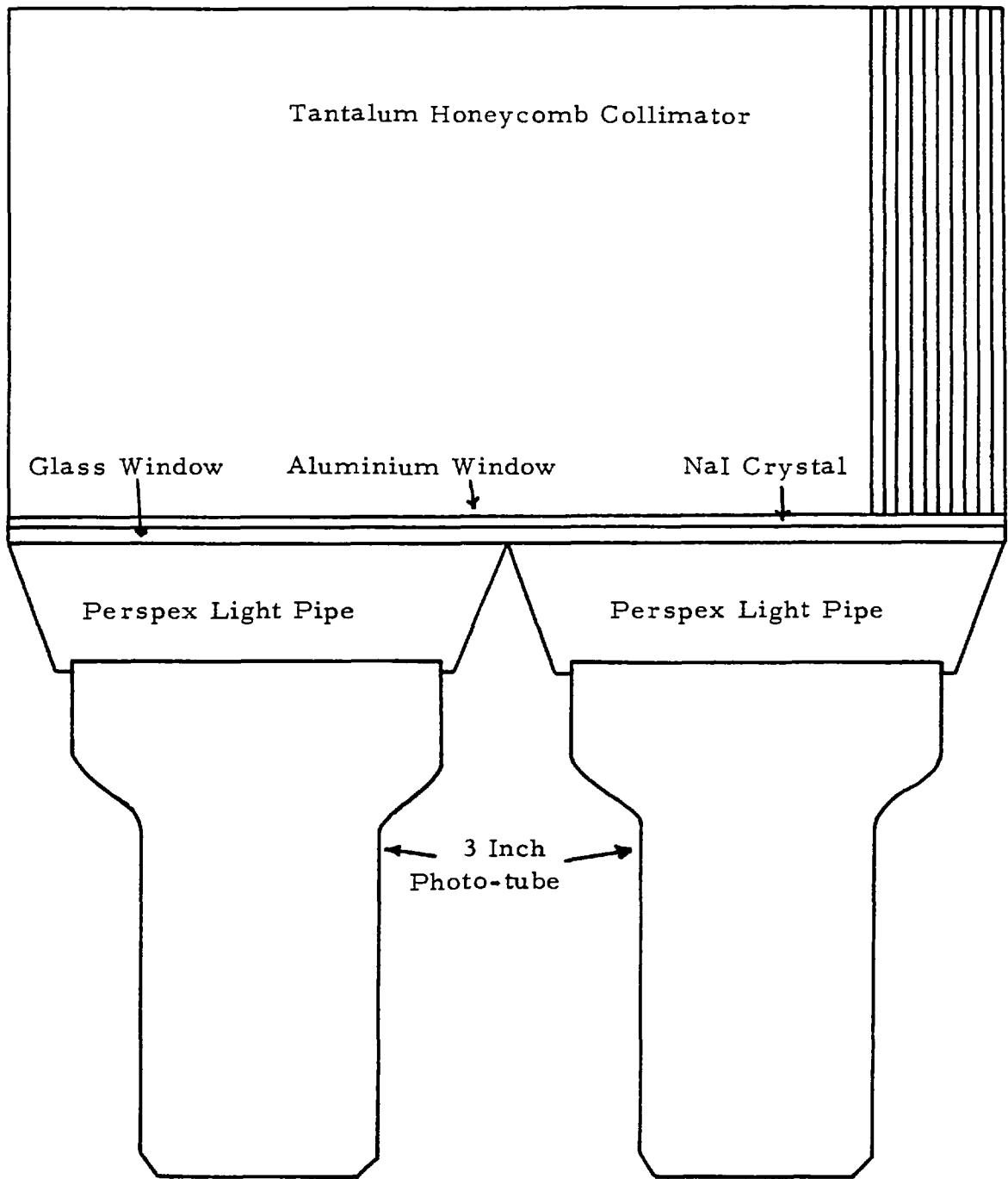


Fig 5.2: Layout Of A Detector Module

(i) A phoswich technique to remove upward moving photons and high energy x-rays/gamma rays which leak through the collimator. This involves coupling a 13 mm thick CsI(Na) crystal between the light pipe and the NaI crystal, and using a pulse shape discriminator to distinguish between events occurring in the two different scintillators. Events which occur in the shield alone are ignored as are events which occur simultaneously in both detectors. This will remove a large part of the background in the detector which results from Compton scattering of high energy photons in the NaI crystal, as a second Compton interaction in the CsI is highly probable.

(ii) Passive screening around the collimator consisting of lead, a graded shield of Sn with Cn on the inside to reduce the leakage of high energy photons, and Cd to absorb thermal neutrons.

(iii) A plastic scintillator anti-coincidence shield around the whole module (except the 3" phototubes) including the collimator aperture, to eliminate any prompt background produced by charged particles entering the collimator and other material surrounding the detector.

The proportional counter, which is complementary to the hard x-ray detector, has been developed by the Mullard Space Science Laboratory. This device is also designed to be built in modular form and have a total area equal to the NaI detector. The counter is sensitive to x-rays in the range 1.5-20 keV and is collimated to  $2^{\circ}$  FWHM.

## 5.2. Scintillator Elements and Light Collection

### 5.2.1. Detectors used in x-ray astronomy

Several types of detectors are used to observe x-rays in the 20-200 keV band of the electromagnetic spectrum.

(i) Proportional counters. These are normally used to detect x-rays with energies between 1 and 30 keV. The lower limit of such devices is set by window absorption and the upper limit by the transparency of the gas. Figure 5.3 shows the energy dependence of the detection efficiency of xenon, and it is interesting to note that a high efficiency (>50%) is theoretically attainable at 150 keV if a pressure of ten atmosphere is used. Such a device would certainly be very useful for spectral determinations in the 20-200 keV range, having a resolution of  $\sim 6\%$  at 50 keV (Adams 1971) compared to the 20% resolution typical of crystal scintillators at this energy (Morfill 1971). (The figures quoted refer to the value of  $\frac{\Delta E}{E}$  where  $\Delta E$  is the FWHM at energy E.) However, the high xenon pressure required would mean that only very small detectors could be built, and the window thickness necessary would result in a very low detection efficiency at 20 keV ( $\sim 0.2$ ).

(ii) Plastic scintillators. The use of plastic scintillators in x-ray astronomy has several limitations.

(a) Above 30 keV, the dominant interaction between x-rays and plastic scintillators is Compton scattering, which means that the energy of the incoming photons cannot be determined.

(b) Due to their small effective atomic number (see Table 5.1) plastic scintillators have a low stopping power. For example, at 100 keV 0.17 cms of CsI is equivalent

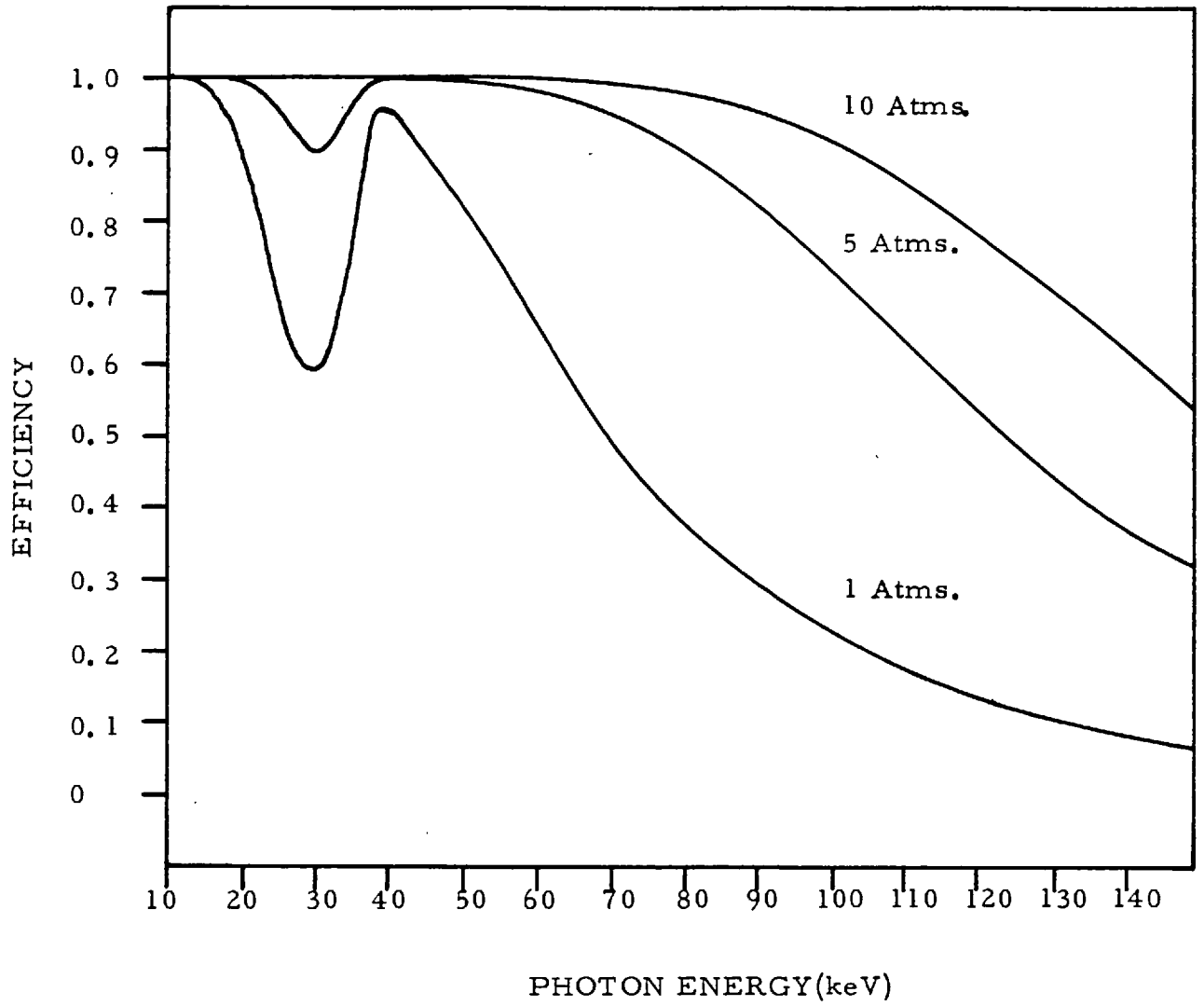


Fig 5. 3: Photoelectric Efficiency Of 25 cms. Of Xenon Gas At Various Pressures.

to 10 cms of Ne102A. This results in plastic scintillator detectors being substantially heavier than equivalent crystal detectors.

- (c) Plastic scintillators have a low light output. For example, Ne102A has an output which is only 64% that of anthracene compared to the ~200% output of NaI and CsI.

As a result of these limitations scintillators such as Ne102A are not used in applications where the determination of spectra is important. They are useful however, as large area photon counters such as the gamma-burst detectors described in earlier chapters.

(iii) Crystal scintillators. The crystals normally used in x-ray astronomy are the alkyl halides CsI and NaI. Both of these have some intrinsic scintillation efficiency but they are usually doped to give a high light output. Table 5.1 compares the various doped alkyl halides in common use and Ne102A, a typical plastic scintillator.

Up to 200 keV the photoelectric effect is the dominant process whereby x-rays interact with crystal scintillators. This means that such devices are ideally suited for determining the energy of incoming photons, because each interacting photon deposits all its energy in the crystal.

Of the three types of crystal scintillator listed in Table 5.1, NaI(Tl) has the greatest light output and therefore the best potential energy resolution. The larger  $Z_{eff}$  of CsI means that it is more efficient at stopping x-rays, but as Figure 5.4 shows, the difference between the cross-sections of NaI and CsI is small. The main

Table 5.1

	<u>NaI(Tl)</u>	<u>CsI(Na)</u>	<u>CsI(Tl)</u>	<u>Ne102A</u>
Density ( grms-cm <sup>-3</sup> )	3.67	4.5	4.5	1
Effective Atomic Number (See Definition Below)	53(P) 54(C)	62(P) 76(C)	62(P) 76(C)	6.0(P) 6.1(C)
Scintillation Light Output (With Respect To Anthracene)	230%	170%	85%	67%
Decay Time Of Pulse (Microseconds)	0.23	0.65	1.1	0.0024
Peak Wavelength For Scintillation (Angstroms)	4130	4200	5800	4250

Definition:

$$\text{Effective Atomic Number} = \sqrt[n]{( a_1 Z_1^n + a_2 Z_2^n + a_3 Z_3^n \dots + a_N Z_N^n )}$$

$a_1, a_2 \dots a_N$  are constants depending on the number ratio of the N constituent atoms.

$n = 5$  for photoelectric interactions (denoted by P in the above table)

$n = 2$  for Compton interactions (denoted by C)

Table 5.1: Comparison Of The Properties Of Various Scintillators.

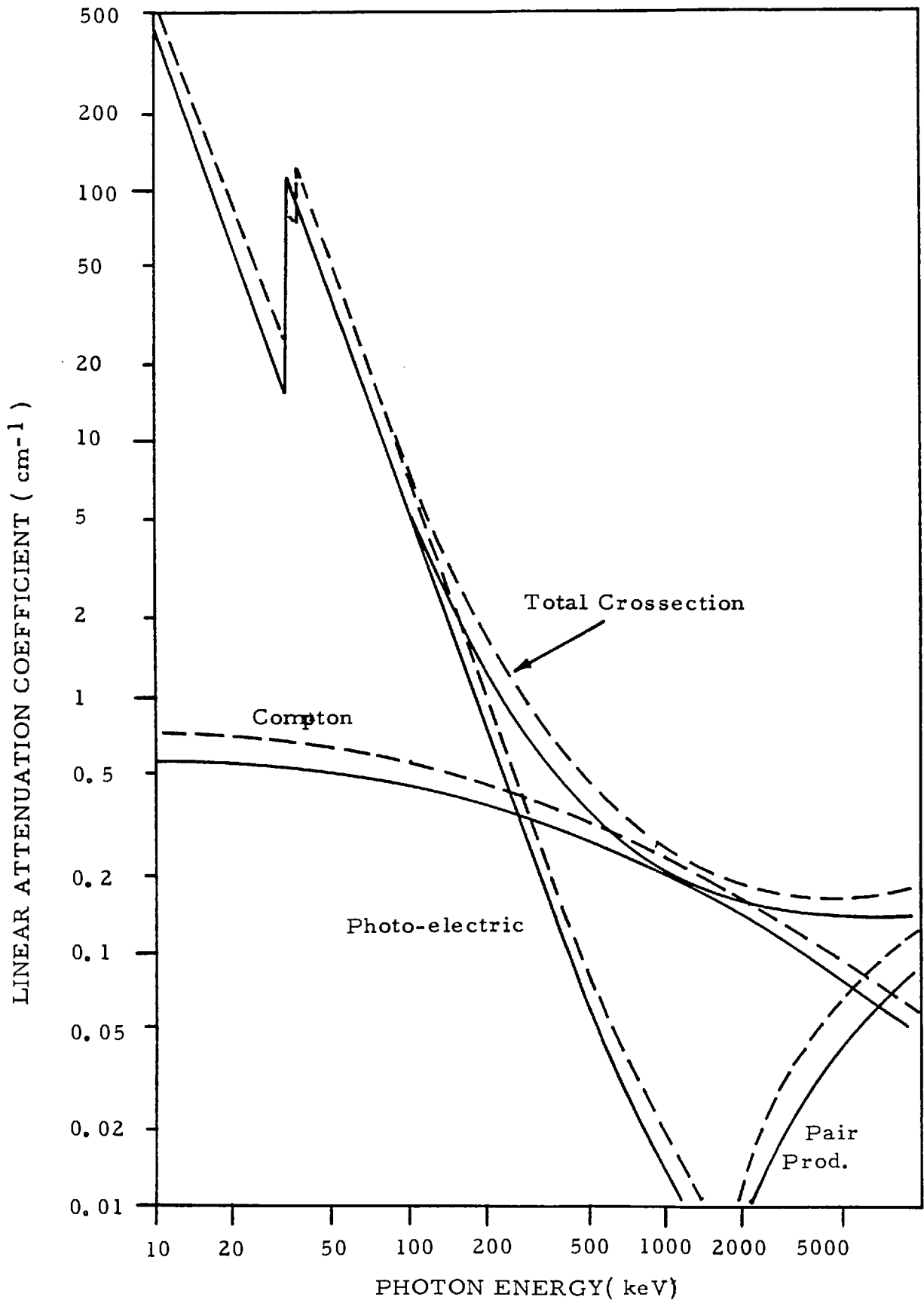


Fig 5.4: X-Ray Cross-section Curves For CsI And NaI.

disadvantage with using NaI is that the crystal is hygroscopic, and if it is exposed to water forms NaOH which does not scintillate. Thus sodium iodide crystals must be kept in sealed units.

### 5.2.2. Scintillator Element

The main detector element consists of a NaI(Tl) crystal 2 mms thick. Although there is little difference between NaI(Tl) and CsI(Na), the higher light output of the former means it has the best potential energy resolution, and it was therefore considered to be the best crystal to use.

A critical limiting factor in previous x-ray experiments has been the high level of background radiation. The two main components of this are:

(i) Partial energy losses in the central detector elements of higher energy photons, from the spacecraft and the diffuse sky flux, which leak through active or passive shields. The LAD will be subjected to the latter over a large fraction of the front  $2\pi$ , and to gamma-ray photons from proton induced electromagnetic cascades over the remaining solid angle. Results from Apollo missions indicate that if the detector is in a geomagnetically shielded environment, the two effects will have approximately the same magnitude.

(ii) Induced radioactivity in the crystal. This component results from the interaction of cosmic ray protons and trapped protons with the detector elements, and also from the interactions of secondary neutrons produced in the spacecraft by these particles.



Both of these effects are proportional to the volume of the central detector element. To maximise the sensitivity the thickness of the NaI crystal was chosen as follows:

Let  $N_B(E)$  = Background count rate (cts  $\text{cm}^{-2} \text{s}^{-1} \text{keV}^{-1}$ )

$N_S(E)$  = Source flux at detector (photons  $\text{cm}^{-2} \text{s}^{-1} \text{keV}^{-1}$ )

$\epsilon(E)$  = Detection efficiency

$A$  = Area of detector ( $\text{cm}^2$ )

$t$  = Time available for observation (s)

It is proposed to use a collimator rocking technique to determine the source strength whereby the source and background are viewed equally i.e. for  $\frac{t}{2}$  s each. This produces the minimum statistical error for a total observing time of  $t$  secs. (Carpenter 1975).

Counts from source + background ( $E - E + dE$ ) =  $N_S \epsilon A \frac{t}{2} dE + N_B A \frac{t}{2} dE$

Background counts =  $N_B A \frac{t}{2} dE$

Therefore measured source signal =  $\epsilon N_S A \frac{t}{2} \pm \sqrt{N_B A t} dE$  (assuming  $N_S \ll N_B$ )

Thus inferred source strength =  $N_S dE \pm \frac{2\sqrt{N_B} dE}{\epsilon \sqrt{A t}}$  cts  $\text{cm}^{-2} \text{s}^{-1}$   
( $E - E + dE$ )

And the smallest  $3\sigma$  change detectable in time  $t$

$$dN_S dE = \frac{6\sqrt{N_B} dE}{\epsilon \sqrt{A t}}$$

Assuming that all the interacting photons are seen

$$\epsilon = 1 - e^{-\mu x} \quad \mu(\epsilon) = \text{Linear attenuation coefficient (cm}^{-1}\text{)}$$

$x$  = thickness of scintillator

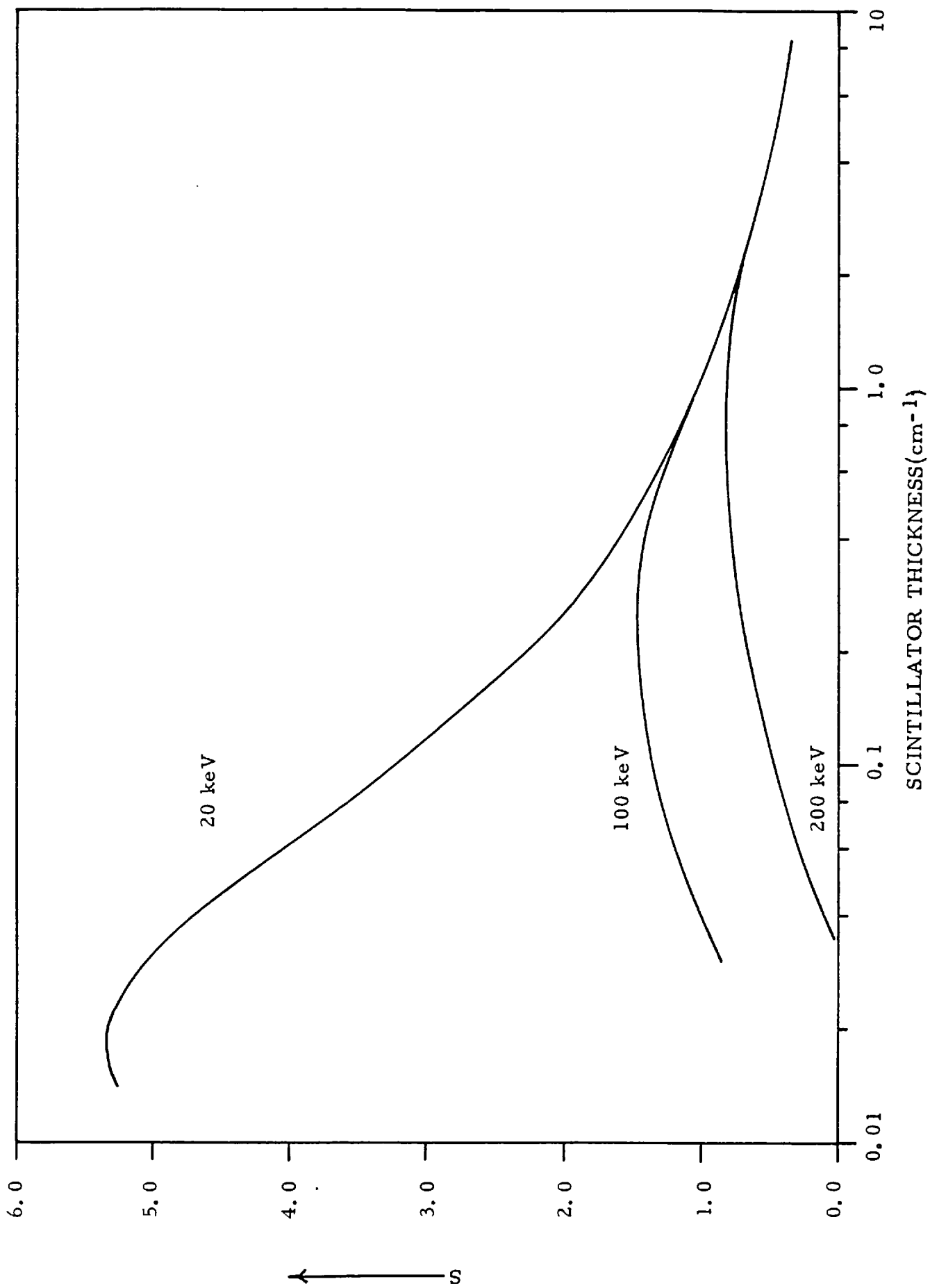


Fig 5. 5: Variation Of The Sensitivity Function S With Scintillator Thickness.

If the background rate is dominated by the two mechanisms already mentioned namely leakage and spallation,

$$N_B(E) \propto \underbrace{xN'_B(E)}$$

approx constant 30-200 keV

$$\therefore dN_S \propto \frac{\sqrt{x}}{1 - e^{-\mu x}}$$

and the sensitivity which is  $\propto \frac{1}{dN_S}$  is given by  $S(E) \propto \frac{1 - e^{-\mu x}}{\sqrt{x}}$

Figure 5.5 shows how S varies with the thickness of the scintillator and with the energy of the incoming photons, E. At 20 keV the sensitivity of the detector is critically dependent upon the thickness of the scintillator, whereas for energies >100 keV the variation in sensitivity with thickness is much less marked. It was decided to make the thickness of the crystal 2 mm to maximise the sensitivity at 100 keV. With such a thickness the sensitivity at 200 keV is within 15% of the maximum possible value, which would be obtained with an 8 mm crystal.

### 5.2.3. Energy Resolution and Light Collection

A photon interacting with a crystal scintillator via the photo-electric effect deposits all its energy in the crystal. Figure 5.6 lists the sequence of events leading up to the detection of the photon.

Figure 5.6 Photon Detection

- (i) Energy  $E$  is deposited in crystal
- (ii) Detector effects:
  - (i) Light is produced in scintillator,  $n$  photons per scintillation.
  - (ii) A certain fraction of the light is collected at the photo-cathode.
- (iii) Photomultiplier effects:
  - (iii) Production of electrons at the photo-cathode.
  - (iv) Collection at the first dynode.
  - (v) Multiplication down the dynode chain.
  - (vi) Conversion of the charge to an electrical pulse of size  $V$ .

A monoenergetic input does not produce a unique value of  $V$ . Intrinsically the scintillation photons would be represented by a Gaussian distribution with a FWHM  $\epsilon(E) \propto n^{\frac{1}{2}} \propto E^{\frac{1}{2}}$ . However, other effects arise from:

(i) Scintillation Process

- (a) Intrinsic line widths
- (b) Inhomogeneity of the crystal, e.g. doping
- (c) Non-proportionality of the scintillation process, especially at low energies where  $n$  is small (see Figure 5.7)
- (d) If the energy  $E$  is deposited by a multiple interaction (e.g. Compton then photoelectric effect), the number of scintillation photons is not the same as in a single interaction because of (b) and (c).

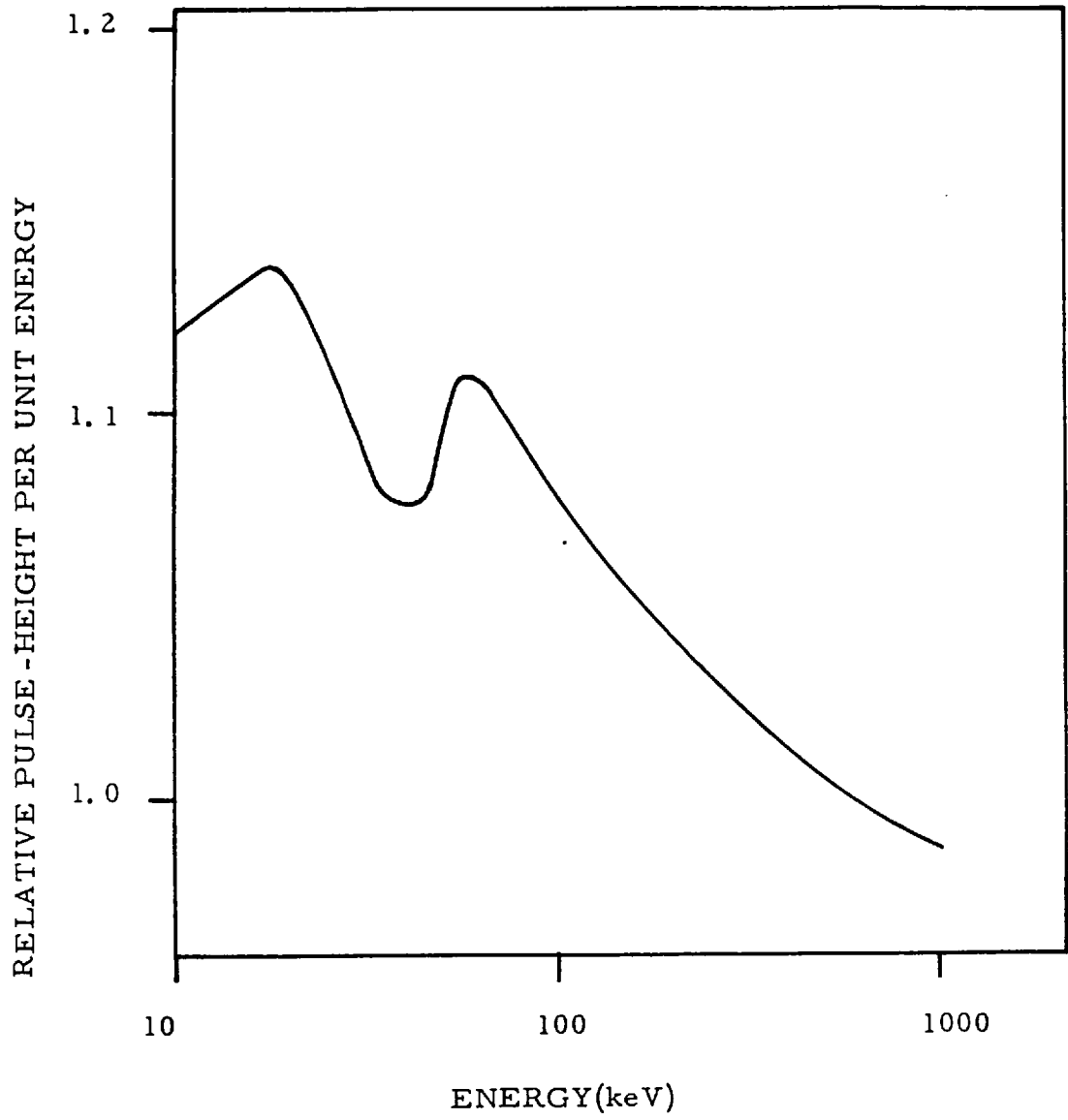


Fig 5.7: Proportionality Of The Scintillation Process.

(ii) Light Collection Process

- (a) Non-uniform geometry of light collection
- (b) Impurities in the crystal hinder uniform light collection

(iii) Photomultiplier Effects

Once collected at the photo-cathode some photons eject photo-electrons. The quantum efficiency of this process is only ~20% and this probably causes the largest statistical variation. In detectors where the number of photo-electrons per interaction is small (e.g. as in the case of the burst detectors already described), statistical variations introduced at the photo-cathode dominate all other variations.

Most of the photoelectrons are collected at the first dynode and multiplication then proceeds down the dynode chain.

The distribution of output pulses resulting from a mono-energetic input  $E$  is unique to the detector and must be determined empirically. The distribution is usually a Gaussian like curve whose FWHM determines the energy resolution possible with the detector at energy  $E$ . In the case of Experiment F on Ariel V

$$\Delta E = k E^{0.637} \quad (\text{Morfill 1971})$$

$\Delta E$  is the FWHM of the output in terms of energy. The distribution is obviously wider than the intrinsic spread  $\epsilon \propto E^{\frac{1}{2}}$ .

Non-uniformities in the light collection have the effect of increasing the value of  $k$ , hence causing an energy independent broadening. A low collection efficiency results in a large broadening due to the statistics of electron emission at the photo-cathode.

Several methods of collecting light from the NaI(Tl) crystal

were investigated, with the object of maximising the average collection efficiency but not at the expense of uniformity. All the experiments were conducted with a piece of perspex measuring 20x10x0.5 cms thick. This thickness of perspex was used because the NaI(Tl) crystal has a 3 mm glass window optically coupled to the lower surface, which serves to protect the scintillator from the effects of moisture.

(a) Light diffusion chambers

Such chambers are best suited for collecting light from scintillators with a circular geometry. Such a geometry was impossible for the LAD module because of space filling considerations. However, two diffusion chambers were investigated, one 6" high, the other 3" high. Each chamber was constructed from Darvic and painted on the inside with the special white paint developed at Imperial College (reflectance  $\sim 0.97$ ). A 3" photomultiplier was used to collect the light in each case. The light collection efficiency was measured using a flashing photo-diode whose light output was known. Holes to accept the diode were drilled in the perspex block on the face away from the diffusion chamber and filled with Ne585 optical coupling grease. The holes formed a two dimensional grid and were separated in both the x and y directions by 2 cms. All the exposed perspex surfaces were coated with silver foil with the shiny side to the perspex. It has already been demonstrated that using such a reflector is the best way of keeping light in a scintillator.

The collection efficiency from each diode location was found by feeding the photo-tube output into a PHA, and displaying it on the screen. The number of photoelectrons produced per diode flash was then calculated from the formula

$$N_{p.e.} = 5.56 \left( \frac{\text{Max Posn.}}{\text{FWHM}} \right)^2$$

Fig 5.8 : Light Collection Efficiency Produced By 6 Inch  
Diffusion Chamber.

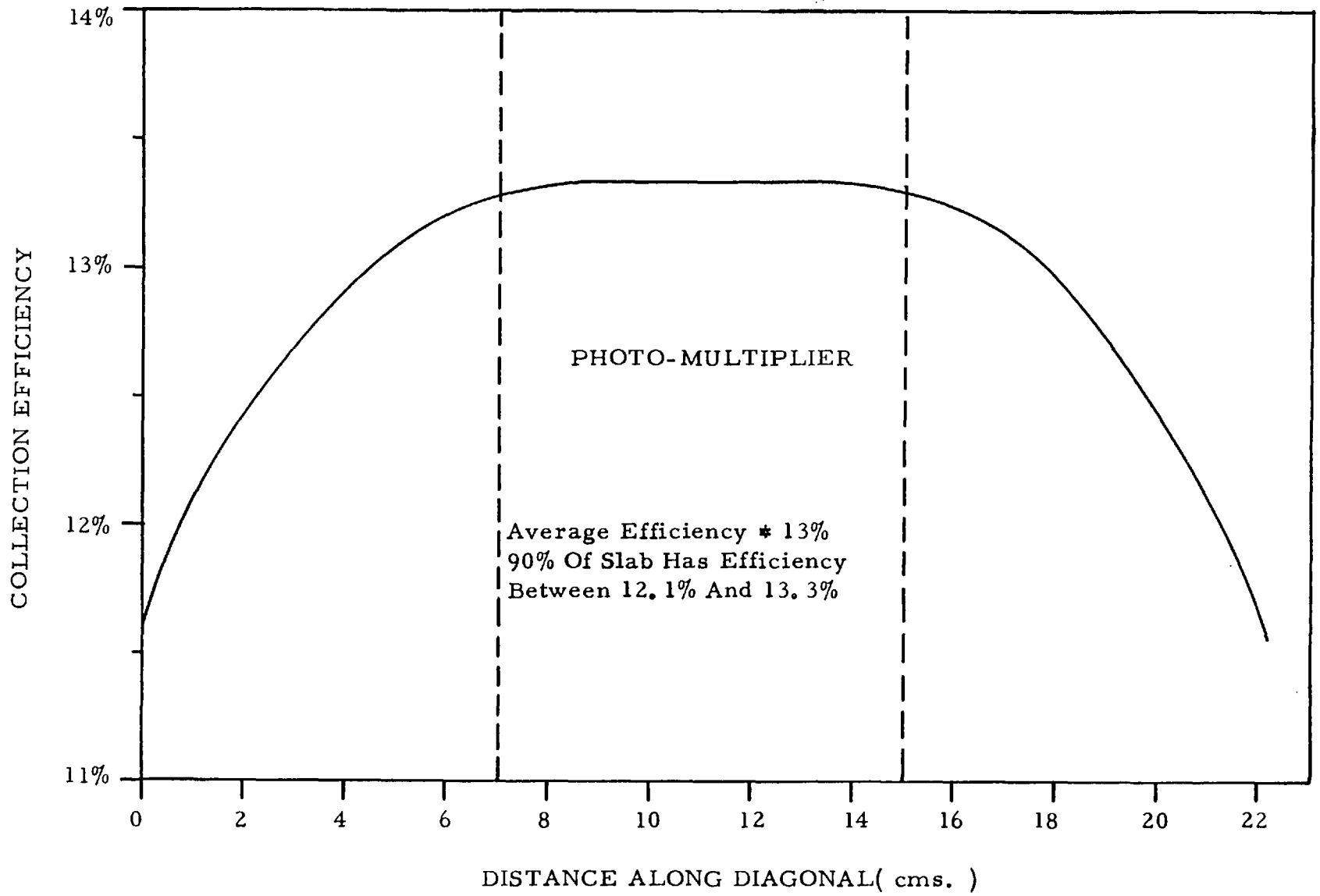




Fig 5. 9: Light Collection Efficiency Produced By 3 Inch Diffusion Chamber.

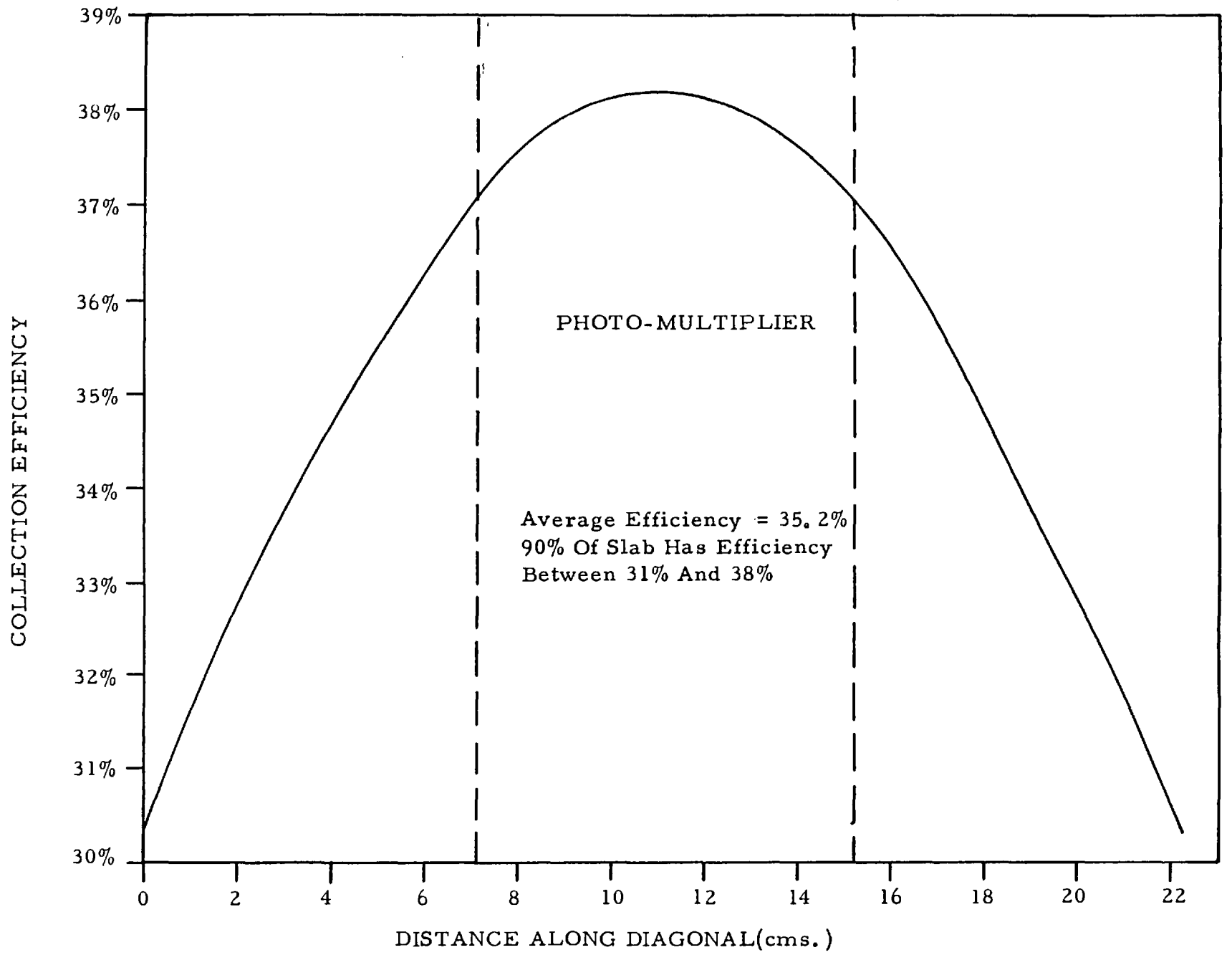
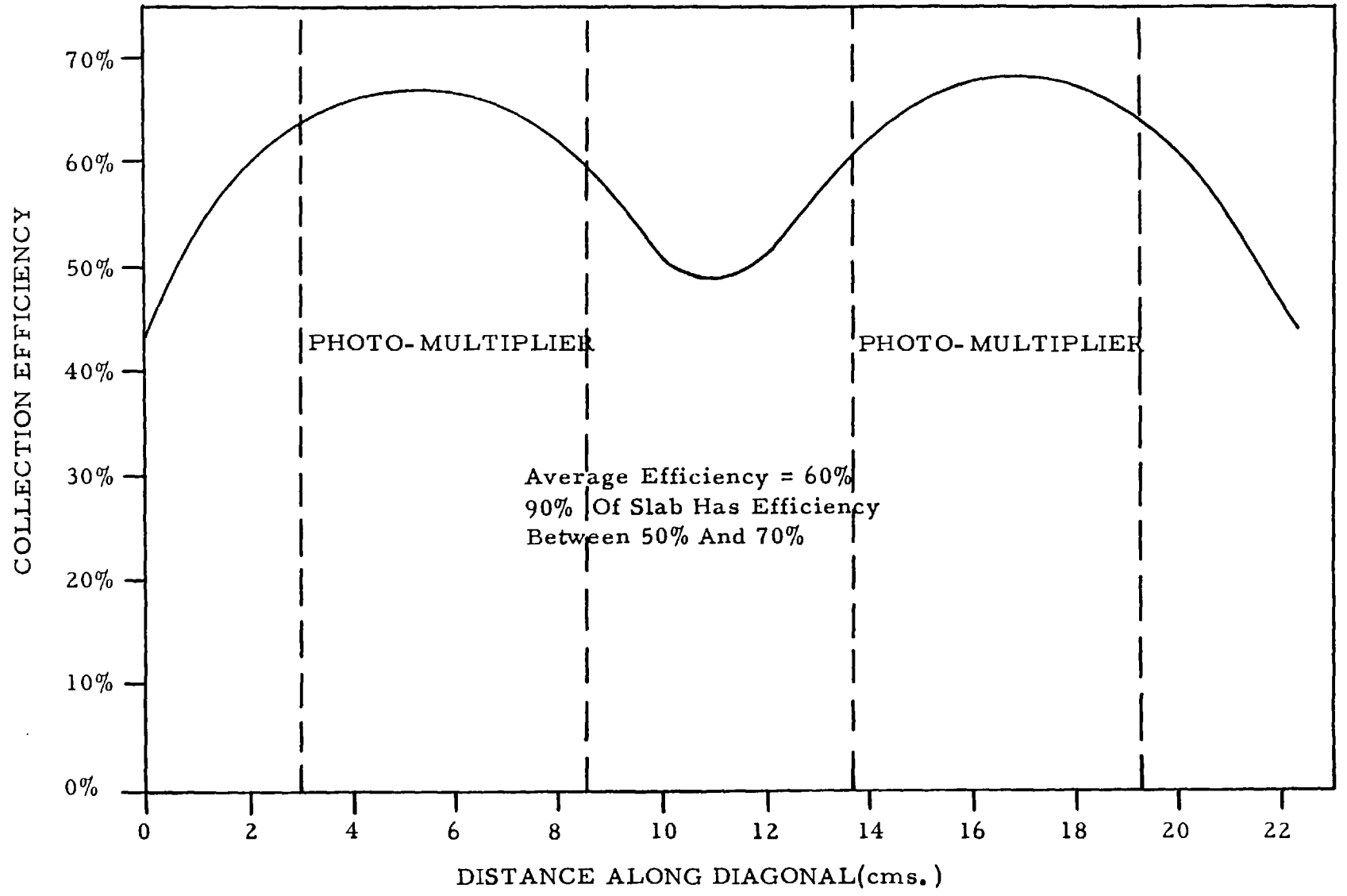


Fig 5; 10: Light Collection Efficiency With Two 3 Inch Photomultipliers Coupled Directly To The Slab.



knowing the light output of the diode, and hence the number of photoelectrons corresponding to a collection efficiency of 100%, enabled the actual efficiency from each grid point to be found. The results are shown in Figures 5.8 and 5.9. It is evident that reducing the height of the guide resulted in an increase in the average collection efficiency together with a decrease in the uniformity of collection.

(b) Direct Coupling

Two 3" photomultipliers were coupled directly onto the surface of the perspex using silicon fluid as the coupling agent. All the exposed surfaces were coated with silver foil. The two tubes were balanced and their outputs were summed. The resulting signal was fed into the PHA. The collection efficiency was measured using the technique described above and the results are shown in Figure 5.10. This technique produced a large average efficiency but large non-uniformities also.

(c) Perspex Light Guides

Two distinct techniques were investigated

(i) Looking at the slab edge on. A  $1\frac{1}{2}$  inch diameter photomultiplier was connected to each short edge of the perspex block via a solid perspex light guide, as shown in Figure 5.11. The tubes were balanced, their outputs summed and the resulting signal was fed into the PHA. This set-up resulted in the most uniform collection system tested, but the average collection efficiency was low, equal to that obtained using the large diffusion chamber. A proper "light pipe" collection system would improve the efficiency somewhat possibly up to a factor of two. The

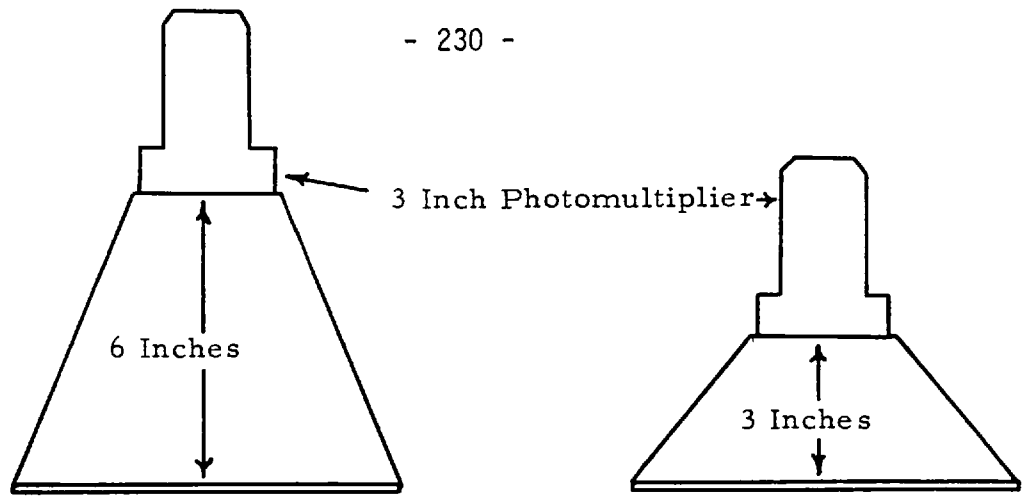


Fig 5. 11(a): Light Diffusion Chambers

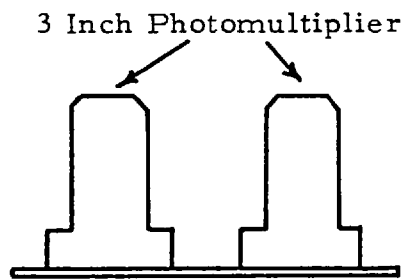


Fig 5. 11(b): Direct Coupling

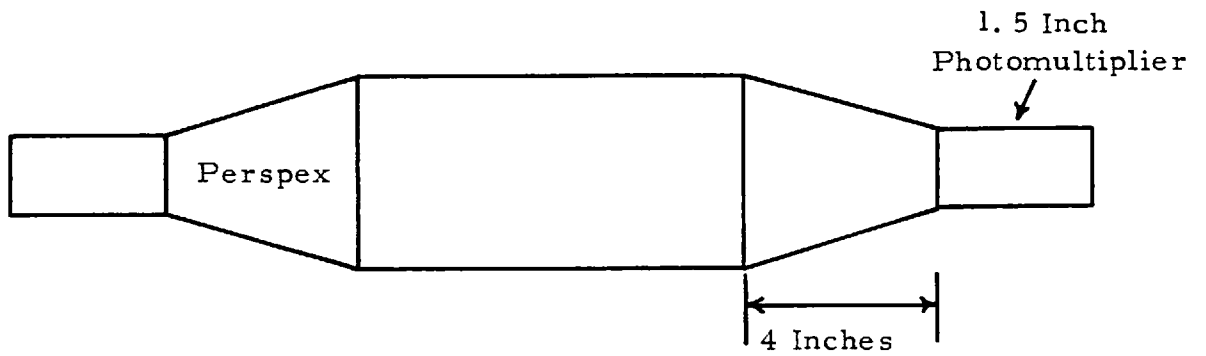


Fig 5. 11(c): Perspex Light Pipes

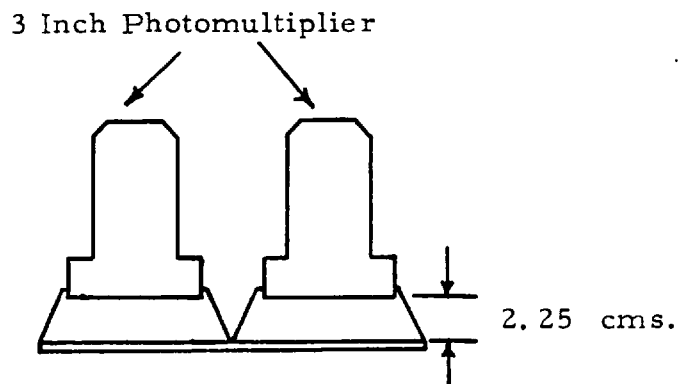


Fig 5. 11: Light Collection Techniques.

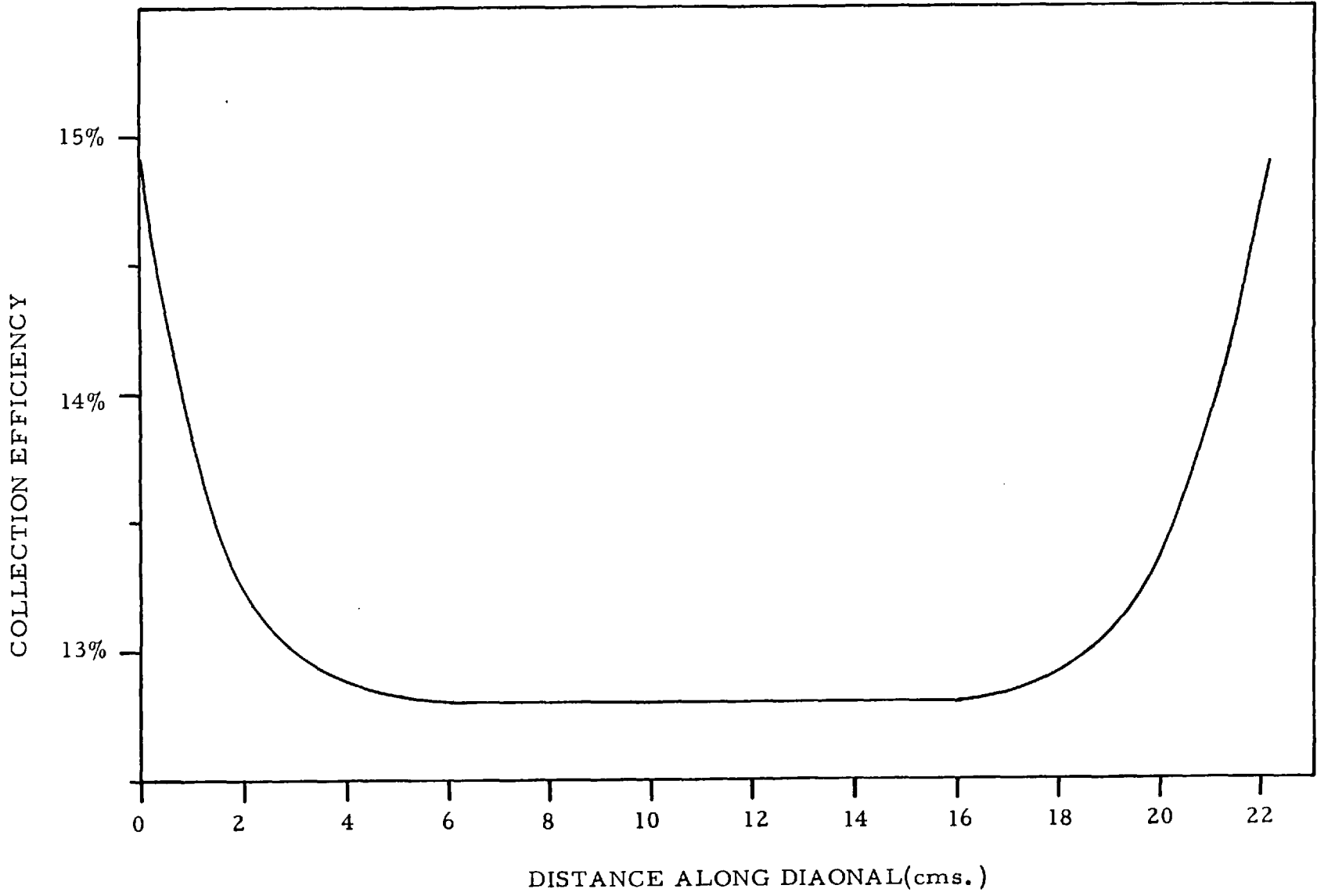
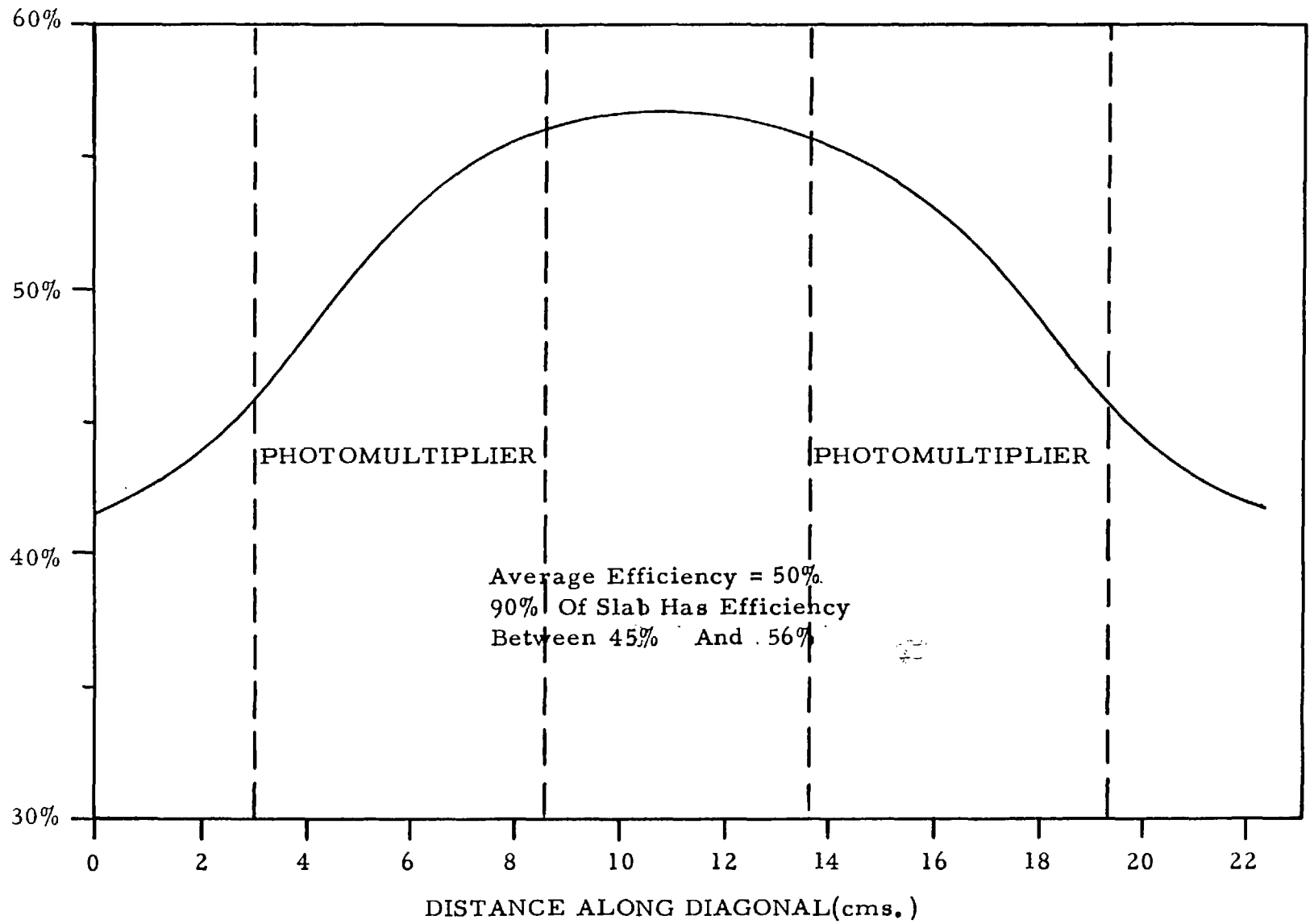


Fig 5. 12: Collection Efficiency Produced By Looking At  
The Slab Edge On.

Fig 5. 13: Collection Efficiency Using Solid Perspex Light Guide.



limiting factor in such a case is the large number of reflections a photon has to undergo before reaching a photo-tube, the number being large for a thin crystal. However, a light pipe would be very cumbersome and would increase the size of the module considerably.

(ii) Looking at the slab face on. Two 3" photomultipliers were coupled to the lower face of the slab using solid perspex light guides. The tube outputs were summed. The results are shown in Figure 5.13. This technique resulted in a lower (10%) collection efficiency than that obtained in case (b). However, the geometry of collection was more uniform and in particular there was no drop in the collection efficiency in the centre of the slab.

Table 5.2 Summary of light collection results

Method	Average efficiency ( $C_e$ )	Spread ( $\Delta C_e$ )	$\frac{\Delta C_e}{C_e}$
1. 6" Diffusion Box	13.0%	12.1-13.3%	0.09
2. 3" Diffusion Box	35.2%	31.0-38.0%	0.20
3. Direct Coupling	60.0%	50.0-70.0%	0.33
4. Looking edge on	13.1%	12.8-13.7%	0.07
5. Looking face on	50.0%	45.0-56.0%	0.22

In view of the need for a system giving a high and uniform collection efficiency it was decided to adopt method 5 whereby the photo-tubes are connected to the NaI(Tl) surface via a solid perspex

light-guide. This system has a collection efficiency which is only 10% less than that obtained with the direct coupling method, although the geometry of collection is much more uniform than in the latter case. The uniformity is almost equal to that obtained with the 3" diffusion box, although the average efficiency is a factor of 1.4 greater. The physical arrangement is compact, much more so than with the cumbersome arrangements needed to look edge on at the crystal and which give low efficiencies in any case. The system therefore represents a good compromise between the need for a high collection efficiency, and a uniform geometry of collection.



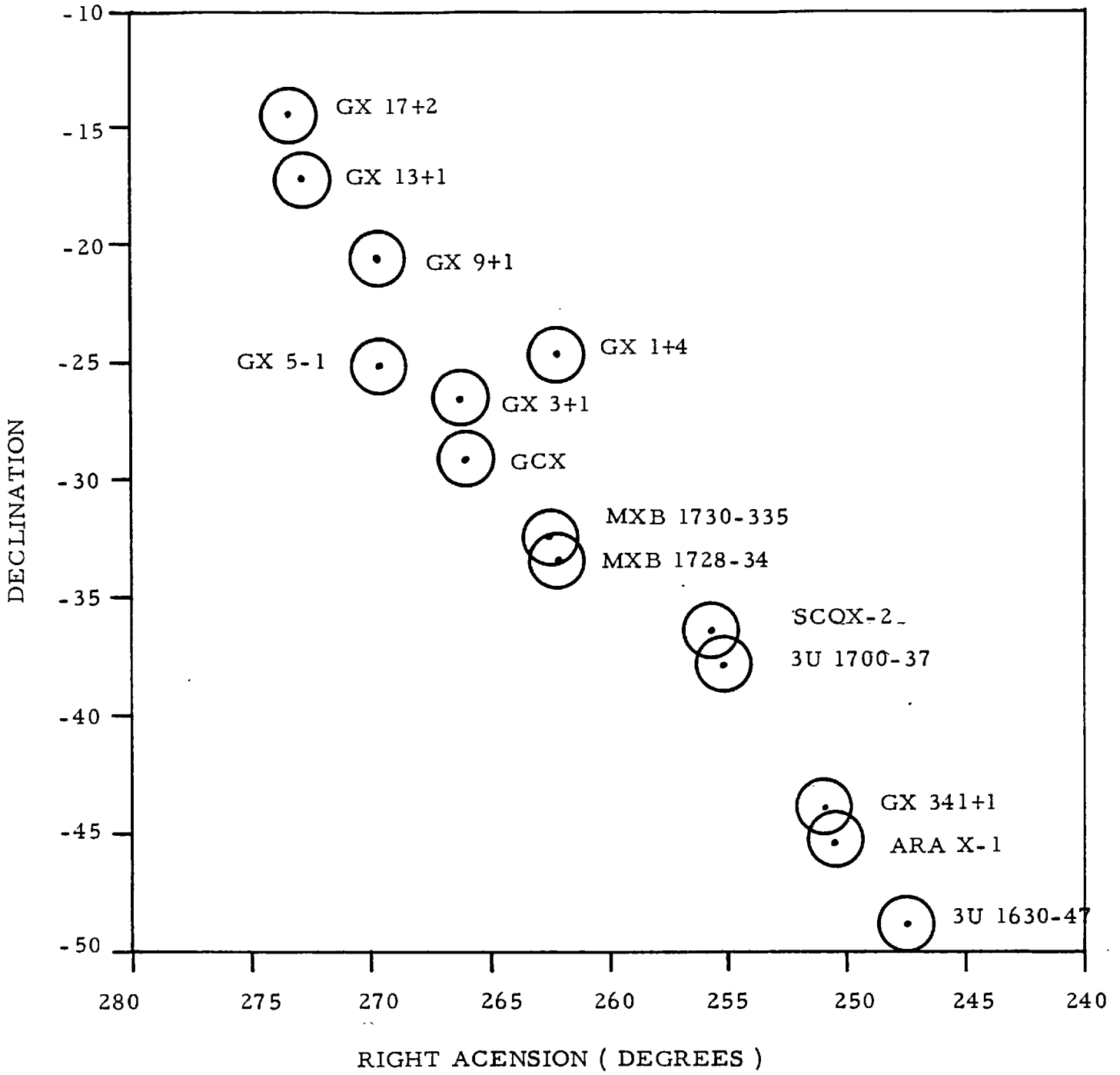


Fig 5. 14: X -Ray Sources In The Galactic Centre Region.

### 5.3. The Collimator

#### 5.3.1. Collimator Requirements

(i) Shown in Figure 5.14 is one of the more crowded regions of the sky from a hard x-ray point of view. The map covers the galactic centre region and illustrates the principal sources, each one surrounded by a circle of  $2^{\circ}$  diameter. It is evident that if a detector is to resolve SCOX-2 from 3U1700-37, or GX341+1 from ARAX-1, it must have an angular resolution not worse than  $2^{\circ}$ . It was therefore decided to use a collimator with a  $2^{\circ}$  FWHM response.

(ii) The collimator must have a high transmission factor at normal incidence ( $> 0.8$ ).

(iii) The collimator must be effective up to 200 keV.

#### 5.3.2. Collimation Technique

Three types of collimator are commonly used in x-ray astronomy:

(i) Active collimators. These are usually constructed from CsI or NaI and are used to collimate hard x-ray detectors such as Experiment "F". The scintillator forms a well, at the bottom of which is located the main detector crystal. Photons which produce a pulse in the shield and in the main crystal are ignored, and thus energetic x-rays which leak through the active shield are discriminated against. Active collimators can only be used in applications where the main detector crystal has a small effective area (c/f  $8 \text{ cm}^2$  of Experiment F).

(ii) Rotation modulation collimators (RMC) are used to collimate both hard and soft x-ray detectors. They are particularly suitable for

experiments designed to study and accurately position steady x-ray sources. However, the wide field of view of such collimators means that several sources are observed simultaneously, and thus rapid time variations from a source cannot be followed unless the source is very strong.

(iii) Passive honeycomb collimators, constructed from a high z material, have been used in the past to collimate detectors up to  $\sim 30$  keV, e.g. Experiment "C" on Ariel V. The collimator in this case consists of a gold plated aluminium honeycomb of  $100 \text{ cm}^2$  area.

Such collimators are able to provide a narrow field of view (c/f  $3.5^\circ$  FWHM of Experiment C) for a large area detector, and thus enable the detector to observe sources individually.

In view of the large effective area of each detector module ( $200 \text{ cm}^2$ ), the need for a narrow field of view and the desirability of following fast time variations, it was decided to develop a honeycomb collimator for the detector.

### 5.3.3. Design Criteria

Consider a collimator consisting of an array of square section tubes. If the walls are thick enough to be considered as perfect absorbers, the angular response function in the  $\phi = 0$  plane is theoretically triangular, and the FWHM is fixed by the dimensions of each tube.

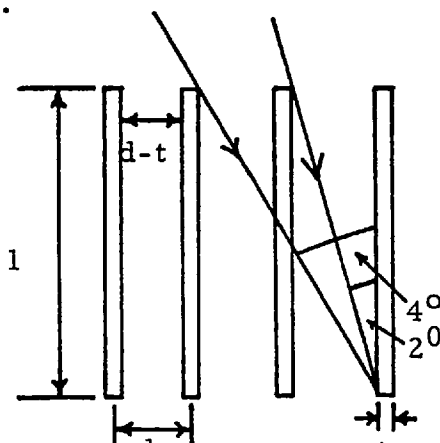
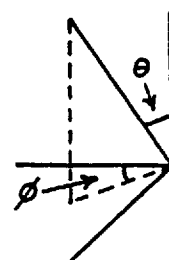


Fig 5. 15: Collimator Structure



For a FWHM of  $2^\circ$

$$\tan 2^\circ = \frac{d - t}{\ell} \quad \text{which gives } \ell = 28.6(d - t)$$

$$\text{Cell area} = d^2$$

$$\text{Open area} = (d - t)^2$$

$$\text{Require } \frac{(d - t)^2}{d^2} > 0.8$$

$$d^2 - 2dt > 0.8 d^2 \quad (t^2 \ll d^2)$$

$$\underline{\text{Thus } d > 10 t}$$

In practice the walls are not perfect absorbers. Consider the worst case ray which has an incidence angle of  $4^\circ$  and is subject to the least attenuation.

$$\text{Path length through wall} = \frac{t}{\sin 4^\circ} = 14.3 t$$

The path length must be of the order of one interaction length at 200 keV ( $\lambda_{200}$ ) or at the k edge if the interaction length here is greater than the former value.

$$\text{Therefore } \underline{t = \frac{\lambda_{200}}{14.3}}$$

$$\text{also } d > 10 \frac{200}{14.3} \quad \text{and } \ell > 18.0 \lambda_{200}$$

Increasing the value of  $d$  and correspondingly the value of  $\lambda$  produces a larger open area.

The collimator mass is virtually independent of  $d$ .

$$\text{cell mass} = \frac{A\lambda^2 t d e}{d^2}$$

$A$  = Collimator area

$e$  = Density of collimator material

$$\text{Thus weight} = \frac{2Aet}{\tan^2 \theta}$$

The collimator should be constructed from a high  $Z$  ( $>40$ ) material to keep the weight to a minimum. This is because the dominating interaction between such a material and x-rays up to 200 keV is the photo-electric effect, the cross section for which is given by

$$\sigma \propto Z^4 \text{ cm}^2 \text{ gm}^{-1}.$$

Thus increasing the  $Z$  value brings about a dramatic reduction in the collimator weight.

Table 5.3 considers collimators constructed from various materials. The weights and dimensions have been calculated by applying the above criteria. The masses assume a collimator area of  $200 \text{ cm}^2$ .

Copper and iron are included just for comparison. In practice the value of  $d$  is determined by the manufacturing process and is usually  $> 0.1 \text{ cms}$ .

The advantages to be gained by constructing the collimator from one of the heavy elements listed overleaf, Pb, Au and Tl are readily

Table 5.3. Collimator Dimensions

Material	Z	$\lambda_{200}$ (cms)	t(cms)	d(cms)	$\rho$ (cms)	Mass(grms)
Lead	82	0.094	0.0066	>0.066	>1.7	852
Gold	79	0.060	0.0042	>0.042	>1.1	926
Tantalum	73	0.083	0.0058	>0.058	>1.5	1100
Copper	29	0.718	0.050	>0.5	>12.9	5102
Iron	26	0.873	0.061	>0.61	>15.7	5507

apparent. These substances are the heaviest elements from which it is practical to construct a collimator and all three were investigated.

#### 5.3.4. Gold Collimator

Gold is a very soft metal and has little tensile strength. The wall thickness required for a gold collimator is only 0.004 cms and thus some form of support is needed to give the collimator strength. To collimate Experiment C, the MSSL group developed a gold plated honeycomb collimator with a hexagonal cell structure. Copper was initially electro-plated onto a preformed aluminium honeycomb and then a thin layer of gold was plated onto the copper. The copper layer is necessary because gold will not plate directly onto aluminium.

Hexagonal cells have several advantages over the square cells described in the previous section.

- (i) The variation of the open angle with the azimuthal angle  $\phi$  is smaller.
- (ii) A hexagonal structure is easier to produce. The aluminium

honeycomb is produced commercially by coating flat aluminium sheets with equally spaced strips of glue, and then sticking a large number of sheets together. When the glue is dry, a pull is applied to ends of the stack of sheets, which open out and assume a honeycomb configuration.

An attempt was made to gold plate such a structure to produce the required collimator. The hexagonal cells of the preformed honeycomb have a width of 3.2 mms (distance between flats). The depth of honeycomb required was found from

$$\tan 2^{\circ} = \frac{3.2}{\ell} \quad \therefore \ell = 9.2 \text{ cms.}$$

Attempts were then made to gold plate a small 3x3x9.2 cm honeycomb. The required copper layer was plated to the aluminium without any problem, but it was impossible to get the required thickness of gold to electroplate onto the copper. A small amount of gold adhered very easily, but as the thickness increased the process slowed down and eventually stopped. Several different intermediary surfaces and plating solutions were tried, but the same problem was encountered in each case, only a quarter of the gold required could be plated onto the honeycomb. The method was therefore abandoned.

#### 5.3.5. Lead Collimator

Lead is a more suitable collimator material than gold for several reasons:

(i) The higher Z value of lead means that theoretically lighter collimators can be constructed.

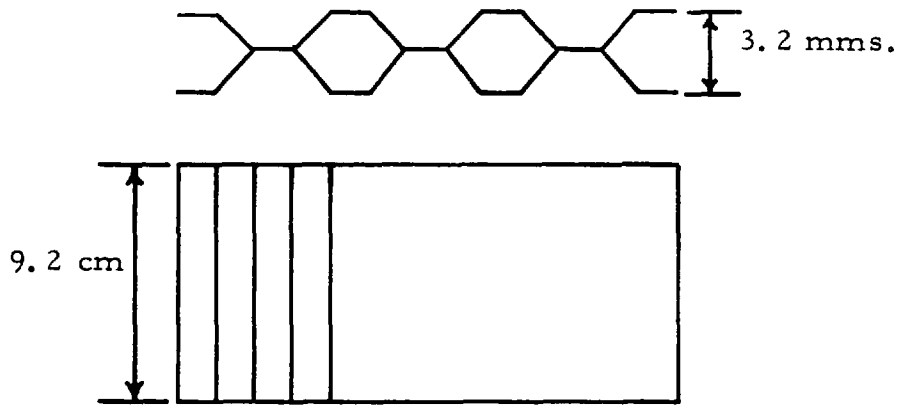


Fig 5. 16(a): Preformed Aluminium Honeycomb.

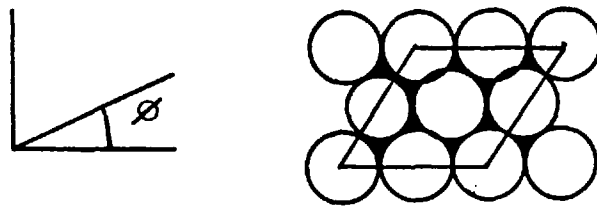


Fig 5. 16(b): Array Of Close Packed Lead Tubes.

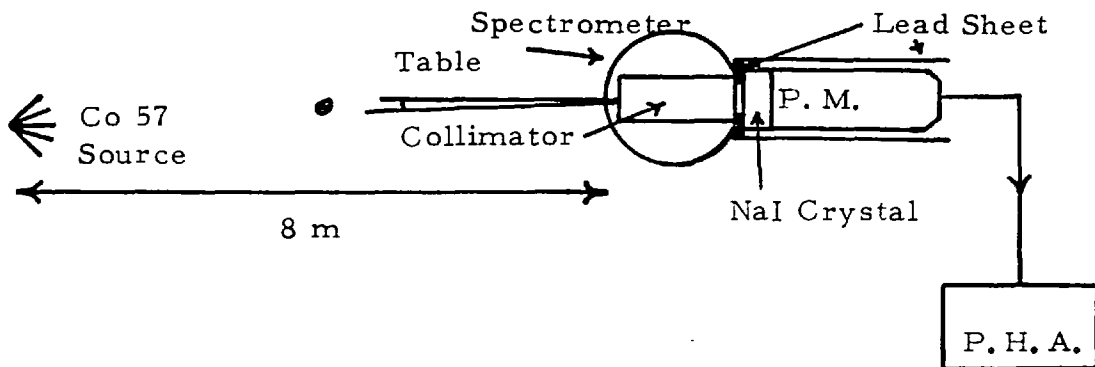


Fig 5. 16(c): Determination Of Angular Response Function Of Lead Collimator.



- (ii) It is very much cheaper.
- (iii) Lead is stronger than gold.

Arrays of lead tubes are frequently used to collimate large area balloon borne detectors. The tubes are usually >1 cm wide and several tens of cms long. A similar idea, but with much smaller tubes, was used to produce a small (3x3 cm) collimator suitable for use up to 200 keV. The collimator consisted of an array of close packed lead tubes constructed from 3 thou lead sheet, (giving a minimum path length slightly greater than one interaction length at 200 keV) the thinnest sheet available. The tubes were made by rolling pre-cut pieces of sheet around a piece of perfectly straight, circular cross-section rod. The tubes were then coated with araldite and stacked into an aluminium frame-work to produce the required array. The tube diameter was 3 mms and the length 8.6 cms. The length was fixed by requiring

$$\tan 2^\circ = \frac{\text{Diameter}}{\text{Length}}$$

The gap between the tubes was filled with araldite and thus x-rays could only be transmitted down the tubes.

With such an arrangement if the tubes are perfectly packed, the ratio of the open area to the total area is independent of the tube diameter (if  $t \ll d$ ). From Figure 5.16(b))

$$\text{Cell area} = 8r^2 \sqrt{3}$$

$$\text{Open area} = 4\pi r^2$$

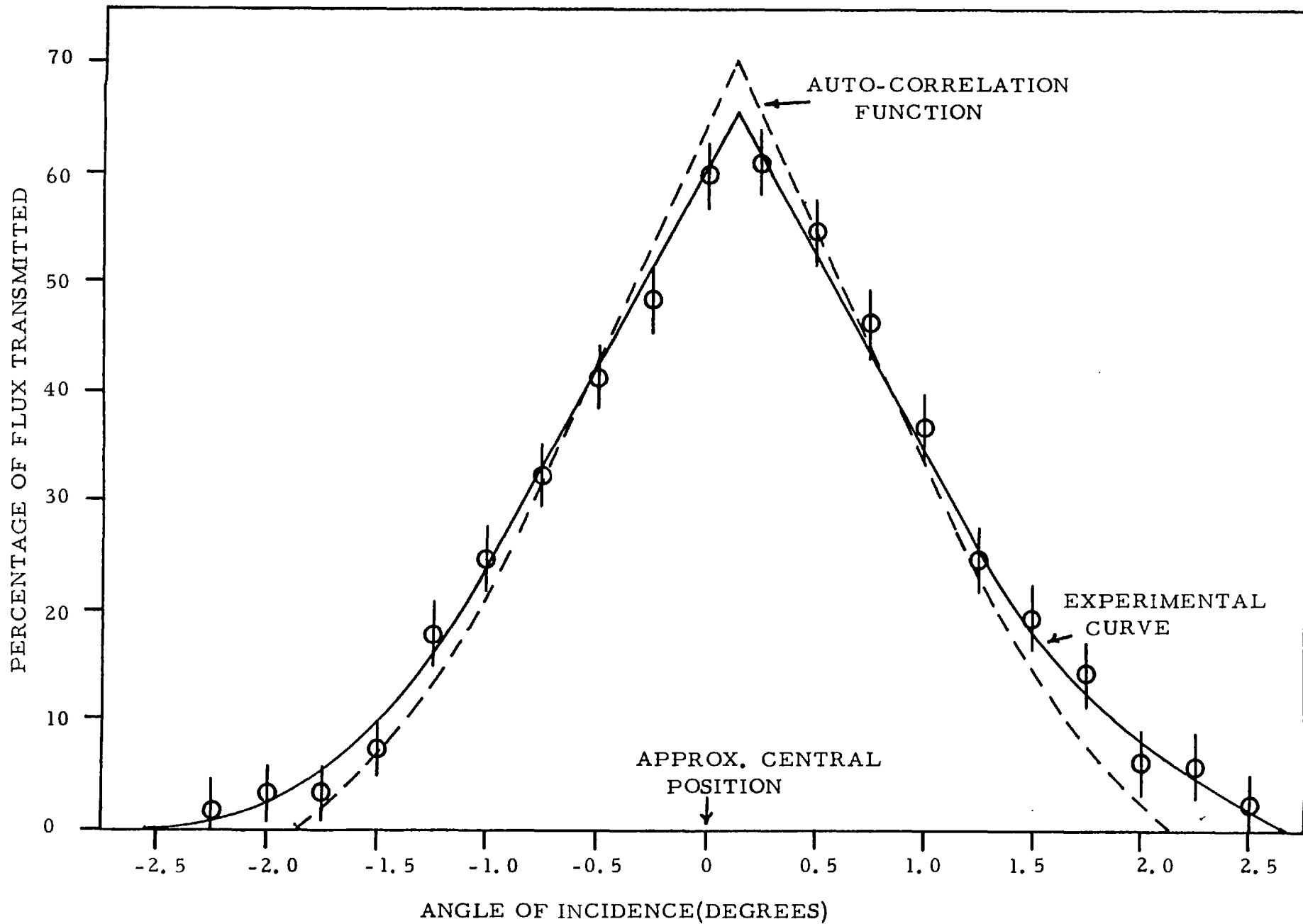
$$\text{Ratio} = 0.91 \quad \text{i.e. independent of } r.$$

Thus theoretically a high transmission at normal incidence is possible. However, when the tubes were stacked together it was found that the above ratio was only  $\sim 0.7$ . This was primarily due to non-uniformities in the tubes preventing perfect packing. The effect of such non-uniformities could have been reduced by using a larger tube diameter, but this would have made the tubes more difficult to roll due to the required increase in length. In addition the whole structure would have been weakened.

The angular response function of the collimator in the  $\phi = 0$  plane at 122 keV, was tested using the setup shown in Figure 5.16(c). Lead sheet was placed between the collimator and the NaI crystal to mask off some of the scintillator, and leave an open area slightly less than the collimator area. The output from the detector with a weak CO-57(122 keV) source directly in front of the collimator, was a very good approximation to a gaussian distribution. However, as the source was moved further away a second peak at lower energy began to form, and with the strong CO-57 source 8 m away, this second peak dominated the photopeak. Working upon the assumption that this secondary peak was a scattering effect, additional shielding was placed around the PM tube and crystal, leaving only the collimator aperture clear. This reduced the size of the peak considerably but did not completely eradicate it. The size of the secondary peak proved to be virtually independent of whether the collimator was in position or not, and therefore can only have been due to Compton scattering of 122 keV photons by the air, the materials in the laboratory and the materials around the crystal. In order to remove the scattered photons, only counts in the photo-peak were considered.

The normal incidence position was found approximately, by viewing the source through the collimator with the detector removed. The source was then moved vertically until the count rate was maximised. The

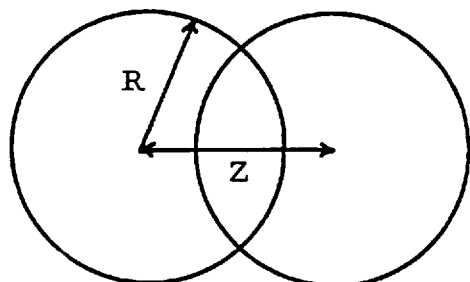
Fig 5. 17: Angular Response Function Of Lead Collimator.



collimator was then rotated through  $3^\circ$ , and moving in  $\frac{1}{4}^\circ$  steps the count rate from the source as a function of the input angle  $\phi$  was determined. The actual photon incidence rate upon the collimator was found by measuring the count rate from the source with the collimator removed. The background rate with the collimator in position was determined before and after the angular survey, and found to be invariant. The response function in terms of the percentage of incident photons transmitted is shown in Figure 5.17. A correction has been applied to account for the fact that the incident wavefront was not perfectly plane.

Within the errors, the curve is symmetrical about the point  $\theta = 0.013^\circ$ , and thus the approximate normal incidence position was very close to the true position. The response function is triangular up to  $\theta \sim 1.25^\circ$  and has a FWHM of  $1.9^\circ$  (c/f required value of  $2^\circ$ ). The transmission at normal incidence is 65%, very close to the theoretical maximum transmission as given by the ratio of the open to closed area of the array. The difference is almost certainly due to the tubes not being perfectly aligned.

If the lead tubes are considered to be perfect absorbers of 122 keV photons, the angular response function in all azimuthal directions is theoretically given by the autocorrelation function of two 3 mm diameter circles.



Area of Overlap

$$= 2 \times \left[ \frac{R^2}{360} \cos^{-1} \frac{Z}{2R} - \frac{ZR}{2} \sqrt{1 - \frac{Z^2}{4R^2}} \right]$$

The values of  $Z$  corresponding to an incidence angle  $\theta$  is given by

$$Z = \rho \tan \theta \qquad \rho = 8.6 \text{ cms.}$$

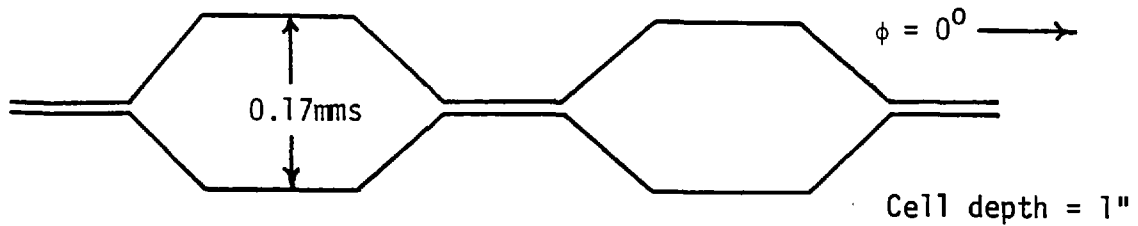
$Z = 0$  corresponds to a transmission factor of 70% in this case.

As can be seen from Figure 5.17, there is a good agreement between the auto-correlation function and the actual response curve. The wider base and lower peak of the experimental curve are due to non perfect tube alignment and to a small proportion of the incident flux penetrating the tube walls.

The main drawback of using an array of lead tubes to collimate the module is the low normal incidence transmission factor (65%). Attempts were made to corrugate lead sheets with the idea of sticking such sheets together to build up a lead honeycomb. It was expected that the transmission factor of such a device would be greater than that obtained with the array of tubes. However, it was found that the lead could not be bent as desired, the metal tore easily and the corrugated sheets could not be produced free of distortion.

#### 5.3.6. Tantalum Collimator

In view of the problems encountered in making a honeycomb collimator from corrugated lead sheet, building such a device from corrugated tantalum sheet was investigated. The thickness of Tn sheet required is  $\sim 2$  thou., and it was found that sheets of this thickness could be easily bent to give a half-hex profile. Sticking such sheets together produced the required hexagonal array.



The collimator was manufactured using existing tooling and as a result the cell dimensions, including the depth, were pre-determined. The maximum open angle in the  $\phi = 0$  direction =  $4.5^\circ \sim$  twice the size of the required open angle.

The response function of the collimator in the  $\phi = 0^\circ$  plane was determined as for the lead collimator and is shown in Figure 5.18. The function is symmetrical about  $\theta = 0.5^\circ$ , triangular for incidence angles less than  $\pm 3.5^\circ$  and has a FWHM which is very close to the maximum open angle. The transmission at normal incidence (85%) is less than the theoretical value as given by the geometry of the array (0.93), and is due to factors such as glue thicknesses, non-perfect packing etc.

Of the three techniques investigated, the tantalum collimator constitutes the best method of collimating the NaI crystal.

- (i) Such a device has a high transmission function at normal incidence.
- (ii) The collimator is strong.
- (iii) The response function is triangular up to large incidence angles.
- (iv) The collimator is relatively easy to produce and set up.

The actual collimator will need to have different dimensions to the test device to give the correct opening angle. However, no serious problems are envisaged in the production of such a device.

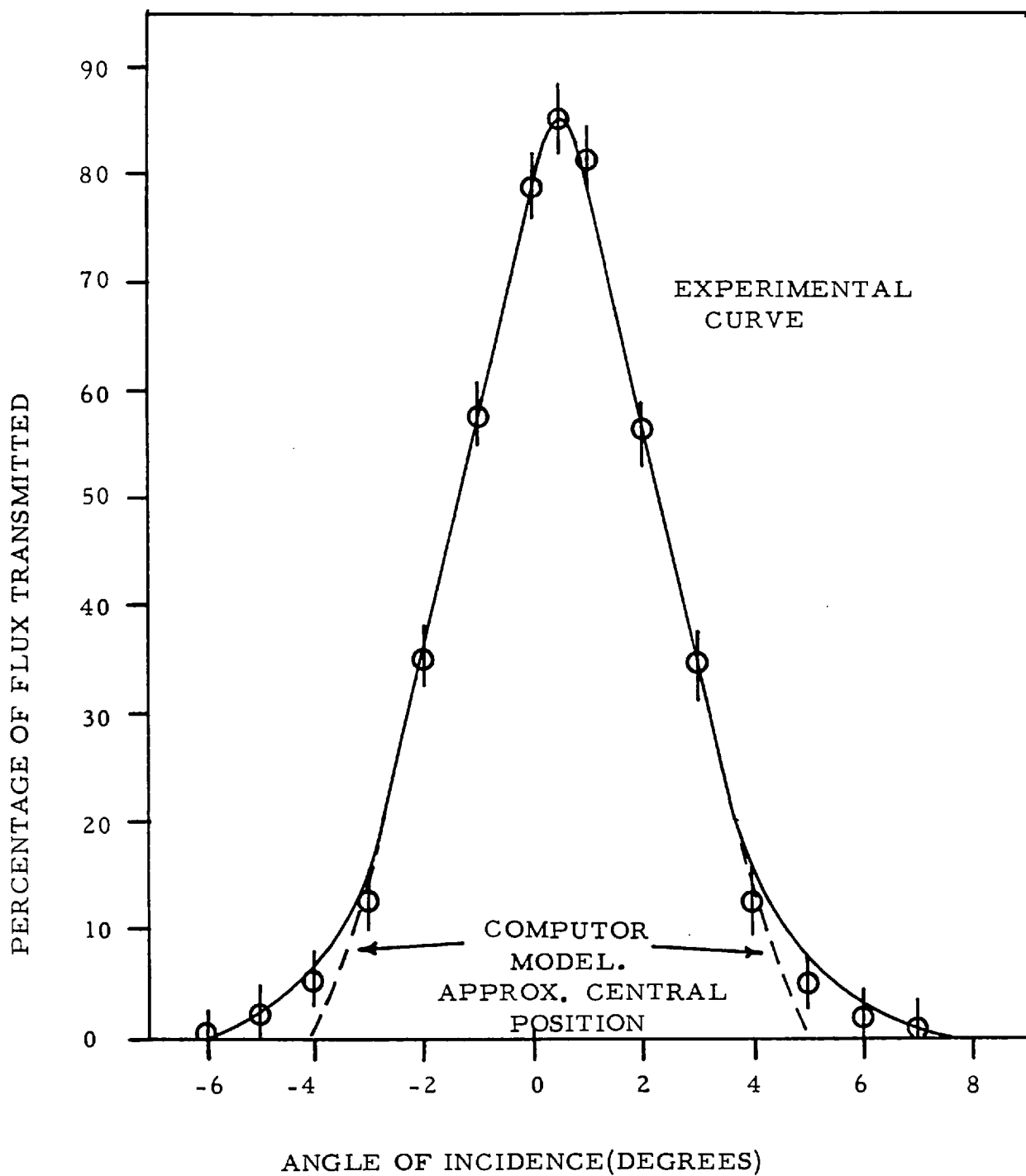


Fig 5. 18: Angular Response Function Of Tantalum Collimator.

### 5.3.7. Computer Model

To aid further design studies, a computer model which simulates the tantalum collimator was developed. The program traces the histories of up to 10,000 rays, incident upon a collimator of specified dimensions at a particular azimuthal angle  $\phi$  and incidence angle  $\theta$ . The entry point of each ray is chosen randomly, and the ray is then stepped through the collimator until it reaches the bottom surface. Every time the ray passes through a tantalum wall the thickness of tantalum traversed ( $dp_n$ ) is calculated and added to the path length  $p_n$ . The amount of attenuation the ray is subjected to is then given by

$$1 - e^{-\mu p_n}$$

$\mu(E)$  is the linear attenuation coefficient of tantalum at the energy considered.

By calculating the path length through the collimator of each ray, the transmission factor to photons of energy  $E$  at  $\theta$  and  $\phi$  can be found from

$$T(E, \theta, \phi) = \Sigma \frac{e^{-\mu p_n}}{10^4}$$

The program is then run at other incidence angles ( $\theta$ ) until the angular response function at azimuthal angle  $\phi$  is determined.

The model enables the transmission factor at large incidence angles ( $\theta > 5^\circ$ ) to be estimated. This is very difficult to do experimentally, as only a small percentage of the incident flux actually reaches the detector at such angles, and the resulting signal is swamped by the background count rate.



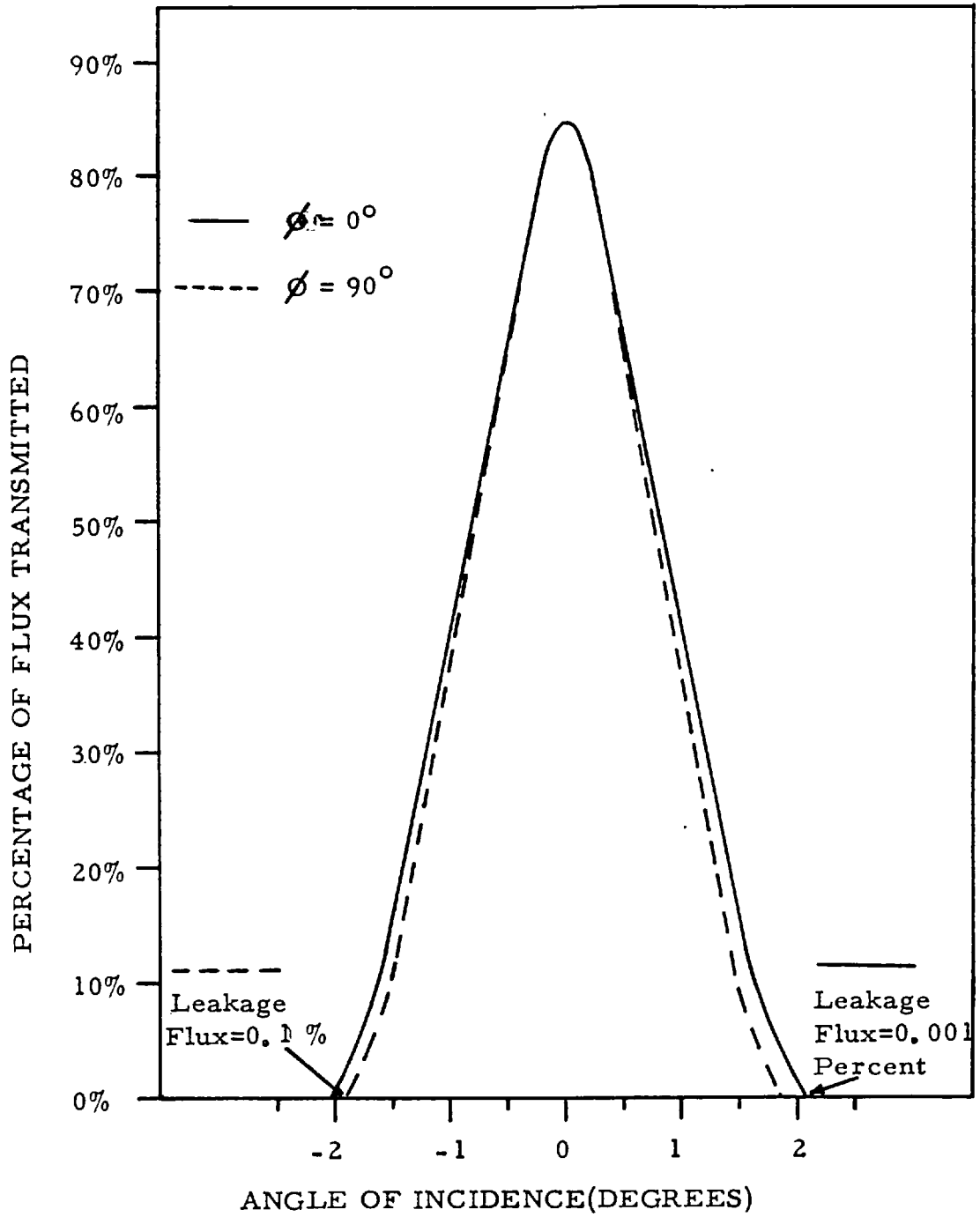


Fig 5. 19: Theoretical Angular Response Functions

The program was initially run using a collimator of the same dimensions as the one actually constructed, taking into account the double wall thickness where adjacent corrugated sheets are stuck together. The energy of the incident photons was taken to be 122 keV. The angular response function in the  $\phi = 0^\circ$  plane was calculated and compared to the experimental curve in Figure 5.18. The two curves have been normalised to give the same transmission function at normal incidence (0.85 as determined experimentally). As can be seen the agreement between the theoretical and experimental results is excellent up to large  $\theta$  values. The slower decay of the experimental plot is almost certainly due to non-perfect cell alignment. The program predicts a transmission factor of  $\sim 10^{-3}$  for incidence angles  $> 6^\circ$ .

These results indicate that the FWHM of the response function at  $\phi = 0^\circ$  is virtually equal to the maximum opening angle. The program was re-run for a theoretical collimator measuring 20x10 cms x 6 cms deep and a cell spacing (distance between flats) of 2.7 mms. Such a collimator is equal in overall size to the one required and has a maximum opening angle of  $2^\circ$ . The angular response functions to 122 keV photons at  $\phi = 0^\circ$  and  $\phi = 90^\circ$  were computed and are shown in Figure 5.19. It is evident that the predicted field of view is near circular with a FWHM of  $\sim 2^\circ$ . The required collimator should therefore be built with the above dimensions.

Figure 5.19 predicts a considerable variation in the leakage flux with azimuth. To investigate this effect further, the theoretical transmission factors were determined as a function of azimuth for two angles of incidence, namely 5 and 10 degrees. The results exhibit considerable variations, especially in the latter case where variations in the predicted leakage flux span three orders of magnitude, as  $\phi$  increases from 0-90 degrees. This is particularly important when deciding what is the

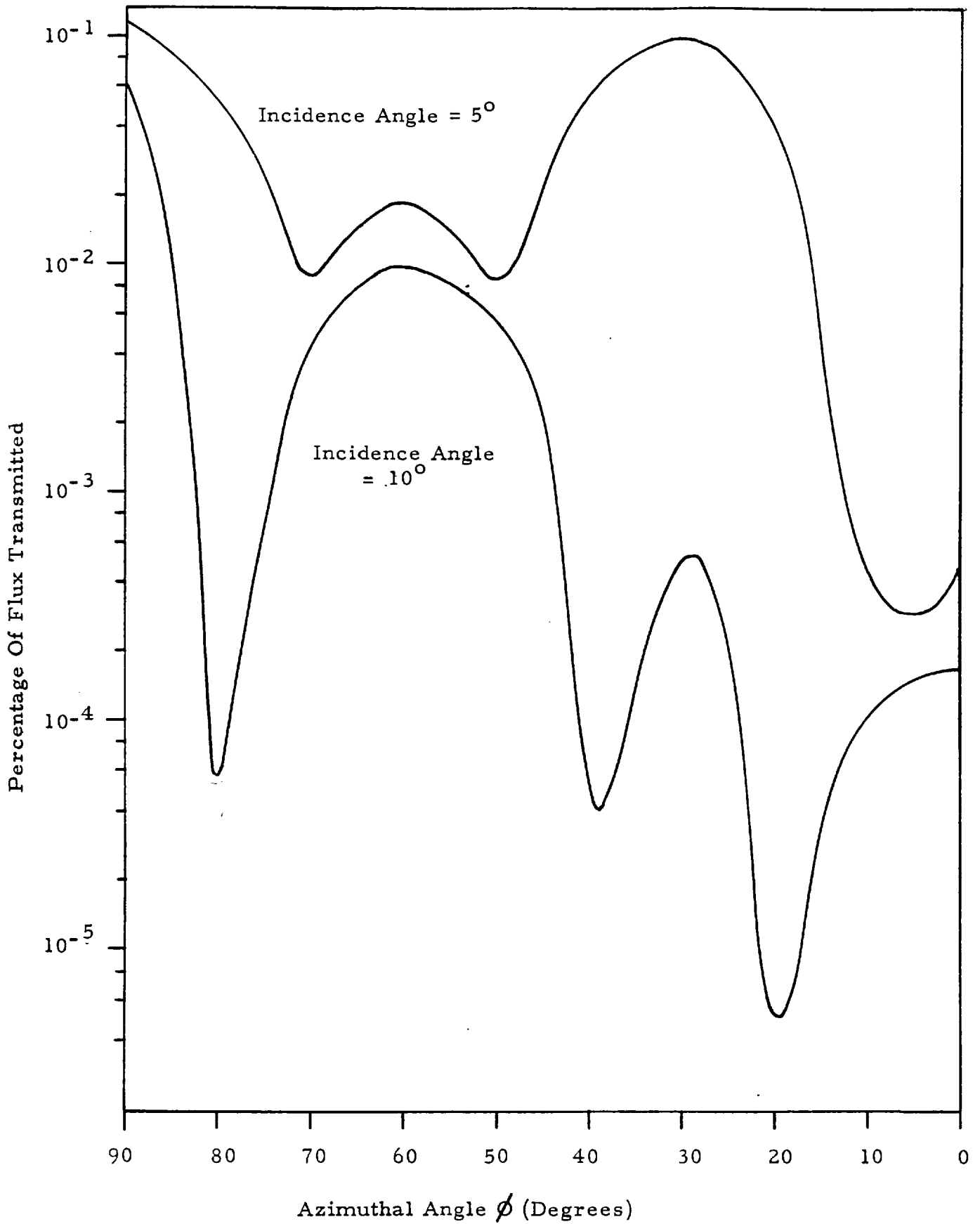


Fig 5. 20: Variation In Leakage Flux With Azimuth.

best method of using the collimator to resolve a source signal from the background count rate.

#### 5.3.8. Signal Detection

If a detector is to measure the x-ray flux from a particular source, then both the source and background counting rates must be determined. As the background rate in the detector will vary with time, it must be determined simultaneously with the source measurement. To achieve this, many satellite detectors use an offset technique which is particularly applicable in cases where the satellite is spinning. The detector is offset from the satellite spin axis by a few degrees, and the spin axis is pointed a few degrees away from the source of interest. As the satellite rotates, the collimator modulates the source signal but not the background. If the collimator has a near triangular response, the resulting signal at the detector is very nearly sinusoidal with a period equal to the satellite rotation period. The peak to peak signal amplitude depends upon the source strength, the two offset angles and the collimator response function, knowing the latter parameters enables the source strength to be determined.

However, using such a technique with the LAD detector poses certain problems.

(i) As the detector is designed to be used on a non-spinning vehicle, each collimator and hence each module would have to be offset and spun. This would require a complicated and cumbersome mechanism with a correspondingly high power consumption.

(ii) As can be seen from Figure 5.20 there is a considerable variation

predicted in the leakage flux at large  $\theta$  values with azimuth. Thus a strong source at a large offset would have the effect of modulating the background, which could cause considerable confusion if a weak source was being studied.

(iii) The detector's varying orientation with respect to the spacecraft would also cause the background to be modulated, due to induced radio-activity, differing attenuation lengths etc.

It is proposed instead to use a collimator rocking technique as was mentioned in section 5.2.2. This section gives a rather simplified approach to the problem which is nevertheless sufficient for determining the optimum thickness of scintillator to use. Individual modules are grouped together in quadrants containing equal numbers of modules. Each quadrant can be rocked independently over a small angle ( $\pm 3^\circ$ ) about an axis perpendicular to the viewing direction. Quadrants in a pair are rocked about parallel axes but with a phase difference, so that when the outputs are summed a flat top response is synthesised. The other pair of quadrants is rocked about a perpendicular axis. The response of a quadrant perpendicular to its plane of rocking will be flattened over a small angle ( $\sim \frac{1}{4}^\circ$ ), by slightly off-setting the viewing axes of individual modules. As well as each quadrant pair providing independent measurements, this technique has the merit that a flat top response can be synthesised in two dimensions, or the method can be used for determining the positions of stronger sources.

The modulation of the source signal will be the convolution of the collimator response function and the rocking profile. The amplitude of the modulated waveform will be directly related to the source strength. The main advantages in using this technique are:

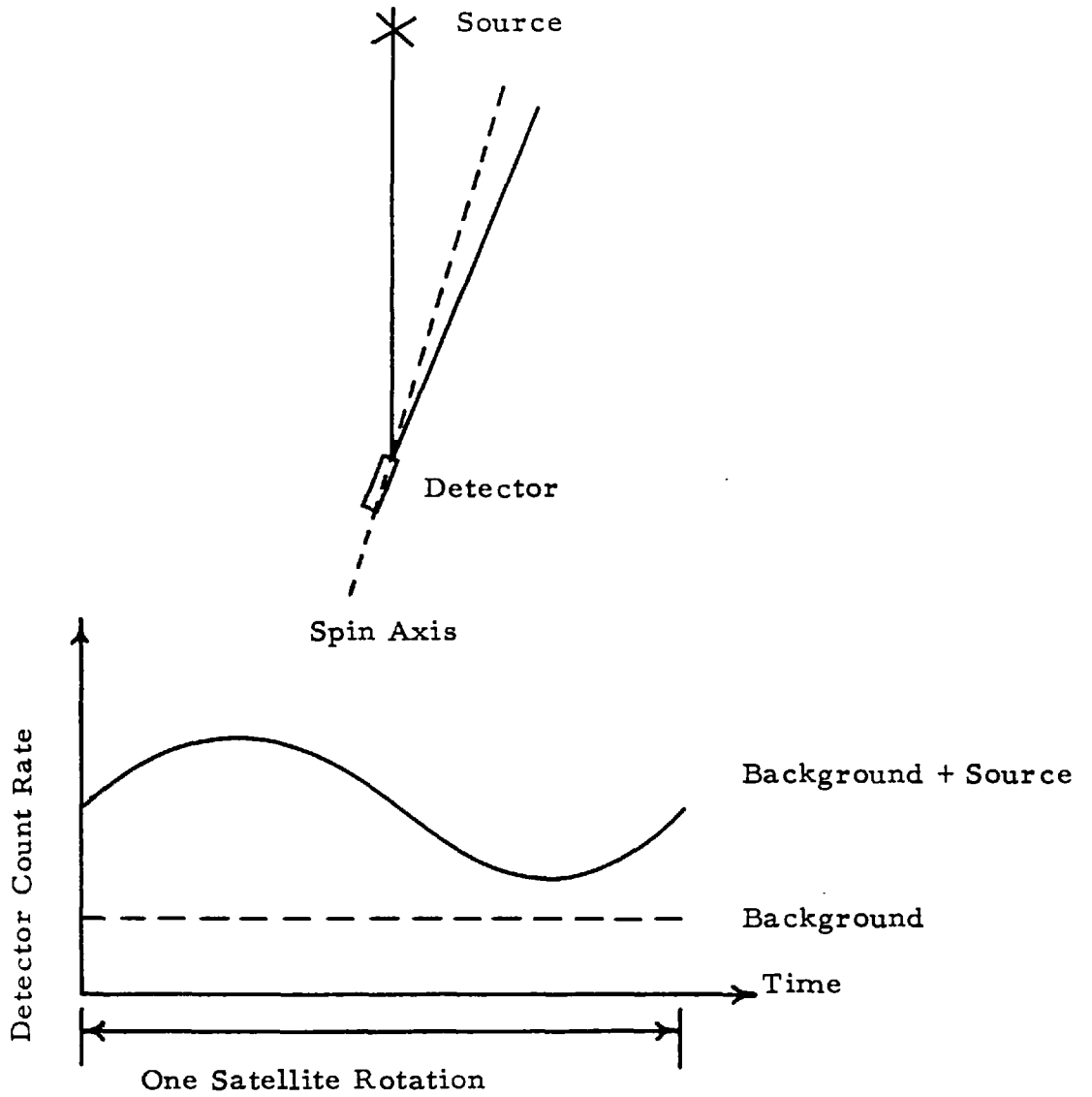


Fig 5. 21: Modulation Technique With A Spinning Satellite.

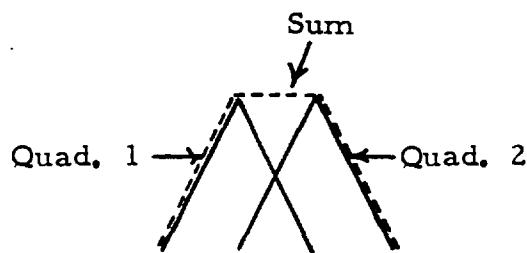


Fig 5. 22(a): Angular Response Function Of A Quadrant Pair.

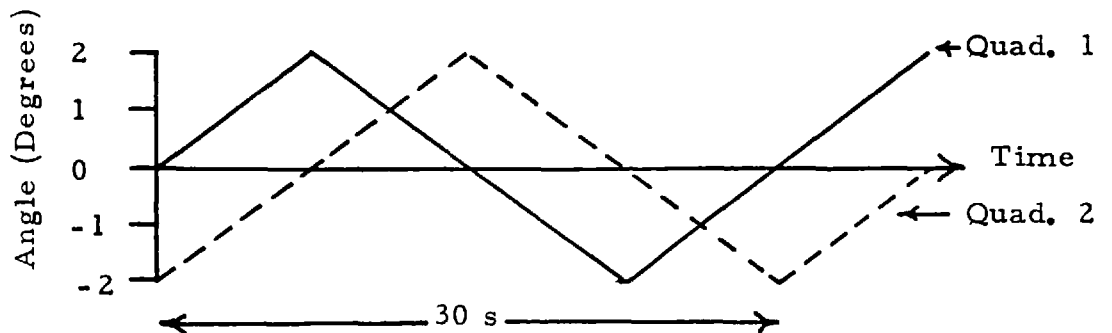
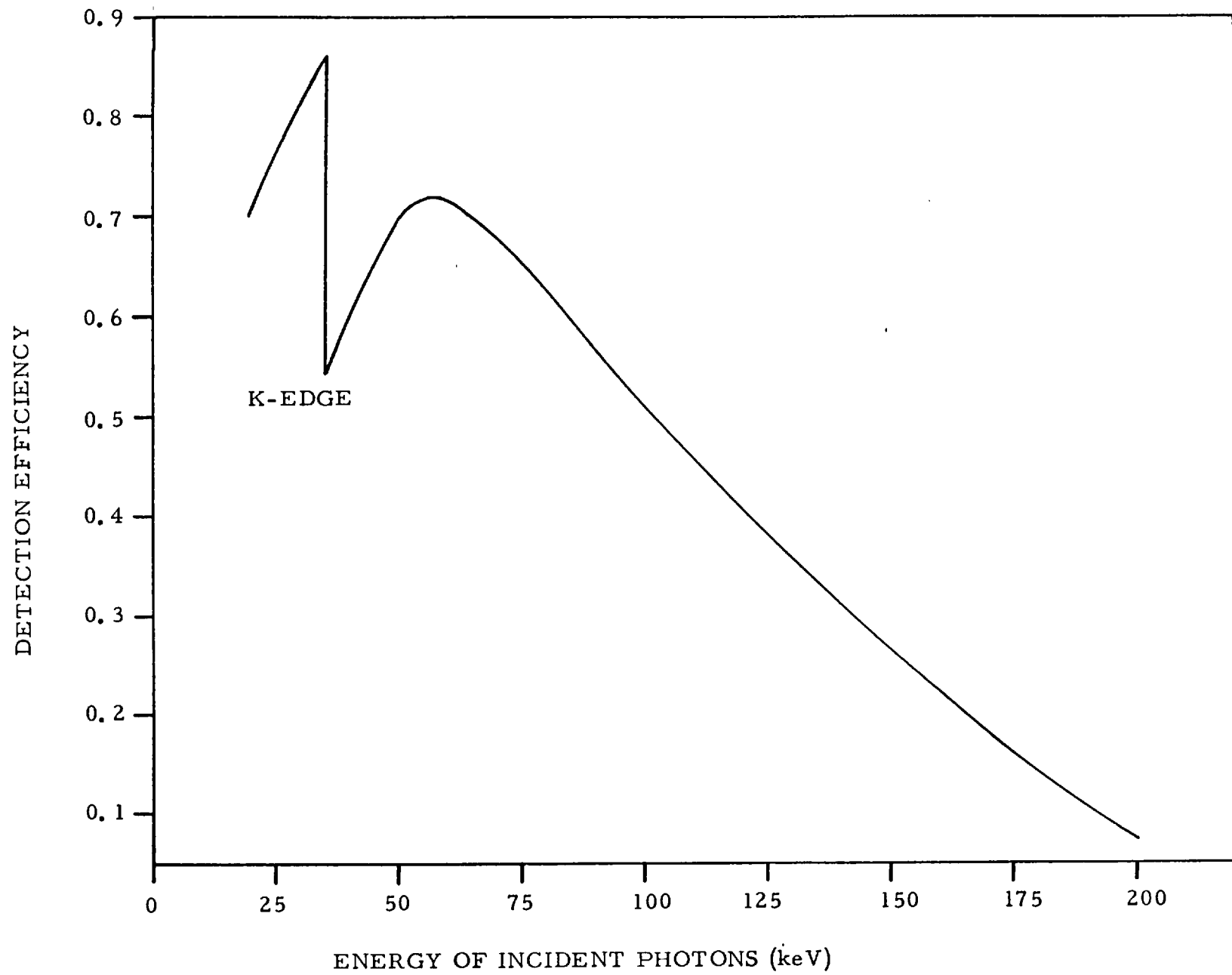


Fig 5. 22(b): Possible Rocking Profile.

(i) The required rocking mechanism is much simpler than a rotational device and is therefore less likely to malfunction.

(ii) Background modulation is kept to a minimum because the detector's orientation with respect to the spacecraft stays virtually constant, and variations in the leakage flux from strong sources will be small.

Fig 5. 23: Theoretical Efficiency Of The NaI Crystal.





#### 5.4. Performance

##### 5.4.1. Detection Efficiency

To aid development work, a full size module minus collimator and shielding was constructed. The detector consists of a 20x10 cm x 2 mm thick NaI(Tl) crystal, sealed on top by a 0.05 mm aluminium window and underneath by 3 mm of glass. The crystal is viewed by two 3" photo-tubes connected to the glass via a perspex light pipe as described in section 5.2.3. The two tubes are balanced and their outputs are summed.

Figure 5.23 shows the theoretical efficiency of the scintillator after accounting for k escape losses (Engel 1977) and absorption by the aluminium window. Photomultiplier statistics and variations in light collection efficiency, will mean that the actual efficiency curve will be a smoothed out version of Figure 5.23.

The efficiency at 122 keV was measured using a calibrated Co-57 source. The source was set up 8 m from the crystal and the summed photo-tube output was fed into a PHA and displayed on a screen. A rather complex spectrum was obtained, which was similar to the spectrum obtained during the angular survey of the lead tube collimator. As the Co-57 source was brought closer to the crystal, the relative size of the peak at ~60 keV decreased, until at a distance of 50 cms more than 90% of the counts were contained within the photopeak. The secondary peak was most probably due to Compton scattering of 122 keV photons, as was thought to be the case with the lead collimator experiment. Thus to measure the efficiency at 122 keV, the PHA discriminator was set so that only photons with energies inside the photopeak were accepted. The count rates above the discriminator threshold were then measured with and without the source in position. A correction was applied to the former to account for air attenuation. The efficiency of the detector was found to be 0.54 which is in good agreement with the theoretical value of 0.6.

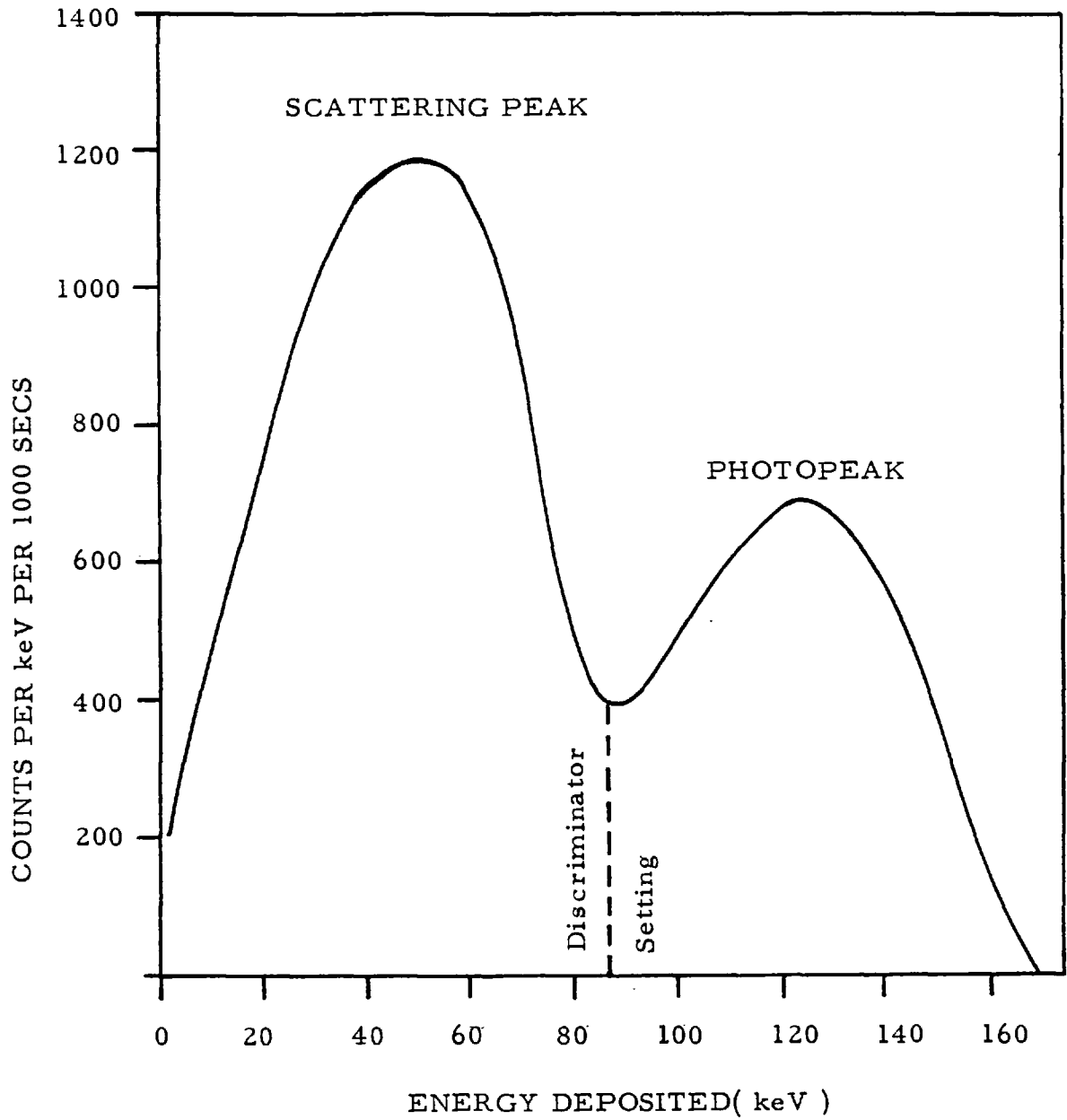


Fig 5.24: The Spectrum Produced In The NaI Crystal By A Co-57 Source Positioned 8 m Away. The Background Count Rate Has Been Subtracted.

#### 5.4.2. Energy Resolution

Due to the processes detailed in section 5.2.3., a monoenergetic input E to the detector will produce a distribution of output pulses. The resolution possible at energy E is effectively given by the FWHM of this distribution. In the CO-57 calibration described in the previous section, the photopeak produced by placing the source 50 cm from the detector was a gaussian like curve with a FWHM of 24 keV. In order to determine the resolution at other energies, the detector was exposed to a variety of radioactive sources. Each source was placed 50 cm in front of the detector and the resulting signal was fed into the PHA. The background was subtracted and the FWHM of the resulting distribution was measured in each case.

Source	Energy	FWHM
Barium-133	31-36 keV	9 keV
Americium-241	60 keV	17 keV
Cobalt-57	122 keV	24 keV
Caesium-137	662 keV	75 keV

These results are well fitted by a relationship of the form

$$\Delta E = kE^{0.66} \quad (1)$$

(FWHM)

Thus the resolution at other energies can be determined. For example at 200 keV, equation (1) gives a FWHM of 35 keV which is the maximum resolution possible at this energy.

It is planned to feed the output of each module into a 64 channel PHA. This will ensure that the resolution is not limited by the electronics.

## 5.5. Balloon flight of test module

### 5.5.1. Introduction

It was decided to fly the test module on the same balloon platform as the large burst detector described in Chapter 3. There were two main reasons for this.

(i) The well defined event average spectrum of gamma-bursts means that a balloon detector capable of measuring spectra, is able to differentiate between genuine gamma-bursts and spurious events of magnetospheric origin. The large burst detector was incapable of determining the energies of incoming photons. Although the test module did not have a large enough area to detect small bursts, it was considered desirable to fly the device so that spectra of any large events could be determined.

(ii) Test flying satellite experiments on balloons prior to their launching into space is a good way of revealing design faults. It was hoped that a similar flight of the test module would correspondingly reveal faults and shortcomings, which could be rectified before building the full size detector.

### 5.5.2. Description of Detector

The outputs of the two balanced phototubes were summed, amplified and fed into a six channel PHA. Six channels only were used, instead of the sixty-four planned for each LAD detector module, because of telemetry constraints. The six individual PHA addresses were pre-scaled and read out once a second. This was considered adequate as the detector's prime function was the determination of spectra, and not the study of fast time variations.

Table 5.4. Energy Channels and Scaling Factors

<u>Channel No.</u>	<u>Energy (keV)</u>	<u>Scaling Factor</u>
0	20-40	4
1	40-80	4
2	80-140	8
3	140-200	8
4	>200 keV	16
5	Total 20-200 keV	16

The channel widths were chosen as a compromise between the range to be covered and the number of channels available. Each bin width was approximately twice the detector's resolution at the mid-bin energy. Channel 4 was used to monitor the total count rate above 200 keV. The scaling factors were chosen so that only bursts equivalent to the larger Vela events ( $>2 \times 10^{-4}$  ergs  $\text{cm}^{-2}$ ), would cause the data handling system to saturate.

The energy channels were established as follows. The amplified photo-tube output was fed directly into a PHA, and a Co-57 source was used to produce a photopeak on the screen, the position of which was noted. A photo-diode, incorporated in the scintillator, was then used to generate pulses from the photo-tubes which were also fed into the now-calibrated PHA. By adjusting the photo-diode setting and noting the position of the corresponding photopeak, pulses corresponding to energy inputs other than 122 keV could be produced. Each channel boundary was then fixed by setting the photo-diode to the boundary energy, feeding the output of the head amplifier into the module's PHA and adjusting the discriminator

corresponding to the boundary in question until half the photo-diode pulses fell above the boundary, and half below it. The final settings were then checked with the aid of radioactive sources.

### 5.5.3. Environmental Tests

Before being flown the detector was subjected to extensive environmental testing.

(i) The detector was operated for several days at a pressure of 5 mbars, to ensure that all high voltage points were properly insulated and coronal discharging did not occur.

(ii) The complete detector assembly was thermally cycled between  $-20^{\circ}\text{C}$  and  $+40^{\circ}\text{C}$  whilst exposed to a Co-57 source. The channel counting rates were monitored and are plotted in Figure 5.25. It was immediately apparent that the detector had a large temperature coefficient, and it was suspected that the electronics dominated this coefficient. In order to check this hypothesis and thermally calibrate the detector, the photomultiplier outputs were disconnected from the head amplifier and pulses from an AC coupled pulse generator were fed in instead. The pulse level corresponding to each channel boundary was then determined as a function of temperature, which enabled the changes in the boundary energies to be found.

It was evident that the electronics did have a large temperature coefficient. The counting rate changes observed during the Co-57 calibration, were consistent with the boundary changes inferred by the electronics calibration. It was therefore assumed that the channel boundaries at a particular temperature could be determined directly from the electronics temperature curve. In order to determine the temperature of the electronics

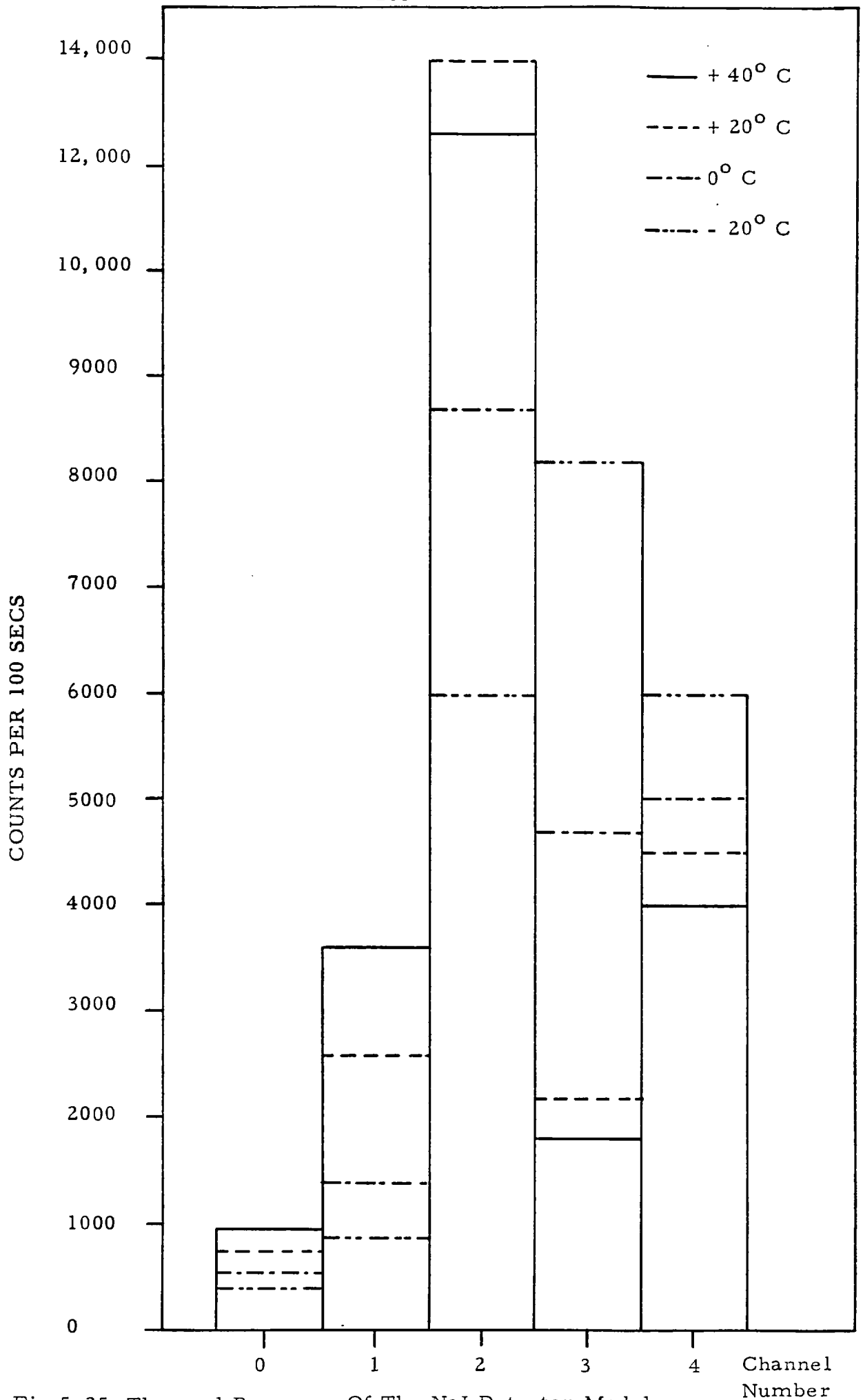


Fig 5.25: Thermal Response Of The NaI Detector Module.

during flight, a thermistor was thermally coupled to the box containing the circuit boards.

Table 5.5. Variation in channel energies with temperature

<u>Temperature</u>	<u>ch 0</u>	<u>ch 1</u>	<u>ch 2</u>	<u>ch 3</u>	<u>ch 4</u>
	(keV)	(keV)	(keV)	(keV)	(keV)
-20 <sup>0</sup> C	14-28	28-54	54-92	92-120	> 120
+20 <sup>0</sup> C	20-40	40-80	80-140	140-200	> 200
+40 <sup>0</sup> C	23-46	46-94	94-164	164-238	> 238

#### 5.3.4. Performance during flight.

The counting rates rose slowly during the balloon's ascent and peaked at the same time as the burst detector count rate. The rates then gradually decreased, and levelled off when the payload reached its operating altitude. The background count rates then remained invariant throughout the flight. The temperature of the module dropped to a minimum of 13<sup>0</sup>C during the ascent, and then gradually rose throughout the flight due to the effects of solar heating. The package temperature just before shutdown was 20<sup>0</sup>C. Data analysis is not yet complete, but a preliminary analysis of the burst detector data revealed that there were no bursts during the flight large enough to appear above the statistical fluctuations on the module data. The steady count rate obtained throughout the flight indicates that little if any radioactivity developed in the crystal.



Table 5.6. Crystal Count Rates (cts s<sup>-1</sup>)

Channel No.	Lab. Rate	In Flight Rate
0	22	139
1	58	132
2	119	160
3	47	55
4	29	93
5	246	486

The above figures indicate that the x-ray spectrum at altitude was considerably softer than the spectrum at ground level. The observed count rate at altitude in each energy channel is theoretically given by,

$$C_n = \left(\frac{dN}{dE}\right)_{Av} \Delta E_n \epsilon_n \frac{A}{2}$$

$\left(\frac{dN}{dE}\right)_{Av}$  = The average value of the photon number index over the energy range covered by the channel in question (n). The photon number index is the average number of background photons crossing a unit sphere per second per MeV.

$\Delta E_n$  = Width of the energy channel.

$\epsilon_n$  = Average detection efficiency in channel n

$\frac{A}{2}$  = Projected area averaged over  $4\pi$

$C_n$  = Count rate in channel n.

The various values of  $(\frac{dN}{dE})_{Av}$  as given by the observed count rates, are compared to those obtained by Ling (1975) using a semi-empirical model of the atmospheric background spectrum.

Table 5.7. Photon Number Index

Channel	Energy	$(\frac{dN}{dE})_{Av}$	Ling's prediction
0	20-40	$8.8 \times 10^{-2}$	$11.0 \times 10^{-2}$
1	40-80	$4.5 \times 10^{-2}$	$5.0 \times 10^{-2}$
2	80-140	$4.5 \times 10^{-2}$	$2.5 \times 10^{-2}$
3	140-200	$3.0 \times 10^{-2}$	$1.1 \times 10^{-2}$

In actual fact Ling's calculations only cover the energy range 300 keV - 10 MeV. In this range the spectrum is well represented by a power law of the form

$$\frac{dN}{dE} = 1.0 E^{-1.39} \text{ photons cm}^{-2} \text{ s}^{-1} \text{ MeV}^{-1}$$

crossing a unit sphere. These results are in good agreement with those obtained by Peterson et al. (1973). Peterson's results indicate that the power law remains unchanged down to ~80 keV where the spectrum turns over. The theoretical values of  $\frac{dN}{dE}$  as given in Table 5.7, have been evaluated by assuming that the power law spectrum holds over the range covered by the NaI detector.

In view of the above discussion, it is not surprising that the observed count rates in channels 0 and 1 are lower than the values as given by extrapolating Ling's spectrum. However, the count rates

in channels 2 and 3 are considerably higher than the predicted values ( $\sim$  a factor of two). This indicates that the spectrum of atmospheric x-rays was somewhat different from that as measured by Peterson over Palestine at energies below 200 keV. However, the good agreement between the theoretical and observed background counting rates of the large burst detector, shows that the overall background spectrum from  $\sim$  50 keV upwards must be in reasonable agreement with Ling's predictions. Thus the deviations from the  $E^{-1.39}$  power law, as evidenced by the results from the NaI detector, must be confined to a small energy range of perhaps only  $\sim$  100 keV.

This problem is obviously worthy of further study, and requires a detector with narrower energy channels than the channel widths employed here.

REFERENCES

- Adams, D. J. (1971) *Contemp. Phys.* 12, 471
- Allen, C. W. (1963) "Astrophys. Quantities" ( London Athlone Press )
- Arnett, W. D. (1969) *Astro. Space Sci.* 5, 180
- Baan, W. (1976) Preprint
- Babuskina, O. P., Bratalubova-Tsulukidze, L. S., Kudyavtsev, M. I.,  
Melioranski, A. S., Savenko, I. A. and Yushkov, B. Yu. (1975)  
*Soviet Astron. (Lett.)* 1, 32
- Barnaby, C. F. and Barton, J. C. (1961) *Proc. Phys. Soc.* 76, 745
- Blumenthal, G., and Gould, R. J. (1970) *Rev. Mod. Phys.* 42, 237
- Bondi, H. and Hoyle, F. (1944) *Monthly Notices Royal Astron. Soc.*  
104, 273
- Brecher, K. and Morrison, P. (1974) *Astrophys. J. (Lett.)* 187, L97
- Brini, D., Evangelisti, F., Fuligni Di Grande., Pizzichini, G., Spizzichino,  
A. and Vespignani, G. R. (1973) *Astron. and Astro.* 25, 17
- Bunner, A. N. (1976) *Bull. A. A. S.* 8, 330
- Canizares, C. R. (1976) *Astrophys. J. (Lett.)* 207, L101
- Carpenter, G. F. (1975) Ph. D. Thesis (University Of London, Imperial  
College)
- Carpenter, G. F., Skinner, G. K., Wilson, A. M. and Willmore, A. P. (1976a)  
*Nature* 262, 473
- Carpenter, G. F., Skinner, G. K., Wilson, A. M. and Willmore, A. P. (1976b)  
Preprint
- Carter, J. D., Dean, A. J., Manchanda, R. K. and Ramsden, D. (1976)  
*Nature* 262, 370
- Coe, M. J., Engel, A. R. and Quenby, J. J. (1976) *Nature* 259, 544
- Clark, G. (1975) *Astrophys. J. (Lett.)* 199. L143
- Clark, G. W., Jernigan, J. C., Bradt, H., Canizares, C., Lewin, W. H. G.,  
Li, F. K., Mayer, W., McClintock, J. E. and Schnopper, H. (1976)  
*Astrophys. J.* 207, L105
- Clark, G. W. and Li, F. K. (1977a) *I. A. U. Circ.* 3092
- Clark, G. W., Li, F. K., Canizares, C., Jernigan, J. C. and Lewin, W. H. G.  
(1977b) *Monthly Notices Royal Astron. Soc.* 179, 651
- Cline, T. L. (1976) *Astro. Space Sci.* 42, 17
- Cline, T. L. and Desai, U. D. (1973) *Astrophys. J. (Lett.)* 185, L1

- Cline, T. L. and Desai, U. D. (1975) *Astrophys. J. (Lett.)* 185, L43
- Cline, T. L. and Desai, U. D. (1976) *Astrophys. J. (Lett.)* 196, L43
- Cline, T. L. and Schmidt, W. K. H. (1977) *Nature* 266, 749
- Crannell, C. J. and McClintock, J. E. (1974) *Nature* 252, 659
- Crispin, A. and Hayman, P. J. (1964) *Proc. Phys. Soc.* 83, 1051
- Davidson, K. and Ostriker, J. P. (1973) *Astrophys. J.* 179, 585
- Doxsey, R. (1976) *I. A. U. Circular* 2983
- Fireman, E. E. (1974) *Astrophys. J.* 187, 57
- Frost, K. (1969) *Astrophys. J. (Lett.)* 158, L159
- Fuligni, F., Brini, D., Dusi, and Frontera, F. (1976) *Astrophys. J. (Lett.)* 208, L111
- Gott, J. R., Gunn, J. E. and Ostriker, J. P. (1970) *Astrophys. J. (Lett.)* 160, L91
- Grindlay, J. E. (1970) *Astrophys. J.* 162, 187
- Grindlay, J. E. and Gursky, H. (1976a) *Astrophys. J. (Lett.)* 205, L131
- Grindlay, J. E., Gursky, H., Schnopper, H., Parsignault, D., Heise, J., Brinkman, A. C. and Schrijver, J. (1976b) *Astrophys. J. (Lett.)* 205, L127
- Guo, D. D. S. and Webber, W. R. (1975) *Proc. 14th. International Cosmic Ray Conference, Munich* 1, 162
- Hansen, C. J. and Van Horn, H. M. (1975) *Astrophys. J.* 195, 735
- Haymes, R. C., Glenn, S. W., Fishman, G. J. and Harndend, F. R. (1969) *J. G. R.* 74, 24
- Heise, J., Brinkman, J. C., Schrijver, J., Mewe, R., Groneschild, E., Den-Boggende, A. and Grindlay, J. E. (1975) *Astrophys. J. (Lett.)* 202, L73
- Heise, J., Brinkman, A. C., Den-Boggende, A., Parsignault, D., Grindlay, J. E. and Gursky, H. (1976) *Nature* 261, 562
- Herzo, D., Dayton, B., Zych, A. D. and White, R. S. (1976) *Astrophys. J. (Lett.)* 203, L115
- Hills, J. G. (1976) *Monthly Notices Royal Astron. Soc.* 175, 1P
- Hoffman, J. A., Doty, J. and Lewin, W. H. G. (1977) *I. A. U. Circular* 3025
- Hoffman, J. A., Lewin, W. H. G., Doty, J., Hearn, R. D., Clark, G. W., Jernigan, G. and Li, F. K. (1976) *Astrophys. J. (Lett.)* 210, L13
- Horstman, H. M., Bassani, L., and Moretti-Horstman, E. (1977) *Proc. 12th. Eslab Symp. ESA SP-124*, 361
- Hillier, R. R., Jachron, W. R., Murray, A., Redfern, R. M. and Sale, R. G. (1970) *Astrophys. J.* 162, L177

- Hynds, R. J. (1974) Private Communication
- Imhof, W. L. , Nakano, G. H. , Johnson, R. G. , Kilner, J. R. , Reagan, J. B. , Klebesadel, R. W. and Strong, I. B. (1974) *Astrophys. J. (Lett.)* 191, L7
- Imhof, W. L. , Nakano, G. H. , Johnson, R. G. , Kilner, J. R. , Reagan, J. B. , Klebesadel, R. W. , and Strong, I. B. (1975) *Astrophys. J.* 198, 717
- Imhof, W. L. , Nakano, G. H. and Reagan, J. B. (1976) *Astro. Space Sci.* 42, 43
- Kahler, S. and Shulman, S. (1972) *Nature Physical Science* 237, 101
- Kaluzienski, L. J. , Holt, S. S. , Boldt, E. A. , and Serlemitsos, P. J. (1975) *I. A. U. Circular* 2859
- Kellogg, E. , Gursky, H. , Murray, S. , Tananbaum, H. , and Giacconi, R. (1971) *Astrophys. J. (Lett.)* 169, L99
- Klebesadel, R. W. and Strong, I. B. (1976) *Astro. Space Sci.* 42, 3
- Klebesadel, R. W. , Strong, I. B. and Olson, R. A. (1973) *Astrophys. J. (Lett)* 182, L85
- Lamb, D. Q. , Lamb, F. K. and Pines, D. *Nature Physical Science* (1973a) 246, 52
- Lamb, F. K. , Pethick, C. J. and Pines, D. (1973b) *Astrophys. J.* 184, 271
- Landau, L. and Lifshitz, E. (1958) "Statistical Physics" (Addison Wesley)
- Landau, L. and Lifshitz, E. (1959) "Fluid Mechanics" (Addison Wesley)
- Lewin, W. H. G. , Doty, J. , Clark, G. W. , Rappaport, S. A. , Bradt, H. V. D. , Doxsey, R. , Hearn, D. R. , Hoffman, J. A. , Jernigan, J. C. , Li, F. K. , Mayer, W. , McClintock, J. E. , Primini, F. and Richardson, J. (1976a) *Astrophys. J. (Lett.)* 207, L95
- Lewin, W. H. G. , Doty, J. , Clark, G. W. , Jernigan, J. C. , Li, F. K. and McClintock, J. E. (1976b) Preprint
- Lewin, W. H. G. , Hoffman, J. A. , Doty, J. , Hearn, D. R. , Clark, G. W. , Jernigan, J. C. , Li, F. K. , McClintock, J. E. and Richardson, J. (1977a) *Monthly Notices Royal Astron. Soc.* 177, 83
- Lewin, W. H. G. , Hoffman, J. A. , Doty, J. , Li, F. K. and McClintock, J. E. (1977b) *I. A. U. Circular* 3075
- Lewin, W. H. G. , Li, F. K. , Hoffman, J. A. , Doty, J. , Buff, J. , Clark, G. W. and Rappaport, S. A. (1977c) *Monthly Notices Royal Astron. Soc.* 177, 93
- Li, F. K. (1976) *I. A. U. Circular* 2936
- Li, F. K. , Lewin, W. H. G. , Clark, G. W. , Doty, J. , Hoffman, J. A. and Rappaport, S. A. (1977) *Monthly Notices Royal Astron. Soc.* 179, 21P

- Lichfield, E. W. and Carlson, N. E. (1967) NCAR Report No. TN-32
- Liller, W. (1976) I. A. U. Circular 2936
- Ling, J. C. (1975) J. G. R. 80, 3241
- L'Heureux, J. (1974) *Astrophys. J. (Lett.)* 187, L53
- Manchanda, R. K. (1975) *Indian J. Radio Space Phys.* 4, 177
- Markert, T. H., Backman, D. E. and McClintock, J. E. (1976) *Astrophys. J. (Lett.)* 208, L115
- Mason, K. O., Bell-Burnell, S. J. and White, N. E. (1976) *Nature* 262, 474
- Metzger, A. E. and Parker, R. H. (1974) *Astrophys. J. (Lett.)* 194, L19
- Morfill, G. E. (1971) Ph. D. Thesis (University Of London, Imperial College)
- Ogelman, H., Fichtel, C. E. and Kniffen, D. A. (1975) *Nature* 225, 203
- Palumbo, G. G. C., Pizzichini, G. and Vespignani, G. R. (1974) *Astrophys. J. (Lett.)* 189, L9
- Peterson, L. E., Schwartz, D. A. and Ling, J. C. (1973a) *J. G. R.* 78, 7942
- Peterson, L. E., Putlowe, D. W. and McKenzie, D. L. (1973b) *Symp. On High Energy Phenomena On The Sun NASA/GSFC Preprint*
- Pringle, J. and Rees, M. (1972) *Astron. and Astrophys.* 21, 1
- Quenby, J. J., Coe, M. J., Engel, A. R. and Mills, J. S. (1976) *Nature* 262, 471
- Ricker, G., Gerassimenko, M., McClintock, J. E., Ryckman, S. G. and Lewin, W. H. G. (1976a) *Astrophys. J.* 207, 333
- Ricker, G., Sheepmaker, J. E., Ballantine, J., Doty, J., Kriss, G., Ryckman, G., and Lewin, W. H. G. (1976b) *Astrophys. J. (Lett.)* 204, L73
- Rosenbluth, M. N., Ruderman, M., Dyson, F., Bahcall, J. N., Shaham, J. and Ostriker, J. (1973) *Astrophys. J.* 184, 907
- Sandford, P. W., Ives, J. C., Bell-Burnell, S. J., Mason, K. O. and Mardin, P. (1975) *Nature* 256, 109
- Seward, F. D., Page, C. G., Turner, M. J. L. and Pounds, K. A. (1976) *Monthly Notices Royal Astron. Soc.* 175, 39P
- Shakura, N. I. and Sunyaev, R. A. (1973) *Astron. and Astrophys.* 24, 337
- Share, G. H. (1976) *Astro. Space Sci.* 42, 29
- Strong, I. B., Klebesadel, R. W. and Olson, R. A. (1974) *Astrophys. J. (Lett.)* 188, L1
- Swank, J. H., Becker, R. H., Boldt, E. A., Holt, S. S., Pravdo, S. H., Rothschild, R. E., and Serlemitsos, P. J. (1976) *Bull. A. A. S.* 8, 364

- Swank, J. H. , Becker, R. H. , Boldt, E. A. , Holt, S. S. , Pravdo, S. H. and Serlemitsos, P. J. (1977) *Astrophys. J. (Lett.)* 212, L73
- Sweet, P. A. (1969) *Rev. Astron. Astrophys.* 7, 149
- Tananbaum, H. , and Tucker, W. H. (1974) "X-Ray Astronomy" (D. Reidel Publishing Co.)
- Tananbaum, H. , Chaisson, L. J. , Jones, C. , Forman, W. and Matilsky, T. A. (1977) *Astrophys. J. (Lett.)* 209, L125
- Tandberg-Hanssen, E. (1967) "Solar Activity" (Blaisdell Waltham Mass.)
- Trombka, J. I. , Eller, E. L. , Schmiedebeck, R. L. , Adler, I. , Metzger, A. E. , Gilman, D. , Gorenstein, P. and Bjorkholm, P. (1974) *Astrophys. J. (Lett.)* 194, L27
- Van-Den-Heuvel, E. P. J. (1975) *Astrophys. J. (Lett.)* 198, L109
- Weidemann, V. (1968) *Rev. Astron. Astrophys.* 6, 351
- Wheaton, W. A. , Ulmer, M. P. , Baity, W. A. , Datlowe, D. W. , Elcan, M. J. , Peterson, L. E. , Klebesadel, R. W. , Strong, I. B. , Cline, T. L. and Desai, U. D. (1973) *Astrophys. J. (Lett.)* 185, L57
- Wheeler, R. A. (1975) Ph. D. Thesis (University Of London, Imperial College)
- White, R. S. , Ryan, J. M. , Wilson, R. B. and Zych, A. D. (1978) *Nature* 271, 635
- Woodsley, S. E. and Taam, R. E. (1976) *Nature* 263, 101

Additional reference for Chapter 3.

- Kane, S. R. (1973) *Symp. On High Energy Phenomena On The Sun*  
NASA/GSFC Preprint